

INTERFEROMETRY AT LOW FREQUENCIES:
OPTICAL PHASE MEASUREMENT FOR
LISA AND LISA PATHFINDER

Von der Fakultät für Mathematik und Physik
der Gottfried Wilhelm Leibniz Universität Hannover
zur Erlangung des Grades

Doktor der Naturwissenschaften
– Dr. rer. nat. –
genehmigte Dissertation

von

Dipl.-Phys. Vinzenz Wand
geboren am 13. November 1976, in Hagenow/Mecklenburg

2007

Referent: Prof. Dr. K. Danzmann
Korreferent: Prof. Dr. W. Ertmer
Tag der Promotion: 25. Mai 2007

ABSTRACT

This work describes contributions to the design and the development of the interferometry for the technology demonstration mission *LISA Pathfinder*, which is intended to test deciding technologies in order to implement the planned space-born gravitational wave detector LISA - Laser Interferometer Space Antenna. LISA will use free floating test masses as end mirrors of interferometers - to act as reference points for the length measurement.

The mission objective of LISA Pathfinder is to prove the drag free behavior of test masses and to verify that they can be isolated from other disturbances such that the residual force noise is better than $3 \cdot 10^{-15} \text{ N}/\sqrt{\text{Hz}}$. Using interferometry the position changes of the test masses will be monitored.

The first part of this work introduces the concepts of the LISA Pathfinder interferometry and its experimental implementation. Particular attention will be payed to the optical phase readout of the heterodyne Mach-Zehnder interferometers that achieve a precision of $10 \text{ pm}/\sqrt{\text{Hz}}$ in the frequency range from 3-30 mHz.

A unique feature of this type of interferometer is that the full sensitivity is maintained for a large dynamic range (much larger than one fringe). Using *differential wavefront sensing* in addition to the longitudinal position readout attitude information of the test masses can also be obtained. The precision thus achieved is approximately $10 \text{ nrad}/\sqrt{\text{Hz}}$ (from 3-30 mHz).

In addition to the development of the interferometry on the laboratory level, measurements performed with an *engineering model* (EM) of the optical bench, are presented. The EM is a prototype of the flight hardware of similar design and dimensions.

The second part of the work is dedicated to the technology development for LISA. In particular the phase readout of the LISA interferometers provides considerably increased requirements compared to LISA pathfinder. This work describes the baseline concept and the current status of the work concerning the LISA phasemeter at the AEI.

Furthermore, an experiment concerning laser ranging will be introduced. In addition to the measurement of distance changes, LISA also requires the knowledge of the absolute distances between the spacecraft is necessary. Laser ranging is capable to provide this and is of importance beyond its application for LISA.

KEYWORDS: gravitational waves, interferometry, space, phase readout, LISA, LISA Pathfinder

ZUSAMMENFASSUNG

Diese Arbeit dokumentiert Beiträge zur Planung und Entwicklung der Interferometrie für die Technologie-Demonstrations-Mission *LISA Pathfinder*, die entscheidende Techniken zur Realisierung des geplanten weltraumbasierten Gravitationswellendetektors LISA - (Laser Interferometer Space Antenna) testen wird. LISA wird als Endspiegel der Interferometer frei fliegende Testmassen nutzen, welche die Referenzpunkte für die Längenmessung bilden.

Das Ziel von LISA Pathfinder ist es zu zeigen, dass frei fliegende Testmassen hinreichend gut von äusseren Störungen isoliert und damit kräftefrei ($3 \cdot 10^{-15} \text{ N}/\sqrt{\text{Hz}}$) gehalten werden können. Interferometrisch werden relative Positionsänderungen der Testmassen überwacht.

Im ersten Teil der Arbeit werden das Konzept der Interferometrie von LISA Pathfinder und dessen experimentelle Realisierung vorgestellt. Einen Schwerpunkt bildet hierbei die optische Phasenauslesung der heterodynen Mach-Zehnder Interferometer, welche eine Genauigkeit von bis zu $10 \text{ pm}/\sqrt{\text{Hz}}$ im Frequenzbereich von 3-30 mHz erreicht. Besonderes Merkmal dieses Interferometer Typs ist, dass die volle Sensitivität für einen grossen dynamischen Bereich zur Verfügung steht (mehrere finges). Durch den Einsatz von *Differential-wafront-sensings* können zusätzlich zur longitudinalen Auslesung, auch Lageinformationen der Testmassen gewonnen werden. Die hierbei erreichte Genauigkeit beläuft sich auf $10 \text{ nrad}/\sqrt{\text{Hz}}$ (von 3-30 mHz).

Neben der Entwicklung der Interferometrie auf Labor-Level werden Messungen an einem *Engineering Model* der optischen Bank präsentiert, das bezüglich seines Designs und seiner Ausmasse einen Prototyp der Flughardware darstellt.

Der zweite Teil der Arbeit widmet sich der Technologieentwicklung für LISA. Insbesondere die Phasenauslesung der LISA Interferometer bietet erheblich gesteigerte Anforderungen im Vergleich zu LISA Pathfinder. Beschrieben wird das *baseline concept* und der aktuelle Stand der Arbeiten zum LISA-phasemeter am AEI.

Weiterhin wird ein Experiment zum Laser Ranging vorgestellt. Zusätzlich zur relativen Abstandmessung ist für LISA die Kenntnis der absoluten Entfernung der Satelliten zueinander notwendig. Laser Ranging kann dies leisten und ist über seine Anwendung bei LISA hinaus von Bedeutung.

STICHWORTE: Gravitationswellen, Interferometrie, Weltraum, Phasenauslesung, LISA, LISA Pathfinder

CONTENTS

ABSTRACT	iii
ZUSAMMENFASSUNG	v
CONTENTS	x
LIST OF FIGURES	xiv
LIST OF TABLES	xv
LIST OF ACRONYMS	xvii
1 INTRODUCTION	1
1.1 LISA - Laser Interferometer Space Antenna	1
1.1.1 Mission concept	2
1.1.2 Sensitivity	3
1.1.3 Key technologies	5
1.2 LISA Pathfinder - The technology demonstrator mission	6
2 INTERFEROMETRY FOR THE LISA TECHNOLOGY PACKAGE	9
2.1 Interferometric concept	10
2.1.1 Heterodyne interferometry	12
2.1.2 Split interferometry	16
2.2 Expected noise sources	18
2.2.1 Frequency modulation	18
2.2.2 Laser power noise within the measurement bandwidth	19
2.2.3 ADC digitization noise	21
2.3 Implementation	25
2.3.1 Laser	25
2.3.2 Acousto-optical modulators (AOMs)	26
2.3.3 AOM driving electronics	27
2.3.4 The optical layout	30
2.3.5 Interferometer assembly	35
2.3.6 Phase measurement system	38
2.3.7 LISA Pathfinder phase measurement concept	42
2.4 Interferometer ground testing	53
2.4.1 The interferometer and the testbed	54

2.4.2	Functional tests	56
2.4.3	Functional alignment tests	57
2.4.4	Full stroke tests	57
2.4.5	Tilt tests	63
2.4.6	Performance tests	70
2.5	Conclusion	74
3	NON-LINEARITIES IN THE LTP PHASE READOUT	75
3.1	Residual phase noise at the picometer level	76
3.1.1	Description of the phenomenon	76
3.1.2	Optical pathlength difference stabilization	79
3.2	Sideband-induced noise: theory	81
3.2.1	Modelling the coupling process	81
3.2.2	Analytical description of the sideband induced phase error	85
3.3	Experimental investigation of sideband-induced errors	93
3.3.1	Setup	94
3.3.2	Conversion of electrical sidebands into optical sidebands in the AOM	95
3.3.3	Dependence on carrier level	96
3.3.4	Verification of the theory	98
3.3.5	Origin of sidebands	110
3.4	Conclusion	118
4	PHASE MEASUREMENT SYSTEM FOR LISA	119
4.1	The LISA phase measurement system	120
4.1.1	Requirements	120
4.1.2	Comparison of the Laser Interferometer Space Antenna (LISA) and the LISA Pathfinder phase measurement system	123
4.1.3	Phasemeter baseline concept	124
4.1.4	Modified approach	127
4.2	Implementation	130
4.2.1	Hardware platform	130
4.2.2	PLL as phase measurement device	131
4.2.3	DDS operation	132
4.2.4	VHDL Implementation of an ADPLL	134
4.2.5	Loop analysis	135
4.2.6	Front end readout and phase reconstruction	139
4.2.7	Noise estimation	140
4.3	Results	143
4.3.1	Lock acquisition	144

4.3.2	Phasemeter calibration	145
4.3.3	Performance	147
4.4	Conclusion	149
5	ADVANCED LINK CAPABILITIES	151
5.1	Clock synchronization, ranging and data transfer	152
5.1.1	Requirement for the laser's frequency stability	152
5.1.2	Time delay interferometry	153
5.1.3	Modulation scheme	156
5.2	First experimental steps towards advanced link capabilities	160
5.2.1	Spectrum of a PSK modulated signal	160
5.2.2	Pseudo Random noise code generation	163
5.2.3	The optical phase modulator	166
5.2.4	Ranging setup	168
5.2.5	Demodulation results	170
5.2.6	Correlation results	173
5.3	Conclusion	174
6	SUMMARY AND OUTLOOK	175
6.1	LISA Pathfinder interferometry	175
6.2	LISA Interferometry	176
A	APPENDIX A - DIGITAL SIGNAL PROCESSING	179
A.1	Digital signal processing - Nyquist Theorem	179
A.2	Some aspects of the Fourier transform and applications	179
A.3	Digitization noise	182
B	APPENDIX B - SUPPLEMENTAL MEASUREMENTS	185
B.1	Transfer function of the AM input of the AOM driver	185
B.2	Open loop gain of digital OPD stabilization and DWS servo	186
C	APPENDIX C - CIRCUITS	187
C.1	Phasemeter circuits	187
C.2	Sample and Hold circuits	194
D	APPENDIX D - LISTINGS	199
D.1	VHDL code of the DDS (abstract)	199
D.2	C implementation of a phasetracking algorithm	202
D.3	C embedded configuration of the DAP5216a	203
INDEX		207
BIBLIOGRAPHY		211

CONTENTS

DANKSAGUNG 219

CURRICULUM VITAE 221

LIST OF FIGURES

Figure 1	LISA orbits	2
Figure 2	Force noise and displacement noise for LISA and LISA Pathfinder	4
Figure 3	LISA sensitivity	5
Figure 4	Requirement breakdown	7
Figure 5	Basic setup of a non-polarizing heterodyne Mach-Zehnder Interferometer	10
Figure 6	Optical metrology system overview	11
Figure 7	Field amplitudes at a 50/50 beam combiner	13
Figure 8	Frequencies and amplitudes of the electric fields in a heterodyne Mach-Zehnder interferometer	14
Figure 9	Phase difference of two heterodyne signals	16
Figure 10	Split interferometry	17
Figure 11	Digitization error for a 4 bit ADC	21
Figure 12	Phase error due to digitization noise	22
Figure 13	Overview of requirements	24
Figure 14	The TESAT laser head and its frequency noise	25
Figure 15	Photograph of the modulation bench	27
Figure 16	Photograph and CAD drawing of the Contraves modulation bench	28
Figure 17	Block diagram of the frequency synthesizers	28
Figure 18	Measured phase noise of the frequency synthesizers	29
Figure 19	Block diagram of the power amplifier and amplitude control, and its measured RF amplitude noise	30
Figure 20	OptoCAD drawing of the reference interferometer	32
Figure 21	OptoCAD drawing of the $\chi_1 - \chi_2$ interferometer	32
Figure 22	OptoCAD drawing of the χ_1 interferometer	33
Figure 23	OptoCAD drawing of the auxiliary frequency noise interferometer	33
Figure 24	OptoCAD drawing of all interferometers, beams and components	34
Figure 25	Pictures of the fiber injectors and the alignment jig	35
Figure 26	Picture of the optical bench	37
Figure 27	Phase measurement via multiplier	38
Figure 28	Multiplier output	39
Figure 29	Mixer output for different phase states	40

Figure 30	Zero crossing phase measurement	41	
Figure 31	I-Q phase demodulation for a signal with constant frequency		43
Figure 32	Transfer function of the antialiasing filters	44	
Figure 33	Block diagram illustrating the data processing flow		48
Figure 34	QPD-quadrant labelling	49	
Figure 35	Illustration of the averaging of the longitudinal phases		50
Figure 36	Photograph of the phasemeter user interface	52	
Figure 37	Picture of the Optical Bench with photodiode harness and NTC sensors attached	54	
Figure 38	Pictures of one test mirrors substituting the test masses		55
Figure 39	Results of full stroke test with test mass TM1 actuated	61	
Figure 40	Results of full stroke test with test mass TM2 actuated	62	
Figure 41	Results of tilt test with test mass TM1	64	
Figure 42	Results of tilt test with test mass TM2	65	
Figure 43	Calibration of DWS alignment signals by linear fit to the central part of the measured data	67	
Figure 44	Calibration of DC alignment signals by linear fit to the central part of the measured data	68	
Figure 45	Photograph of the ground testing team	70	
Figure 46	Time series of the χ_1 - χ_2 measurement	71	
Figure 47	Contrast of the $\chi_1 - \chi_2$ measurement	72	
Figure 48	Linear spectral density of the $\chi_1 - \chi_2$ interferometer		73
Figure 49	Linear spectral density of the DWS alignment	74	
Figure 50	Split interferometry 2	77	
Figure 51	Time series of a $\varphi = \varphi_M - \varphi_R$ measurement	78	
Figure 52	Measurement of the periodic nonlinearity in the LTP EM interferometer	79	
Figure 53	Interferometer noise performance with OPD stabilisation		80
Figure 54	DWS sensitivity with OPD stabilisation	81	
Figure 55	Illustration of the FFT based phase measurement	82	
Figure 56	Illustration of the main beat note with presence of a spurious component at the heterodyne frequency	83	
Figure 57	Illustration of the main beat note with presents of a spurious component at the heterodyne frequency with changing phase	84	
Figure 58	Illustration of the sidebands at offsets of $\pm f_{\text{het}}$ and $\pm 2 \times f_{\text{het}}$ from both beams	86	
Figure 59	Overview of the test setup for the sideband measurements		94
Figure 60	Dependence of the coupling efficiency $\varepsilon/\varepsilon_{\text{el}}$ on the carrier power	98	
Figure 61	φ as function of Δ_F when the OPD PZT is scanned	100	

Figure 62	Experimental setup for sideband investigations using sidebands with frequency offset	101
Figure 63	Phase error induced by first- and second-order sidebands	104
Figure 64	Measured and predicted phase error by first- and second-order sidebands	104
Figure 65	Phase $\varphi = \varphi_M - \varphi_R$ when strong sidebands at an offset of f_{het} are added.	105
Figure 66	Phase $\varphi = \varphi_M - \varphi_R$ when strong sidebands at an offset of $2 \times f_{\text{het}}$ are added	105
Figure 67	Measured scaling behaviour of single sideband induced phase errors	106
Figure 68	Measured and predicted phase error by first-order sidebands for AM and FM	109
Figure 69	Spectra of AOM RF drive signal under various conditions	111
Figure 70	Spectra of AOM RF drive signal with PLL disconnected	112
Figure 71	Change in spectra of AOM RF drive signal by moving components	113
Figure 72	Spectra of AOM RF drive signal with added FM	114
Figure 73	Spectra of AOM RF drive signal with added AM	115
Figure 74	Spectra of AOM RF drive signal with added FM	116
Figure 75	Spectra of AOM RF drive signal with added FM at $2f_{\text{het}}$	117
Figure 76	Direct measurement of variations of testmass distance	120
Figure 77	Current interferometry baseline	121
Figure 78	Proposed frequency scheme for LISA	122
Figure 79	I-Q phase demodulation for a signal with constant frequency	125
Figure 80	I-Q phase demodulation for a signal with drifting frequency.	126
Figure 81	Modified phasemeter approach	128
Figure 82	Noise aliasing in alternative concept	129
Figure 83	Photograph of the first prototype hardware of LISA phasemeter	131
Figure 84	DDS scheme	134
Figure 85	Length of phase increment register and phase accumulator	135
Figure 86	Overview of the phasemeter core design	136
Figure 87	Open loop gain of the ADPLL	138
Figure 88	s-domain model of the ADPLL	139
Figure 89	PIR vs. PA readout	140
Figure 90	ADPLL test setup	144
Figure 91	Lock acquisition of the ADPLL	145
Figure 92	Frequency steps on phasemeter input	146
Figure 93	Verification of PM frequency to phase conversion	147
Figure 94	Phase noise of external 20 MHz signal	148

LIST OF FIGURES

Figure 95	Performance of the phasemeter	149
Figure 96	Illustration of TDI	154
Figure 97	Proposed frequency scheme for LISA	158
Figure 98	Carrier- and data power vs. modulation index	163
Figure 99	Typical implementation of the linear feedback shift register (LFSR)	164
Figure 100	Time series from implemented PRN generator	165
Figure 101	Spectra of Manchester and NRZ codes	166
Figure 102	Picture of the fiber coupled electro-optical modulator (EOM)	167
Figure 103	Modulation index measurement of the fiber coupled EOM	168
Figure 104	Ranging setup	169
Figure 105	Spectrum of generated PRN code	171
Figure 106	Spectrum of PRN modulated beat signal	172
Figure 107	Demodulated PRN sequence	172
Figure 108	Correlation of the initial PRN code and the demodulated replica	173
Figure 109	PRN code and demodulated replica	173
Figure 110	Illustration of the digitization process	182
Figure 111	Transfer function of the AOM driver AM input	185
Figure 112	Open loop gain of digital OPD stabilization and DWS servo	186
Figure 113	Schematic of the phasemeter prototype board - ADC converter	188
Figure 114	Schematic of the phasemeter prototype board - FPGA	189
Figure 115	Schematic of the phasemeter prototype board - parallel port interface with FIFO	190
Figure 116	Schematic of the phasemeter prototype board - clock generation and RAM	191
Figure 117	Schematic of the phasemeter prototype board - DAC output filters	192
Figure 118	Schematic of the phasemeter prototype board - DACs	193
Figure 119	Schematic of the 16 channel Sample and Hold circuit - AD781	195
Figure 120	Schematic of the 16 channel Sample and Hold circuit - power supply	196
Figure 121	Schematic of the 16 channel Sample and Hold circuit - clock dividers and buffers	197

LIST OF TABLES

Table 1	Labelling of QPDs and dedicated phases	36
Table 2	Predicted and measured DWS calibration factors	69
Table 3	Predicted and measured DC calibration factors	69
Table 4	Results of single sideband injection experiments	97
Table 5	Phase error $\delta\varphi$ rms-amplitude for different sideband orders (measured and from theory)	103
Table 6	Results of AM modulation	108
Table 7	Results of FM modulation	110
Table 8	Comparison of the LISA and the LISA Pathfinder phase measurement system	124
Table 9	List of components used on the new prototype PMS board	130
Table 10	Fourier transform theorems COUCH II (1997)	181

LIST OF ACRONYMS

A/D	analog/digital
ADC	analog to digital converter
ADPLL	all digital phase-locked loop
AEI	Albert Einstein Institute, MPI für Gravitationsphysik
AM	amplitude modulation
AOM	acousto-optical modulator
a.u.	arbitrary units
BS	beamsplitter
BPSK	binary phase shift keying
DAC	digital to analog converter
DAP	data acquisition processor
DAQ	data acquisition
DBM	double balanced mixer
DDS	direct digital synthesis
DFACS	drag free and attitude control system
DFT	discrete Fourier transform
DMU	data management unit
DRS	disturbance reduction system
DSN	deep space network
DSP	digital signal processor
DWS	differential wavefront sensing
EM	engineering model

LIST OF ACRONYMS

EOM	electro-optical modulator
ESA	European Space Agency
FIFO	first in first out
FIR	finite impulse response
FT	Fourier transform
FFT	fast Fourier transform
FTW	fastest Fourier transform in the west
FM	flight model
F/PM	frequency or phase modulation
FPGA	field programmable gate array
FSR	feedback shift register
Ge	Germanium
GPS	global positioning system
HF	high frequency
IIR	infinite impulse response
InGaAs	Indium Gallium Arsenide
IRS	inertial reference sensors
LFSR	linear feedback shift register
LISA	Laser Interferometer Space Antenna
LO	local oscillator
LPSD	logarithmic frequency axis power spectral density (C-program by M. Tröbs and G. Heinzel used for spectral analysis (Tröbs and HEINZEL, 2006))
LPF	LISA Pathfinder
LSB	least significant bit
LSD	linear spectral density
LTP	LISA technology package

LUT	look-up table
MSB	most significant bit
MZI	Mach Zehnder interferometer
NASA	National Aeronautics and Space Administration
NCO	numerically controlled oscillator
NPRO	nonplanar ring oscillator
NRZ	non return to zero
NTC	negative temperature coefficient
OB	optical bench
OBI	optical bench interferometer
OMS	optical metrology system
OPD	optical pathlength difference
PA	phase accumulator
PBS	polarizing beam splitter
PD	photodiode
PDH	Pound-Drever-Hall
PFD	phase frequency detector
PI	proportional plus integral controller (component of a classical servo design)
PID	proportional plus integral plus derivative controller (component of a classical servo design)
PIR	phase increment register
PLL	phase-locked loop
PMS	phase measurement system
PM	phasemeter
PRN	pseudo random noise
PSK	phase shift keying

LIST OF ACRONYMS

PZT	piezo-electric transducer
QAM	quadrature amplitude modulation
QPD	quadrant photodiode
QPSK	quadrature phase shift keying
RAM	random access memory
RF	radio frequency
RIN	relative intensity noise
RLU	reference laser unit
ROM	read only memory
Si	Silicon
SBDFT	single bin discrete Fourier transform
SNR	signal to noise ratio
ST7	Space Technology 7
TCVCXO	temperature compensated voltage controlled crystal oscillator
TDI	time delay interferometry
ULE	ultra low expansion glass
USO	ultra stable oscillator
VCO	voltage controlled oscillator
VHDL	very high speed hardware description language

INTRODUCTION

*"Das letzte, was man findet, wenn man ein Werk schreibt,
ist, zu wissen, was man an den Anfang stellen soll."*

BLAISE PASCAL

(1623-1662) französischer Mathematiker,
Physiker, Literat und Philosoph

1.1 LISA - LASER INTERFEROMETER SPACE ANTENNA

About a century ago, Albert Einstein described in his work on special and general relativity, the structure of space and time and thereby revolutionized the basics of physics.

One of the most exciting predictions of the theory of general relativity is the existence of gravitational waves, by which systems of accelerated masses emit energy. This is the gravitaional analog to the appearance of electro magnetic waves by accelerated charges.

Gravitational waves propagate with the speed of light and influence measured distances within its propagation medium¹. However, it proves to be extremely ambitious to detect gravitational waves, since even despite of their high energy, the interaction with the space-time is very small. This becomes clear, if one compares the enormous energy of a supernova explosion² that is partly converted into gravitational waves with the length changes they cause, for a distance earth-sun which are in the order of a diameter of a hydrogen atom, corresponding to a relative length change of $\delta L = \Delta L/L = 10^{-21}$.

Einstein himself considered gravitational waves as a pure theoretical phenomenon that will not be of experimental interest. Today, a global network of ground based gravitational wave observatories is running in continuous operation and is able to provide measurements of relative length changes of 10^{-21} by the means of laser interferometry. Technological developments

¹ Depending on their sources gravitational waves occur in the frequency regime of approximately $10^{-6} - 10^3$ Hz.

² in a neighbor galaxy

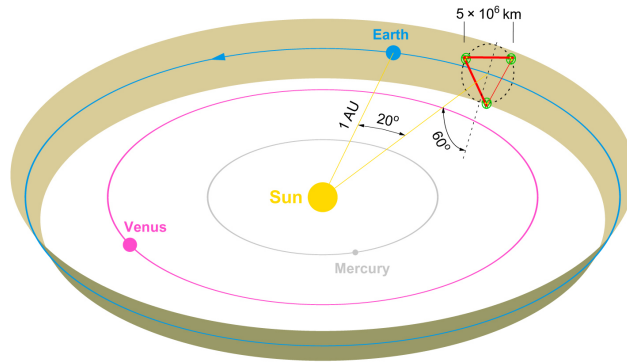


Figure 1. LISA orbits. Each of the three identical spacecraft is following the earth by 20° in a heliocentric orbit. The constellation forms an equilateral triangle with an armlength of 5 million kilometers which is 60° out of the ecliptic.

such as lasers and new concepts such as power and signal recycling applied in interferometers are the key to achieving better measurement performance.

Many interesting sources of gravitational waves emit in a frequency regime below 1 Hz. Despite the complex seismic isolation, detection by ground based detectors becomes practically impossible below 10 Hz due to various disturbances some of which are unshieldable in principle, such that only a measurement in space is promising. The Laser Interferometer Space Antenna (LISA) is a joint European Space Agency (ESA)- National Aeronautics and Space Administration (NASA) mission, designed to observe gravitational waves in the frequency regime from 0.1 mHz to 100 mHz.

1.1.1 Mission concept

Gravitational waves change the light travel time when reflected between free floating test masses. Thus, laser interferometers are the ideal measurement device in order to detect gravitational waves that change the length of the interferometer arms. Ground based detectors use "near free floating" test masses as end mirrors of the interferometers. A time delay due to a gravitational wave affects the differential round trip travel times of the light between the two interferometer arms and becomes maximal if the armlength corresponds to the half of the wavelength of the gravitational wave. For armlengths shorter than a half wavelength, the time delay is proportional to the armlength. For this case, longer arms increase the detection sensitivity. Modern interferome-

ter topologies are using advanced techniques such as signal recycling, power recycling and arm cavities in order to increase the interaction time.

LISA is a cluster of 3 identical spacecraft separated by 5 million kilometers, and will trail the Earth by 20° in an equilateral triangle formation (Figure 1). Each spacecraft carries a set of two drag-free-controlled proof masses, whose relative positions are given only by gravitational radiation. These proof masses act as end mirrors of inter-spacecraft laser interferometers.

1.1.2 Sensitivity

As light sources, LISA will utilize Nd:YAG lasers¹ with an output power of approximately 1 Watt. The beam radius after the 5 million kilometer propagation is determined by the beam size at the transmitting spacecraft. Even if the beam on the transmitter side is expanded to approximately 30 cm (the telescope aperture), in a distance of 5 million kilometers, the beam radius increases to 20 km. The light power detected by the telescope on the remote spacecraft is in the order of 100 pW.

The relative changes in separation of the proof masses will be measured with a shot noise limited sensitivity of $40 \text{ pm}/\sqrt{\text{Hz}}$ occurring as pathlength noise in the measurement. One picometer corresponds to one millionth of the used laser wavelength. An additional limiting factor is residual force noise affecting the test masses (acceleration noise, 1 kg test mass). LISA aims for a residual force noise that is better than $3 \times 10^{-15} \text{ N}/\sqrt{\text{Hz}}$. Thus, the common noise contribution of these fundamental limitations of the detection sensitivity, expressed as force noise² $S_F(\omega)$, yields (see Figure 2(a))

$$S_F(\omega) = \sqrt{\left(40 \text{ pm}/\sqrt{\text{Hz}} \cdot \omega^2\right)^2 + \left(3 \times 10^{-15} \text{ N}/\sqrt{\text{Hz}}\right)^2}, \quad (1.1)$$

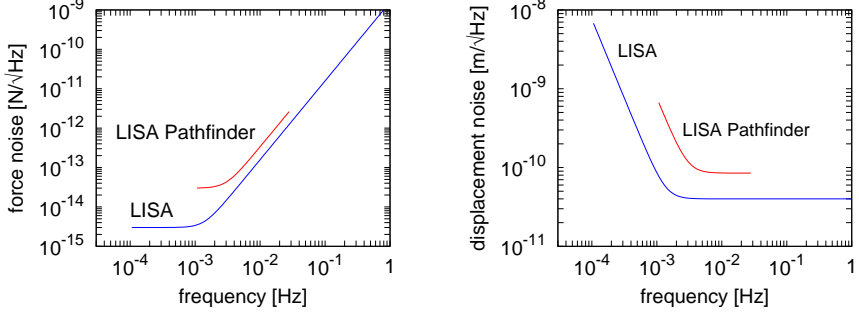
with $\omega = 2\pi f$. Equation (1.1) can also be expressed as position noise $S_x(\omega)$ (see Figure 2(b))

$$S_x(\omega) = \sqrt{\left(40 \text{ pm}/\sqrt{\text{Hz}}\right)^2 + \left(\frac{3 \times 10^{-15} \text{ N}/\sqrt{\text{Hz}}}{\omega^2}\right)^2}. \quad (1.2)$$

From Equation (1.2) the main frequency dependence of all interferometer-

¹ Nd:YAG lasers provided a high intrinsic frequency and power stability and operate at a wavelength of 1064 nm

² Pathlength noise converts in the Fourier domain into force/acceleration noise via multiplication with ω^2 .



(a) Force noise for LISA and LISA pathfinder as- (b) Displacement noise for LISA and LISA summing a test mass of 1 kg pathfinder.

Figure 2. Force noise and displacement noise for LISA and LISA Pathfinder

related noise budgets $y(f)$ can be found. This is given by

$$y(f) = y(30 \text{ mHz}) \cdot \sqrt{1 + \left(\frac{f_{\text{cutoff}}}{f}\right)^4}. \quad (1.3)$$

$y(30 \text{ mHz})$ is the pathlength noise due to the shot noise limitation of $40 \text{ pm}/\sqrt{\text{Hz}}$. The cutoff frequency (f_{cutoff}) marks the transition from shot noise limitation to force noise limitation (see Figure 2) and is given by

$$f_{\text{cutoff}} = \sqrt{\frac{3 \cdot 10^{-15}}{40 \cdot 10^{-12}}} \frac{1}{2\pi} [\text{Hz}], \quad (1.4)$$

and thus, Equation (1.3) yields:

$$y(f) = 40 \text{ pm}/\sqrt{\text{Hz}} \cdot \sqrt{1 + \left(\frac{0.001378 \text{ Hz}}{f}\right)^4}. \quad (1.5)$$

Thus LISA will be able to detect gravitational waves with a sensitivity of approximately $40 \text{ pm}/\sqrt{\text{Hz}}$ (at 3 mHz) corresponding to a strain sensitivity $h_{\text{pkpk}} = 10^{-23}$ for an integration time of 1 year and a signal to noise ratio (SNR) of 5 (Figure 3). Below 3 mHz, the sensitivity will be limited by residual acceleration noise of the proof masses. At high frequencies, the sensitivity is limited by poles at multiples of the inverse light travel time for one round trip. At these frequencies, a full period of the gravitational wave fits into one

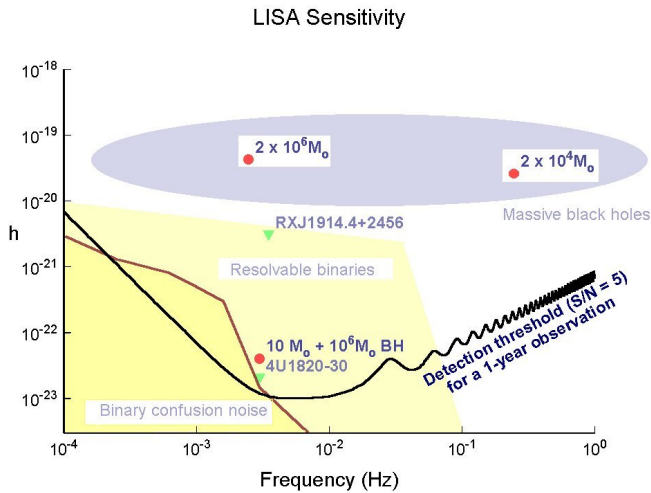


Figure 3. LISA sensitivity. LISA is designed to measure gravitational waves in the mHz range, in order to complement the observation bandwidth of ground based detectors, that is limited by seismic noise. The design sensitivity is 10^{-23} at 3 mHz for an integration time of 1 year. At low frequencies LISA is limited by the residual acceleration noise, while at high frequencies the armlength and their variations dominate. Within the measurement band of LISA, several interesting sources for gravitational wave have been located. In the low band, the sensitivity is disturbed by the binary confusion background which will be unresolvable for LISA.

arm such that the elongation of the proof masses is zero¹. In addition to the strain sensitivity of LISA, Figure 3 shows the signal strength of typical sources in the measurement bandwidth of LISA.

1.1.3 Key technologies

The LISA concept contains a number of challenging technology developments. In order to verify key technologies, such as drag-free proof masses with a residual force noise of $3 \times 10^{-15} \text{ N}/\sqrt{\text{Hz}}$ in the mHz range and picometer precision interferometry in space, the LISA technology demonstrator LISA

¹ Variation of the armlength of LISA spread the poles into a wider bandwidth

Pathfinder will be launched in 2009. *LISA Pathfinder* (LPF) currently enters its Critical Design Review (CDR) phase in the ESA/NASA project time line, and its implementation phase has already begun.

1.2 LISA PATHFINDER - THE TECHNOLOGY DEMONSTRATOR MISSION

LISA Pathfinder is an European Space Agency (ESA) mission, part of its scientific space program with contributions of National Aeronautics and Space Administration (NASA), designed to verify key technologies needed for LISA. These key technologies are not testable on ground (ANZA *et al.* (2005)).

On LISA Pathfinder (LPF) two independent technology packages (payloads) will be flown. The European side is the LISA technology package (LTP) consisting of two inertial reference sensors (IRS), the interferometer metrology system and a set of micro newton thrusters. The second payload is the disturbance reduction system (DRS), a similar experiment provided by NASA.

The launcher is a small low cost vehicle provided and operated by ESA (e.g. a ROCKOT/Dnepr launched from Plesetsk or a small ESA launcher from KURU). After the injection into a low-Earth orbit (LEO) the LPF own propulsion will transfer the spacecraft to L₁, which is Lagrange point 1 of the Earth-sun system, 1.5 million kilometers from earth. L₁ was chosen due to tight requirements to differential gravity, thermal stability and visibility from the ground station (LANDGRAF *et al.*, 2005).

The launch is planned for late 2009, followed by a half year transfer phase. After the initial commissioning, set-up and test phase, a 90 day LTP operation will be performed. The DRS operation is planned for 70 days after that. The mission ends with a joint LTP/DRS operation phase which will last about 20 days.

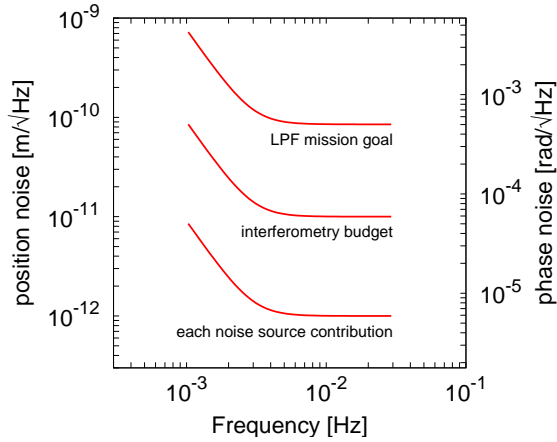


Figure 4. Requirement breakdown.

Mission objectives

LPF is intended to verify technology readiness of three key technologies needed for LISA:

- IRS providing the drag free of the test masses (VITALE, 2002),
- ultra-stable interferometry in space,
- micro newton thrusters.

The main goal of the mission is to verify the drag-free system built around two free floating test masses. In order to monitor these test masses independently and with higher accuracy ($10 \text{ pm}/\sqrt{\text{Hz}}$), an optical metrology system (OMS) consisting of a set of interferometers will be used in the mission.

Due to higher disturbances at L1 compared to the LISA orbits, the requirements to the LPF interferometry are relaxed by a factor of 10 in frequency range and sensitivity with respect to LISA. The top-level mission goal corresponds to $85 \text{ pm}/\sqrt{\text{Hz}}$ test-mass motion at 30 mHz (top curve in Figure 4), which is equivalent to $170 \text{ pm}/\sqrt{\text{Hz}}$ optical pathlength fluctuations. The allocated interferometry noise budgets is $10 \text{ pm}/\sqrt{\text{Hz}}$ (middle curve in Figure 4). For each of different noise sources, a budget of $1 \text{ pm}/\sqrt{\text{Hz}}$ was allocated (lower curve in Figure 4). All budgets are also expressed as phase noise on the right vertical axis in Figure 4.

2

INTERFEROMETRY FOR THE LISA TECHNOLOGY PACKAGE

*"Fortschritt ist der Weg vom Primitiven
über das Komplizierte zum Einfachen."*

WERNHER VON BRAUN

(1912-1977) dt.- US-amerik. Raketenforscher und -Ingenieur

This Chapter gives an overview of the optical metrology system (OMS) of the LTP and describes the development and testing of its core components performed within this work. LPF uses a heterodyne Mach Zehnder interferometer (MZI) in order to continuously monitor position and orientation two free floating test masses. The first Section 2.1 focuses on a global description of the measurement device. It gives an introduction to heterodyne interferometry and its application aboard LPF.

With the knowledge about the measuring concepts, Section 2.2 considers the influence of different expected noise sources related to the design of the interferometric measurement and derives requirements for them.

Section 2.3 is concerned with the implementation of the OMS. A Nd:YAG laser is used as light source for the LTP interferometry. Its properties are described in Section 2.3.1 including the subsequent laser modulations unit. A free beam setup laboratory level setup is presented which was tested together with a breadboard. When the interferometric design was consolidated, the individual subsystems were designed and implemented as hardware. The assembly of the optical bench interferometer (OBI) engineering model (EM) was a milestone during the preinvestigation phase¹. Its optical layout and important aspects of its assembly are described in Section 2.3.4.

A further key item within the OMS of LTP is the phase measurement system (PMS). Section 2.3.6 and 2.3.7 are dedicated to this. Starting with a comparison

¹ The preinvestigation phase is a laboratory level prototyping phase during that the global concepts of the instruments to be build are tested and verified before hardware on industrial level will be designed.

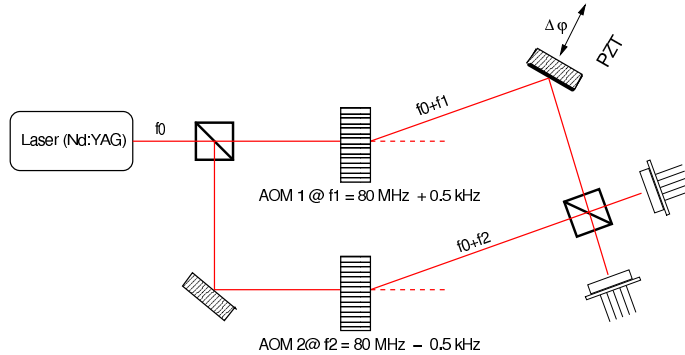


Figure 5. Basic setup of a non-polarizing heterodyne Mach-Zehnder Interferometer. A Nd:YAG laser beam is split into two beams and subsequently each of both is frequency shifted by an AOM. After travelling different paths the beams are brought to interference. Path length variations induced by a piezo electric actuator affect the phase of the interference signal.

of different phase measurement techniques, the LTP prototype phasemeter is presented.

After the development and implementation of the different subcomponents the complete setup was needed to be tested. The Chapter concludes with a report summarizing the results of the optical bench (OB) preinvestigation phase that ended with a comprehensive measurement campaign during which the OB EM and its dedicated hardware, such as modulation bench and phasemeter, were successfully shown to meet the required performance (HEINZEL *et al.* (2005a), BRAXMAIER *et al.* (2004)). The results of this OB EM ground testing campaign are summarised in Section 2.4.

2.1 INTERFEROMETRIC CONCEPT

As described in Chapter 1, onboard the LTP the free fall of two test masses will be tested. The position and orientation of these test masses need to be monitored with picometer accuracy along the sensitive x-axis independently from the capacitive sensor by an interferometer as an out-of-loop measurement device. The LISA Technology Package uses a heterodyne Mach-Zehnder interferometer for this task. Figure 5 illustrates the basic setup of a non-polarizing heterodyne Mach-Zehnder interferometer where a piezo-electric transducer (PZT)-mounted mirror represents the pathlength changes caused by the test mass motion.

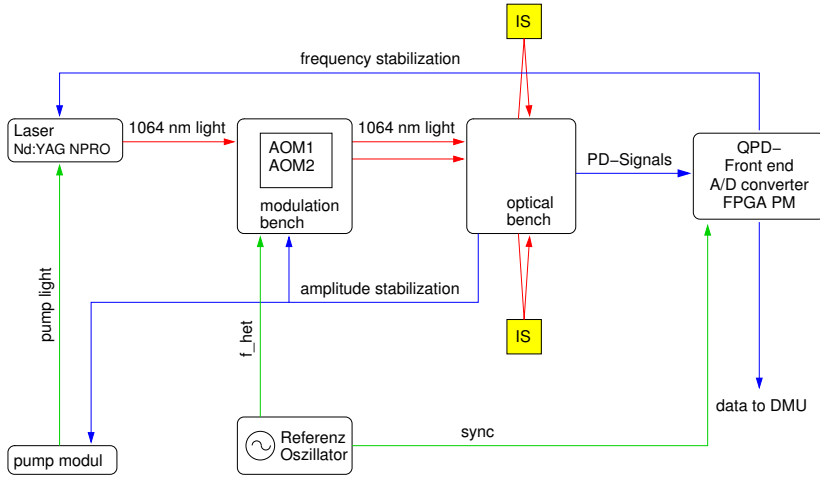


Figure 6. Optical metrology system overview

The laser beam is split in two parts, which are separately frequency shifted by acousto-optical modulators and are brought to interference at a beam-combiner after travelling different paths. The resulting beatnote oscillates at the heterodyne frequency f_{het} , e.g. the difference between the two frequency shifts applied by the AOMs. By detecting the beat note at the quadrant photodiode (QPD) and measuring the beatnote phase shift, $\Delta\varphi$ can be recovered. This needs an appropriate PMS.

Figure 6 shows schematically the OMS which consists of the reference laser unit (RLU) - a Nd:YAG NPRO with 25 mW output power at 1064 nm wavelength and the modulation bench providing the beam conditioning. The two beams with 5 mW each are injected via two polarization maintaining optical fibers onto the optical bench located in between the two test masses (IS in Figure 6). The interference signals are detected by a set of QPD. The trans-impedance preamplifiers for the QPDs are located within the phasemeter unit, which is dedicated in order to sample the data coming from the each quadrant of the photodetectors separately with a resolution of 16 bit at a sampling rate of 100 kHz¹ and to preprocess the datastreams delivering the raw phase information. The data management unit (DMU) post-processes the raw data to determine the position and angular alignments of the test masses.

¹ PM₁, PM₂: 16 bit 25 kHz
 PM₃: 18 bit 800 kHz
 PM FM: 16 bit 50 – 100 kHz
 PM=phasemeter, FM=flight model (see Section 2.3.6)

Besides the main measurement interferometers, an additional interferometer (with an intentional arm length difference) measures frequency fluctuations of the laser and is used to stabilize the laser frequency with a control loop.

In addition, as will be shown later, the laser power needs to be stabilized, too. Thus two photodiodes are foreseen to detect the laser power of the two beams, thus acting as sensors in a laser power control loop.

All frequencies used in this metrology need to be phase locked to a master reference clock, in particular f_{het} and the analog to digital converter (ADC) sampling clock.

2.1.1 Heterodyne interferometry

In order to understand the basics of the phase measurement process, this Section describes the theoretical concepts of heterodyne interferometry. Therefore these considerations focus on the interference of two frequency shifted linearly polarized laser beams at one 50/50 non-polarizing beam combiner. The formalism used here for the description of the reflection and transmission at optical components is based on HEINZEL (1999). ρ and τ are the reflection and transmission coefficients of an optical surface relating to the amplitudes of the electro-magnetic field. As the power of the field is proportional to the square of the amplitudes, the coefficients for the powers are given by

$$T = \tau^2 \quad \text{and} \quad R = \rho^2, \quad (2.1)$$

with $T + R = 1$. For this purpose any losses will be neglected. For ρ and τ this means:

$$\tau^2 + \rho^2 = 1. \quad (2.2)$$

In particular for the case of a 50/50 beam combiner (Figure 7) we have

$$\rho = \tau = \frac{1}{\sqrt{2}}. \quad (2.3)$$

The naive approach to calculate the field amplitudes c and d (see Figure 7) at the output port of a beam combiner for two interfering beams a and b shown in Equation (2.4) does not fulfill the conservation of energy (HEINZEL (1999)).

$$\begin{pmatrix} c \\ d \end{pmatrix} = \begin{pmatrix} \tau & \rho \\ \rho & \tau \end{pmatrix} \begin{pmatrix} a \\ b \end{pmatrix} \quad \text{[wrong]} \quad (2.4)$$

In this notation the input fields are represented by a and b . The output fields are written as c and d . In (HEINZEL (1999)) different possibilities are described

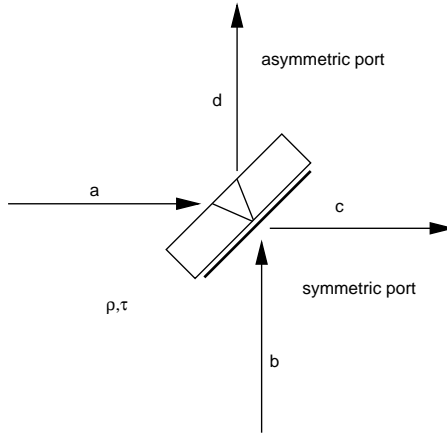


Figure 7. Field amplitudes at a 50/50 beam combiner

to solve that problem:

$$\begin{pmatrix} c \\ d \end{pmatrix} = \begin{pmatrix} \tau & -\rho \\ \rho & \tau \end{pmatrix} \begin{pmatrix} a \\ b \end{pmatrix}. \quad (2.5)$$

The negative ρ ensures the conservation of energy by inducing an extra phase jump of π at the symmetric output port of the beam combiner. This phase jump affects the fields that will be reflected at the medium with the higher optical density. For symmetry reasons often the following matrix is preferred:

$$\begin{pmatrix} c \\ d \end{pmatrix} = \begin{pmatrix} i\tau & \rho \\ \rho & i\tau \end{pmatrix} \begin{pmatrix} a \\ b \end{pmatrix}. \quad (2.6)$$

To calculate the interference at the output ports of the beam combiner, the laser fields at its inputs are assumed as $(\vec{E}_{R1}(\vec{r},t))$ and $(\vec{E}_{R2}(\vec{r},t))$, whose frequencies ω_1 and ω_2 differ by:

$$\Delta\omega = \omega_2 - \omega_1 \ll \omega_1, \omega_2 \quad (2.7)$$

with $\omega_i = 2\pi f_i$. Figure 8 is an illustration of the laser fields within the MZI. The initial beam intensity is split at a 50/50 beam splitter and the initial frequency is shifted by the AOMs. The new laser fields are recombined at the beam combiner.

For a comprehensive three-dimensional description of the two laser fields the amplitudes are time dependent and can be written as $E_{o1}(t)$ and $E_{o2}(t)$.

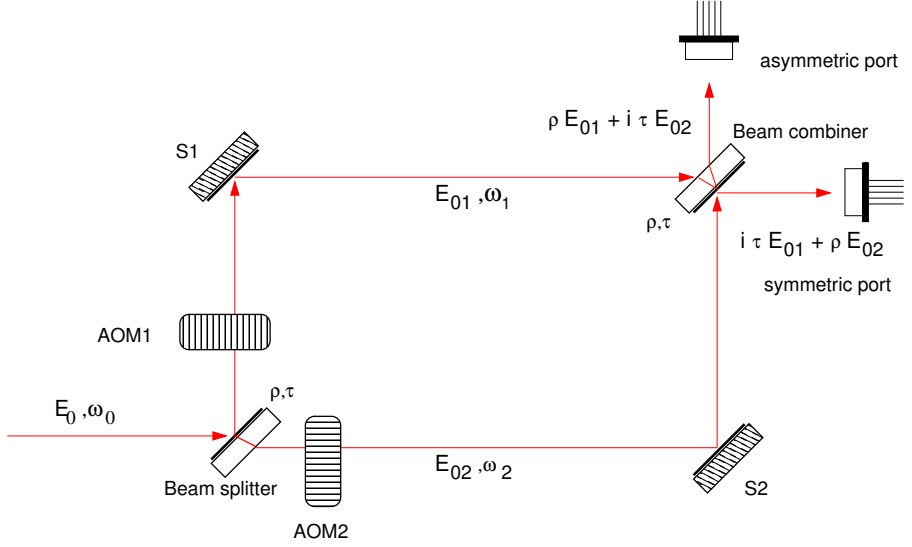


Figure 8. Frequencies and amplitudes of the electric fields in a heterodyne Mach-Zehnder interferometer

This becomes important if the effect of power fluctuations of the laser beams need to be taken into account. The two beams can be written as:

$$\begin{aligned}\vec{E}_{R1}(\vec{r}, t) &= E_{01}(t) \vec{e}_y \exp(-i(\vec{k}\vec{r} - \omega_1 t - \varphi_{R1})), \\ \vec{E}_{R2}(\vec{r}, t) &= E_{02}(t) \vec{e}_y \exp(-i(\vec{k}\vec{r} - \omega_2 t - \varphi_{R2})).\end{aligned}\quad (2.8)$$

φ_{R1} and φ_{R2} are arbitrary phases of the light fields yielding the phase difference of both at the observation point \vec{r} . Figure 8 shows the basic setup of the MZI including the initial beam E_0 which is split into two fields. Each of both is frequency shifted by an AOM. The resulting fields E_{01} and E_{02} with the frequencies ω_1 and ω_2 are recombined at the beam combiner. In order to find the main dependence of the interference signals, some simplifications can be made. The light fields will be considered as a scalar field and the position of observation will assumed to be fixed ($x = x_0 = \text{const.}$). Furthermore, at this point the field amplitudes $E_{01}(t)$ and $E_{02}(t)$ will be assumed to be constant. This leads to the following form of the fields:

$$\begin{aligned}E_{R1}(t) &= E_{01} \exp(i(\omega_1 t + \varphi_{R1})), \\ E_{R2}(t) &= E_{02} \exp(i(\omega_2 t + \varphi_{R2})).\end{aligned}\quad (2.9)$$

$E_{R1}(t)$ and $E_{R2}(t)$ are now brought to interference. The outputs of the beam

combiner are calculated according to Equation (2.6):

$$\begin{pmatrix} E_R(t)_{\text{sym}} \\ E_R(t)_{\text{asym}} \end{pmatrix} = \begin{pmatrix} i\tau & \rho \\ \rho & i\tau \end{pmatrix} \begin{pmatrix} E_{R1}(t) \\ E_{R2}(t) \end{pmatrix} = \begin{pmatrix} i\tau E_{R1}(t) + \rho E_{R2}(t) \\ \rho E_{R1}(t) + i\tau E_{R2}(t) \end{pmatrix}. \quad (2.10)$$

The photocurrent (which is proportional to the light power) measured at a photodetector at the symmetric output port is given by

$$\begin{aligned} I_{\text{Ref}}(t)_{\text{sym}} &\propto |i\tau E_{R1}(t) + \rho E_{R2}(t)|^2 \\ &\propto (i\tau E_{R1}(t) + \rho E_{R2}(t)) (i\tau E_{R1}(t) + \rho E_{R2}(t))^* \\ &\propto \tau^2 E_{01}^2 + \rho^2 E_{02}^2 + i\tau\rho (E_{R1}(t)E_{R2}(t)^* - E_{R2}(t)E_{R1}(t)^*) \\ &\propto \tau^2 E_{01}^2 + \rho^2 E_{02}^2 + 2\tau\rho E_{01}E_{02} \sin(\Delta\omega t + \varphi_{R2} - \varphi_{R1}), \end{aligned} \quad (2.11)$$

whilst the phase of the current at the asymmetric port is shifted by π^1 :

$$I_{\text{Ref}}(t)_{\text{asym}} \propto \rho^2 E_{01}^2 + \tau^2 E_{02}^2 \underbrace{- 2\tau\rho E_{01}E_{02} \sin(\Delta\omega t + \varphi_{R2} - \varphi_{R1})}_{\pi \text{ phase jump compared to 2.11}}. \quad (2.12)$$

$I_{\text{Ref}}(t)_{\text{sym}}$ and $I_{\text{Ref}}(t)_{\text{asym}}$ will be called *heterodyne signals*. Equation (2.11) and (2.12) show that the periodicity of the heterodyne signals is given by the frequency difference of the two interfering beams. The phase difference $\varphi_{R1} - \varphi_{R2}$ represents the arm length difference between the two paths $\Delta L = L_2 - L_1$ and can be written as:

$$\Delta\varphi = \frac{2\pi\Delta L}{\lambda}, \quad (2.13)$$

where λ is the wavelength of the light used². LPF uses one of the two arms as a reference length while the other one contains the pathlength whose length changes have to be measured. Taking into account that $\rho = \tau = \frac{1}{\sqrt{2}}$ and assuming $E_{01} = E_{02} = 1$ Equation (2.11) and (2.12) yielding to

$$I_{\text{Ref}}(t) \propto 1 \pm \cos\left(2\pi f_{\text{het}} t + \frac{2\pi\Delta L}{\lambda}\right). \quad (2.14)$$

The observable for the MZI is this phase difference which will be estimated by a measurement of the heterodyne signal detected by a photodiode (PD):

$$\cos \varphi = \cos(\Delta\omega t + \Delta\varphi) = \cos\left(2\pi f_{\text{het}} t + \frac{2\pi\Delta L}{\lambda}\right). \quad (2.15)$$

Figure 9 illustrates the phase difference $\delta\varphi$ between two heterodyne signals.

- ¹ The constant phase difference of π between the two complementary output ports of the beam combiner has been often used to test the performance of phase measurement systems.
- ² For the case of an Nd:YAG laser $\lambda = 1064 \text{ nm}$

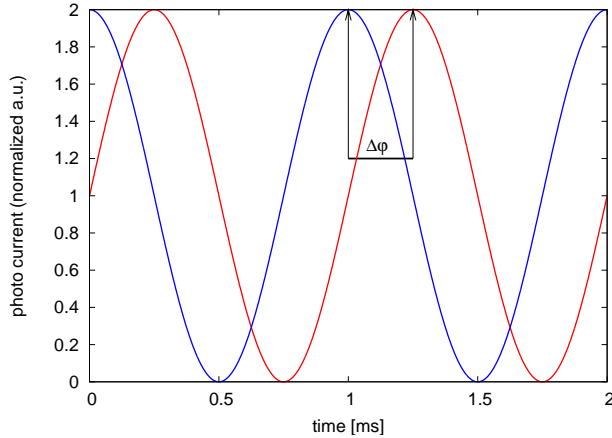


Figure 9. Phase difference of two heterodyne signals

2.1.2 Split interferometry

Since the interferometry of LFP needs to monitor the positions of two test masses with picometer accuracy, a single MZI is not sufficient to provide this feature.

This is due to the presence of the AOMs in each path of the interferometer and the resulting impossibility to have the whole interferometry mounted on an ultra stable optical bench.

To monitor both test masses aboard LFP, four MZI are necessary. A reference interferometer measures a reference phase which contains all environmental noise such as thermal and mechanical fluctuations that affect the unstable part of the interferometer. The two main interferometers measure the relative pathlength fluctuations between the first test mass and the optical bench, and the relative distance of the two test masses to each other. A fourth interferometer is sensitive to laser frequency noise and its output signal is used for an active stabilization of the laser.

For each of the main longitudinal phase measurements the differential phase between the reference and the relevant measurement interferometer $\varphi = \varphi_R - \varphi_M$ is calculated to determine the actual displacement of the test masses. Figure 9 shows idealized the heterodyne signals (for arbitrary frequencies and amplitudes) for two interferometers and the phase difference between them. As shown in Figure 10, the LTP interferometry is split into two functional parts. The modulation bench provides the beam preparation.

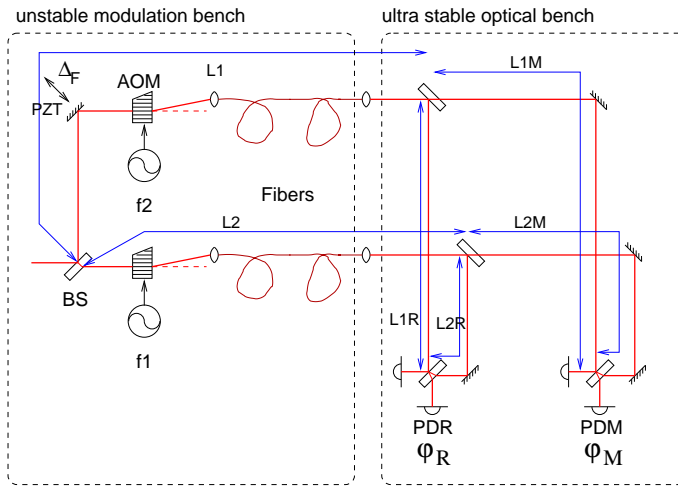


Figure 10. Illustration of the split interferometry. The LTP interferometry consists of the modulation bench and the ultra stable optical bench. Pathlength fluctuations of the unstable part of the interferometry are measured in each individual interferometer and cancel in the differential phase $\varphi_R - \varphi_M$. The differential phase only contains pathlength fluctuations coming from the optical bench. Not shown in this picture are the test mass positions which are part of the stable optical paths.

A 25 mW linear polarized single mode and single frequency laser beam with a wavelength of 1064 nm is divided into two parts by a 50/50 beam splitter. Each of the two beams is separately frequency shifted by an AOM. This first part of the OMS is, due to the heat dissipation of the AOM (as both are driven by a 80 MHz RF signal with a power of 2 Watts), separated from the ultra stable optical bench.

The modulation bench (including the optical fibres which are guiding the two beams to the optical bench) constitutes the common first part of four interferometers in total. In other words, the optical paths L_1 and L_2 are part of each interferometer. The differential pathlength fluctuations ΔF affecting the unstable part of the interferometer appear in the reference interferometer as well as in the measurement interferometer. Their phases φ_R and φ_M will be subtracted such that the noise ΔF should cancel (*noise cancellation*), and the differential phase $\varphi_R - \varphi_M$ contains exclusively the pathlength variations on the ultra stable optical bench¹.

¹ The test masses aboard LISA Pathfinder acting as mirrors within the ultra stable part of the

2.2 EXPECTED NOISE SOURCES

2.2.1 Frequency modulation

Frequency fluctuations δf of the laser in a heterodyne MZI with unequal arm-lengths directly affect the phase of the heterodyne signal. Assuming an arm-length difference ΔL and the two light fields with the frequencies ω_1 and ω_2 such that with

$$\begin{aligned}\omega_1 &= \omega_0 - \omega_{\text{het}}, \\ \omega_2 &= \omega_0,\end{aligned}\tag{2.16}$$

the fields can be written as

$$\begin{aligned}E_1(t) &= E_{01} e^{i\Phi_1(t)}, \\ E_2(t) &= E_{02} e^{i\Phi_2(t)}\end{aligned}\tag{2.17}$$

where $\Phi_1(t)$ and $\Phi_2(t)$ are the full phase arguments ($\omega t + \varphi$) plus the additional sinusoidal laser frequency modulation under study, which is introduced with Fourier frequency ω_m and amplitude $\Delta\omega$. Thus we can write, using the identity $\varphi = \int dt\omega$:

$$\begin{aligned}\Phi_1(t) &= \int dt [\omega_0 - \omega_{\text{het}} + \Delta\omega \sin(\omega_m t)], \\ &= (\omega_0 - \omega_{\text{het}})t - \frac{\Delta\omega}{\omega_m} \cos(\omega_m t) + \varphi_1\end{aligned}\tag{2.18}$$

$$\begin{aligned}\Phi_2(t) &= \int dt (\omega_0 + \Delta\omega \sin(\omega_m t)) \\ &= \omega_0 t - \frac{\Delta\omega}{\omega_m} \cos(\omega_m t) + \varphi_2.\end{aligned}\tag{2.19}$$

The integration constant φ_1 is set to zero without loss of generality

$$\varphi_1 = 0,\tag{2.20}$$

while φ_2 is associated with the pathlength difference ΔL between the interferometer arms.

$$\varphi_2 = \frac{2\pi\Delta L}{\lambda}\tag{2.21}$$

interferometer

φ_2 can be expressed as a time delay $\tau = \frac{\Delta L}{c}$ for the field $E_2(t)$. Equation (2.19) becomes

$$\begin{aligned} E_1(t) &= E_{01} \exp(i(\omega_0 - \omega_{\text{het}})t) \exp\left(-i\frac{\Delta\omega}{\omega_m} \cos(\omega_m t)\right), \\ E_2(t) &= E_{02} \exp(i\omega_0(t - \tau)) \exp\left(-i\frac{\Delta\omega}{\omega_m} \cos(\omega_m(t - \tau))\right). \end{aligned} \quad (2.22)$$

If now both fields are brought to interference with equal amplitudes ($E_{01} = E_{02} = 1$), the photocurrent at the detector is given by

$$\begin{aligned} I_{\text{PD}} &\propto |E_1(t) + E_2(t)|^2 \\ &\propto 1 + \cos(\omega_{\text{het}}t - \omega_0\tau - \Phi(t)). \end{aligned} \quad (2.23)$$

where $\Phi(t)$ is HEINZEL *et al.* (2002c):

$$\Phi(t) = -\Delta\omega \tau \sin\left(\omega_m t - \frac{\omega_m \tau}{2}\right) \times \frac{\sin\left(\frac{\omega_m \tau}{2}\right)}{\left(\frac{\omega_m \tau}{2}\right)}. \quad (2.24)$$

The leading factor $\Delta\omega \tau$ determines the coupling of a sinusoidal frequency modulation with an amplitude $\Delta\omega$ into phase. This can be expressed for frequency fluctuations $\delta\omega$

$$\begin{aligned} \delta\varphi &= \tau \cdot \delta\omega \\ &= \frac{\Delta L}{c} \cdot \delta\omega. \end{aligned} \quad (2.25)$$

Hence frequency fluctuations $\delta\omega$ in rad/s/ $\sqrt{\text{Hz}}$ couple directly via a time delay between the two arms into a phase fluctuations $\delta\varphi$ measured in rad/ $\sqrt{\text{Hz}}$. This leads to a requirement for the frequency stability of the laser:

$$\delta f = \frac{c}{2\pi\Delta L} \cdot \delta\varphi \quad (2.26)$$

$$= \frac{c}{2\pi\Delta L} \cdot 5.9 \cdot 10^{-6} \text{ rad}/\sqrt{\text{Hz}} \cdot \sqrt{1 + \left(\frac{3 \text{ mHz}}{f}\right)^4}, \quad (2.27)$$

assuming an allocation of 1 pm/ $\sqrt{\text{Hz}}$ with the usual frequency dependence. Assuming a maximum pathlength difference of 1 cm, a frequency stability of 40 kHz/ $\sqrt{\text{Hz}}$ is needed at 3 mHz and 28 kHz/ $\sqrt{\text{Hz}}$ from 30 mHz (see Figure 13(b)).

2.2.2 Laser power noise within the measurement bandwidth

Since the test masses, acting as mirrors, need to be controlled drag free, the radiation pressure caused by the reflection of the laser light at the test mass

surface is a process to be taken into account. A constant laser power P yields a DC force $F = 2P/c$ (for normal incidence) which can be neglected since it is outside the measurement bandwidth from 3-30 mHz. The numerical value for this DC force is (under the assumption of a 5 mW beam) $1.7 \cdot 10^{-11}$ N which is comparable to static gravity imbalance on the spacecraft. Fluctuations of the laser power cause a fluctuating radiation pressure and consequently a fluctuating force given by:

$$\widetilde{\delta F} = \frac{2 \widetilde{\delta P}}{c}. \quad (2.28)$$

disturbing the free fall of the test masses. With the test mass m the acceleration noise can be estimated as:

$$\widetilde{\delta a} = \frac{\widetilde{\delta F}}{m} = \frac{2 \widetilde{\delta P}}{mc} \quad (2.29)$$

The laser power noise often is expressed as relative intensity noise (RIN) given by:

$$\text{RIN} = \frac{\widetilde{\delta P}}{P}. \quad (2.30)$$

where P is the DC power of the light. Therewith Equation (2.29) can be written as

$$\widetilde{\delta a} = \frac{\widetilde{\delta F}}{m} = \frac{2P}{mc} \left(\frac{\widetilde{\delta P}}{P} \right). \quad (2.31)$$

This Equation can be solved for x in the Fourier domain, leading to:

$$\widetilde{\delta x} = \frac{\widetilde{\delta a}}{\omega^2} = \frac{2P}{m\omega^2 c} \left(\frac{\widetilde{\delta P}}{P} \right), \quad (2.32)$$

where $\omega = 2\pi f$. The position noise of the test mass converts via a factor of 2 into optical pathlength noise measured by the interferometer yielding

$$\widetilde{\delta s} = 2 \widetilde{\delta x} = \frac{4P}{m\omega^2 c} \left(\frac{\widetilde{\delta P}}{P} \right), \quad (2.33)$$

$$\left(\frac{\widetilde{\delta P}}{P} \right) = \frac{m c f^2 \pi^2}{P} \widetilde{\delta s}. \quad (2.34)$$

By using the following allocation for the optical pathlength noise:

$$\widetilde{\delta s}(f = 3 \dots 30 \text{ mHz}) = 1 \text{ pm}/\sqrt{\text{Hz}} \cdot \sqrt{1 + \left(\frac{3 \text{ mHz}}{f} \right)^4} \quad (2.35)$$

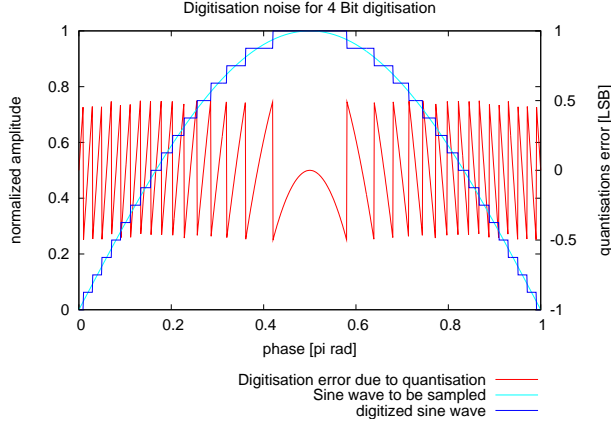


Figure 11. Digitization error for a 4 bit ADC

and a test mass of 2 kg, the required **RIN** of the laser can be calculated as:

$$\text{RIN} = \left(\frac{\delta P}{P} \right) = 2.7 \cdot 10^{-5} \frac{1}{\sqrt{\text{Hz}}} \sqrt{1 + \left(\frac{f}{3 \text{ mHz}} \right)^4} \cdot \left[\frac{\text{m}}{2 \text{ kg}} \right] \cdot \left[\frac{\text{P}}{2 \text{ mW}} \right]^{-1} \cdot (2.36)$$

Figure 13(c) shows this requirement.

2.2.3 ADC digitization noise

Since the **LTP** phasemeter is based on a rapid digitization of the heterodyne signals, the digitization noise induced by the **ADC** is a noise issue to be investigated. Digitization noise is a special kind of amplitude noise since it affects directly the amplitude of the heterodyne signal to be measured. While the signal to be digitized is a continuously varying voltage, the **ADC** delivers $n = 2^B$ discrete quantization steps each representing a voltage range of U_{LSB} given by:

$$U_{\text{LSB}} = \frac{U_{\text{max}}}{2^B}, \quad (2.37)$$

where U_{max} is the dynamic range of the **ADC** and B its effective number of bits. The maximum error of the digitized value compared to the origin continuous input voltage at the **ADC** is 1 least significant bit (**LSB**). The peak-to-peak amplitude of this error is equivalent to $\frac{1}{2}$ **LSB**. Figure 11 shows the amplitude error due to digitization noise for the case of a 4 bit converter. From Figure 11

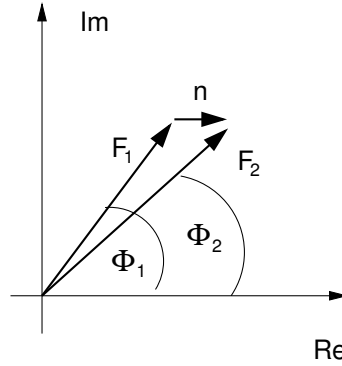


Figure 12. Phase error due to digitization noise

can be easily seen that the noise power of the error distributes over a wide frequency range in the frequency domain. In fact, under certain assumptions that are fulfilled here, the quantization noise has a white noise characteristic and its linear spectral density is described by (see Appendix A.3):

$$\hat{n}_{\text{dig}} = \frac{U_{\text{max}} 2^{-B}}{\sqrt{6} \cdot f_{\text{sampl}}}. \quad (2.38)$$

U_{max} is the dynamic range, B is the effective number of bits and f_{sampl} the sampling rate of the ADC.

Figure 12 shows how this error affects the phase measurement. F_1 represents an arbitrary sine wave as a complex vector and its phase Φ_1 . In contrast to a similar picture Φ_1 is here still not referred to a reference phase (e.g. from a fast Fourier transform (FFT)) but is the full argument of the sine wave:

$$\Phi_1 = 2\pi f_{\text{het}} t + \varphi_1. \quad (2.39)$$

The phase to be measured φ_{meas} is obtained by referring Φ_1 to a reference phase Φ_{ref} :

$$\Phi_{\text{ref}} = 2\pi f_{\text{het}} t + \varphi_{\text{ref}} \quad (2.40)$$

such that

$$\varphi_{\text{meas}} = \Phi_1 - \Phi_{\text{ref}} = \varphi_1 - \varphi_{\text{ref}}. \quad (2.41)$$

n represents the digitization error affecting only the real part of the signal. F_2 is the resulting signal with the phase Φ_2 . The phase error is given by

$\Phi_{\text{err}} = \Phi_2 - \Phi_1$. This error can be estimated as

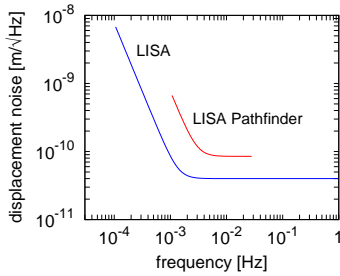
$$\Phi_{\text{err}} = \frac{n}{|F_1| \approx |F_2|} \cdot \sin(\Phi_1). \quad (2.42)$$

For the worst case scenario where the error n is $\frac{\pi}{2}$ phase shifted with respect to the signal the phase error is $\varphi_{\text{err}} = \frac{n}{F_1}$. Taking into account the white noise distribution of the linear spectral density of the quantization noise of an ADC (Equation (2.38)) and setting $U_{\text{max}} = |F_1|$ Equation (2.42) yields

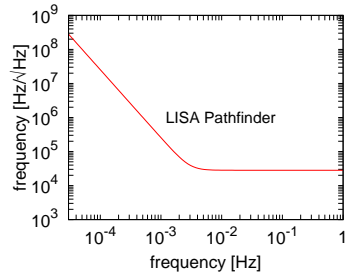
$$\tilde{\varphi}_{\text{dig}} \approx \frac{2^{-B}}{\sqrt{6} \cdot f_{\text{Sampl}}} \cdot \sin(\varphi_1). \quad (2.43)$$

$\tilde{\varphi}_{\text{dig}}$ is the linear spectral density of the phase noise (which does not depend on the Fourier frequency) of a sinusoidal signal caused by digitization noise. Figure 13(d) shows the digitization noise induced phase noise for different ADC resolutions depending on the sampling frequencies.

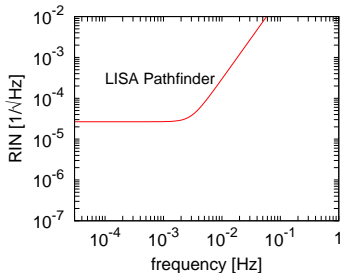
In order to achieve the necessary noise requirement of $1 \text{ pm}/\sqrt{\text{Hz}}$, an ADC with an effective resolution of 12 bits at a sampling rate of 100 kHz is sufficient. Since the effective resolution of common ADCs is 1-2 bits lower than specified, 16 bit ADCs with an update rate of 100 kHz were chosen for the LTP flight model (FM) phasemeter.



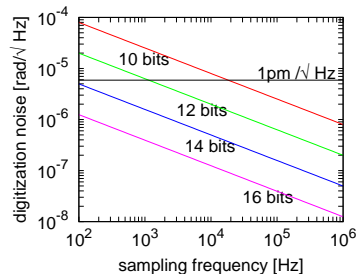
(a) Pathlength noise requirement



(b) Frequency stability requirement



(c) Requirement on RIN at low frequencies.



(d) Digitization noise

Figure 13. Overview of requirements.

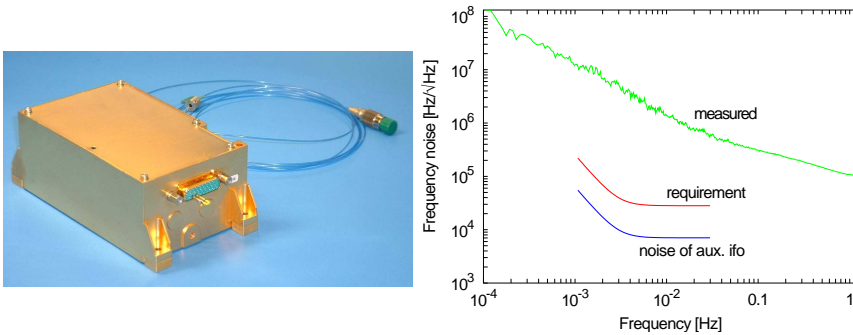


Figure 14. The TESAT laser head and its measured free-running frequency noise (top curve). The middle curve is the frequency noise requirement (to be achieved by frequency stabilization using the signal from the auxiliary interferometer), and the lower curve shows the predicted noise level of that interferometer.

2.3 IMPLEMENTATION

2.3.1 Laser

Two different models of Nd:YAG NPRO lasers were used in the optical setup at different times. This type of laser has a low intrinsic frequency noise - typically characterized by a $\frac{10 \text{ kHz}}{f} / \sqrt{\text{Hz}}$ envelope over a wide frequency range (TRÖBS (2005), BURDACK *et al.* (2004)) - due to its monolithic resonator which is simultaneously the active medium. The emitted light has a wavelength of approximately 1064 nm. The laser operates in single transverse mode and single frequency and its output is linearly polarized. The first laser used was a TESAT laser (Figure 14) which is a preflight model of the laser intended to be used for the LTP. This laser is fiber coupled and delivers 25 mW at the end of an optical fiber. The second laser was an INNOLIGHT MEPHISTO 500 delivering up to 500 mW as a free beam which needs external fiber coupling. The measured frequency noise of the free-running TESAT laser is shown in Figure 14. In addition to that the pictures shows the required frequency stability for the interferometers with a pathlength difference of 1 cm (see Section 2.2.1 and Figure 13(b)) and the predicted sensitivity to frequency noise of the auxiliary frequency interferometer with a pathlength difference of 40 cm. The results of the performance test described in Section 2.4 did not depend on which laser was used, and they could both be used interchangeably.

In spite of the low frequency noise of both lasers, a frequency stabiliza-

tion is necessary¹. Each laser has two frequency actuators - a fast one with a bandwidth of approximately 100 kHz, which is a [PZT](#) acting on the laser crystal, and a slow one with approximately 1 Hz bandwidth realized by a Peltier element changing the crystal temperature.

2.3.2 *Acousto-optical modulators (AOMs)*

As explained in Section [2.1](#), the initial laser beam was split into two parts, with each separately frequency shifted by an [AOM](#) and then fiber coupled afterwards. The [AOM](#) consists of a crystal which is transparent for the wavelength of the laser. A [PZT](#) transducer mounted on the crystal induces ultrasonic waves in the crystal that cause periodic density fluctuations. Thus the crystal acts as a phase grating for a light beam incident perpendicular to the ultrasonic wave. A more detailed description of this effect can be found in [YARIV \(1989\)](#). The deflected light gets a frequency shift equal to the ultrasonic frequency. The amplitude of the ultrasonic wave determines the deflection efficiency and can be changed by the RF power applied to the [PZT](#). For the preinvestigation setup two [AOM](#) made by ISOMET have been used whose nominal operating frequency is specified at 80 MHz. In order to deflect about 80 % of the incident beam into the first order, a RF power of 2 W or 33 dBm is necessary. Figure [15](#) shows the free-beam modulation unit.

In the foreground the INNOLIGHT laser can be seen with its dedicated optics such as a Faraday isolator and a single-mode fiber. After the fiber injector at the end of the optical fibre a beam splitter splits the beam into the two interferometer arms. In each arm an [AOM](#) can be seen. The two frequency shifted beams are fibre coupled. Due to the fact that this setup was assembled from standard optical components, it provides high flexibility e.g. to implement additional optical components such as a [PZT](#) mounted mirror in order to stabilize the optical pathlength difference between the two fiber paths (see section [3.1.2](#)). A second modulation bench with the same functionality was manufactured as pre-EM, very similar in size and weight to the flight model. Its very compact form and the completely fiber coupled setup made this modulation bench, manufactured by Contraves, easy to use. Figure [16](#) shows a picture and the CAD drawing of this modulation bench. The photograph shows the Contraves box containing the first beam splitter and the two [AOMs](#). Furthermore one can see the two optical output ports (fibers attached) delivering the two frequency shifted beams, the optical input and the two 80 MHz RF inputs. The main disadvantage of this modulation unit was its low coupling efficiency which could not be optimized due to the compact assembly. However, the two modulation units could be used

¹ The frequency stabilization is not discussed in this work

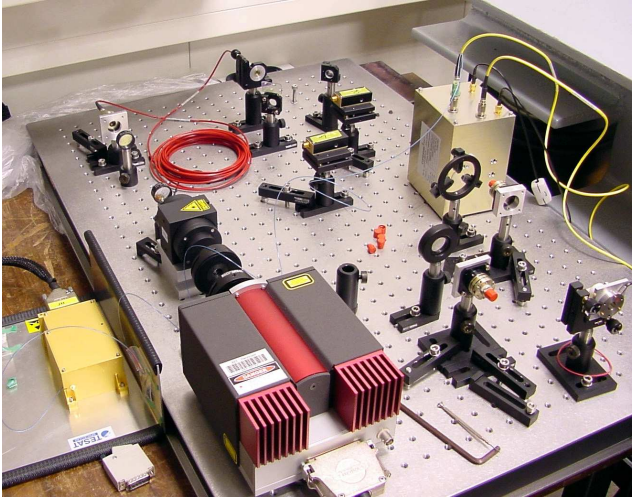


Figure 15. The modulation bench, showing (from left to right) the TESAT laser, the Innolight laser, the discrete (free-beam) modulation and fiber coupling components and the Contraves bench. In this picture, the fibers are connected such that the TESAT laser and the Contraves bench are used. The alternative components could be used by reconnecting the fibers.

interchangeably. Because of the necessity to implement the optical pathlength difference (OPD) stabilization for the performance tests, we have used the free-beam setup for most of the tests.

2.3.3 AOM driving electronics

A critical item for a sufficient performance of the whole interferometry is the AOM driving electronics. Both AOMs need to be driven by 2 Watts near 80 MHz, with a frequency difference of the heterodyne frequency (1623 Hz in the case of the EM, for the FM exactly 1000 Hz) between them. Since this frequency difference determines the frequencies and the phase of the optical heterodyne signal, both 80 MHz signals need to be offset phase locked with a precision better than the required optimal phase noise of $5.90 \times 10^{-6} \text{ rad}/\sqrt{\text{Hz}}$ at the heterodyne frequency. The driving electronics providing the required power and phase stability of the RF signals were developed and built at the AEI during the preinvestigations and were used for all tests. Figure 17 shows a block diagram of the frequency synthesizers. The output of each of the two 80 MHz temperature compensated voltage controlled crystal oscillator

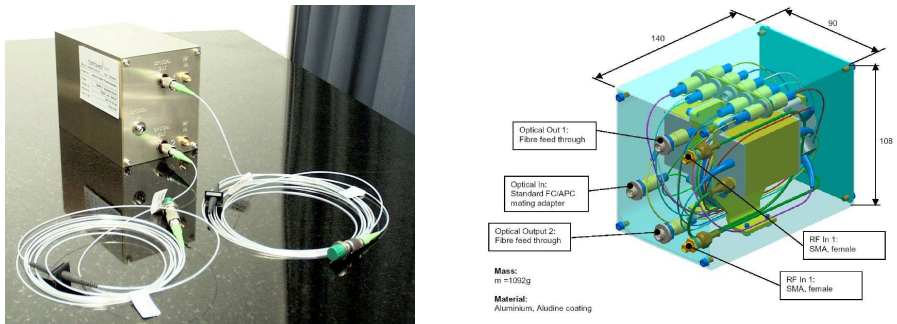


Figure 16. Photograph and CAD drawing of the Contraves modulation bench.

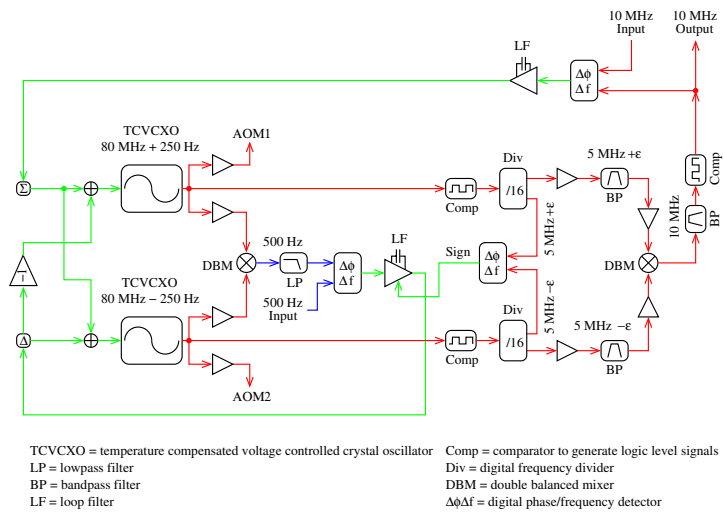


Figure 17. Block diagram of the frequency synthesizers. 500 Hz is used in the Figure as example for the heterodyne frequency, which was in reality 1623 Hz in our tests.

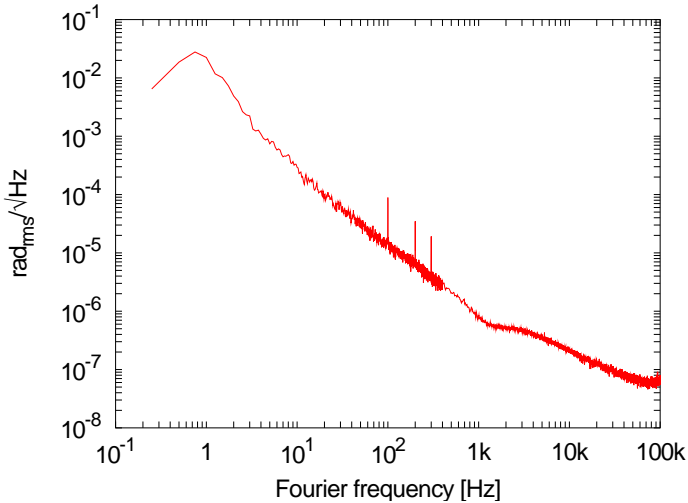
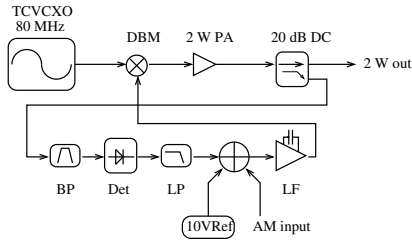


Figure 18. measured phase noise of the frequency synthesizers.

(TCVCXO)s is split into three paths. One path of each is connected to the AOM radio frequency (RF) power amplifier. The second path of each is the inputs of a double balanced mixer (DBM) that detects the frequency difference of both TCVCXOs which is compared with the heterodyne frequency reference by a digital phase frequency detector (PFD). Its output is used to control the frequency difference of both TCVCXOs. The third path of each TCVCXO is used to detect via a further DBM the sum frequency of the TCVCXO in order to control their center frequencies to be exactly around 80 MHz. Figure 18 shows the phase noise measured with this system, which is smaller than 10^{-6} rad/ $\sqrt{\text{Hz}}$ at 1 kHz.

Figure 19 shows a block diagram of the power amplifier including the amplitude control circuit. The DBM is used as a current-controlled attenuator for the input level of the power amplifier. The amplified signal is split by a power splitter. The main path is connected directly to the AOM, and the power of the low level path is compared to a 10 V voltage reference after rectification by Schottky diodes. The error signal thus obtained is the control voltage for the DBM. The adder shown in Figure 19 provides a fast amplitude modulation (AM) input (BW > 100 kHz) in order to shift the operating point of the circuit such that light power fluctuations that are measured at the end of the optical fibers can be fed back for compensation. A laser power stabilization with a bandwidth of 50 kHz using the AM input as an actuator



TCVCXO = Temp. compens. VCXO
 DBM = double balanced mixer (used as attenuator)
 PA = Power Amplifier
 DC = Directional Coupler
 BP = 80 MHz Bandpass
 Det = Schottky Detector
 LP = 10 MHz Lowpass
 LF = Loop Filter

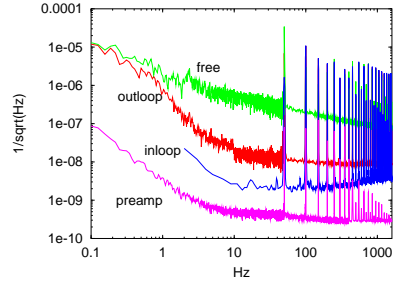


Figure 19. Block diagram of the power amplifier and amplitude control, and its measured RF amplitude noise.

was implemented (see Appendix B.1). The RF amplitude noise measured of the system is shown in Figure 19 as RIN of the signal, which is smaller than $\approx 10^{-8} / \sqrt{\text{Hz}}$ at 1 kHz.

2.3.4 The optical layout

Different interferometer topologies were suggested during a tradeoff study in order to decide the most promising candidate fulfilling the design requirements, which are:

1. *ability to monitor the test masses along the sensitive (x-) axes with picometer accuracy* Position changes of the test masses with respect to each other need to be monitored and the pathlength changes between each of the test masses and the optical bench.
2. *differential wavefront sensing (DWS)*, since the alignment of the two test masses needs to be monitored, the interferometer has to act as an alignment sensor. The most powerful technique providing this is DWS. The layout should give the ability to implement this technology.
3. *continuous tracking of the test mass over several wavelengths* - This constraint cannot be fulfilled by common Michelson or Fabry Perot interferometers since a fixed operating point is needed for optimal precision.
4. *as simple as possible optical layout*: This requirement initially suggests the usage of polarizing components which allows normal beam incidence

on the test masses¹. However, the temperature dependency of polarizing components and could potentially limit the performance as well as the imperfection of polarizing components with respect to their polarizing properties (HEINZEL and HERDEN (2002)).

The design constraints mentioned above lead to a fast convergence of the different interferometer designs with the result that the nonpolarizing Mach Zehnder interferometer can provide the required functionality.

Figures 20-24 show the OptoCAD model of the interferometer². The path-length difference of 356.7 mm between the measurement and the reference arm is compensated by an extra delay in the fiber path of the reference interferometer. In total there are four interferometers:

1. The reference interferometer measures environmentally induced path-length noise (mainly occurring within the fiber paths). The phases of the other interferometers are referenced to the output phase φ_R of the reference interferometer.
2. The X1 interferometer measures the pathlength variations of TM1 with respect to the optical bench (the associated phase is labelled as φ_1 and is also used as error signal for the OPD stabilization (see Section 3.1.2)).
3. The X12 interferometer measures the pathlength variations between TM1 and TM2 delivering the phase φ_{12} .
4. And the frequency interferometer with an intentional pathlength difference intended to detect laser frequency noise measures the phase φ_F .

Remark: *The FM layout was changed in some details.*

¹ for the incoming and the reflected beam the same optical components could be used

² In fact, the pictures show only the second part of the interferometer located on the optical bench while the first part, as described in Section 2.1.2, is located at the modulation bench.

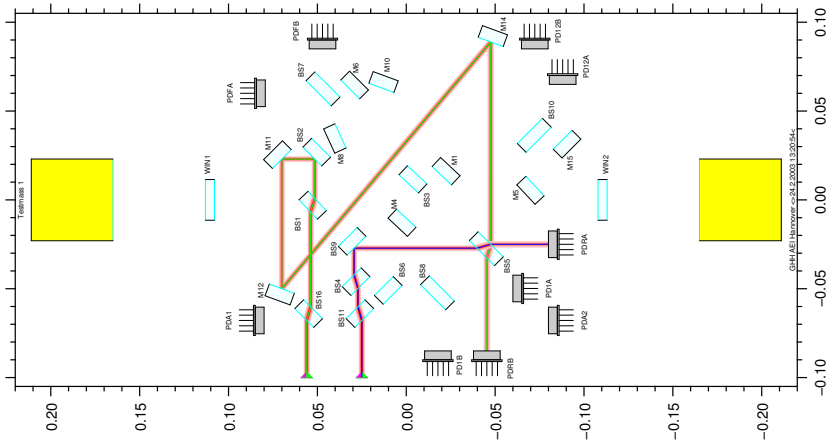


Figure 20. OptoCAD drawing of the reference interferometer. With an extra pathlength of 356.7 mm in the reference fiber, the nominal pathlength difference is 0.016 mm.

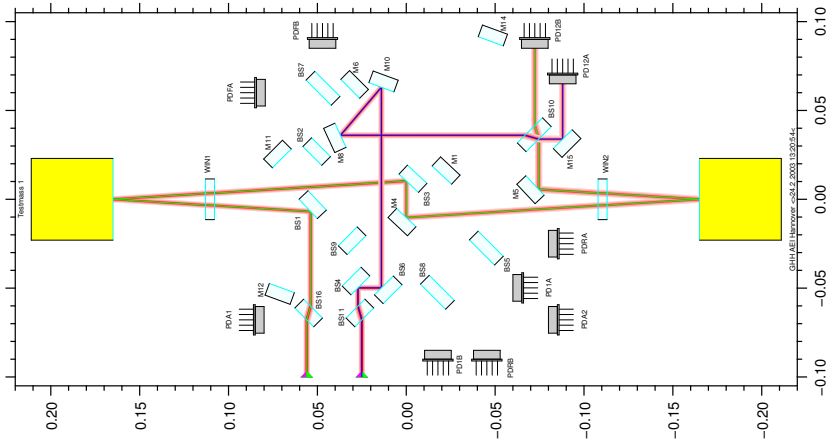


Figure 21. OptoCAD drawing of the x_1 - x_2 interferometer. With an extra pathlength of 356.7 mm in the reference fiber, the nominal pathlength difference is 0.000 mm.

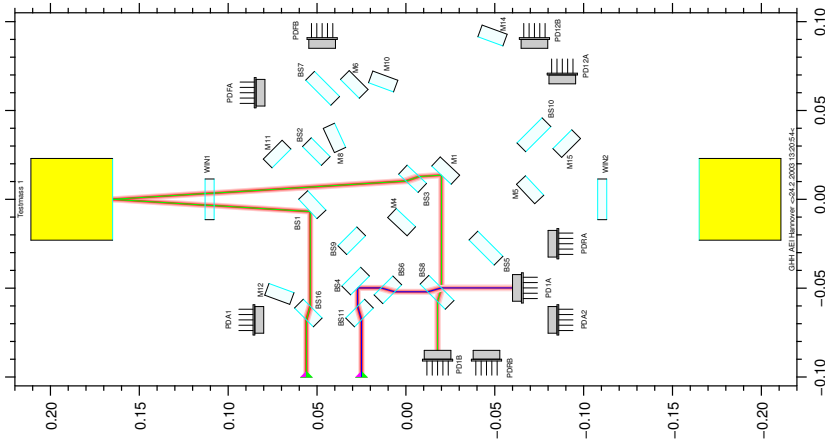


Figure 22. OptoCAD drawing of the x_1 interferometer. With an extra pathlength of 356.7 mm in the reference fiber, the nominal pathlength difference is 0.02 mm.

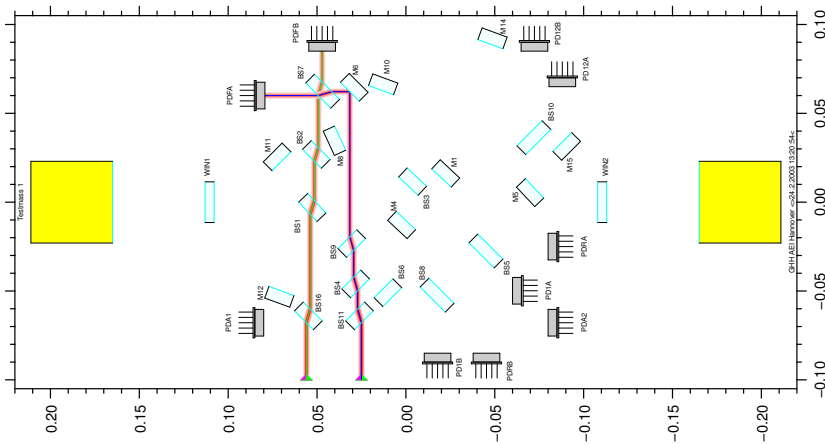


Figure 23. OptoCAD drawing of the auxiliary frequency noise interferometer. With an extra pathlength of 356.7 mm in the reference fiber, the nominal pathlength difference is -380 mm.

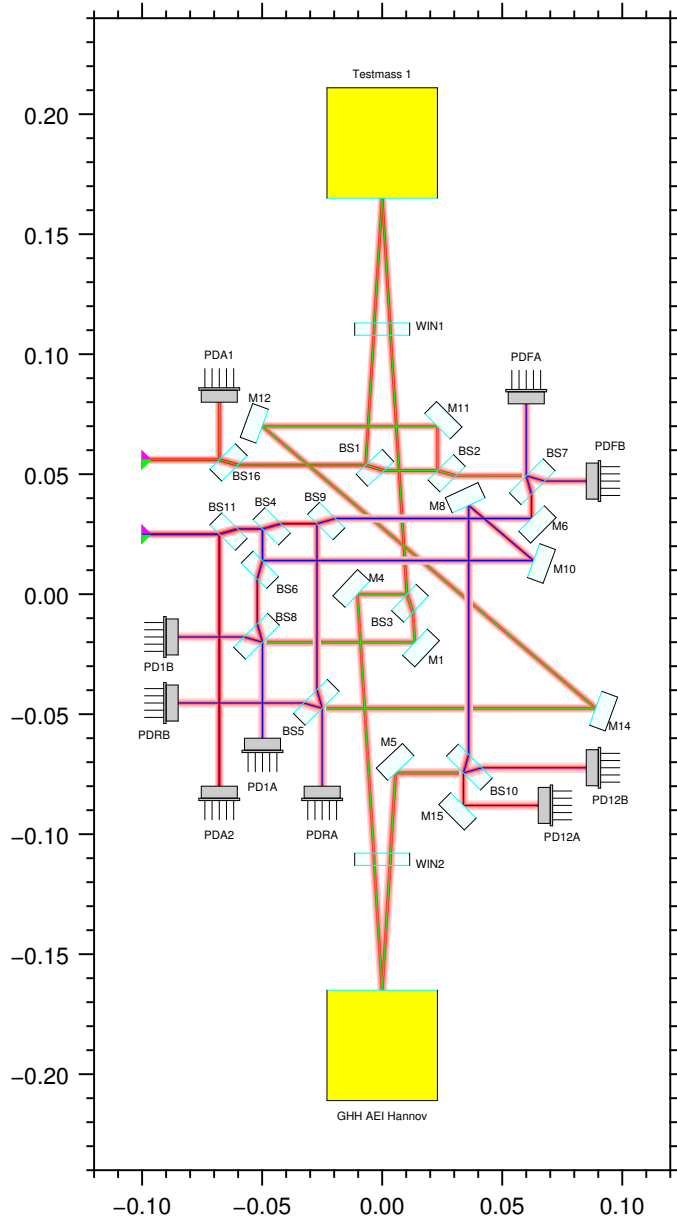
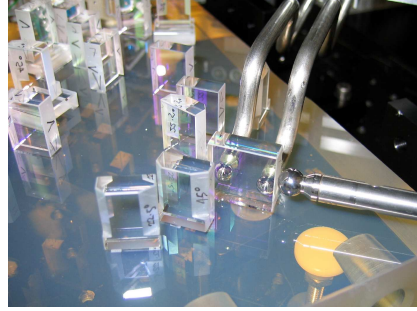


Figure 24. OptoCAD drawing of all interferometers, beams and components.



(a) Picture of the fiber injectors



(b) Alignment jig

Figure 25. Pictures of the fiber injectors (a) and the alignment jig (b)

2.3.5 Interferometer assembly

The optical bench was manufactured and the interferometers constructed according to the CAD drawing at the Rutherford Appleton Laboratory (RAL) in Abington (UK) with support of the bonding expertise from the University of Glasgow and the phasemeter support from the AEI.

In order to guarantee the thermal stability of the interferometer, a 20x20x4 cm Zerodur structure was chosen as its baseplate. Zerodur provides an extremely low coefficient of expansion of $10^{-8}/\text{K}$ within the expected temperature range of operation around 20 °C. However, the thermal stability at the nominal operating point of OMS still needs to be controlled at a level of $0.1 \times 10^{-3} \text{ K}/\sqrt{\text{Hz}}$ in order not to exceed the requirement of $1 \text{ pm}/\sqrt{\text{Hz}}$ as contribution from a single noise source.

The mirrors are based on a fused silica substrate and were bonded onto the Zerodur baseplate. The applied silicate (or hydroxy catalysis) bonding techniques requires surfaces with a flatness of $\lambda/20$. In total 22 components had to be bonded onto the interferometer baseplate.

The mounting and alignment of the fiber injectors was the most critical task. For the OBI EM the fiber injectors were glued in place after an iterative shimming process. As no out-of-plane alignment feature is foreseen, the alignment of the fiber injectors determines the final vertical alignment of the laser beams. The shimming method achieved a vertical alignment error of 100 μrad , which is marginally acceptable but should be better for the FM.

The alignment procedure has been accompanied by the phasemeter discussed in the next Section. This gave the possibility for an online adjustment

label	interferometer	output port	dedicated phase
PDRA	reference	A	Φ_{RA}
PDRB	reference	B	Φ_{RB}
PD _{1A}	X ₁	A	Φ_{1A}
PD _{1B}	X ₁	B	Φ_{1B}
PD _{12A}	X ₁₂	A	Φ_{12A}
PD _{12B}	X ₁₂	B	Φ_{12B}
PDFA	frequency	A	Φ_{FA}
PDFB	frequency	B	Φ_{FB}

Table 1. Labelling of QPDs and dedicated phases

of the optical components in the case when the interference signal can be detected. Figure 98 (a) and Figure 25 (b) show the mounting of the fiber injectors and the alignment jig used to actuate the optical components.

Apart from the mirrors, beamsplitter and fiber injectors, 8 QPD and two single element photodetectors were mounted on the optical bench. As shown in Figure 24, QPDs are located at both output ports¹ of the beam combiner of each of the four interferometers. They are labelled as shown in Table 1.

The letters A and B are used to distinguish the redundant output ports. Taking into account the two additional power detection photodiodes, there are 26 photodiode channels to handle.

Indium gallium arsenide photodiodes were used which typically have a responsivity of 0.8 A/W for the 1064 nm (WERNER *et al.* (2000)) light compared to a value of 0.2 A/W typical for standard Silicon (Si) diodes. The diameters of the QPDs are 5 mm with a 50 μ m wide slit separating the quadrants.

Each QPD has its dedicated amplifier unit providing four low noise transimpedance amplifiers with changeable trans-impedance resistor. This offers the opportunity to accommodate the dynamic range of the signal, such as to achieve a reasonable usage of the A/D converter range (which extends from -5 V to $+5$ V)². In order to increase the bandwidth of the amplifiers, each quadrant was biased with $+5$ V derived from a 7805 regulator. Figure 26 shows a photograph of the assembled OB including the QPDs and the fiber injectors.

¹ Both output ports contain the same information with 180° phase difference (see Equation (2.12)) and are measured for redundancy reasons

² These specifications are related to the second phasemeter prototype *PM2*

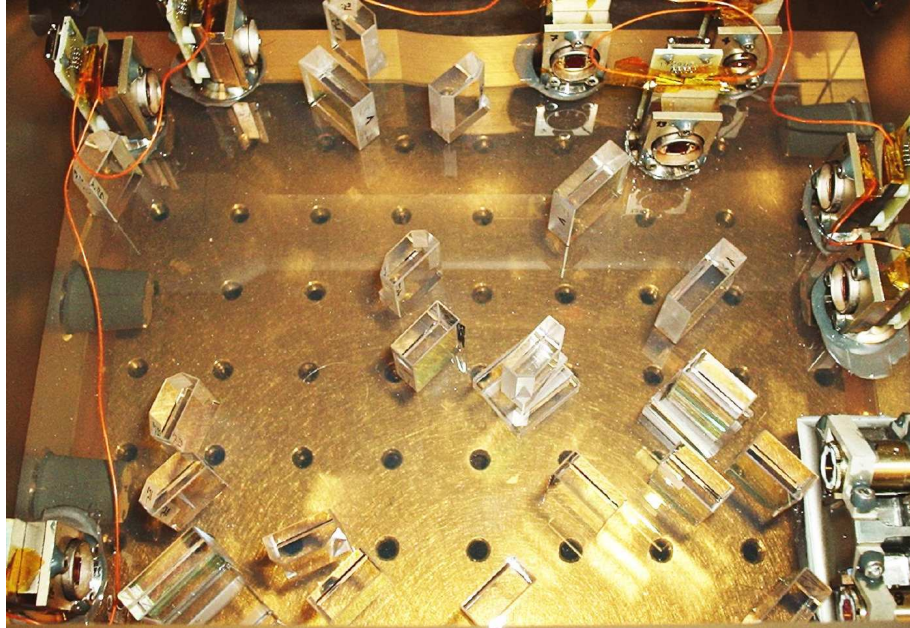


Figure 26. Picture of the optical bench. In the lower right the two fiber injectors can be seen. Distributed around the optical components, the quadrant photodiodes are mounted on the Zerodur baseplate.

2.3.6 Phase measurement system

After a global discussion of several phase measurement techniques¹ with particular emphasis to mixers/multipliers this section describes the phase measurement system developed for LISA pathfinder.

Phase measurement techniques

The measurement of the phase of a signal always means the measurement of that phase with respect to the phase of another signal or in other words - the estimation of the phase shift between a signal and a reference signal. In order to estimate the phase difference between two sinusoidal signals² different well established phase measurement techniques can be used. These techniques can be distinguished in two main classes - analog and digital. In the following an overview of the most common phase detection techniques will be given.

Mixers as phase detectors

An typical analog phase detection circuit with dedicated low pass filtering is shown in Figure 27.

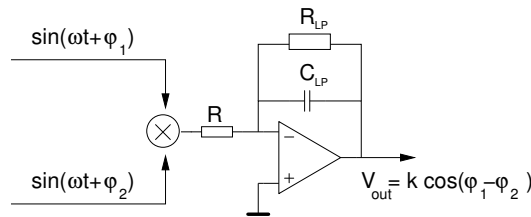


Figure 27. Phase measurement via multiplier

Using the identities

$$\sin(x) \cdot \cos(y) = \frac{1}{2} \{ \sin(x - y) + \sin(x + y) \} \quad (2.44)$$

and

$$\sin(x) \cdot \sin(y) = \frac{1}{2} \{ \cos(x - y) - \cos(x + y) \} \quad (2.45)$$

¹ The basic ideas described here are also relevant for Chapter 4.

² In the context of this work, only sinusoidal signals are of importance

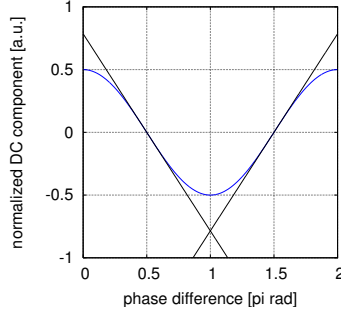


Figure 28. Multiplier output. This picture illustrates the slope near the zero crossing of the signal. This is the region where the phase detector works linearly.

with $x = \omega t + \varphi_1$ and $y = \omega t - \varphi_2$ shows that the product of the two sinusoidal signals is given by two terms where one of them represents the phase difference $\Delta\varphi = \varphi_1 - \varphi_2$ whilst the other one represents the sum $\sum \varphi = \varphi_1 + \varphi_2$ of the phases of the input signals. Thus the first terms in Equation (2.44) and (2.44) provide a phase measurement. In general this is also true for two different input frequencies. Since the frequencies $\omega_1 = 2\pi f_1$ and $\omega_2 = 2\pi f_2$ can be written as $\Phi_1 = \int dt \omega_1 = \omega_1 t + \varphi_1$ and Φ_2 similarly, the output of the phase measurement has a slowly oscillating term at the difference frequency $\Delta\omega = \omega_1 - \omega_2$ and a fast one oscillating at the sum frequency $\sum \omega = \omega_1 + \omega_2$. This can be written as:

$$\sin(x) \cdot \sin(y) = \frac{1}{2} \left\{ \cos(\Delta\omega t + \Delta\varphi) - \cos\left(\sum \omega t + \sum \varphi\right) \right\}. \quad (2.46)$$

For the phase measurement the fast term is needed to be removed. This can be achieved by averaging Equation (2.46) over a period T which is large compared to the inverse of the sum frequency. Practically this can be achieved by the use of an appropriate low pass filter (Figure 27). Its cutoff frequency (approximately 3 dB attenuation) is $f_{\text{cutoff}} = \frac{1}{T - i\omega R_{\text{LP}} C_{\text{LP}}}$. With

$$\Delta\Phi = \Delta\omega t + \Delta\varphi \quad (2.47)$$

thus the main characteristic of the mixer is given by:

$$f(\Delta\Phi) = \frac{1}{2} \cos(\Delta\Phi) \quad (2.48)$$

and is illustrated in Figure 28. The slope at the zero crossings where for small changes of $\Delta\Phi$ the mixer works in its linear range is $\pm k \frac{1}{2}$ where k is the

product of the amplitudes of the two input voltages (and the gain of the low pass filter). Figure 29 is an illustration of the mixer output for different phase states $\Delta\Phi$. This kind of phase detector can be implemented as analog circuit as shown above in Figure 27 or as a digital circuit or algorithm as well.

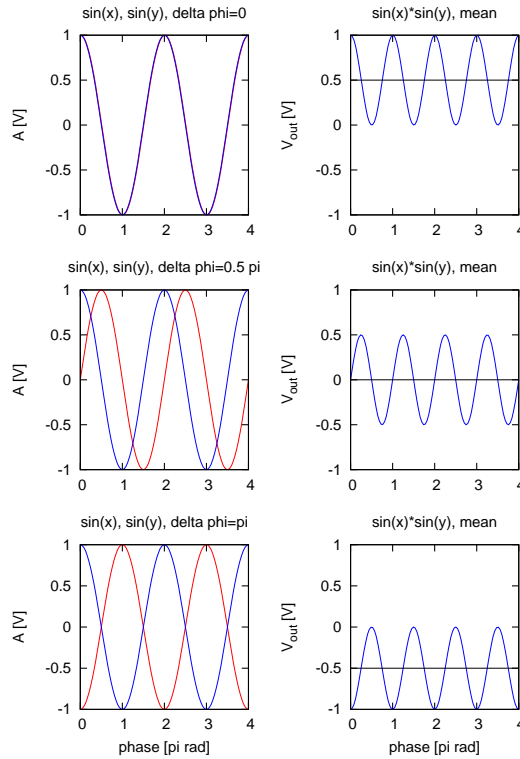


Figure 29. Mixer output for different phase states

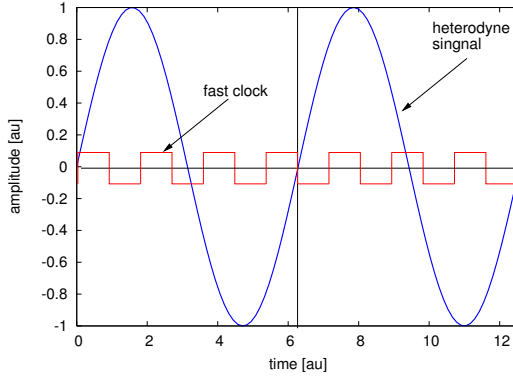


Figure 30. Illustration of zero crossing phase measurement technique. A counter counts the clock cycles between e.g. positive zero crossings of the heterodyne signal.

Zero crossing technique

A fundamentally different phase detector is the so called *Zero crossing technique* where the clock cycles of a fast clock between two e.g. positive zero crossings of the signal to be measured¹ will be counted. This type of phase detector can be implemented in digital logic very easily. Therefore the two signals whose phases are to be compared can be digitized by comparators². The outputs of the comparators will be used to trigger the START, STOP and RESET lines of two counters. The difference of the counter values gives the phase difference between the two signals. Figure 30 shows the principle of this method.

DFT based phase measurement

Due to its computational complexity the Fourier transform (FT) is a typically application for digital systems. Its common form

$$\tilde{h}(f) = H(f) = \int_{-\infty}^{\infty} dt e^{-2\pi ift} h(t), \quad (2.49)$$

¹ DC subtracted

² A comparator acts as a 1 bit ADC

where $\tilde{h}(f) = H(f)$ is the Fourier transform of a function $h(t)$, can be implemented in digital hardware by using the discrete FT:

$$\tilde{f}_l = \frac{1}{N} \sum_{k=-\frac{N}{2}}^{\frac{N}{2}-1} e^{-\frac{2\pi i l k}{N}} f_k \quad (2.50)$$

with

- N length of the FT
- l Bin number
- f_k the k^{th} sample.

l determines the Fourier frequency which is given by

$$f_F = l \cdot f_{\text{res}} = l \cdot \frac{f_{\text{sampl}}}{N} \quad (2.51)$$

it is clear that N is an integer multiple of $\frac{f_{\text{sampl}}}{f_F}$. Taking the identity

$$e^{i\omega t} = \cos(\omega t) + i \sin(\omega t) \quad (2.52)$$

into account it becomes clear that FT and its discrete form, the discrete Fourier transform (DFT), can be considered as a set of two quadrature mixers¹ with a moving average filter provided by the integration over an integer number of cycles of the Fourier frequency. The phase can be derived from

$$\varphi(\omega) = \arctan \left(\frac{\text{Im DFT}(x(t))}{\text{Re DFT}(x(t))} \right). \quad (2.53)$$

Thus for each frequency component within the signal $x(t)$ a phase can be estimated. In order to reduce the computational effort required for a full FFT in the case of LTP the calculation can be reduced to the phase estimation for one fixed frequency in the kHz range. Figure 31 shows an analog implementation of such an algorithm.

2.3.7 LISA Pathfinder phase measurement concept

One of the two independently investigated phasemeter prototypes for the LTP PMS is based on the zero crossing method and was developed at the University of Glasgow (UK) ROBERTSON *et al.* (2005). The second prototype, that in the end has been chosen as LTP baseline, uses an FFT based phase estimation algorithm and was developed at the Albert Einstein Institute, MPI für Gravitationsphysik (AEI) Hannover (HEINZEL *et al.* (2004b) and WAND (2003)).

¹ one set for each Fourier frequency

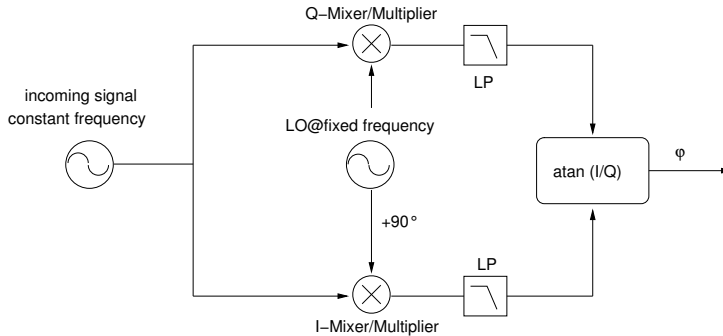


Figure 31. I-Q phase demodulation for a signal with constant frequency. A digital version has been implemented for the PMS for LISA Pathfinder. Mathematically this demodulation is equivalent to a DFT (Discrete Fourier Transform) for one frequency.

Hardware

The laboratory level phasemeter prototype *PM2* is based on a FFT algorithm called fastest Fourier transform in the west (FFTW) (FRIGO (1999), FRIGO and JOHNSON (1997), FRIGO and JOHNSON) and has been implemented on standard off the shelf PC hardware components.

- DAQ card (Microstar DAP 5216a) with 333 kS/sec ADC,
- Standard portable PC hardware

supplemented by the following developed hardware as there are

- antialiasing filter
- sample and hold circuit

ANTI_ALIASING FILTERS: In order to limit the bandwidth of the PD signals to be sampled, an appropriate analog antialiasing lowpass filter is needed. The filter used for the *PM2* is a box consisting of 16 individual and separated channels. Each channel consists of a low-noise 9th order elliptical lowpass filter with 8 kHz corner frequency, optimized for 16-bit A/D converters with 20 kHz sampling frequency¹. This means that the low pass filter needs a suppression of 96 dB at the half sampling rate if under the assumption the noise level to be suppressed is in the order of the full dynamic range of the ADC. Figure 32 shows the transfer function of each channel.

¹ A 16-bit ADC has a dynamic range of 96 dB.

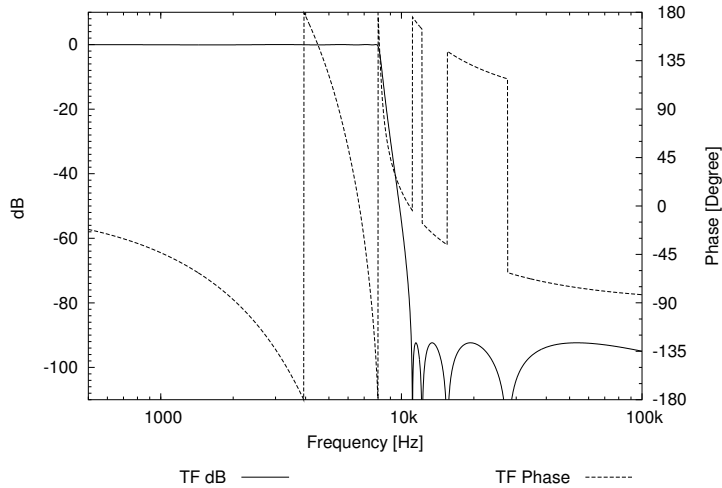


Figure 32. Transfer function of the antialiasing filters.

DATA ACQUISITION CARD: The data acquisition card is a Microstar Labs DAQ card (Microstar DAP 5216a) ([MSTARLABS](#)) PCI card with a multiplexed 500 kS/sec ADC converter (Successive Approximation type) providing a resolution of 16 bit and a dynamic range from -5 to +5 volts. A gain switch allows the input range to be changed (-10 to +10 volts also +/-1.25 volts and +/-2.5 volts). The built in multiplexer allows to sample up to 16 channels.

For full 16 bit resolution and sampling of more than one channel the sampling rate needs to be limited to 333 kS/sec and a gain factor of 1 such that the dynamic range is limited to +/-5 volts. The frequency reference of the DAQ board is an 100 ppm accuracy crystal clock. A very important feature of this data acquisition ([DAQ](#)) is the ability to use an external reference clock. This is necessary to synchronize the phasemeter clock with the heterodyne frequency.

Besides its analog input the DAP 5216a provides 2 analog outputs which have been used to implement a digital frequency stabilization loop for study purposes.

The implementation of real time control loops is supported due to the capabilities of an on board DSP with a dedicated 32 MB RAM. The real time operating system DAPL2000, which allows a task scheduling on a 0.1 ms time scale, runs on a 400 MHz AMD K6-III+ processor.

Within the phasemeter setup the DAP has been configured for 16 channel¹ sampling with 20 kHz, yielding a total sampling rate of 320 kHz. In this configuration up to 4 QPDs could be measured in parallel such that all four LTP interferometers should be observed simultaneously.

SAMPLE-AND-HOLD CIRCUITS: In order to compensate errors introduced by of the cyclic AD conversion of the multiplexed ADC², an appropriate 16-channel sample-and-hold board using AD781 integrated circuits and appropriate timing circuitry were build to supplement the DAQ (see C.2).

Phase estimation algorithm

Since the FFT computes the Fourier coefficients for all frequencies $f_f < \frac{f_{\text{sampl}}}{2}$, whilst the LTP interferometer is operated at a fixed frequency the calculation of all Fourier coefficients places unnecessary burden on the limited computational capacity of the LTP computer. This means that the FFT can be reduced to the calculation of one single bin representing the heterodyne frequency. This reduced form of the DFT is called single bin discrete Fourier transform (SBDFT) (HEINZEL *et al.* (2004b)) in the LTP project.

For diagnostic purposes (and for a better understanding of the parameters used for the SBDFT) a FFT algorithm has been implemented and tested in the beginning of the preinvestigation right before it has been substituted by the SBDFT.

The FFT algorithm that has been used is a very efficient implementation of the FFT described in FRIGO (1999), FRIGO and JOHNSON (1997), FRIGO and JOHNSON.

SIGNAL CONDITIONING: The raw signals coming from the quadrants of the photodetectors $x(t)$ are low-pass filtered and digitized with a sampling frequency of $f_{\text{sampl}} = 20$ kHz as described above. The resulting time series is called $x_n = x(t_n)$ with

$$t_n = nT_s = n \frac{1}{f_{\text{sampl}}}. \quad (2.54)$$

For each channel a sinusoidal test signal with $f = f_{\text{het}}$ was digitized and a sine function

$$f(x) = \text{scale} \times \sin(\omega t + \varphi) + \text{offset}. \quad (2.55)$$

- 1 The 16 analog inputs and the external clock and trigger inputs can be accessed by a connector box with BNC connectors.
- 2 A multiplexed ADC introduces time delays between the different channels which affect the phase measurement. Theoretically these offsets are constant and can be subtracted but in practice they are varying.

was fitted to the data for each individual channel. The derived fit parameters scale, φ and offset were later used to correct the sampled data. The reason these corrections were necessary for are spurious offsets and different gains caused by the antialiasing filters and the sample-and-hold circuit where φ is representing a phase delay.

HOW THE FFT IS APPLIED: As shown above, the **FFT/DFT** of N real data points calculates N complex values which occur as complex conjugate pairs. This redundancy is a consequence of the Nyquist criterion stating that only frequency components of a digitized signal up to half of the sampling frequency can be reconstructed uniquely. The complex FFT results are labelled as \tilde{x}_n where n varies from 0 to $\frac{N}{2} - 1$. Each result contains the amplitude and the phase of Fourier frequency components of the sampled signal $x_n = x(t_n)$ for a fixed resolution bandwidth of the FFT which is given by

$$f_{\text{res}} = \frac{f_{\text{sampl}}}{N_{\text{FFT}}}, \quad (2.56)$$

where f_{sampl} is the sampling frequency and N_{FFT} is the length of the FFT. Thus the n^{th} bin of the FFT means the Fourier frequency components at $n \times f_{\text{res}}$. In particular for $n = 0$ the DC of the signal is meant and the element $n = \frac{N}{2} - 1$ indicates the Fourier component at the Nyquist frequency.

For the phase measurement the length of the **FFT** (N_{FFT}) is the first parameter to be chosen. Since the measurement band for the phase estimation is limited from 3-30 mHz the data rate for the phase output can be theoretically reduced¹ down to $f_p \approx 2 \times 30 \text{ mHz} = 60 \text{ mHz}$. Besides this constraint, the fact that different control loops such as the frequency and **OPD** stabilization loop use the estimated phase as error signal, the phase estimation rate f_p is increased for the **LTP** up to 100 Hz on order to provide a sufficient bandwidth for the loops. Therewith the length of the FFT can be estimated as:

$$N_{\text{FFT}} \leq \frac{f_{\text{sampl}}}{f_p}. \quad (2.57)$$

Another constraint is given by the fact that the heterodyne frequency needs to be an integer multiple of the **DFT** resolution f_{res} such that

$$f_{\text{het}} = n f_{\text{res}} = n \frac{f_{\text{sampl}}}{N_{\text{DFT}}} \quad (2.58)$$

This ensures that the heterodyne frequency is located exactly in the center of a bin. Otherwise the phase measurement would be affected by a linear drift. For the **LTP EM** the heterodyne frequency was chosen to be

¹ in order to fulfill the Nyquist criterion

10 MHz/6160 \approx 1623.37 Hz since it is easy to handle with standard ADCs and digital electronics.

The parameters used for most of the time were (during the measurement campaign described in Section 2.4)

$$\begin{aligned} f_{\text{het}} &= 10 \text{ MHz}/6160 = 1623.37 \text{ Hz}, \\ n_{\text{DFT}} &= 616, \\ f_{\text{sampl}} &= 20 \text{ kHz}, \\ f_{\text{ph}} &= 32.467 \text{ Hz}, \\ k &= 50 \quad (\text{bin number}). \end{aligned} \tag{2.59}$$

However, in some of the earlier tests to verify the operation of the phasemeter a different set of parameters was used:

$$\begin{aligned} f_{\text{het}} &= 10 \text{ MHz}/6160 = 1623.37 \text{ Hz}, \\ n_{\text{DFT}} &= 924, \\ f_{\text{sampl}} &= 25 \text{ kHz}, \\ f_{\text{ph}} &= 27.056 \text{ Hz}, \\ k &= 60 \quad (\text{bin number}). \end{aligned} \tag{2.60}$$

An important issue is, that the sampling clock and the heterodyne frequency were both derived from a common master oscillator (a 10 MHz crystal oscillator) in order to avoid phase variations due to different system clocks.

The phase difference between the two signals $x_n = x(t_n)$ and $y_n = y(t_n)$ can be estimated using:

$$\varphi = \arctan \left(\frac{\text{Im}(\text{DFT}(x_n))_{f_{\text{het}}}}{\text{Re}(\text{DFT}(x_n))_{f_{\text{het}}}} \right) - \arctan \left(\frac{\text{Im}(\text{DFT}(y_n))_{f_{\text{het}}}}{\text{Re}(\text{DFT}(y_n))_{f_{\text{het}}}} \right). \tag{2.61}$$

Figure 33 is an illustration of the data processing flow. It shows, representatively for all signals, two input signals - a measurement and a reference signal at the heterodyne frequency. In order to remove spurious signal components with frequencies larger than the half sampling rate, both channels are low-pass filtered before the digitization occurs. Due to different offsets and gains in the signal chain before, a DC offset is subtracted after the digitization and a scaling factor is applied for each channel. These data are now packed into segments of the length of the FFT (in this scheme 616 points) which is then calculated for each channel. The Fourier coefficients at the heterodyne frequency are in the 50th bin and are used for the phase estimation.

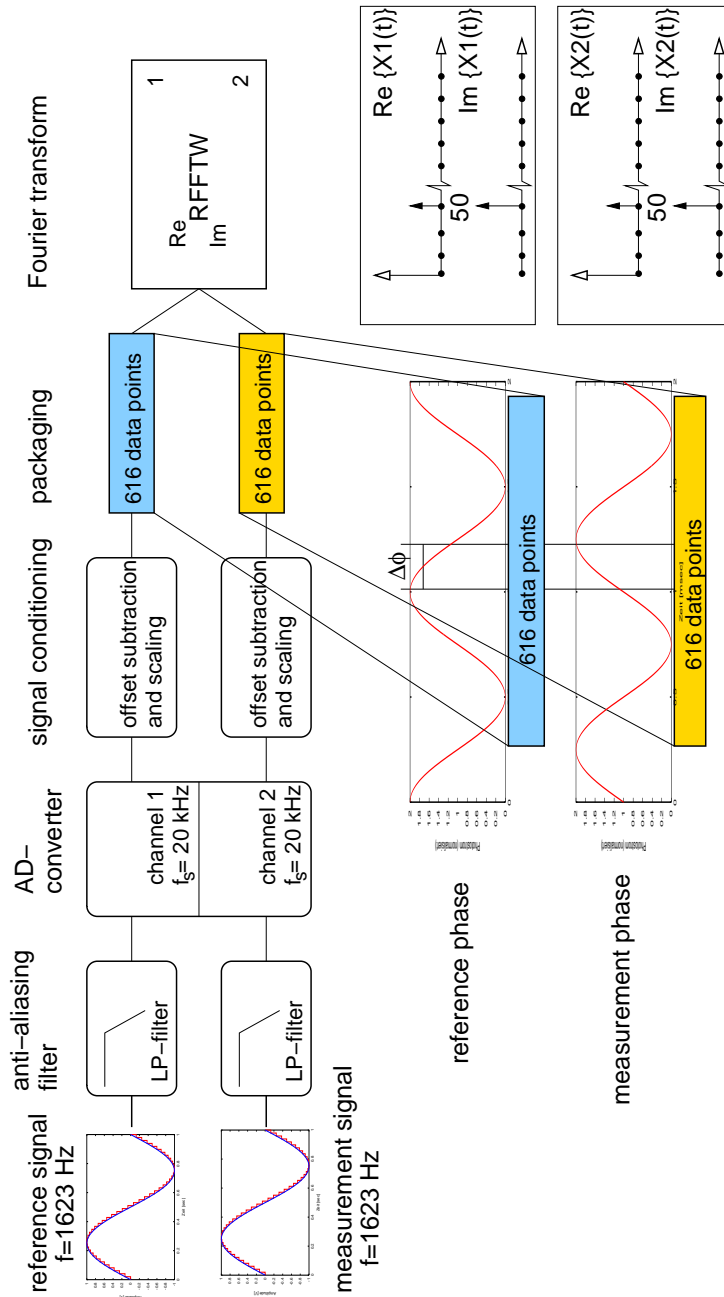


Figure 33. Block diagram illustrating the data processing flow

Longitudinal phase readout

Assuming the signals (1) and (2) of two QPDs (e.g. PRA from the reference interferometer and PD1A from the X1 interferometer) have been digitized at 20 kHz while the four data streams from each QPD are labelled as $U_A^{(k)}(t)$, $U_B^{(k)}(t)$, $U_C^{(k)}(t)$, $U_D^{(k)}(t)$ according to Figure 34 that shows the frontal view on the QPD and the labelling convention of the quadrants that was used for the EM. The upper index k indicates the QPD.

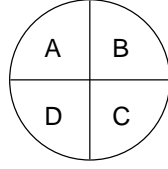


Figure 34. QPD-quadrant labelling.

The FFT is processed in parallel for the 16 channels of the DAQ system¹, after which the DC averages and the heterodyne bin are computed. The real DC components, labelled as $DC_A^{(k)}$, $DC_B^{(k)}$, $DC_C^{(k)}$, $DC_D^{(k)}$ are one output of the FFT:

$$DC^{(k)}_{A,B,C,D} = \text{FFT} \left(U_{A,B,C,D}^{(k)}(t) \right) |_{f=0}, \quad (2.62)$$

and the complex amplitudes at the heterodyne frequency $F_A^{(k)}$, $F_B^{(k)}$, $F_C^{(k)}$, $F_D^{(k)}$ are given by:

$$F_{A,B,C,D}^{(k)} = \text{FFT} \left(U_{A,B,C,D}^{(k)}(t) \right) |_{f=f_{\text{het}}, \text{bin}_i=50}. \quad (2.63)$$

In order to estimate the phase for each of the four individual interferometers, the averages of the complex amplitudes for all four quadrants of the dedicated QPD are estimated. This is representatively shown for two quadrant photodiodes here:

$$F_{\Sigma}^{(1)} = F_A^{(1)} + F_B^{(1)} + F_C^{(1)} + F_D^{(1)}, \quad (2.64)$$

$$F_{\Sigma}^{(2)} = F_A^{(2)} + F_B^{(2)} + F_C^{(2)} + F_D^{(2)}. \quad (2.65)$$

The approach to first average the 4 complex amplitudes of the quadrants and then calculating one single phase (illustrated in Figure 35) is significantly less sensitive to phase jumps than averaging the individual phases of each

¹ this means that up to 4 QPD data streams can be processed in parallel

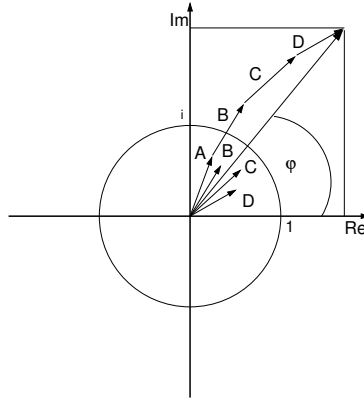


Figure 35. Illustration of the averaging of the longitudinal phases.

quadrant. The phase difference φ_{long} between two signals (from separate PDs) is given by:

$$\begin{aligned}\varphi_{\text{long}} &= \arctan\left(\frac{\text{Im}(F_{\Sigma}^{(1)})}{\text{Re}(F_{\Sigma}^{(1)})}\right) - \arctan\left(\frac{\text{Im}(F_{\Sigma}^{(2)})}{\text{Re}(F_{\Sigma}^{(2)})}\right) + n \cdot 2\pi \\ &= \arg(F_{\Sigma}^{(1)}) - \arg(F_{\Sigma}^{(2)}) + n \cdot 2\pi.\end{aligned}\quad (2.66)$$

The extra term $n \cdot 2\pi$ unwraps the final phase if a shift of more than 2π occurs. The integer n will be determined by a phase tracking algorithm.

For alignment and diagnostic purposes the DC - sums are calculated according to

$$\text{DC}_{\Sigma}^{(1)} = \text{DC}_A^{(1)} + \text{DC}_B^{(1)} + \text{DC}_C^{(1)} + \text{DC}_D^{(1)}, \quad (2.67)$$

$$\text{DC}_{\Sigma}^{(2)} = \text{DC}_A^{(2)} + \text{DC}_B^{(2)} + \text{DC}_C^{(2)} + \text{DC}_D^{(2)}. \quad (2.68)$$

The contrast of each interferometer is calculated using:

$$c^{(k)} = 2 \cdot \frac{|F_{\Sigma}^{(k)}|}{\text{DC}_{\Sigma}^{(k)}}. \quad (2.69)$$

Differential wavefront sensing

The DWS techniques, described in MORRISON *et al.* (1994), are widely used in ground based gravitational wave detectors. In contrast to the longitudinal readout, to obtain the DWS alignment signals no further optical reference

signal is needed since the DWS signals are obtained by referring the phases of the individual quadrants to each other. The alignment information of the test masses can either be obtained from linear combinations of the DC components DC_x , or from the heterodyne components F_x of the individual quadrants of the QPD as well. Whilst the combinations of the DC components give access to the center of gravity of the beam with respect to the QPD center, the combination of the heterodyne components allow to measure the wavefront angle between the reference and the measurement beam which contains information about the alignment of the test masses (HEINZEL *et al.* (2002b)).

The DC components can be combined as follows:

$$\begin{aligned} DC_{\text{right}} &= DC_B + DC_C, \\ DC_{\text{left}} &= DC_A + DC_D, \\ DC_{\text{top}} &= DC_A + DC_B, \\ DC_{\text{bottom}} &= DC_C + DC_D. \end{aligned} \quad (2.70)$$

While the reference beam is initially perfectly aligned¹ with respect to the center of the QPDs, the position of the measurement beam changes according to the test mass motion. The deviation can be calculated as:

$$\Delta x = \frac{DC_{\text{left}} - DC_{\text{right}}}{DC_{\Sigma}}, \quad \Delta y = \frac{DC_{\text{top}} - DC_{\text{bottom}}}{DC_{\Sigma}}. \quad (2.71)$$

Considering the heterodyne components of the signal, the same linear combinations can be obtained as in Equation (2.70):

$$\begin{aligned} F_{\text{right}} &= F_B + F_C, \\ F_{\text{left}} &= F_A + F_D, \\ F_{\text{top}} &= F_A + F_B, \\ F_{\text{bottom}} &= F_C + F_D, \end{aligned} \quad (2.72)$$

From these linear combinations the angle between the incident wavefronts of the reference beam and, depending on the test mass alignment, the wavefronts of the measurement beam can be measured:

$$\Phi_x = \arg(F_{\text{left}}) - \arg(F_{\text{right}}), \quad (2.73)$$

$$\Phi_x = \arg(F_{\text{left}}) - \arg(F_{\text{right}}) \quad (2.74)$$

Using the identity

$$e^{i\varphi_1} e^{i\varphi_2} = e^{i(\varphi_1 + \varphi_2)} \quad (2.75)$$

¹ The reference beam passes no test mass such that its position is fixed during the interferometer assembly

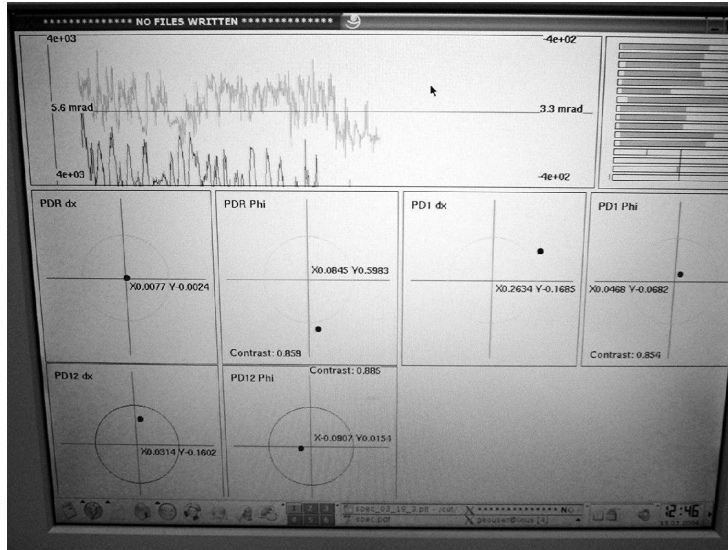


Figure 36. Photograph of the phasemeter user interface.

Equation (2.77) can be written as

$$\Phi_x = \arg \left(\frac{F_{\text{left}}}{F_{\text{right}}} \right), \quad (2.76)$$

$$\Phi_y = \arg \left(\frac{F_{\text{top}}}{F_{\text{bottom}}} \right). \quad (2.77)$$

where the resulting *DWS* alignment is more immune to phase jumps, because in Equation (2.77) only one arctan operation is to be performed while in Equation (2.74) two are needed.

The software implementing the phase measurement technique described above is written in C under Linux, using the gcc compiler. It features a graphical user interface that displays in real-time the dynamic range of all A/D channels, the alignment and contrast of 3 quadrant diodes and the time evolution of the x_1 and $x_1 - x_2$ longitudinal measurements. Figure 36 shows a photograph of the user interface. In addition, all output data (raw phases, x_1 and $x_1 - x_2$, alignments, contrasts etc.) are written to a disk file in ASCII format with a data rate of $f_{\text{ph}} = 32.467$ Hz for later analysis. The disk files are automatically labelled using the date and time when the measurement was started as the filename.

The software was developed during the preinvestigations and was used for the complete LPF OBI preinvestigation phase until a new hardware implementation of the phasemeter was developed.

Currently a highly integrated field programmable gate array (FPGA) based phasemeter prototype (PM3) is in use that is very similar to the real flight hardware.

2.4 INTERFEROMETER GROUND TESTING

During the LTP preinvestigation process different subsystems of the LTP core assembly EMs were developed and tested in order to verify the design and to test their performance. The EMs are prototypes very similar to the real flight hardware in functionality, design, masses etc. After the construction of the LTP interferometer and the assembly of the mounting structure (called H-bench due to its shape) the whole LISA Pathfinder Optical Bench Engineering model (LPF OB EM) had to undergo a set of functional, performance, vibrational and environmental tests. Therefore a test campaign was arranged at TNO (an institute for applied physics) in Delft (The Netherlands) where an appropriate thermal vacuum chamber is available that provides the required environmental conditions such as size, vacuum pressure and thermal dynamic range. In addition a vibration facility was available to test the mechanical integrity of the LPF OBI EM.

The results shown below have been obtained during this measurement campaign and have been published in the report *Lisa Pathfinder Optical Bench Engineering model: functional and performance tests - Test Report, S2-AEI-TN-3017* (HEINZEL *et al.* (2004a)). The measurement campaign team consisted of G. Heinzl, A. F. García Marín, F. Draaisma and myself. A summary of the results of the test are as follows:

- *All functions of the Optical bench work as expected.*
- *No measurable change in the optical alignment and performance was observable after the thermal and vibrational tests.*
- *The longitudinal and alignment signals behave as predicted over their full dynamic range.*
- *The noise level of the longitudinal signals is below the interferometer budget in most of the frequency range; the remaining noise that is slightly above the budget at some frequencies is subject of ongoing investigations¹.*
- *The noise level and dynamic range of the alignment signals are even better than expected.*

¹ understood and removed by now

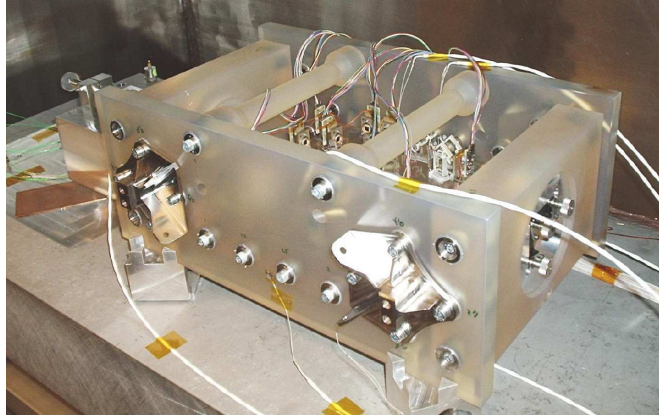


Figure 37. Picture of the Optical Bench with photodiode harness and NTC sensors attached.

- *The interferometer has proven its predicted robustness against disturbances such as momentary drop in laser power etc.*
- *In order to achieve an acceptable noise level of the longitudinal signals it is mandatory to actively stabilize the optical pathlength difference (OPD) between the two fibers. One method to achieve this has been demonstrated during the tests at TNO, and other methods are under investigation.*

2.4.1 *The interferometer and the testbed*

Figure 37 shows the fully assembled OBI, also called the H-bench due to its shape. The interferometers are in between two Zerodur plates. Instead of the test mass housings the picture shows the mirrors, which were mounted on standard optical mounts as substitutes for the real test masses. The OBI is located in a vacuum chamber.

Harness

All photodiodes are attached via vacuum-compatible coaxial cable and Nano-D connectors. A set of negative temperature coefficient (NTC) sensors used as thermometers have been placed over the bench and the vacuum chamber. Three 50 pole sub-D connectors are arranged on a feedthrough flange attached to the vacuum chamber. Before the first evacuation the protective covers of the photodiodes were removed.

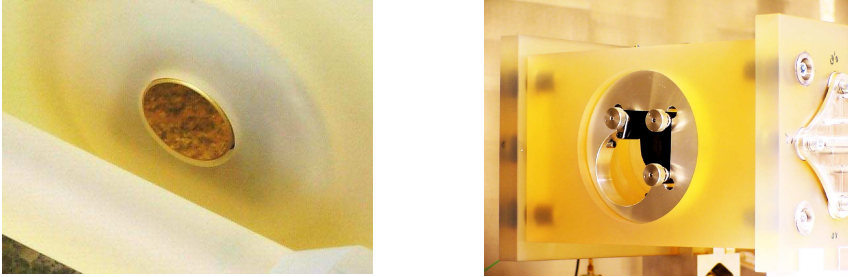


Figure 38. Picture of one test mirror from the front and back.

Test mirrors

Instead of the real test masses, which were not available, two test mirrors were used for all interferometric tests. The mirrors were made from Zerodur with a gold coating and mounted in commercial precision mirror mounts (Figure 38). The mounts were fixed in Zerodur adapter plates connected to both end of the H-structure. The metal components of the mirror mount had a much larger thermal expansion than the optical bench, such that the interferometric length measurements χ_1 and $\chi_1 - \chi_2$ at low frequencies were dominated by these thermal expansions.

At the beginning of the measurement campaign it was planned that the Zerodur mirrors should be directly glued onto the Zerodur adapter plate. However, several attempts with different kinds of vacuum compatible adhesives failed due to its relaxation producing strong irregular forces onto the mirrors, such that after curing, a large misalignment of several $100 \mu\text{rad}$ of the mirrors caused a significant loss of contrast. With the standard mounts the mirrors could easily be adjusted by hand. In order to monitor the alignment process, the interferometer DC and DWS signals displayed in realtime on the phasemeter were used. As planned, the DC signals gave a good initial alignment whilst the DWS signals, after archiving sufficient contrast in the interferometer, were used for the final alignment. With some practice, the whole process could be performed from scratch within a few minutes.

Except for the full stroke and alignment tests described below, these mirror mounts were used for all tests. For the full stroke test one of them was replaced by a PZT-mounted mirror.

2.4.2 *Functional tests*

In order to have a first quick view on the basic functionality of the [OBI](#) and all its subcomponents as well as on the dedicated electronics such as phasemeter, modulation optics and electronics, functional tests were performed at several times: As a first test after installation of the OB in the test chamber, after thermal cycling and after vibration.

These initial tests consisted of applying the two frequency shifted laser beams through the two fibers and observing the photocurrent in each photodiode channel. When the phasemeter was used for these tests (this includes all final tests after the environmental tests), data was recorded for at least several seconds, such that alignment information, contrast etc. were recorded and could later be processed. In particular from the interferometers containing no movable optical components (dummy mirrors) - namely the reference and the frequency interferometer - DWS information about static misalignments of the bonded components including the fiber injectors could be derived. Each functional test was considered successful if each channel showed a signal at the heterodyne frequency with contrast $> 50\%$ and of an amplitude comparable to all other channels.

By this criterion, all function tests succeeded with the following two exceptions:

PHOTODIODE PDA1: When the optical bench had been delivered by RAL, all photodetectors were covered by a plastic strip glued onto the diode mounts to protect the sensitive area against dust particles. After removing these covers from the photodiodes each of them was tested. The single-element photodiode PDA1 showed abnormal behaviour. In particular, a very high photocurrent was measured in dark state which was comparable to the photocurrent measured with a few mW light on it. The reason for this behaviour could not be found, particularly when the photodiode returned to normal operation after performing the environmental tests. Perhaps some kind of contamination on the diode was introduced when the protective cover was removed and disappeared again during the environmental tests.

PHOTODIODE CONNECTOR OF PDRA: One of the two [QPDs](#) (PDRA) of the reference interferometer did not work sufficiently. It showed intermittent abnormal behaviour after the first functional test when all photodiode harnesses were connected. This effect could be triggered by moving the connector, suggesting that there was a bad contact within the connector. Instead of this photodiode its redundant counterpart PDRB was used for the test.

2.4.3 Functional alignment tests

The functional alignment test was performed to verify that the DC and DWS alignment signals behave as expected. The importance of this becomes clear taking into account that they are planned to be used as error signals for the drag free and attitude control system (DFACS) of the proof-masses.

Already during the setup phase of the interferometers it became clear that the behaviour of the signal is in full accordance with the expectations and they were used for all tests to realize the final alignment. In order to compare the alignment, in particular for the completely bonded reference and frequency interferometer, before and after the environmental test, for each photodiode an alignment data stream was taken. The comparison of this data yielded the following upper limits:

- The beam position on no photodiode has moved more than 5 μm .
- The angle of no beam injector has moved more than 20 μrad .

Changes within these tolerances do not affect the functionality and performance of the optical bench. They also imply that none of the bonded components moved significantly.

2.4.4 Full stroke tests

As the LTP interferometry has to track the positions of the TM₁ and TM₂ over several 10 μm , this functionality had to be demonstrated experimentally. Therefore a full stroke test was performed, intended to show that x_1 senses only the motion of the first test mass TM₁, whereas $x_1 - x_2$ senses the distance changes between TM₁ and TM₂. Furthermore it was required to verify that each interferometer works equally well independent of where the test mass is located within a range of 100 μm . This test was able to demonstrate that the phasemeter and phase-tracking algorithm can keep track of the test mass position even when it moves with a velocity near the theoretical maximum v_{max} (which is given by 180° phase difference between two adjacent phase measurements, equivalent to 2 measurements per fringe). v_{max} is given by:

$$v_{\text{max}} = \lambda f_{\text{ph}} = \frac{1}{4} \cdot 1064 \text{ nm} \cdot 32.46 \text{ Hz} = 8.6 \mu\text{m/s}. \quad (2.78)$$

The factor 1/4 considers the as phase difference of 180° and the reflection in the test mass.

Actuator

To simulate a long-range movement of a TM, a mirror was glued to a stack-PZT providing a wide dynamic range (approximately $90\ \mu\text{m}$). The PZT was accompanied by an appropriate driver, controllable via a software from the PZT manufacturer to program a periodic voltage. The mathematical model that was used for the voltage to be applied ensures a smooth slope at the reversal points of a ramp to protect the PZT against strong changes of the voltage. The periodicity of the ramp was set to 0.018Hz and it had an amplitude of $95\ \mu\text{m}$. This function recommended by the software manual from the manufacturer was converted into the following Mathematica code and was used to provide a comparison with the interferometric measurements:

```

1  f1[x_] := a*(x/p-Sin[Pi*x/p]/Pi)
   f2[x_] := b*x+c
3  d1[x_] := D[f1[xx],xx]/.xx->x
   d2[x_] := D[f2[xx],xx]/.xx->x
5  p=0.15
   g1=f1[p]==f2[p]
7  g2=d1[p]==d2[p]
   g3=f2[.25]==.5
9  sol= Solve[{g1,g2,g3},{a,b,c}] [[1]]

11 f[x_] := (f1[x]/.sol) /; x<p
   f[x_] := (f2[x]/.sol) /; x>=p && x<=0.25
13 f[x_] := (1-f[0.5-x]/.sol) /; x>0.25

15 g[x_] := f[x] /; x<0.5
   g[x_] := f[1-x] /; x>=0.5
17
19 h[x_] := g[Mod[x,1]]
   Plot[h[x],{x,-0.5,2}]
21
   tab = Table[{x, 190*(1-h[(x+23)*0.018])}, {x, 0, 110, 0.1}];

```

The time series of the data produced by the Mathematica code is plotted in the following Figures 39 and 40 as lower curve (“mirror x PZT motion”). In order to fit the interferometer data, the time series was time shifted and the position was converted to optical pathlength.

From the interferometric measurements shown in Figure 39 and Figure 40, a velocity of the PZT of $4.96\ \mu\text{m/s} = 2\ \text{fringes/s}$ was estimated compared to a value of $5\ \mu\text{m/s}$ determined from the settings of the software.

The conversion of these longitudinal phase measurements to optical pathlength is straightforward (it involves only the laser wavelength $\lambda \approx 1064\ \text{nm}$

and the angle of incidence $\approx 3.6^\circ$).

Results for motion of TM₁

The results when the TM₁ mirror had been substituted by the PZT mounted mirror are shown in Figure 39. The PZT motion is shown in the lower graph. The interferometric measurements are shown in the upper graph as there are:

- the results for the x_1 and the x_{12} interferometer, whose optical path-length change uniformly and periodically between 0 and $-150\ \mu\text{m}$,
- the interferometric contrast for the x_1 and the x_{12} interferometer which show a reduction from their nominal values of approximately 80 % for velocities of the mirror near zero down to 60 % when the PZT mirror is actuated faster,
- the contrast of the reference interferometer which stays completely unaffected by the mirror motion at approximately 75 %.

SUMMARY The interferometric signals behave according to the expectations. Since the actuated mirror at the TM₁ position affect both the x_1 and the x_{12} interferometer, the associated phases measuring the pathlengths x_1 and $x_1 - x_2$ faithfully follow the PZT motion.

Results for motion of TM₂

The results when the TM₂ mirror was substituted by the PZT mounted mirror are shown in Figure 40. The PZT motion is shown in the lower graph. The interferometric measurements shown in the upper graph are:

- the results for the x_1 and the x_{12} interferometer, where in this case only the optical pathlength of the x_{12} interferometer changes periodically between 0 and $-150\ \mu\text{m}$,
- the interferometric contrast for the x_1 and the x_{12} interferometer, where now only the contrast of the x_1 interferometer shows a reduction from its nominal value of approximately 80 % for velocities of the mirror near zero down to 60 % when mirror is actuated faster,
- the contrast of the reference interferometer which stays completely unaffected by the mirror motion at approximately 80 %.

SUMMARY The interferometric signals behave according to the expectations. Since the actuated mirror at the TM2 position affects only the x_{12} interferometer, the associated phase measuring the pathlength $x_1 - x_2$ faithfully follows the PZT motion while the x_1 phase stays constant.

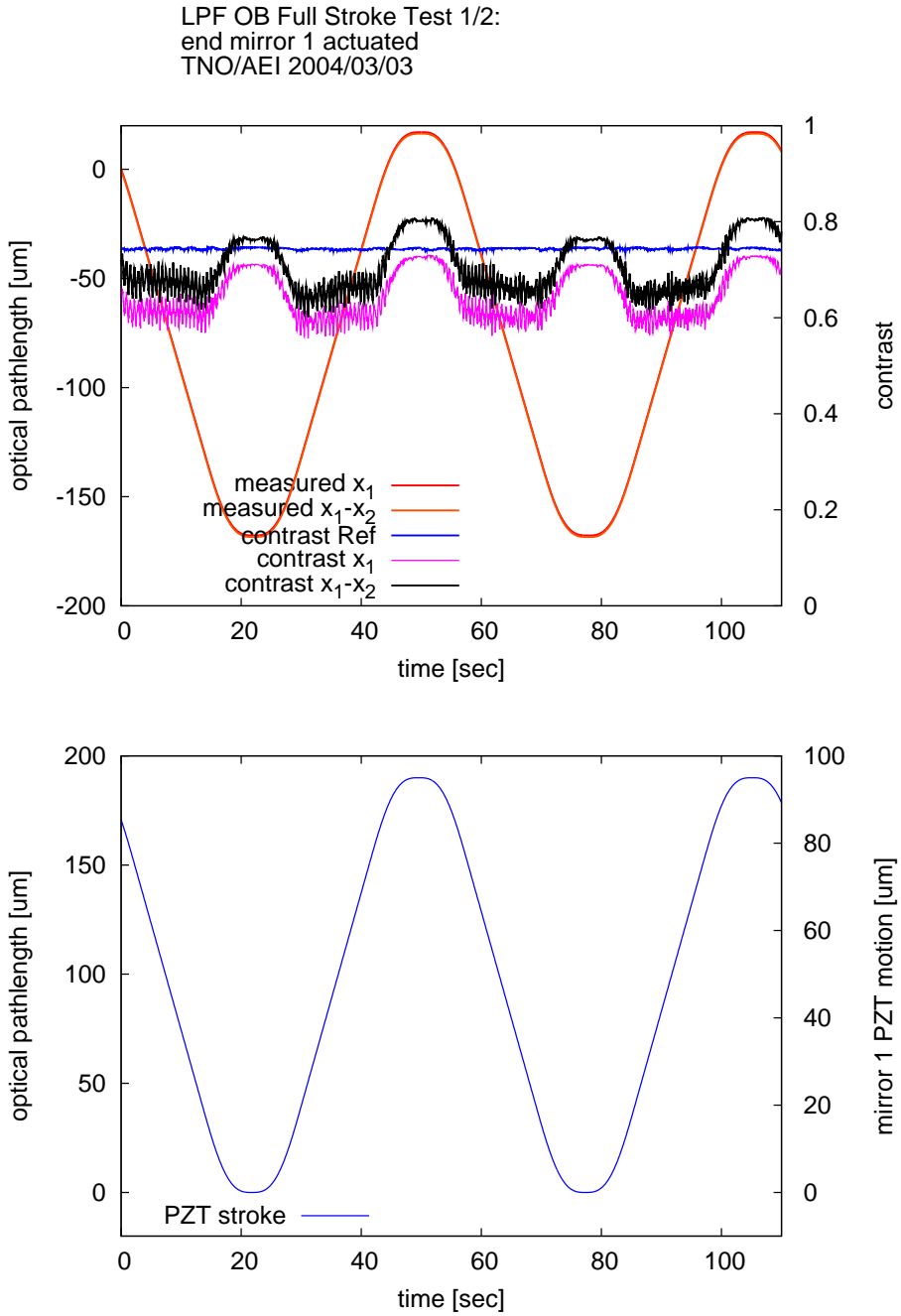


Figure 39. Results of full stroke test with test mass TM₁ actuated.

LPF OB Full Stroke Test 2/2:
 end mirror 2 actuated
 TNO/AEI 2004/03/04

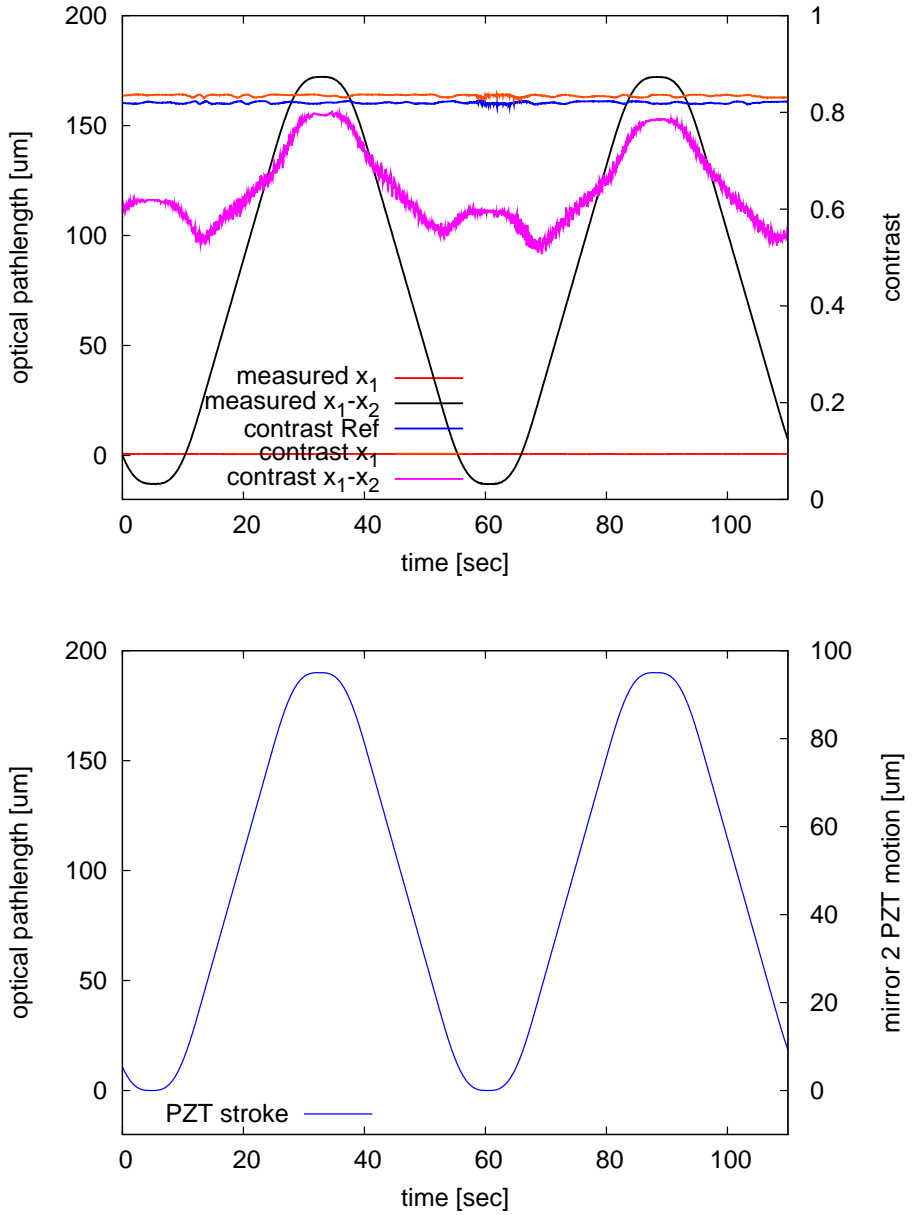


Figure 40. Results of full stroke test with test mass TM2 actuated.

2.4.5 Tilt tests

Besides the main longitudinal TM position, their alignment with respect to the optical bench is important information to be measured in order to control the test mass in 3 degrees of freedom. Therefore the DWS signals as explained in Section 2.3.7 are used. Since the raw DC and DWS signals measure the differential beam position and the wavefront angle between the reference and the measurement beam respectively, this information needs to be converted into real TM angle. To estimate the calibration factors that convert the obtained DWS signals into TM alignment was the purpose of the tilt test. These calibration factors depend on laser beam size, shape, higher order mode contents of the beams etc., such that they can only be determined experimentally. The theory of the alignment measurements is described, e.g., in reference HEINZEL *et al.* (2004b). Here only the methods and results are summarized.

Actuator

In order to simulate a tilted test mass respectively a rotated test mass a one-dimensional tilt PZT with a mirror attached to it was used. Before the calibration of the interferometer alignment signals, the PZT itself had to be calibrated. For this purpose the angle of the mirror was measured with a theodolite for different voltages that were applied to the PZT. The measurement results shown below imply this calibration factor.

Together four sets of measurements were taken. First, the TM₁ mirror was replaced by the PZT-actuated mirror which was tilted horizontally and after that in the vertical direction. Then the TM₂ mirror was replaced by the PZT-actuated mirror and both measurements were repeated.

Results

The results of these four measurements are shown in Figures 41 and 42 below. Figure 41 contains the signal from PD₁ associated with the X₁ interferometer and Figure 42 the second measurement for the TM₂ mirror (PD₁₂ of the X₁₂ interferometer). Each graph shows from top to bottom plotted as function of the tilt angle:

- the raw DWS signals for both interferometers,
- the respective DC alignment signals for both interferometers,
- and the contrast of both interferometers,

for both directions - on the left side for horizontal and on the right side for vertical tilt.

LPF EM Tilt functional test and calibration
 Mirror 1 actuated
 TNO/AEI 2004/03/19

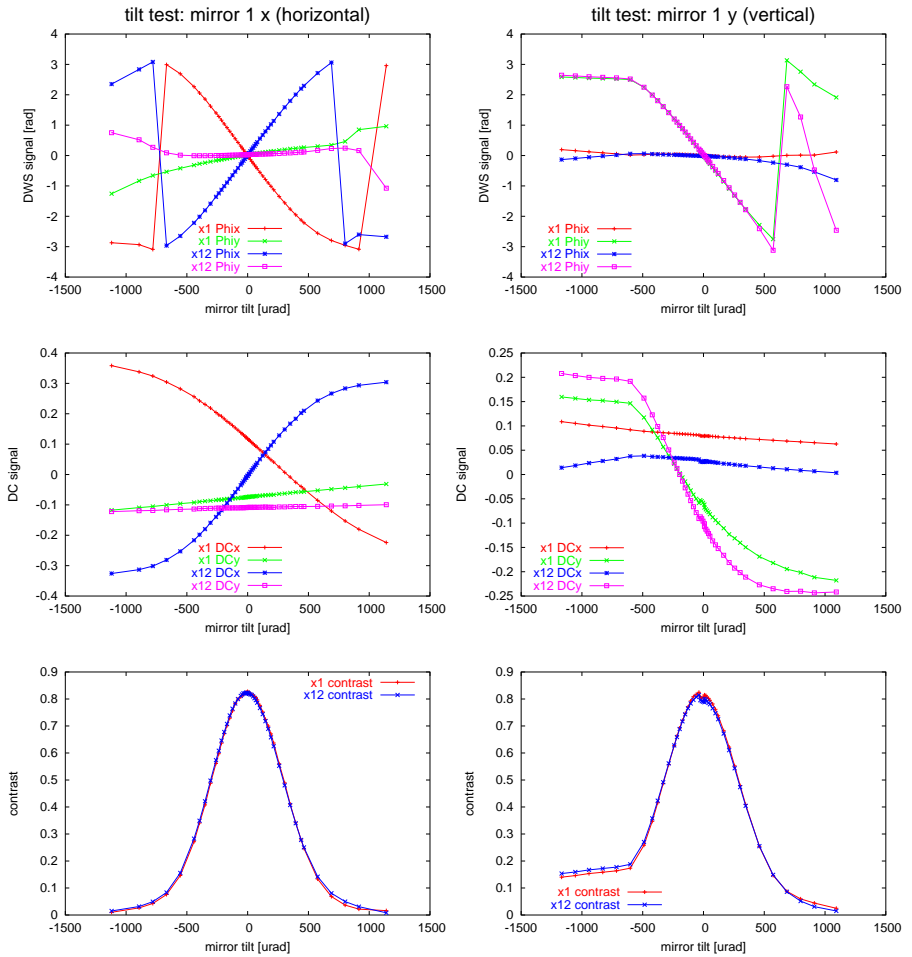


Figure 41. Results of tilt test with test mass TM1.

LPF EM Tilt functional test and calibration
 Mirror 2 actuated
 TNO/AEI 2004/03/19

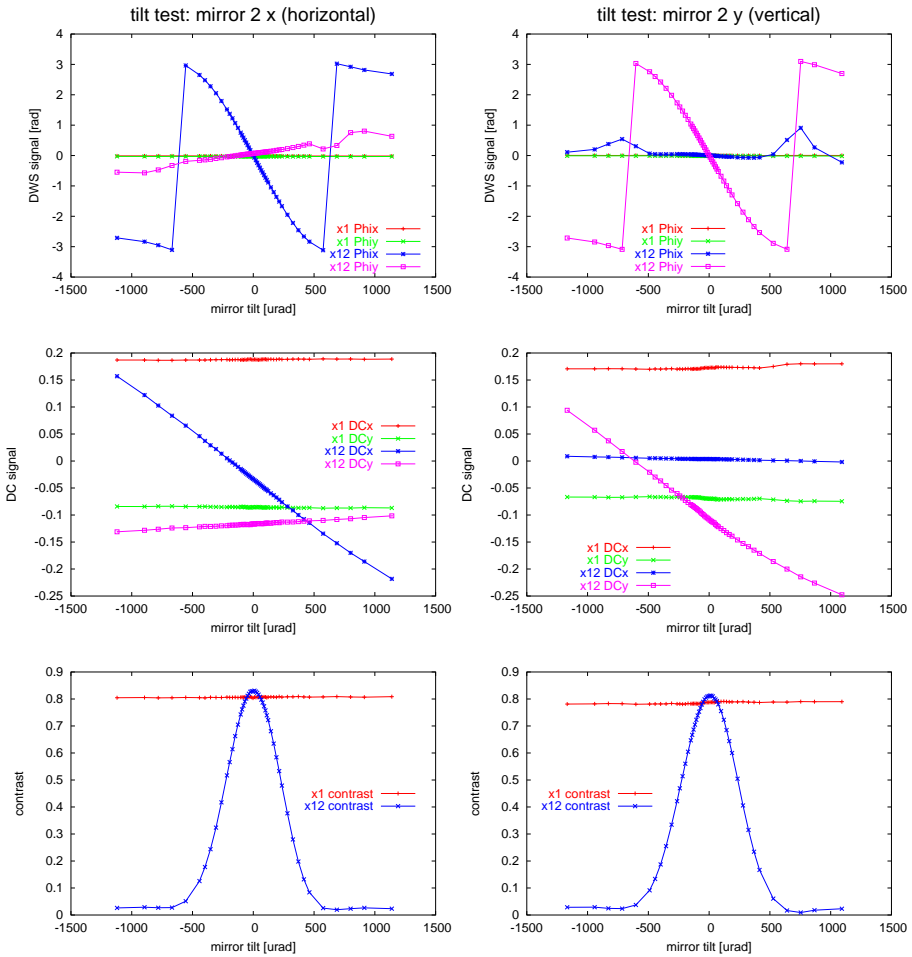


Figure 42. Results of tilt test with test mass TM2.

The measurements show a small cross coupling between the horizontal (x-) and the vertical (y-) direction caused either by imperfect alignment of the tilt axis of the PZT or of the QPDs or both.

The dynamic range within which the DWS signals can be relied upon was predicted to be smaller than 300 μrad . The experiments showed that they are actually be useful up to 500 μrad .

Below $-500 \mu\text{rad}$ in the test with test mass TM1 actuated vertically (right-hand side of Figure 41), the PZT touched the Zerodur adapter plate, leading to a limitation of the mirror motion and a saturation of all signals in this range.

Calibration

In order to derive the calibration factor for the DWS and the DC signals converting the raw alignment signals into real test mass angles, linear functions were fitted to the central parts of each of the measured curve (Figure 43 and 44).

DIFFERENTIAL WAVEFRONT SENSING (DWS) SIGNALS: A simplified analytical model for the DWS calibration factor is given by:

$$\varphi/\alpha = 2\sqrt{2\pi}w(z)/\lambda \approx 5000 \text{ rad/rad} \quad (2.79)$$

where $w(z)$ describes the beam radius at the position z along the propagation axis. α is the test mass angle and φ the differential phase readout.

For this model several simplifying assumptions have been made. To derive more precise predictions, the full geometry of the OBI has to be taken into account. Furthermore the slit of the QPD need to be modeled. This has been done with a numerical computation (qpd.c). Table 2 shows the results derived from the linear fit to the linear part of the measurement as well as the predictions obtained from Equation (2.79). Both are in good accordance to each other.

DC SIGNALS: For the DC alignment signals, the calibration factor from test mass tilt angle α to Δx is (with several idealizations) given by

$$d(\Delta x)/d\alpha = 2\sqrt{2/\pi}L/w, \quad (2.80)$$

where $L \approx 25 \dots 50 \text{ cm}$ is the lever arm from test mass to photodiode, and $w \approx 0.5 \dots 1 \text{ mm}$ the beam radius at the photodiode.

Again, for this analytical model several simplifying assumptions have been made while from the same more precise numerical model described above the following predictions printed in Table 3 have been derived.

LPF EM Tilt calibration DWS
TNO/AEI 2004/03/19

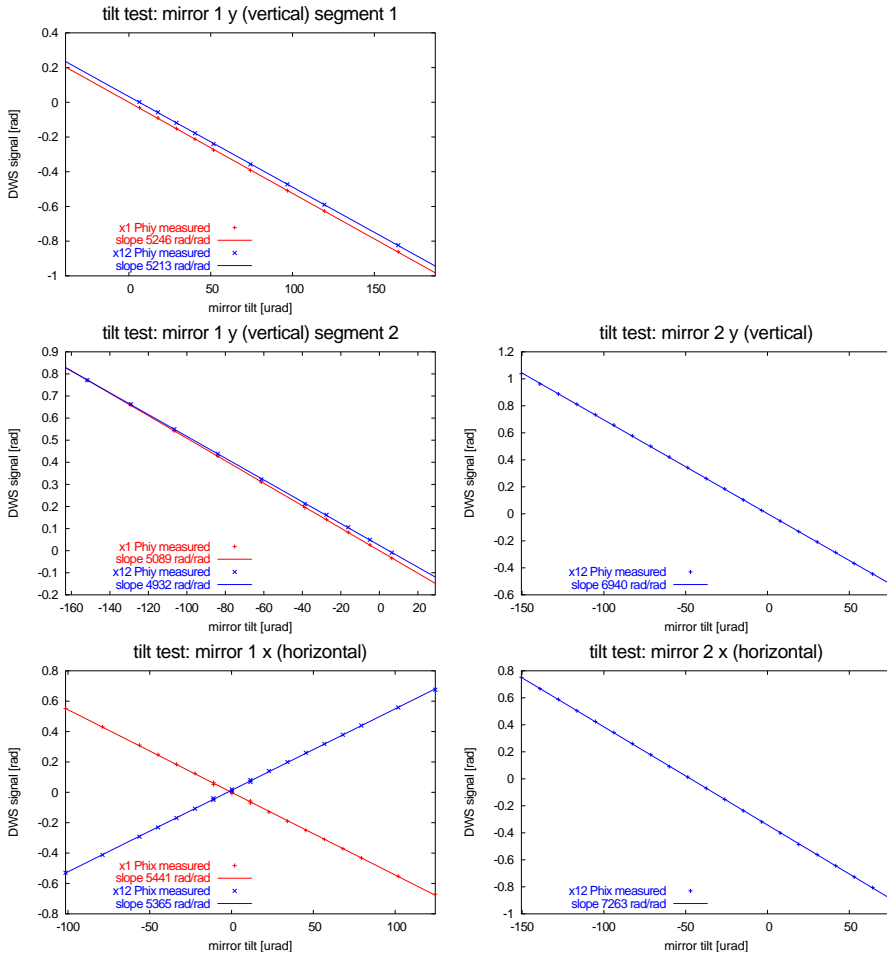


Figure 43. Calibration of DWS alignment signals by linear fit to the central part of the measured data.

LPF EM Tilt calibration DC signals
TNO/AEI 2004/03/19

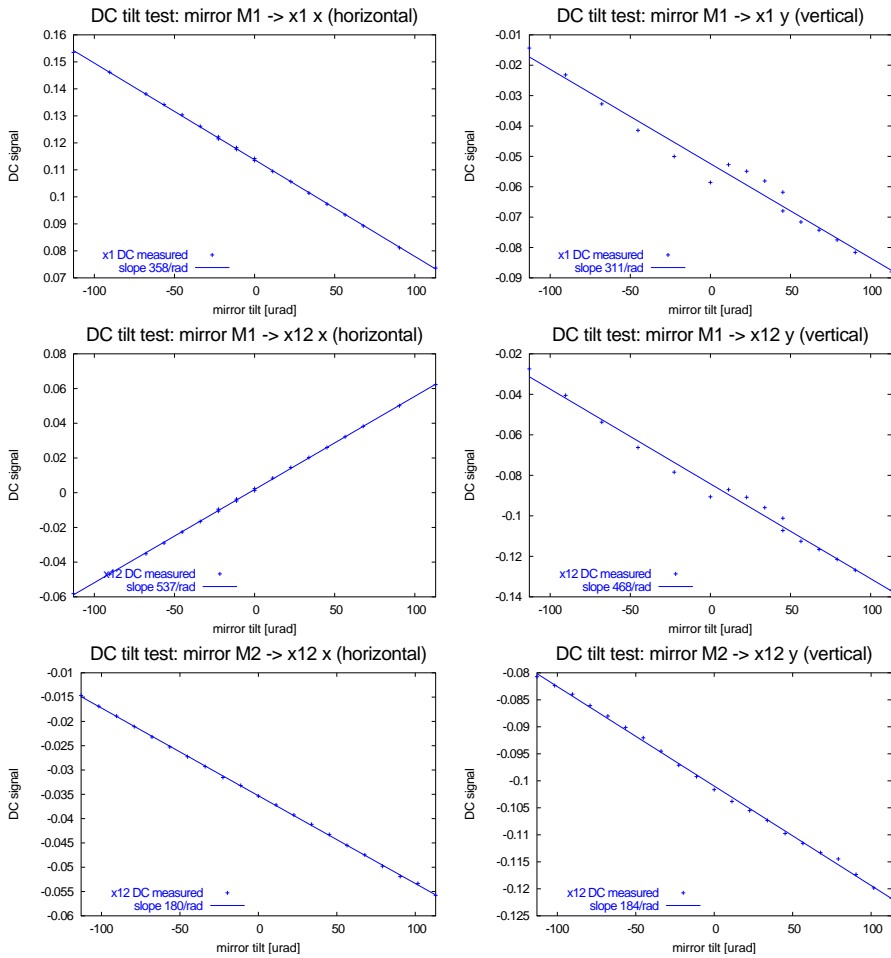


Figure 44. Calibration of DC alignment signals by linear fit to the central part of the measured data.

Tables 2 and 3 show, that the DWS alignment signals are roughly 10 times more sensitive than the DC signals. On the other hand, the dynamic ranges of the DC signals are a factor of two wider than the DWS signals. In that way both types of signals complement each other.

The DC signals are sensitive to a power mismatch between the two beams, which was large during these measurements. They will, however, only be used for a rough initial alignment of the test masses and serve this purpose perfectly even if the calibration factors are not precisely known.

	Tilt TM1	Tilt TM2	units
x_1 ifo predicted (numerical)	5337	0	rad/rad
x_1 ifo measured (x)	5441	0	rad/rad
x_1 ifo measured (y)	5167	0	rad/rad
x_1 - x_2 ifo predicted (numerical)	4963	5994	rad/rad
x_1 - x_2 ifo measured (x)	5365	7263	rad/rad
x_1 - x_2 ifo measured (y)	5072	6940	rad/rad

Table 2. The table shows the numerically predicted and measured DWS calibration factors (derived from a linear to the measured data) for test mass tilt in x and y direction needed to convert the raw DWS signals, obtained from the phasemeter, into real test mass angle.

	Rot. TM1	Rot. TM2	units
x_1 ifo predicted (numerical)	759	0	1/rad
x_1 ifo measured (x)	357	0	1/rad
x_1 ifo measured (y)	310	0	1/rad
x_1 - x_2 ifo predicted (numerical)	1147	304	1/rad
x_1 - x_2 ifo measured (x)	537	180	1/rad
x_1 - x_2 ifo measured (y)	468	184	1/rad

Table 3. The table shows the numerically predicted and measured DC calibration factors (derived from a linear to the measured data) for test mass tilt in x and y direction, needed to convert the raw DC signals, obtained from the phasemeter, into real test mass angle.

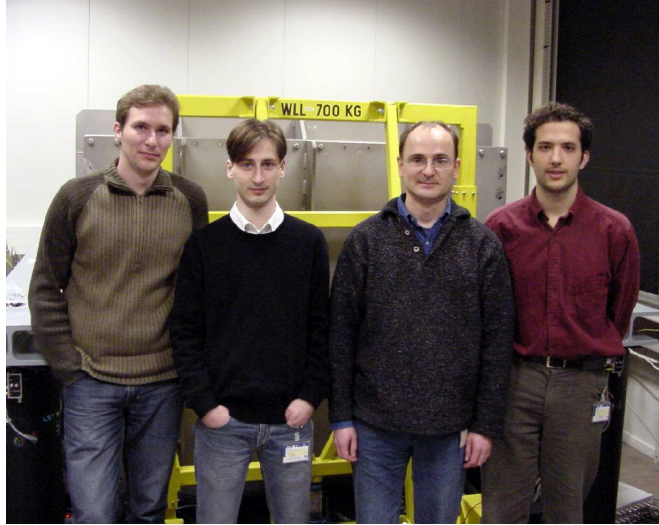


Figure 45. The test team after the first successful evacuation of the test chamber. From left to right: F. Draaisma (TNO), V. Wand (AEI), G. Heinzel (AEI), A. F. García Marín (AEI).

2.4.6 Performance tests

Since the main purpose of the [LTP](#) interferometry is to test and to verify the performance of the test mass drag free and attitude control system by measuring the relative test mass positions, the noise behaviour of the interferometry needs to be known. The requirement set by design is an interferometer noise budget of $10 \text{ pm}/\sqrt{\text{Hz}}$ with the usual frequency dependence within the measurement bandwidth of 3-30 mHz. In order to measure the noise behaviour of the complete [OMS](#) including the [OBI](#) itself, the modulation bench and the phasemeter, several performance tests have been performed. The unavailability of ultra stable test masses was the major problem during these tests. As substitute Zerodur mirrors mounted in commercial precision mounts (described in [Section 2.4.1](#)) were used. The thermal expansion coefficient of these metal mounts is about 1000 times worse compared with Zerodur such that this mounting has to be stated as a weak point within the whole setup.

In order to minimize the effect and to shield the interferometers from air disturbances the optical bench was placed in a chamber which was evacuated. [Figure 45](#) shows the test team after the first successful evacuation of the test chamber.

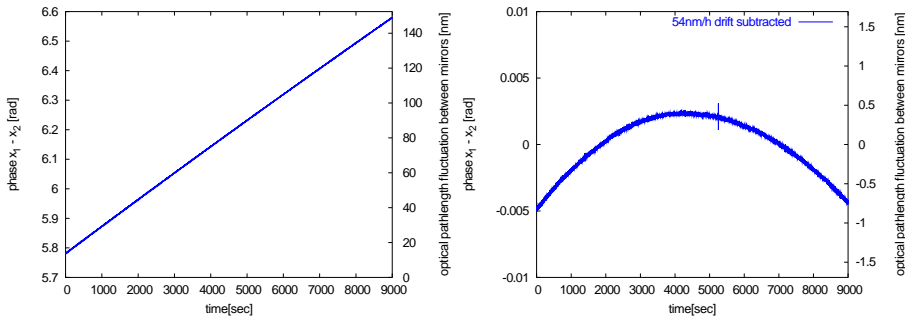


Figure 46. Time series of the x_1-x_2 measurement. In the right-hand graph, a best-fit linear function was subtracted.

The pressure was of the order of 1 mbar. Together with a thermal shield made from steel surrounding the OBI inside the vacuum chamber and the thermal mass of the vacuum chamber itself, the setup acted as a thermal low pass filter. The whole vacuum chamber was isolated from the ground by the use of a passive air damping system whose resonance frequency was inferred from the interferometric measurements to be approximately 1.5 Hz.

Long term time series

In order to reduce environmental disturbances as much as possible, all performance measurements were taken over night. Out of several data stretches, one stretch of 9000 s length was selected for the following graphs that showed little external disturbances.

The time series x_1-x_2 of this measurement is shown in Figure 46. The dominating linear drift of 48 nm/h can be traced back to a thermal expansion of the metal mirror mounts. Even the residual after subtracting a linear function from the time series (right picture of Figure 46), the interferometer data is still dominated by a slowly drifting motion. The interferometer noise itself is indicated by the finite thickness of the line in the right-hand graph.

Contrasts of the interferometers

The contrasts of the reference and x_1-x_2 interferometers associated with the measurement described above are shown in Figure 47. The time series shows a transient deviation from its nominal value of 80% at approximately 5200 s. This spike is probably due to a temporary loss of the laser power - possi-

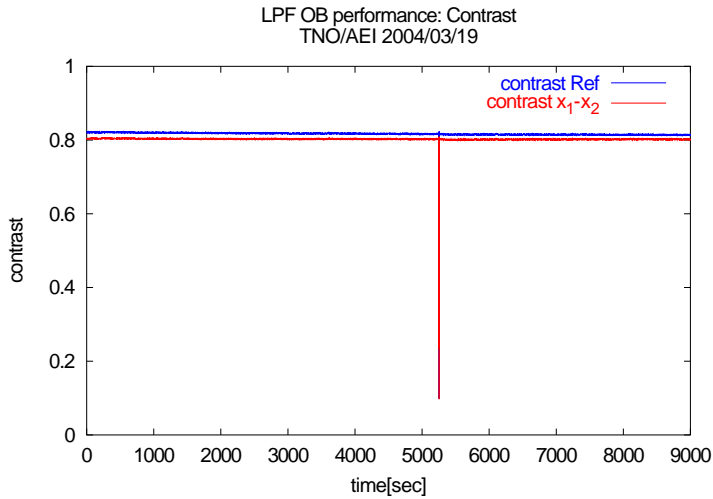


Figure 47. Contrast of the $x_1 - x_2$ measurement.

bly due to a dust particle crossing the beam path. However, the remarkable fact is how the x_1-x_2 measurement (Figure 46) is nearly unaffected by this interruption. This is in strong contrast to most other types of interferometers (Fabry-Perot, Michelson on dark fringe etc.) which probably would have ‘lost lock’ in such a situation and would have required a time-consuming and risky re-initialization.

Figure 48 shows a linear spectral density of the $x_1 - x_2$ measurement. The dark solid curve shows the measurement described here. For comparison, several other curves are also shown (from top to bottom at $2 \cdot 10^{-2}$ Hz):

- A curve measured at TNO in a comparable configuration, but without the fiber optical pathlength (OPD) stabilization (discussed below).
- The LPF mission goal. The y-axis is referring to optical pathlength (and not to the position of the test mass), and the LPF mission goal of $85 \text{ pm}/\sqrt{\text{Hz}}$ test mass displacement is hence plotted as $170 \text{ pm}/\sqrt{\text{Hz}}$ optical pathlength (at 30 mHz).
- The previous ‘best curve’ with quadrant diodes, from the Glasgow prototype interferometer (also developed during the preinvestigations), measured in collaboration between Glasgow and AEI staff at Glasgow using

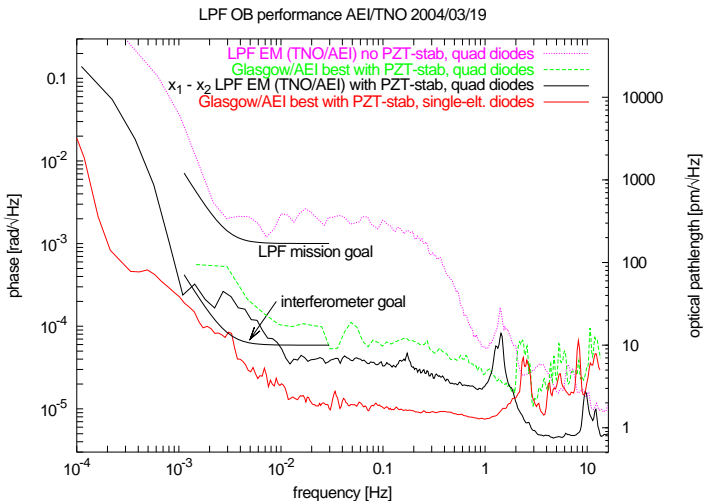


Figure 48. Linear spectral density of the $x_1 - x_2$ measurement (see text).

both Glasgow and AEI equipment.

- The LPF interferometer goal at $9 \text{ pm}/\sqrt{\text{Hz}}$ optical pathlength (at 30 mHz).
- The 'best curve', from the Glasgow prototype interferometer (also developed during the preinvestigations), measured in collaboration between Glasgow and AEI staff at Glasgow using both Glasgow and AEI equipment. This curve was measured with single-element diodes, which consistently show a better noise behaviour than quadrant diodes, the reason for which is under investigation.

Figure 49 shows a linear spectral density of a typical DWS alignment measurement (in this case associated with the dark solid curve from Figure 48).

During the design phase of the interferometry the noise level for the alignment signals has been predicted to be better than $10 \text{ nrad}/\sqrt{\text{Hz}}$ (referred to the test mass misalignment). Figure 49 shows that the noise level is even better. To get an impression of the achieved angular sensitivity, 10 nrad corresponds to an angle of 1 mm on 100 km .

Figure 49 also shows that the noise of the PDR is higher than that measured at PDX. This can be traced back to the fact that this photo diode shows a large static DWS misalignment (due to the imperfect beam injector alignment),

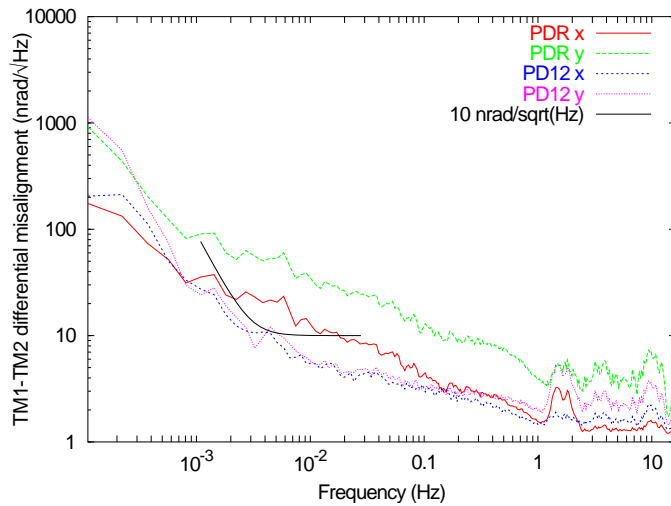


Figure 49. Linear spectral density of the DWS alignment measurements (see text).

whereas the static DWS misalignment could be made negligible for the $x_1 - x_2$ measurement using the adjustable mirror mounts.

The three lower performance curves shown in Figure 48 could only be achieved by the use of an additional actuator without which the noise cancellation (described in Section 2.1.2) works only down to nanometer level but below that, optical pathlength difference fluctuations disturb the measurement. The next Chapter is devoted to this phenomenon.

2.5 CONCLUSION

The interferometric concept of the LISA technology package (LTP) was implemented and tested successfully. Accompanied by the expertise and the experiences acquired during the laboratory development and testing of the interferometry, the electronics and the phasemeter, the industrial implementation of the prototype flight hardware has begun. An engineering model prototype of the optical bench was extensively tested during a measurement campaign. The required longitudinal and angular performance of the interferometer have been demonstrated.

3

NON-LINEARITIES IN THE LTP PHASE READOUT

*"Holzhacken ist deshalb so beliebt,
weil man bei dieser Tätigkeit den Erfolg sofort sieht."*

ALBERT EINSTEIN

(1879-1955) dt.- US-amerik. Physiker

Whilst the successful testing of [LTP OBI](#) and a discussion and mitigation of several noise sources were presented in the previous chapter, this chapter is devoted to one single type of noise: This suggests that the noise described here strongly differs from the other types of noise typically encountered.

A very common method to investigate the behaviour of appearing noise is the concept of *noise projection* where a strong disturbance is applied to the system under test while the reaction of the system is measured. By measuring the real disturbances during normal operation of the system the main observable can be corrected by using the known response and the noise measured simultaneously. This can be performed in the time domain or in the Fourier domain. For the Fourier domain analysis, the full transfer function is needed for the individual noise processes which can be used to predict the effect of occurring disturbances to the main observable. In order to work correctly, the whole concept requires linear coupling processes. During the breadboarding of the [LTP](#) interferometer, a number of such well behaved noise sources were identified and removed by finding the coupling mechanism and measuring the transfer function of the process such that a control loop could be designed giving the ability to suppress the effect of disturbances e.g. environmental noise causing a disturbance of the phase measurement. In contrast to these linear noise sources, the effect of the disturbances investigated in this chapter behaves nonlinearly. This foils the approach of applying the methods applicable to linear systems, in particular the concept of transfer functions.

Section [3.1](#) gives an introduction on the observations of the unexpected non-linear residual phase. It explains the context of its occurrence if the common mode pathlength difference Δ_F changes. These observations lead to a theory of the coupling mechanism based on the appearance of spurious beat notes

at the heterodyne frequency and is described in Section 3.2. In order to verify this theory it had to undergo a comprehensive experimental proof. Section 3.3 is dedicated to this experimental investigation. This chapter concludes with a summary in Section 3.4.

The work presented in this chapter was done together with G. Heinzl, A. García, F. Steier and F. Guzmán and the description given here is partially from an internal project report (HEINZEL *et al.* (2005b)) that was written by that team.

3.1 RESIDUAL PHASE NOISE AT THE PICOMETER LEVEL

As indicated in the previous chapter, the required performance of the LTP optical bench engineering model and its dedicated subsystems was only achieved by the use of an additional actuator and an associated control loop which had not been foreseen in the original baseline design.

As one key feature, repeatedly to be mentioned here, the split interferometry concept (see section 2.1.2 and Figure 50), is intended to measure all environmental noise contributions which affect all four interferometers in common mode (difference between lengths L_1 and L_2 in Figure 50). Since all measurement phases φ_M are referred to the phase of the reference interferometer φ_R and the main observables are obtained as $\varphi_M - \varphi_R$, all common mode pathlength fluctuations appearing in the first part of the interferometers should cancel.

3.1.1 Description of the phenomenon

The noise cancellation worked as expected for all common mode pathlength fluctuations down to nanometer (mrad) level. But below that, a noise level with varying amplitude remained (see Figure 51). On the first view the occurring noise looks arbitrary. In order to analyze the behaviour of the noise, the phases φ_R and φ_M are expressed using the pathlengths as shown in Figure 50

$$\begin{aligned}\varphi_R &= \frac{2\pi}{\lambda}(L_1 + L_{1R} - L_2 - L_{2R}) \\ \varphi_M &= \frac{2\pi}{\lambda}(L_1 + L_{1M} - L_2 - L_{2M}).\end{aligned}\tag{3.1}$$

According to the conceptual splitting of the interferometry into stable and unstable part φ_R and φ_M can now be decomposed into a common contribution Δ_F from the unstable interferometer part and a contribution from the stable

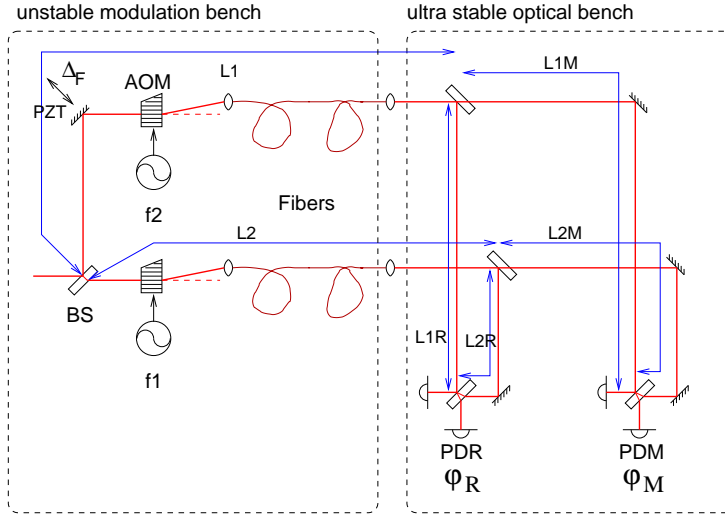


Figure 50. Illustration of the split interferometry. The LTP interferometry consists of the modulation bench and the ultra stable optical bench. Pathlength fluctuations of the unstable part of the interferometry are measured in each individual interferometer and cancel in the differential phase $\varphi_M - \varphi_R$. The differential phase only contains pathlength fluctuations coming from the optical bench. Not shown in this picture are the testmass positions which are part of the stable optical paths.

part Δ_R and Δ_M such that:

$$\begin{aligned}\varphi_R &= \Delta_F + \Delta_R, \\ \varphi_M &= \Delta_F + \Delta_M.\end{aligned}\tag{3.2}$$

with

$$\begin{aligned}\Delta_F &= \frac{2\pi}{\lambda}(L_1 - L_2), \\ \Delta_R &= \frac{2\pi}{\lambda}(L_{1R} - L_{2R}), \\ \Delta_M &= \frac{2\pi}{\lambda}(L_{1M} - L_{2M}).\end{aligned}\tag{3.3}$$

Δ_R and Δ_M represent differential pathlengths in the stable reference and measurement interferometers. Δ_F represents the *differential* pathlength noise

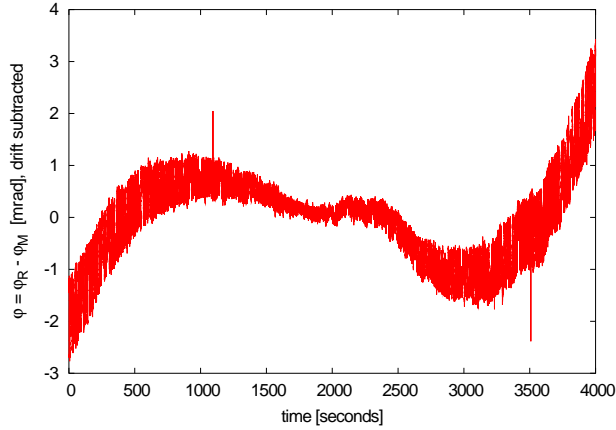


Figure 51. Time series of $\varphi = \varphi_M - \varphi_R$ measurement taken by AEI at TNO using the LTP EM (03/2004). A linear drift was subtracted.

mainly due to the optical fibers which ideally should cancel in the difference

$$\begin{aligned}
 \varphi &= \varphi_M - \varphi_R \\
 &= \frac{2\pi}{\lambda} (\Delta_F + \Delta_M - \Delta_F - \Delta_R) \\
 &= \frac{2\pi}{\lambda} (\Delta_M - \Delta_R). \tag{3.4}
 \end{aligned}$$

The quasi-random noise of this phase difference φ shown in Figure 51 can now be studied as function of the differential fluctuations of the common interferometer paths. Therefore a linear scan was applied to the PZT shown in Figure 50 and thus to the *differential* pathlength Δ_F (on the time scale of the scan, the phases Δ_R and Δ_M can be considered as constant). The dynamic range of the scan of Δ_F extended to several micrometers (corresponding to several fringes). The result is shown in Figure 52. The residual phase error depends on the differential pathlength changes which theoretically should cancel since they are common mode in all interferometers. The error turned out to consists of one component which is periodic with $\sin(\Delta_F + \alpha)$ having an amplitude of 0.72 mrad while a second component with an amplitude of 1.33 mrad is periodic with $\sin(2\Delta_F + \beta)$. This nonlinearity was observed in

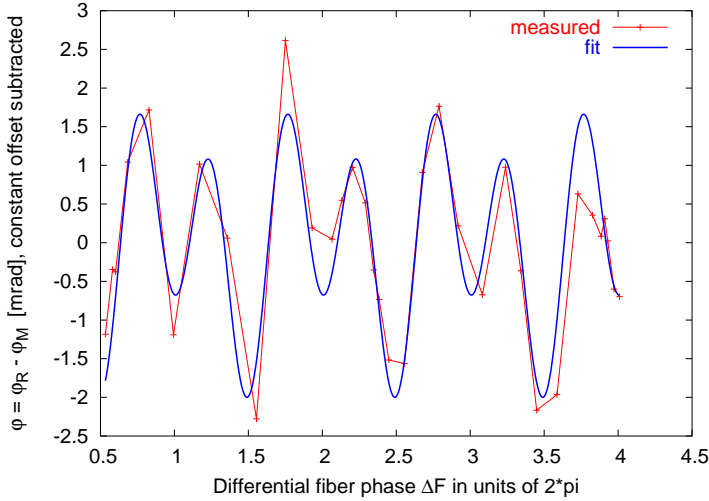


Figure 52. Measurement of the periodic nonlinearity in the LTP EM interferometer (measured by AEI at TNO Delft 03/2004). From the differential phase ϕ a constant offset was subtracted. The $\sin(\Delta_F)$ component has an amplitude of 0.72 mrad, while the $\sin(2\Delta_F)$ component has an amplitude of 1.33 mrad.

different setups¹ at different times with varying phase offsets α and β and error amplitudes but always $\sin(2\Delta_F + \beta)$ was the dominant term.

3.1.2 Optical pathlength difference stabilization

Since the primary source of the residual phase noise turned out to be the differential pathlength variations (e.g. fiber phase noise) Δ_F , this suggests to keep this difference actively stabilized in order to reduce the residual phase noise. Therefore, a PZT mounted mirror was included in one path of the modulation bench. Since the reference phase ϕ_R is measured with the phasemeter with respect to the ADC clock which is coherent with the modulation frequency^{2,3} it can be used as an error signal in order to control the PZT. This additional control loop is called optical pathlength difference (OPD) stabilization. Since the update rate of the phase ϕ_R coming from the phasemeter is

¹ e.g. in a similar setup in Glasgow and during the measurement campaign at TNO

² since both of them are derived from the same master clock

³ For most applications in particular for a complex system such as spacecraft it should be considered, that a system wide synchronization by a common clock is an advantage.

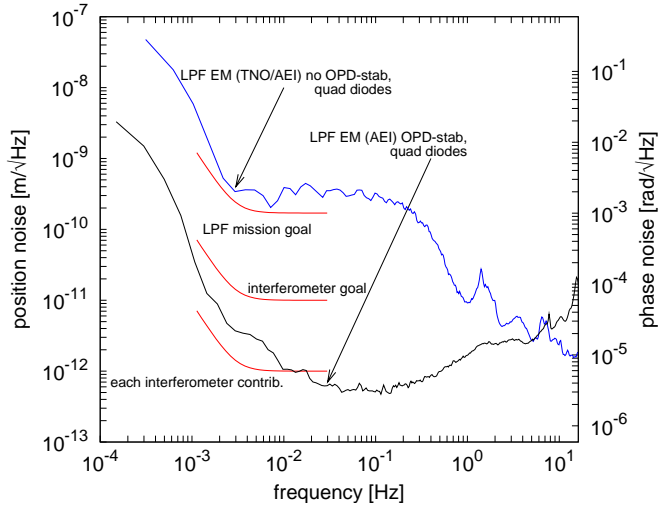


Figure 53. Noise curves of the phase measurement. The upper curve shows the achieved sensitivity when the differential phase is not being stabilized. The lower curve shows the current sensitivity with the OPD stabilisation.

limited to a few ten Hz, a digital control loop implementation did not provide a sufficiently high unity gain frequency in order to achieve reasonable gain¹ at low frequencies (see Section B.2). However, an OPD stabilization was implemented using an analog control loop using an analog multiplier as a phasemeter.

Only by the use of this OPD stabilization the performance of the whole setup could meet the interferometer noise budget of 10 pm (with the usual frequency dependence described in Section 1.1.2). Current performance measurements of the longitudinal phase noise of the interferometer are shown in Figure 53. The goal of about $10 \text{ pm}/\sqrt{\text{Hz}}$ for the longitudinal phase sensitivity has been achieved in the relevant frequency range from 3-30 mHz. The angular resolution of the interferometer for sensing test mass tilt and rotation perpendicular to the sensitive x-axis reaches an accuracy better than $10 \text{ nrad}/\sqrt{\text{Hz}}$ (Figure 54).

Even if the OPD stabilization is able to mitigate the nonlinear error in the time series, the origin and the coupling process of this unexpected error were needed to be understood and investigated in detail.

¹ for disturbances under laboratory conditions. Since onboard the environmental noise induced fiber phase noise is much smaller, for LISA Pathfinder a digital control loop is used.

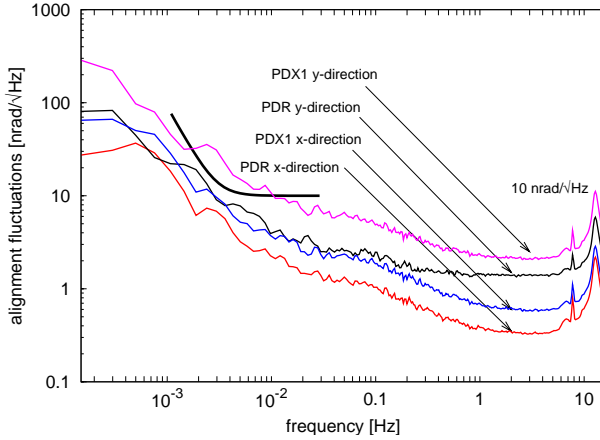


Figure 54. This graph shows the sensitivity of the alignment measurements of the reference interferometer (PDR) and the interferometer that measures the alignment of test mass 1 (PDX1). For both interferometers the x and y direction are plotted.

3.2 SIDEBAND-INDUCED NOISE: THEORY

3.2.1 Modelling the coupling process

The main observable φ is derived as the difference of an optical reference phase φ_R and a measurement phase φ_M , where each of them is obtained from a FFT based phase measurement algorithm that acts as a band pass filter for the photocurrents from the optical signals and takes only signal components within a narrow band centered on the heterodyne frequency f_{het} into account. For this reason only disturbances within this narrow band can affect the phase measurement and thus cause a phase error. Figure 55 illustrates the FFT based phase estimation. The heterodyne component of the measured optical signal F is decomposed into a real and an imaginary part by projection onto the basis vectors $\cos(\omega_{\text{het}}t)$ and $\sin(\omega_{\text{het}}t)$. By taking into account that the optical phases Δ_R and Δ_M can vary (in absence of an OPD stabilization) over several wavelengths, any disturbance of the heterodyne signal with components near f_{het} and an arbitrary phase can cause a periodic phase error.

Figure 56 explains the occurrence of a periodic phase error by the appearance of an additional heterodyne component with constant phase. By the use of this picture the error term $\sin(\Delta_f)$ in Figure 52 can be understood. The

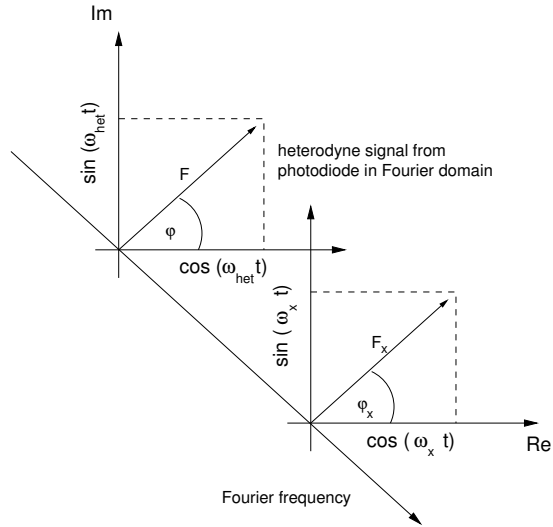


Figure 55. Illustration of the FFT based phase measurement. Each frequency component F_x with phase φ_x is represented by its own basis system consisting of $i \sin(\omega_x t)$ and $\cos(\omega_x t)$. The arrow F represents here the heterodyne component and F_x is a signal component at an arbitrary frequency.

phase φ_x represents all primary phase measurements (φ_R, φ_M). F represents the heterodyne signal as complex vector

$$F = x + iy \quad (3.5)$$

with

$$x = \frac{1}{T} \int_0^T dt I(t) \cos(\omega_{\text{het}} t) \quad (3.6)$$

$$y = \frac{1}{T} \int_0^T dt I(t) \sin(\omega_{\text{het}} t), \quad (3.7)$$

where $I(t)$ is the heterodyne signal. x and y represent the real and imaging part from the [SBDFT](#) and the time interval represents the lengths of the [SBDFT](#). φ is given by

$$\varphi_x = \arg \frac{y}{x}. \quad (3.8)$$

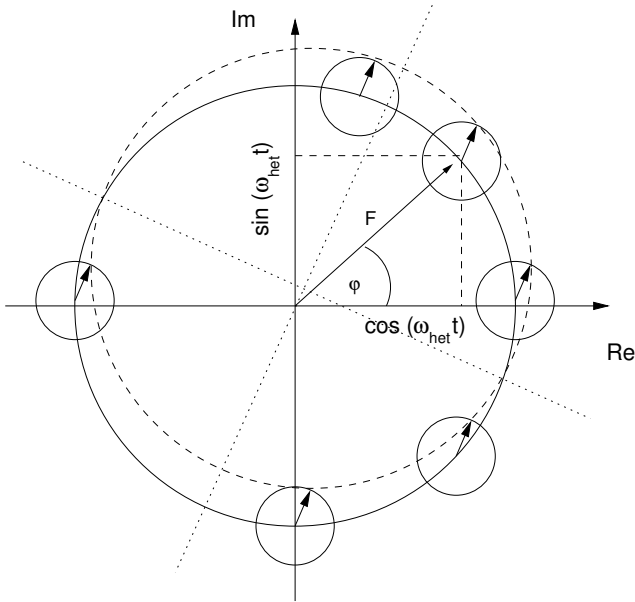


Figure 56. Illustration of the main beat note with presents of an spurious component at the heterodyne frequency. F represents the clean heterodyne signal with a *small vector* with constant phase at its end. This picture explains the occurring $\sin(\Delta_f)$ error term (see text).

If now an additional noise term at the heterodyne frequency must be taken into account (see small arrows in Figure 56), each primary phase measurement gets disturbed by an extra phase variation $\delta\varphi_x$ which is given by

$$\delta\varphi_x = \epsilon \sin(\varphi_x - \gamma). \quad (3.9)$$

ϵ is the amplitude of the error and γ its phase. Thus φ_R and φ_M become

$$\varphi'_R = \varphi_R + \delta\varphi_R = \varphi_R + \epsilon \sin(\varphi_R - \gamma), \quad (3.10)$$

$$\varphi'_M = \varphi_M + \delta\varphi_M = \varphi_M + \epsilon \sin(\varphi_M - \gamma). \quad (3.11)$$

The differences $\Delta\varphi'$ between the reference phase φ'_R and the individual measurement phases φ'_M are the main observables which get affected by the disturbances $\delta\varphi = \delta\varphi_R - \delta\varphi_M$:

$$\Delta\varphi' = \varphi'_R - \varphi'_M = \Delta\varphi + \delta\varphi = \varphi_R - \varphi_M + \delta\varphi_R - \delta\varphi_M. \quad (3.12)$$

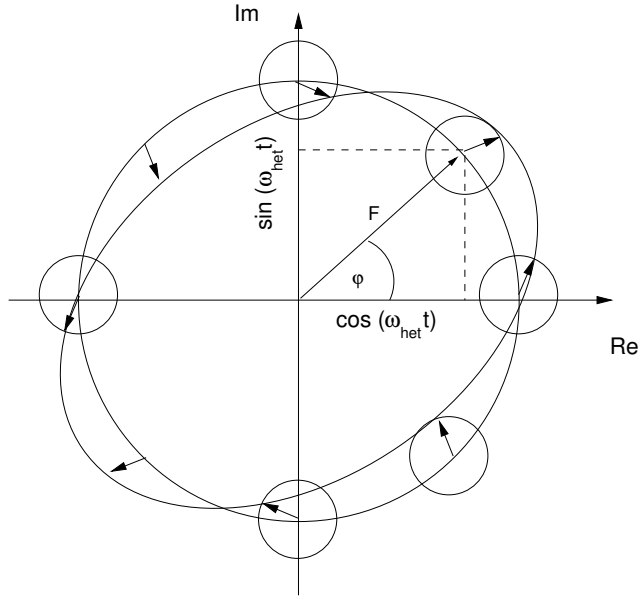


Figure 57. Illustration of the main beat note with presents of an spurious component at the heterodyne frequency with changing phase. F represents the clean heterodyne signal with an *small vector* with changing phase at its end. This picture explains the occurring $\sin(2\Delta_f)$ error term (see text).

While each individual phase measurement φ_x becomes disturbed by $\delta\varphi_x = \epsilon \sin(\varphi_x - \gamma)$, the main observables become disturbed by

$$\delta\varphi = \epsilon \sin(\varphi_R - \gamma) - \epsilon \sin(\varphi_M - \gamma). \quad (3.13)$$

$$\begin{aligned} \frac{\delta\varphi}{\epsilon} &= \sin(\varphi_M - \gamma) - \sin(\varphi_R - \gamma) \\ &= 2 \cos\left(\frac{\varphi_M + \varphi_R}{2} - \gamma\right) \cdot \sin\left(\frac{\varphi_M - \varphi_R}{2}\right). \\ &= 2 \cos\left(\Delta_F + \frac{\Delta_M + \Delta_R}{2} - \gamma\right) \cdot \sin\left(\frac{\Delta_M - \Delta_R}{2}\right). \end{aligned} \quad (3.14)$$

In order to explain the error which is periodic with $2\Delta_F$, an additional error at the heterodyne frequency with a varying phase is assumed. Its phase is proportional to twice the phase of the main beat note. Figure 57 shows the main beat note as the vector F and the spurious beat as small error at its end.

During one full cycle of F the *small vector* rotates twice in reverse direction in the reference frame of F.

This causes a phase error given by:

$$\delta\varphi_x = \varepsilon \sin(2\varphi_x - \gamma). \quad (3.15)$$

ε is the amplitude of the error and γ its initial phase. If one proceeds according to the calculations above, each individual phase measurement φ_x becomes disturbed by $\delta\varphi_x = \varepsilon \sin(2\varphi_x - \gamma)$ and the main observables become disturbed by

$$\delta\varphi = \varepsilon \sin(2\varphi_R - \gamma) - \varepsilon \sin(2\varphi_M - \gamma), \quad (3.16)$$

$$\begin{aligned} \frac{\delta\varphi}{\varepsilon} &= \sin(2\varphi_M - \gamma) - \sin(2\varphi_R - \gamma) \\ &= 2 \cos(\varphi_M + \varphi_R - \gamma) \cdot \sin(\varphi_M - \varphi_R) \\ &= 2 \cos(2\Delta_F + \Delta_M + \Delta_R - \gamma) \cdot \sin(\Delta_M - \Delta_R). \end{aligned} \quad (3.17)$$

3.2.2 Analytical description of the sideband induced phase error

¹ Early in the study it was discovered that the light in each of the two channels, which should ideally be monochromatic and separated by f_{het} , contains additional frequency components that are separated by integer multiples of f_{het} from the nominal frequency. The occurrence of each AOM drive frequency in the other channel, which can be caused by electrical crosstalk between the two AOM drivers and/or AOMs. Measurements (see Section 3.3.5) showed, however, that in addition sidebands at offsets of $\pm f_{\text{het}}$ and $\pm 2 \times f_{\text{het}}$ from the carrier are present in both beams. This section examines the effect of such sidebands, while their possible origin mechanism will be examined in Sections 3.3.5.

Figure 58 illustrates the sidebands at offsets of $\pm f_{\text{het}}$ and $\pm 2 \times f_{\text{het}}$ from each carrier and their frequency relationships. The two beams are described mathematically by

$$\begin{aligned} e_1 &= \exp(i\omega_0 t) + a_{-2} \exp(i(\omega_0 - 2\omega_m)t) + a_{-1} \exp(i(\omega_0 - \omega_m)t) \\ &\quad + a_{+1} \exp(i(\omega_0 + \omega_m)t) + a_{+2} \exp(i(\omega_0 + 2\omega_m)t), \\ e_2 &= \exp(i(\omega_0 + \omega_m)t) + b_{-2} \exp(i(\omega_0 - \omega_m)t) + b_{-1} \exp(i\omega_0 t) \\ &\quad + b_{+1} \exp(i(\omega_0 + 2\omega_m)t) + b_{+2} \exp(i(\omega_0 + 3\omega_m)t), \end{aligned} \quad (3.18)$$

¹ This section 3.2.2 was jointly compiled and written by the noise investigation task force (G. Heinzl, V. Wand, A. F. García Marín, F. Steier, F. Guzmán Cervantes) and distributed in 2005 as final report [HEINZEL et al. \(2005b\)](#) on an ESA contract

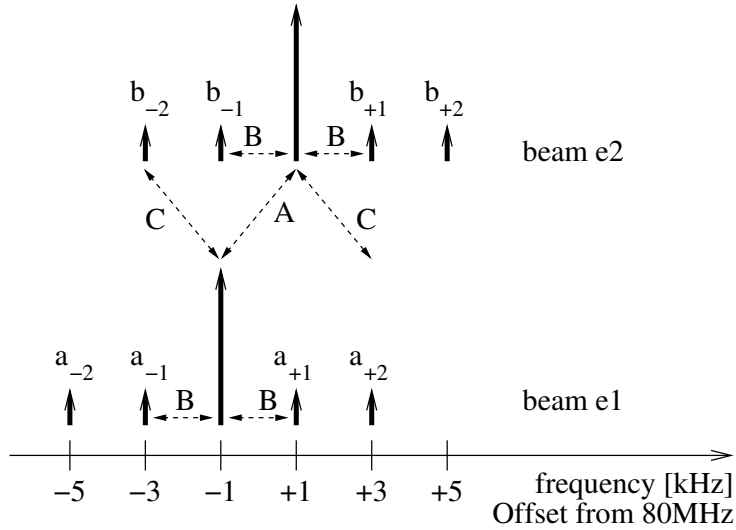


Figure 58. Illustration of the sidebands at offsets of $\pm f_{\text{het}}$ and $\pm 2 \times f_{\text{het}}$ from both beams. The thick vertical arrows represent the light amplitudes, while the dashed arrow 'A' represents the main carrier-carrier beat (desired), and 'B' and 'C' two types of undesired beat notes. For simplicity, $f_{\text{het}} = 2 \text{ kHz}$ has been chosen in this illustration.

where equal and unity carrier amplitude for both beams has been assumed. This general expression includes all possible first- and second-order sidebands of both beams.

Without loss of generality, all phaseshifts can be assigned to one of the two beams (beam 2). The field amplitude at the photodiodes is then given by

$$\begin{aligned} e_M &= e_1 + \exp(-i(\Delta_F + \Delta_M))e_2, \\ e_R &= e_1 + \exp(-i(\Delta_F + \Delta_R))e_2, \end{aligned} \quad (3.19)$$

for the measurement and the reference interferometer, respectively.

The measured photocurrent is proportional to $|e|^2 = ee^*$, which is a lengthy expression, for example the photocurrent for the measurement interferometer

is

$$\begin{aligned}
 |e_M|^2 = & \\
 & 2 + a_{-1}^2 + a_{-2}^2 + a_{+1}^2 + a_{+2}^2 + b_{-1}^2 + b_{-2}^2 + b_{+1}^2 + b_{+2}^2 \\
 & + 2(a_{-1} + a_{-1} a_{-2} + a_{+1} + a_{+1} a_{+2} \\
 & + b_{-1} + b_{-1} b_{-2} + b_{+1} + b_{+1} b_{+2}) \cos(\omega_m t) \\
 & + 2(a_{-2} + a_{-1} a_{+1} + a_{+2} + b_{-2} + b_{-1} b_{+1} + b_{+2}) \cos(2 \omega_m t) \\
 & + 2(a_{-2} a_{+1} + a_{-1} a_{+2} + b_{-2} b_{+1} + b_{-1} b_{+2}) \cos(3 \omega_m t) \\
 & + 2(a_{-2} a_{+2} + b_{-2} b_{+2}) \cos(4 \omega_m t) \\
 & + 2 \cos(\Delta_F + \Delta_M) (a_{+1} + b_{-1} + a_{-1} b_{-2} + a_{+2} b_{+1} \\
 & + (1 + a_{+2} + a_{-1} b_{-1} + a_{+1} b_{-1} + b_{-2} \\
 & + a_{-2} b_{-2} + a_{+1} b_{+1} + a_{+2} b_{+2}) \cos(\omega_m t) \\
 & + (a_{-1} + (a_{-2} + a_{+2}) b_{-1} + b_{+1} + a_{+1} (b_{-2} + b_{+2})) \cos(2 \omega_m t) \\
 & + (a_{-2} + a_{+2} b_{-2} + a_{-1} b_{+1} + b_{+2}) \cos(3 \omega_m t) \\
 & + (a_{-2} b_{+1} + a_{-1} b_{+2}) \cos(4 \omega_m t) + a_{-2} b_{+2} \cos(5 \omega_m t) \\
 & - 2(1 + a_{-1} b_{-1} - a_{+1} b_{-1} + (-1 + a_{-2}) b_{-2} + a_{+1} b_{+1} \\
 & + a_{+2} (-1 + b_{+2})) \times \sin(\Delta_F + \Delta_M) \sin(\omega_m t) \\
 & - 2(a_{-1} + a_{-2} b_{-1} - a_{+2} b_{-1} - a_{+1} b_{-2} + b_{+1} + a_{+1} b_{+2}) \times \\
 & \times \sin(\Delta_F + \Delta_M) \times \sin(2 \omega_m t) \\
 & - 2(a_{-2} - a_{+2} b_{-2} + a_{-1} b_{+1} + b_{+2}) \sin(\Delta_F + \Delta_M) \sin(3 \omega_m t) \\
 & - 2(a_{-2} b_{+1} + a_{-1} b_{+2}) \sin(\Delta_F + \Delta_M) \sin(4 \omega_m t) \\
 & - 2 a_{-2} b_{+2} \sin(\Delta_F + \Delta_M) \sin(5 \omega_m t)
 \end{aligned} \tag{3.20}$$

To avoid mistakes, this and all other complicated expressions were calculated using a computer-algebra system (MATHEMATICA).

Since our SBDFM phasemeter is in effect a bandpass filter that examines only the $\omega_m t$ component of the photocurrent, the next step¹ is to extract all parts of this expression with a $\sin(\omega_m t)$ or $\cos(\omega_m t)$ time dependence:

$$\begin{aligned}
 I_M = (e_M e_M^*)|_{\omega=\omega_m} = & \\
 & 2((a_{-1} + a_{-1} a_{-2} + a_{+1} + a_{+1} a_{+2} + b_{-1} + b_{-1} b_{-2} + b_{+1} + b_{+1} b_{+2}) \times \\
 & \times \cos(\omega_m t) + (a_{+2} + a_{+1} b_{-1} + b_{-2}) \cos(\Delta_F + \Delta_M - \omega_m t) \\
 & + (1 + a_{-1} b_{-1} + a_{-2} b_{-2} + a_{+1} b_{+1} + a_{+2} b_{+2}) \cos(\Delta_F + \Delta_M + \omega_m t))
 \end{aligned} \tag{3.21}$$

¹ Strictly speaking, this step is not necessary because the phase extraction in the next step ignores all other frequency components. Due to the complexity of the intermediate results, however, this step is often helpful to reduce the computation time.

$$\begin{aligned}
 I_R &= (e_R e_R^*)|_{\omega=\omega_m} = \\
 &2((a_{-1} + a_{-1} a_{-2} + a_{+1} + a_{+1} a_{+2} + b_{-1} + b_{-1} b_{-2} + b_{+1} + b_{+1} b_{+2}) \times \\
 &\times \cos(\omega_m t) + (a_{+2} + a_{+1} b_{-1} + b_{-2}) \cos(\Delta_F + \Delta_R - \omega_m t) \\
 &+ (1 + a_{-1} b_{-1} + a_{-2} b_{-2} + a_{+1} b_{+1} + a_{+2} b_{+2}) \cos(\Delta_F + \Delta_R + \omega_m t))
 \end{aligned} \tag{3.22}$$

This expression represents the sinusoidal component of the photocurrent at the frequency ω_m . The phasemeter measures its phase by a DFT operation. Analytically this phase measurement can be realized as follows: First, the amplitudes of the $\sin(\omega_m t)$ and $\cos(\omega_m t)$ components are extracted:

$$\begin{aligned}
 x &= \frac{1}{T} \int_0^T I(t) \cos(\omega_m t) dt, \\
 y &= \frac{1}{T} \int_0^T I(t) \sin(\omega_m t) dt,
 \end{aligned} \tag{3.23}$$

with $T = 2\pi/\omega_m$ being the period of the heterodyne frequency¹. The $\omega_m t$ component of the photocurrent is represented as a complex amplitude

$$z = x + i y. \tag{3.24}$$

The phase ('argument') of this complex number represents the phase that would be measured by an ideal phasemeter.

The main measurement is the phase difference φ between PDM and PDR, which mathematically can conveniently² be represented by the phase of the complex quotient

$$z_M/z_R. \tag{3.25}$$

This expression in the general case (all sidebands present) is far too complex to be useful. Hence the relevant special cases are examined separately.

First-order sidebands

To study the effect of a first order sideband, e.g. a_{-1} , we set

$$a_{-1} = \varepsilon \exp(-i\gamma) \tag{3.26}$$

- ¹ The normalization ($1/T$ or factors of $\sqrt{2}$ etc.) of x and y are irrelevant as long as they are the same for both of them since they will cancel in the next step.
- ² Taking the difference of two arctan functions is analytically more complex and practically susceptible to phase jumps of $\pm 2\pi$ radians.

where ε is the amplitude of the sideband (which will later be assumed to be small such that the results can be linearized in ε) and γ is an arbitrary phase of that sideband with respect to the carrier. All other sideband amplitudes $a_{-2}, a_{+1}, a_{+2}, b_{-2}, \dots$ are set to zero.

Please note that ε represents the amplitude of the optical sideband on the light with respect to the optical carrier amplitude. See Section 3.3.2 on how electrical sidebands are converted into optical sidebands in an AOM.

The calculation then proceeds as described above. For this example, we find

$$z_M/z_R = \frac{\cos(\Delta_F + \Delta_M) + \varepsilon \cos \gamma - i(\sin(\Delta_F + \Delta_M) + \varepsilon \sin \gamma)}{\cos(\Delta_F + \Delta_R) + \varepsilon \cos \gamma - i(\sin(\Delta_F + \Delta_R) + \varepsilon \sin \gamma)} \quad (3.27)$$

The phase error due to the sideband is the phase difference between z_M/z_R and that same quantity for the case that all sidebands are zero. It is represented as a near-unity vector

$$\frac{z_M/z_R}{z_M/z_R|_{\text{sidebands}=0}}. \quad (3.28)$$

Finally, the phase error is the angle of this vector. At this point we make use of the assumption $\varepsilon \ll 1$ and are hence allowed to approximate the angle of this near-unity vector by its imaginary part¹. For this example (single a_{-1} sideband), the result is

$$\begin{aligned} \frac{\delta\varphi}{\varepsilon} &= \sin(\Delta_F + \Delta_M - \gamma) - \sin(\Delta_F + \Delta_R - \gamma) \\ &= \sin(\varphi_M - \gamma) - \sin(\varphi_R - \gamma) \\ &= 2 \cos\left(\Delta_F + \frac{\Delta_M + \Delta_R}{2} - \gamma\right) \cdot \sin\left(\frac{\Delta_M - \Delta_R}{2}\right) \\ &= 2 \cos\left(\frac{\varphi_M + \varphi_R}{2} - \gamma\right) \cdot \sin\left(\frac{\varphi_M - \varphi_R}{2}\right). \end{aligned} \quad (3.29)$$

The corresponding result for the a_{+1} sideband is:

$$\begin{aligned} \frac{\delta\varphi}{\varepsilon} &= \sin(\varphi_M + \gamma) - \sin(\varphi_R + \gamma) \\ &= 2 \cos\left(\Delta_F + \frac{\Delta_M + \Delta_R}{2} + \gamma\right) \cdot \sin\left(\frac{\Delta_M - \Delta_R}{2}\right) \\ &= 2 \cos\left(\frac{\varphi_M + \varphi_R}{2} + \gamma\right) \cdot \sin\left(\frac{\varphi_M - \varphi_R}{2}\right). \end{aligned} \quad (3.30)$$

¹ A unity vector with a small perturbation $1 + \delta \exp(i\alpha)$ has the angle $\arctan(\delta \sin \alpha / (1 + \delta \cos \alpha))$, and the first term in the Taylor expansion around $\delta = 0$ is $\delta \sin \alpha$, i.e. the imaginary part of the perturbation.

The results for the b_{-1} and b_{+1} sidebands are identical to those for the a_{-1} and a_{+1} sidebands, respectively.

Written in the form of Equation (3.30), the error term consists of two factors: The first one varies rapidly as $\cos(\Delta_F)$. It is multiplied by a slowly varying factor that depends on the current operating point of the interferometer. This is in accordance with the observations as shown e.g. in Figure 65.

These error terms correspond to the beatnotes labelled 'B' in Figure 58. The phase error due to **all first-order sidebands** can be written in general form as

$$\delta\varphi = \left\{ \alpha_1 \sin\left(\frac{\varphi_M + \varphi_R}{2}\right) + \alpha_2 \cos\left(\frac{\varphi_M + \varphi_R}{2}\right) \right\} \cdot \sin\left(\frac{\varphi_M - \varphi_R}{2}\right) \quad (3.31)$$

where the constants α_1 and α_2 are combinations of the amplitudes ε and phases γ of the individual first-order sidebands.

Amplitude- and phase-modulation

Particular combinations of first-order sidebands appear when a beam carries *amplitude modulation* or *phase/frequency-modulation*. These will now be considered.

Amplitude modulation (AM) at the heterodyne frequency f_{het} on one beam can be described as a set of sidebands around the carrier with

$$\begin{aligned} a_{-1} &= m/2, \\ a_{+1} &= m/2, \end{aligned} \quad (3.32)$$

where m is the modulation index (HEINZEL, 1999). Alternatively, the other quadrature of the modulation can be described by

$$\begin{aligned} a_{-1} &= i m/2, \\ a_{+1} &= -i m/2, \end{aligned} \quad (3.33)$$

(HEINZEL, 1999). The resulting total phase error for these two cases is

$$\begin{aligned} \delta\varphi &= m (\sin(\varphi_M) - \sin(\varphi_R)), \\ \delta\varphi &= m (\cos(\varphi_M) - \cos(\varphi_R)). \end{aligned} \quad (3.34)$$

The general case is given by (HEINZEL, 1999):

$$\begin{aligned} a_{-1} &= \frac{m}{2} \exp(-i\gamma), \\ a_{+1} &= \frac{m}{2} \exp(i\gamma), \end{aligned} \quad (3.35)$$

and yields an error term of the form

$$\begin{aligned}\delta\varphi &= m (\sin(\varphi_M - \gamma) - \sin(\varphi_R - \gamma)) \\ &= 2m \cos\left(\frac{\varphi_M + \varphi_R}{2} - \gamma\right) \cdot \sin\left(\frac{\varphi_M - \varphi_R}{2}\right).\end{aligned}\quad (3.36)$$

Exactly the same results are obtained when the AM is applied to the second beam instead of the first beam; and consequently the result is double when the same AM is synchronously applied to both beams.

Phase modulation (PM) with a small modulation index on one beam at the heterodyne frequency f_{het} , on the other hand, can be described as a set of sidebands around the carrier with

$$\begin{aligned}a_{-1} &= -m/2, \\ a_{+1} &= m/2,\end{aligned}\quad (3.37)$$

where m is the modulation index (HEINZEL, 1999). The other quadrature of the modulation can be described by

$$\begin{aligned}a_{-1} &= i m/2, \\ a_{+1} &= i m/2,\end{aligned}\quad (3.38)$$

(HEINZEL, 1999). The resulting total phase error for these two cases (and consequently also for a linear combination describing weak PM with arbitrary phase) is

$$\delta\varphi = 0. \quad (3.39)$$

Note that phase modulation also produces higher order sidebands in addition to the first-order sidebands. The effect of the second-order sidebands will be examined in the next section, while sidebands of order three and above cause no phase error.

Second-order sidebands

For the second-order sidebands, we proceed in a similar fashion, e.g. by setting

$$a_{-2} = \varepsilon \exp(-i\gamma) \quad (3.40)$$

and all other sidebands to zero. The resulting phase error for each of the second-order sidebands is:

$$\begin{aligned} a_{-2} : \quad \frac{\delta\varphi}{\varepsilon} &= 0, \\ a_{+2} : \quad \frac{\delta\varphi}{\varepsilon} &= 2 \cos(2\Delta_F + \Delta_R + \Delta_M + \gamma) \sin(\Delta_M - \Delta_R) \\ &= 2 \cos(\varphi_M + \varphi_R + \gamma) \sin(\varphi_M - \varphi_R), \end{aligned} \quad (3.41)$$

$$\begin{aligned} b_{-2} : \quad \frac{\delta\varphi}{\varepsilon} &= 2 \cos(2\Delta_F + \Delta_R + \Delta_M - \gamma) \sin(\Delta_M - \Delta_R) \\ &= 2 \cos(\varphi_M + \varphi_R - \gamma) \sin(\varphi_M - \varphi_R), \end{aligned} \quad (3.42)$$

$$b_{+2} : \quad \frac{\delta\varphi}{\varepsilon} = 0. \quad (3.43)$$

This result has a number of interesting features. These error terms correspond to the beatnotes labelled ‘C’ in Figure 58, and it is hence immediately clear why a_{-2} and b_{+2} have no effect. Correspondingly, AM or PM/FM at $2\omega_{\text{het}}$ has no special features as opposed to the ω_{het} case above, since only one single sideband on each beam is effective.

The dependence on Δ_F of these error terms is given by $\cos(2\Delta_F + \Delta_R + \Delta_M \pm \gamma)$, which shows that they finally can explain the $\cos(2\Delta_F)$ type sidebands (Figure 52).

A less precise but more intuitive explanation is: When Δ_F changes by a certain amount, this corresponds to a shift of all frequencies in one laser beam by that amount. In Figure 58, this would mean e.g. a right-shift of the upper comb of frequencies. The effect on the beatnotes is as follows: The main signal ‘A’ gets ‘longer’ by Δ_F . i.e. its phase changes by $+\Delta_F$. The beatnotes caused by first-order sidebands (‘B’) remain unchanged, and those caused by the second-order sidebands (‘C’) get ‘shorter’, i.e. their phase changes by $-\Delta_F$. The important observation now is that by using the reference interferometer, which undergoes the same changes due to Δ_F , effectively all phases are referred to the main signal ‘A’. With respect to that signal, the sideband beatnotes ‘B’ change by $-\Delta_F$, whereas those caused by the second-order sidebands (‘C’) change by $-2\Delta_F$.

Finally, the error term is proportional to $\sin(\varphi_M - \varphi_R)$ which means that it should vanish when $\varphi_M - \varphi_R = \pm k\pi$, i.e. when the phasors of φ_M and φ_R are parallel or antiparallel, a feature that had been experimentally observed before this theoretical explanation was found (see also Figure 66 for an experimental demonstration).

The phase error due to the **second-order sidebands** can be written in gen-

eral form as

$$\alpha_3 \sin(\underbrace{\varphi_M + \varphi_R}_{=2\Delta_F + \Delta_R + \Delta_M}) \sin(\varphi_M - \varphi_R) + \alpha_4 \cos(\varphi_M + \varphi_R) \sin(\varphi_M - \varphi_R). \quad (3.44)$$

Magnitude and scaling of error terms

All non-zero results in the previous for the first- and second-order error have approximately the same order of magnitude and the same scaling behaviour. As an example, the first-order sideband α_{-1} is discussed here, for which was found

$$\frac{\delta\varphi}{\varepsilon} = 2 \cos\left(\Delta_F + \frac{\Delta_M + \Delta_R}{2} - \gamma\right) \cdot \sin\left(\frac{\Delta_M - \Delta_R}{2}\right). \quad (3.45)$$

In the worst case, $\Delta_R = \Delta_M + \pi$ and hence

$$\delta\varphi = 2\varepsilon \sin(\Delta_F + \Delta_M - \gamma). \quad (3.46)$$

This represents an error which is periodic with Δ_F and which has a peak-peak amplitude of 4ε . Having set the carrier amplitude to unity, ε represents the sideband amplitude with respect to the carrier, which is often expressed in dBc. For example, -60 dBc is equivalent to $\varepsilon = 10^{-3}$ and a peak-peak phase error of $4 \cdot 10^{-3}$ rad.

Please note that ε represents the amplitude of the optical sideband on the light with respect to the optical carrier frequency. See Section 3.3.2 on how electrical sidebands are converted into optical sidebands in an AOM.

Maybe the most important consequence of these results is that the error term scales with the *amplitude* of the offending sideband, not with its power. This means that a reduction of the error (expressed in radian) by a factor of 10 requires a reduction of the sideband by a factor of 10 in amplitude, i.e. by 20 dB, *not* 10 dB. This is true for all sideband-induced errors. Fundamentally it is caused by the fact that the error results as interference product between the small offending sideband and a large carrier, and is as such proportional to the product of the two amplitudes, one of which (the carrier) is large and constant.

Because of the important consequences of this scaling behaviour, we have conducted a series of measurements to verify it (see Section 3.3.4 and Figure 67).

3.3 EXPERIMENTAL INVESTIGATION OF SIDEBAND-INDUCED ERRORS

In order to verify the Formulae (3.13) and (3.16) which describe the periodicity and the amplitude of the sideband induced phase errors, a series of experi-

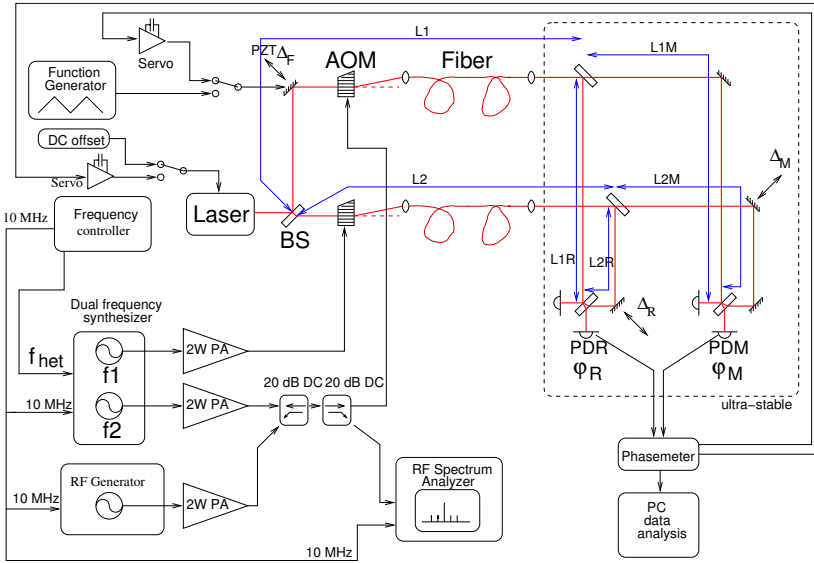


Figure 59. Overview of the test setup for the sideband measurements.

ments were conducted. Additionally the scaling behaviour of the amplitude of the periodic phase error was to be investigated. The two possibilities are:

1. The amplitude of the error scales with the **RF** power of the sidebands.
2. The amplitude of the error scales with the power of the sidebands in the optical spectrum.

3.3.1 Setup

Figure 59 shows the setup for these experiments. Beside the engineering model (EM) of the Lisa Pathfinder Optical Bench (OB) the **FPGA** based phasemeter **PM₃** was used. The setup was supplemented by the generic AOM driving electronics. The basic idea of these experiment was to induce additional sidebands of well defined amplitude and frequencies into the **RF** spectrum of one **AOM** in order to measure the occurring phase error.

Therefore, in these experiments, a synchronized **RF** generator (Figure 59) with dedicated power amplifier was used. This equipment was used to generate a sideband with a defined frequency. In order to combine this additional sideband with the driving signal of one **AOM**, a 20 dB directional coupler in reverse mode was used. A second 20 dB directional coupler in normal direction

was used as sampling device for the combined spectrum. Therefore the -20 dB port was connected to a RF spectrum analyzer (also synchronized). The main output of the second directional coupler was connected to the AOM.

The setup provides two control loops with dedicated actuators:

1. Laser frequency control loop that keeps the laser frequency constant by measuring $\varphi_F - \varphi_R$ and feeding back to the laser PZT and crystal temperature actuator. The error signal of that servo loop can be changed by an analog phase shifter such that the operating point $\varphi_F - \varphi_R$ can be changed. For short term measurements a switch provides the possibility to set the operating point $\varphi_F - \varphi_R$ via a DC voltage that can be applied to the laser PZT.
2. The optical pathlength difference (OPD) stabilization loop keeps the differential fiber phase Δ_F constant. Therefore the optical reference phase is compared with the electrical heterodyne frequency derived from a 10 MHz master clock which is also used as sampling clock for the phasemeter. A second switch allows to apply a scanning signal (triangular, for example) to the OPD.

3.3.2 Conversion of electrical sidebands into optical sidebands in the AOM

For the theoretical analysis presented in Section 3.2 the *optical* carrier-sideband ratio is expressed as ε . Since the experimental investigations are based on inducing electrical sidebands to the RF spectrum the conversion of electrical power into optical power is a relationship to be taken into account. For this reason this Section investigates the conversion of the *electrical* carrier-sideband ratio ε_{el} to ε_{opt} which means here the *optical* carrier-sideband ratio and its dependency on the AOM driving power levels.

The electrical carrier-sideband ratio ε_{el} can be directly measured with the RF spectrum analyzer which is connected to the *sampling* port of the second directional coupler (see Figure 59). From this carrier-sideband ratio measured in dBc, ε_{el} can be found as $\varepsilon_{el} = 10^{\frac{\text{dBc}}{20}}$. In contrast to that, ε_{opt} can not be measured directly but the beat note between a single sideband and the carrier can be detected. The optical signal in the presence of a sideband can be written as:

$$a = \exp(i\omega_0 t) + \varepsilon_{opt} \exp(i(\omega_0 + \Delta\omega)t), \quad (3.47)$$

where the amplitude of the carrier is normalized. This can be measured with a photodiode that detects the beam intensity which is proportional to the square of the amplitude and represents the carrier-sideband beat note:

$$|a|^2 = 1 + 2\varepsilon_{opt} \cos(\Delta\omega t) + \varepsilon_{opt}^2 \approx 1 + 2\varepsilon_{opt} \cos(\Delta\omega t). \quad (3.48)$$

The leading 1 is the normalized DC component of the signal. The amplitude (AC component) of the beat note is $2\varepsilon_{\text{opt}}$. The unknown ε_{opt} can now be obtained as the ratio between the AC and the DC component of the beat note:

$$\varepsilon_{\text{opt}} = \frac{\text{AC}}{2 \text{DC}} = \frac{I_{\text{pk}}(\Delta\omega)}{2 I_{\text{DC}}} = \frac{I_{\text{pk-pk}}(\Delta\omega)}{4 I_{\text{DC}}} = \frac{I_{\text{rms}}(\Delta\omega)}{\sqrt{2} I_{\text{DC}}}. \quad (3.49)$$

3.3.3 Dependence on carrier level

In order to investigate both the conversion of electrical into optical carrier-sideband ratio and the dependency of this conversion on the carrier level a series of measurements were performed. For several carrier levels the optical and electrical carrier-sideband ratio were estimated as described above. The measurements were done for a first order sideband (f_{het} separated from the carrier) and a second order sideband ($2f_{\text{het}}$ separated from the carrier). Table 4 summarizes the results for $\varepsilon_{\text{opt}}/\varepsilon_{\text{el}}$. The conversion ratio $\varepsilon_{\text{opt}}/\varepsilon_{\text{el}}$ is plotted for first and second order sidebands in Figure 60 as function of the carrier power. These results show that the conversion ratio $\varepsilon_{\text{opt}}/\varepsilon_{\text{el}}$ is of the order of 0.8...0.9 for small carrier power levels and decreases for higher power levels near the saturation of the power amplifier to approximately 0.5. The typical operation point of the AOM driver is in this saturation regime near 30 dBm. The results of the columns *interferometer* in Table 4 are discussed in Section 3.3.4. From similar measurements (see Section 3.3.4) where instead of a single sideband, symmetric sidebands were induced by an amplitude modulation of the carrier, the conversion ratio was also estimated. It was estimated from the ratio of the optical and electrical modulation index $m_{\text{opt}}/m_{\text{el}}$ of the AM. The numerical value was estimated as ≈ 0.44 for a carrier power level of +32.8 dBm.

The main results of these measurements can be summarized as follows:

- For sidebands that are considerably smaller than the carrier, an AOM linearly converts electrical sidebands into optical sidebands, i.e. reducing the electrical sideband by a factor of 10 in amplitude results in an optical sideband that is also a factor of 10 smaller in amplitude.
- The ratio of sideband amplitude to carrier amplitude (called ε) is *not exactly* equal in the electrical signals and the optical signals. For all our measurements, we found $\varepsilon_{\text{opt}}/\varepsilon_{\text{el}} \lesssim 1$, with the ratio approaching 1.0 for small carrier powers and getting smaller for those higher carrier powers that approach saturation of the AOM efficiency. Since typically the AOM will be operated in the latter regime, the ratio $\varepsilon_{\text{opt}}/\varepsilon_{\text{el}}$ in practice is expected to be somewhere between 0.4 and 0.8.

offset	electrical				optical			interferometer		
	P_c [dBm]	P_{sb} [dBm]	P_{sb}/P_c [dBc]	ϵ_{el}	U_c [mV _{DC}]	U_{sb} [mV _{pp}]	ϵ_{opt}	$\epsilon_{opt}/\epsilon_{el}$	$\delta\varphi$ [mrad _{pp}]	φ rad
f_{het}	32.3	-8.7	-41.0	0.0089	800	14.2	0.0044	0.494	19.2	0.940 π
f_{het}	31.7	-8.7	-40.4	0.0095	700	14.4	0.0051	0.537	22.3	0.931 π
f_{het}	31.5	-8.7	-40.2	0.0098	600	13.2	0.0055	0.561	22.4	0.928 π
f_{het}	30.7	-8.8	-39.5	0.0106	500	13.0	0.0065	0.613	28.9	0.923 π
f_{het}	29.5	-8.8	-38.3	0.0122	370	12.1	0.0081	0.664	35.8	0.912 π
f_{het}	28.6	-8.8	-37.4	0.0135	280	11.3	0.0101	0.748	43.3	0.911 π
f_{het}	24.4	-8.8	-33.2	0.0219	120	9.1	0.0190	0.867	82.0	0.910 π
$2f_{het}$	32.3	-8.7	-41.0	0.0089	730	13.1	0.0045	0.506	26.5	0.477 π
$2f_{het}$	31.8	-8.7	-40.5	0.0094	640	13.3	0.0052	0.553	28.8	0.475 π
$2f_{het}$	30.8	-8.8	-39.6	0.0105	500	13.1	0.0066	0.628	33.2	0.476 π
$2f_{het}$	30.2	-8.7	-38.9	0.0114	440	13.0	0.0074	0.649	35.4	0.489 π
$2f_{het}$	29.2	-8.8	-38.0	0.0126	360	12.7	0.0088	0.698	42.1	0.492 π
$2f_{het}$	28.2	-8.8	-37.0	0.0141	300	12.7	0.0106	0.752	46.9	0.493 π
$2f_{het}$	26.8	-8.8	-35.6	0.0164	220	11.8	0.0134	0.817	57.6	0.488 π
$2f_{het}$	25.7	-8.8	-34.5	0.0188	190	11.9	0.0157	0.835	62.9	0.486 π
$2f_{het}$	24.9	-8.8	-33.7	0.0207	130	8.9	0.0171	0.826	72.6	0.483 π
$2f_{het}$	23.9	-8.8	-32.7	0.0232	100	8.0	0.0200	0.862	84.3	0.481 π
$2f_{het}$	22.0	-8.8	-30.8	0.0288	80	7.8	0.0244	0.847	106.6	0.481 π
$2f_{het}$	20.7	-8.8	-29.5	0.0335	50	5.5	0.0275	0.821	121.1	0.482 π

Table 4. Results of single sideband injection experiments.

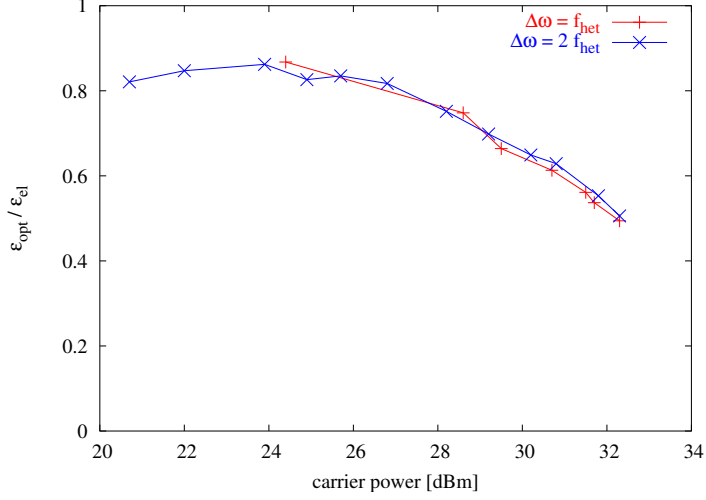


Figure 60. Dependence of the coupling efficiency $\varepsilon/\varepsilon_{\text{el}}$ on the carrier power.

3.3.4 Verification of the theory

The formulae which were found in Section 3.2 in order to describe the occurring error terms caused by first- and second-order sidebands are shown here again:

$$a_{-1} : \frac{\delta\varphi}{\varepsilon} = 2 \cos \left(\Delta_F + \frac{\Delta_M + \Delta_R}{2} - \gamma \right) \cdot \sin \left(\frac{\varphi_M - \varphi_R}{2} \right), \quad (3.50)$$

$$a_{+2} : \frac{\delta\varphi}{\varepsilon} = 2 \cos (2\Delta_F + \Delta_R + \Delta_M + \gamma) \cdot \sin(\varphi_M - \varphi_R), \quad (3.51)$$

where

1. $\delta\varphi$ represents the phase error.
2. ε represents the amplitude of the optical sideband with respect to the optical carrier amplitude.
3. γ is an arbitrary phase of the sideband with respect to the carrier phase.
4. Δ_F is the differential fiber phase.
5. Δ_M and Δ_R represent the optical pathlength differences of the measurement and the reference interferometer on the ultra stable optical bench.

6. φ_M and φ_R represent the optical pathlength differences of the measurement and the reference interferometer within the multi-interferometer setup.

Both Equation (3.50) and (3.51) can be divided into two terms. The first terms

$$2 \cos \left(\Delta_F + \frac{\Delta_M + \Delta_R}{2} - \gamma \right) \quad \text{and} \quad 2 \cos (2\Delta_F + \Delta_R + \Delta_M + \gamma) \quad (3.52)$$

change periodically with the optical pathlength differences Δ_F or $2\Delta_F$ which are, without the OPD stabilization, fluctuating due to environmental noise. These terms explain both periodic nonlinearities shown in Figure 52.

The second terms in Equation (3.50) and (3.51)

$$\sin \left(\frac{\varphi_M - \varphi_R}{2} \right) \quad \text{and} \quad \sin(\varphi_M - \varphi_R) \quad (3.53)$$

depend on $\varphi_M - \varphi_R$ only, which represents pathlength changes on the ultra-stable optical bench (OB) and typically changes much more slowly than the first term.

In order to measure both terms independently the most obvious approach is to keep one of them constant while the other is controlled in a well defined way. Therefore during a first experiment Δ_F was varied linearly over multiples of 2π while the second term ($\varphi_M - \varphi_R$) should be kept constant at several values.

Equation (3.52) shows that instead of Δ_F the arbitrary phase γ can also be changed. This was used in a second experiment where the second term was to be scanned. This requires a change in the phase difference ($\varphi_M - \varphi_R$) on sub-wavelength level which is not possible for the X1 and the X12 interferometer. For this reason, the phase of the frequency interferometer φ_F was used as measurement phase φ_M . Since the frequency interferometer provides an intentional pathlength difference, φ_F can be controlled via the laser frequency whereby ($\varphi_M - \varphi_R$) can be controlled with sufficient precision. Both experiments are explained in more detail in below.

Changing Δ_F : Scanning the OPD piezo

It was found very early during the noise investigation work that the occurring nonlinearities could be mitigated by a stabilization of the optical pathlength difference Δ_F . Therefore a PZT mounted mirror was implemented in the setup. This PZT could be used now in order to scan Δ_F . This is the most

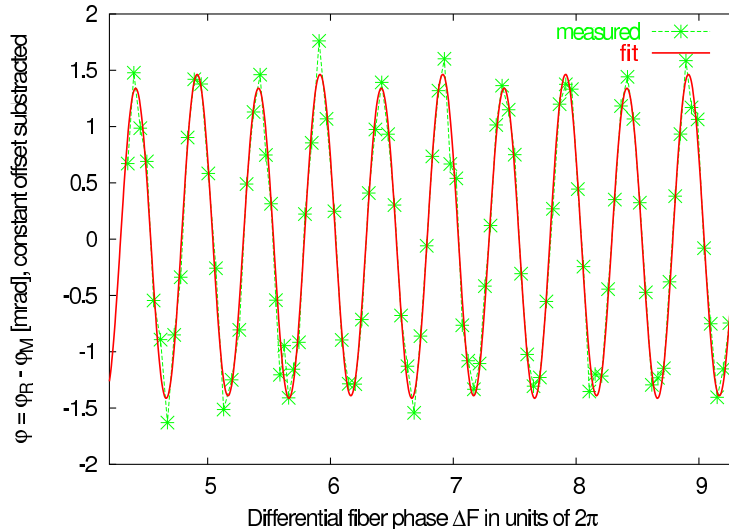


Figure 61. φ as function of Δ_F when the OPD PZT is scanned. In this measurement, the $\sin(2\Delta_F)$ component is dominant. See also Figure 52 for a similar, older, measurement where a significant $\sin(\Delta_F)$ component is also present.

straightforward way to verify Equations (3.50) and (3.51). Therefore a triangular scanning signal was applied to the PZT. The time series of the occurring phase error $\delta\varphi$ in the difference ($\varphi_M - \varphi_R$) is shown in Figure 61. The scan exclusively shows a $\sin(2\Delta_F)$ component. The absence of the $\sin(\Delta_F)$ component leads to the assumption that the first order sidebands are negligible. A similar, older measurement is shown in Figure 52, where a significant $\sin(\Delta_F)$ component is also present.

The main advantage of the Δ_F scan by the PZT ramp is the possibility to directly verify of the formulae found for the nonlinear error and thus easily distinguish between the $\sin(\Delta_F)$ and $\sin(2\Delta_F)$ cases. The disadvantage of this method is the poor SNR that decreases due to the environmental noise that changes the differential fiber phase $\sin(\Delta_F)$ in addition to the PZT scan. Furthermore the amplitude of the applied ramp itself is limited due to the dynamic range of the PZT that allows only a few 10 cycles variation of the OPD Δ_F .

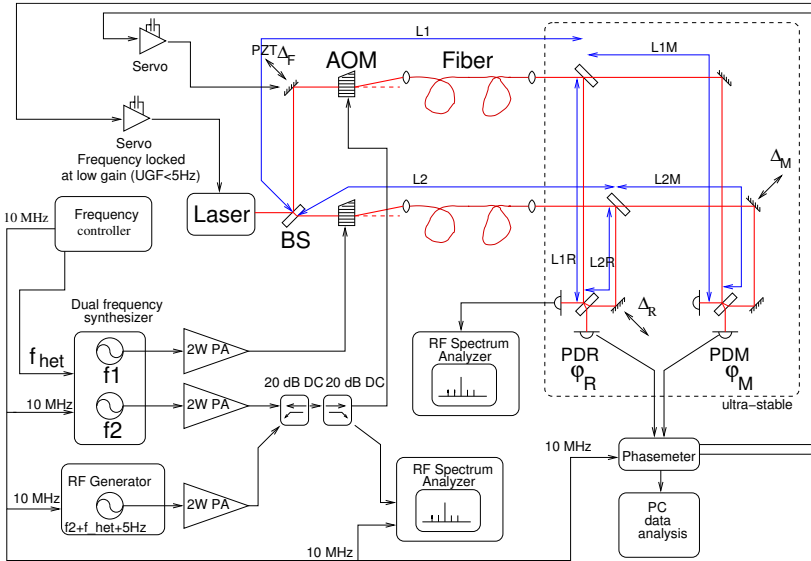


Figure 62. Experimental setup for sideband investigations using sidebands with frequency offset.

Changing γ : sidebands with frequency offset

As shown before, instead of scanning Δ_F also the arbitrary phase offset γ can be changed. γ can be expressed as

$$\gamma = \int \omega_{\text{off}} dt = \omega_{\text{off}} \cdot t + c \quad (3.54)$$

where c is an integration constant. $\omega_{\text{off}} = 2\pi f_{\text{off}}$ can be assumed a frequency offset of the sideband from its nominal frequency. Since Δ_F is not needed to be scanned anymore it can be locked by the dedicated servo whereby a better SNR can be obtained.

For this experiment a single sideband was added to the RF spectrum of one AOM driver. Its frequency was chosen to appear as 1st order sideband and for a second experiment to appear as second-order sideband. For both cases there was an offset f_{off} from the nominal sideband frequency. The frequency offset was chosen as $f_{\text{off}} = 5\text{ Hz}$ such that it was within the bandwidth of the phasemeter but high enough to produce a characteristic output signal well above the noise floor and outside the bandwidth of the laser frequency control loop.

According to Equations (3.50) and (3.51), the phase error will then also be periodic with $f_{\text{off}} = 5$ Hz and can be measured by narrowband spectral analysis¹ (HEINZEL *et al.* (2002a)) of the phase data time series. Long measurement times are possible because the stabilization loops for the laser frequency and, more importantly, the OPD can be used. Figure 62 shows the experimental setup. This setup was used in order to quantitatively verify the theory.

Quantitative verification

In order to verify the Equations (3.50) and (3.51) quantitatively a set of measurements were performed. A single sideband (SSB) with 5 Hz frequency offset was added via the additional power amplifier and the directional coupler in reverse-mode as described in Section 3.3.1. Its amplitude compared to the carrier was

$$\varepsilon_{\text{el}} = -39.6 \text{ dBc} = 0.01047. \quad (3.55)$$

As known from Section 3.3.2, ε_{el} converts via a factor (that depends on the carrier power) into an optical-sideband-carrier-ratio ε_{opt} . The typical operating point for the AOM was 32 dBm. From Table 4 and Figure 60 a conversion factor of $\varepsilon_{\text{opt}}/\varepsilon_{\text{el}}=0.5$ can be estimated². This leads to

$$\varepsilon_{\text{opt}} = 0.0052. \quad (3.56)$$

From Equation (3.50) it follows that the amplitude of the error term $\delta\varphi$ should be

$$\delta\varphi_{0 \rightarrow \text{pk}} = 2 \varepsilon_{\text{opt}} \sin\left(\frac{\varphi_{\text{M}} - \varphi_{\text{R}}}{2}\right), \quad (3.57)$$

and the RMS amplitude

$$\delta\varphi_{\text{rms}} = \sqrt{2} \varepsilon_{\text{opt}} \sin\left(\frac{\varphi_{\text{M}} - \varphi_{\text{R}}}{2}\right). \quad (3.58)$$

Table 5 shows the theoretical and measured RMS values for the phase error $\delta\varphi$ depending from the phase difference $\varphi = \varphi_{\text{M}} - \varphi_{\text{R}}$ for different sideband orders ($\alpha_{-1}, \alpha_{+1}, \alpha_{+2}$). The results from Table 5 are plotted for the first and second order sidebands in Figure 63.

- ¹ We computed a linear spectrum of the fluctuations using improved FFT methods and using a 'flat-top' time-domain window that yields the correct peak amplitude independent of the location of the peak frequency within one frequency bin.
- ² These measurements were done before the discrepancy between ε_{el} and ε_{opt} was discovered, and hence ε_{opt} was not directly measured.

sideband	φ [rad]	$\delta\varphi_{\text{rms}}$ [mrad]	$\delta\varphi_{\text{rms}}(\text{theor.})$ [mrad]	ratio $\delta\varphi_{\text{rms}}(\text{theor.})/\delta\varphi_{\text{rms}}$
α_{-1}	0.0155	0.1	0.057	0.58
α_{-1}	0.7858	3.0	2.8	0.94
α_{-1}	1.5676	5.5	5.2	0.95
α_{-1}	3.1354	7.7	7.4	0.96
α_{+1}	0.0017	0.082	0.0062	0.08
α_{+1}	0.7906	2.9	2.8	0.97
α_{+1}	1.5941	5.1	5.2	1.03
α_{+1}	3.1417	7.6	7.3	0.96
α_{+2}	0.0159	0.2	0.1	0.5
α_{+2}	0.7990	7.5	5.2	0.70
α_{+2}	1.5602	11.0	7.3	0.67
α_{+2}	3.1400	0.087	0.012	0.13

Table 5. Phase error $\delta\varphi$ rms-amplitude for different sideband orders (measured and from theory). The error was measured for several values $\varphi = \varphi_M - \varphi_R$ from 0 to π rad.

The data shown in Table 5 and Figure 63 (a) demonstrate a good agreement with the theory for the results for the first order sidebands. For the second-order sidebands Figure 63 (b) shows a discrepancy of about 30% between the predicted and measured phase errors, for which no final explanation was found, although qualitative experience suggests that the strong second-order sidebands produce further sidebands due to nonlinear intermodulation processes in the power amp (see Section 3.3.5), which contributed to the measured phase error. For a further quantitative verification of the theoretical predictions of the phase error the interferometrically measured phase errors from the *interferometer* data from Table 4 were also analyzed. Figure 64 shows the results, which are in reasonable agreement with the theory. The fact that the measured phase error is a little higher than the predicted one, is possibly caused by an underestimation of ε_{opt} due to a suboptimal setting of the FFT analyzer.

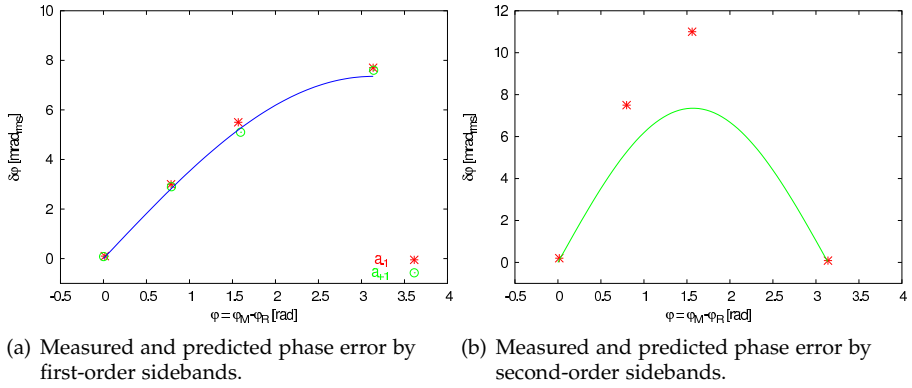


Figure 63. Phase error induced by first- and second-order sidebands.

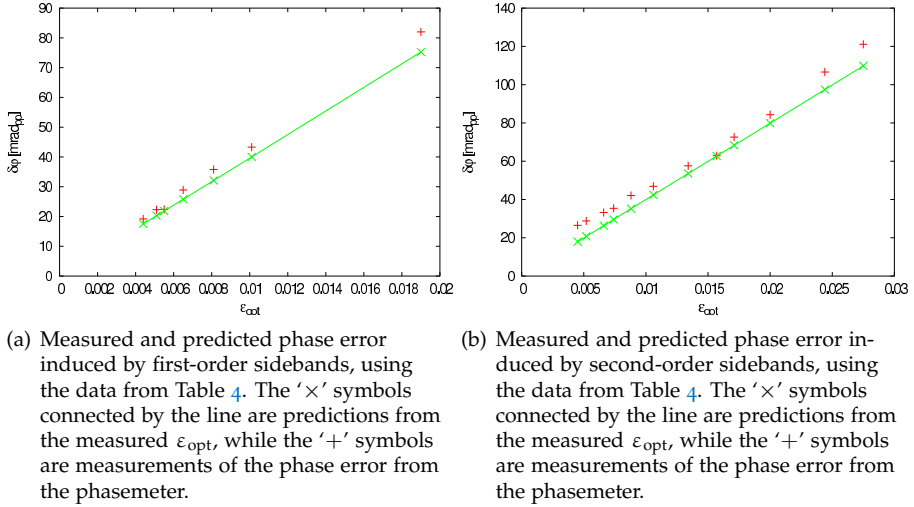


Figure 64. Measured and predicted phase error by first- and second-order sidebands using the data from Table 4.

Changing both terms simultaneously

A slightly different setup was used to verify the full expressions from Equations (3.50) and (3.51). For this purpose both terms were varied simultaneously. As described above, the first term was scanned by inducing sidebands with a 5 Hz offset. For practical reasons the sidebands here were induced as pairs from an AM. In contrast to the setup before, here the laser frequency stabilization loop was turned off and the phase difference ($\varphi_M - \varphi_R$) was scanned by applying a ramp to the laser frequency. This varied the second terms in Equation (3.50) and (3.51).

Figure 65 and Figure 66 show segments from typical time series.

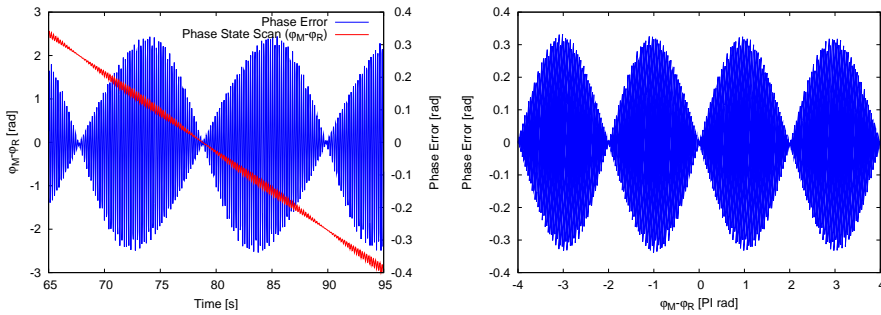


Figure 65. Phase $\varphi = \varphi_M - \varphi_R$ and its error (linear drift subtracted) when strong sidebands at an offset of f_{het} are added to the RF signal. This illustrates and confirms the $\sin([\varphi_M - \varphi_R]/2)$ term in Equation (3.50).

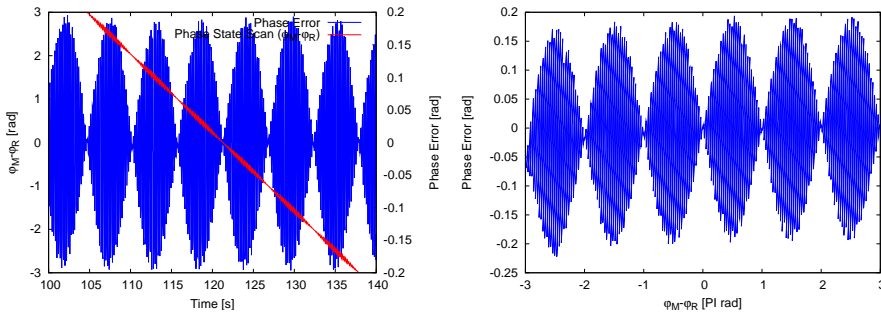


Figure 66. Phase $\varphi = \varphi_M - \varphi_R$ and its error (linear drift subtracted) when strong sidebands at an offset of $2 \times f_{\text{het}}$ are added to the RF signal. This illustrates and confirms the $\sin(\varphi_M - \varphi_R)$ term in Equation (3.51).

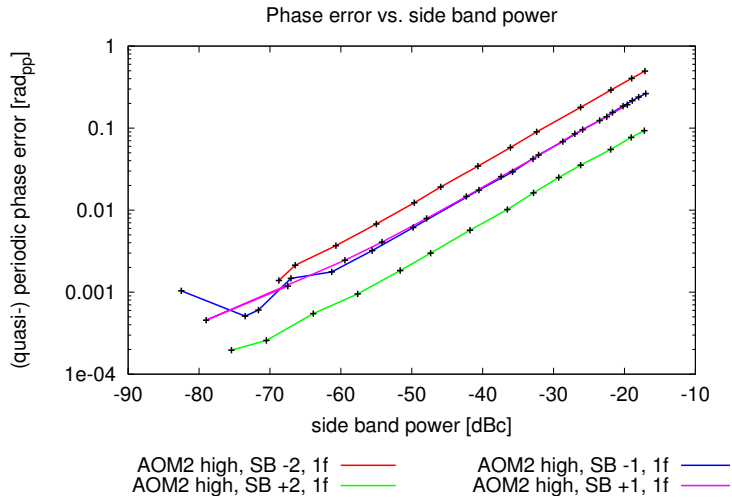


Figure 67. Measured scaling behaviour of single sideband induced phase errors.

The slow oscillation (envelope) corresponds to the $\sin\left(\frac{\varphi_M - \varphi_R}{2}\right)$ and $\sin(\varphi_M - \varphi_R)$ factors in Equations (3.50) and (3.51). The fast oscillation is at a frequency of 5 Hz corresponding to the first term with $\cos(\gamma)$.

Error scaling behaviour

In order to verify the scaling behaviour of the error discussed in Section 3.2.2, the occurring amplitude of the phase error was measured for different carrier-sideband-ratio (ε_{el}). Therefore the same method as described above was used (changing γ via a frequency offset).

Figure 67 shows the results for some first- and second-order sidebands. The absolute level of the curves is not well defined, because $(\varphi_M - \varphi_R)$ was not controlled or recorded during these measurements (they were made at the start of the investigations, when the theoretical analysis was not completed). However, during each measurement, $(\varphi_M - \varphi_R)$ was nearly constant. The main result is a verification of the unfavourable scaling behaviour: A reduction of the sideband amplitude by 20 dB causes a reduction of the phase error by a factor of 10.

Amplitude modulation

In order to verify the results of Section 3.2.2 which describe the occurring phase error for the case of an amplitude modulation on the light beam at the heterodyne frequencies, a set of quantitative measurements was performed by adding intentional amplitude modulation (AM) on one light beam.

The light amplitude was modulated at $f_{\text{het}} + 5\text{ Hz}$ by applying a suitable sinusoidal signal to the amplitude control input of one AOM driver.

The resulting modulation index can be measured from the RF spectrum and depends on the carrier-sideband-ratio (ε_{el})

$$m_{\text{el}} = 2 \cdot 10^{\frac{\varepsilon_{\text{el}}}{20}}. \quad (3.59)$$

Optically the modulation index can be found as

$$m_{\text{opt}} = \frac{U_{\text{pp}}}{4 U_{\text{DC}}} \quad (3.60)$$

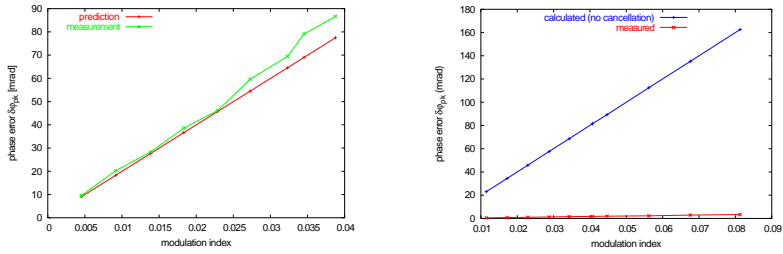
where U_{pp} is the peak-peak amplitude of the resulting sb-carrier beat of the amplitude modulated beam and U_{DC} its DC level. The modulation index was varied over ≈ 1 decade and monitored both by measuring the sideband spectrum in the RF driving signal ('electrical') and by measuring the effective modulation on the light ('optical'). These two modulation indices differ by about a factor of 2, in accordance with the results of Section 3.3.2. For each measurement a time series of $\varphi_{\text{M}} - \varphi_{\text{R}}$ was taken using the phasemeter and a spectrum estimated afterwards. Since the phase error $\delta\varphi$ depends on

$$\delta\varphi \propto \sin\left(\frac{\varphi_{\text{M}} - \varphi_{\text{R}}}{2}\right), \quad (3.61)$$

for the first-order sideband this phase difference was set to π in order to maximize the SNR. Table 6 lists the results, and Figure 68 (a) shows a comparison between predicted and measured phase error, which are in reasonable agreement.

electrical			optical				phasemeter			
carrier [dBm]	SB [dBm]	m_{el}	U_{DC} [mV]	U_{AC} [mV _{pp}]	m_{opt}	m_{opt}/m_{el}	$\varphi_M - \varphi_R$ [rad]	$\delta\varphi_{meas}$ [rad _{pk}]	$\delta\varphi_{calc}$ [rad _{pk}]	ratio
32.8	5.6	0.08730	690	107	0.03877	0.44406	-3.21085	0.08665	0.07749	0.89
32.8	4.7	0.07871	695	96	0.03453	0.43873	-3.21275	0.07913	0.06902	0.87
32.8	4.1	0.07346	650	84	0.03231	0.43982	3.06753	0.06949	0.06457	0.93
32.8	2.5	0.06110	660	72	0.02727	0.44637	3.06722	0.05964	0.05451	0.91
32.8	1.1	0.05200	655	60	0.02290	0.44037	-3.21602	0.04620	0.04577	0.99
32.8	-0.8	0.04179	655	48	0.01832	0.43844	-3.21625	0.03858	0.03662	0.95
32.7	-3.2	0.03206	650	36	0.01385	0.43182	3.06728	0.02832	0.02767	0.98
32.7	-6.6	0.02168	655	24	0.00916	0.42255	-3.21646	0.02028	0.01831	0.90
32.7	-12.8	0.01062	665	12	0.00451	0.42488	3.06672	0.00957	0.00902	0.94

Table 6. Results of AM modulation.



(a) Comparison between prediction and measurement for AM sidebands.

(b) Comparison between prediction and measurement for FM sidebands. The prediction is actually zero phase error. For comparison, the upper curve shows the phase error that was calculated under the (wrong) assumption that the two sidebands do not cancel.

Figure 68. Measured and predicted phase error by first-order sidebands for AM and FM.

Frequency modulation

The same procedure as for the AM was applied for the phase/frequency modulation (PM/FM) with following differences:

1. The first-order FM was applied to one of the beams by modulating one AOM frequency at $f_{het} + 5\text{ Hz}$. This was done by applying a suitable sinusoidal signal to the frequency input of the TCVCXO in one AOM driver in addition to the PLL feedback signal. Since the PLL has a bandwidth of only a few Hz, it does not influence this modulation.
2. Due to the nature of the PM/FM the optical modulation index could not be measured.

Section 3.2.2 predicted that no phase error is caused by a pair of first-order sidebands which originate from PM/FM.

Table 7 lists the results (see also Figure 68 (b)), which show that in accordance with the prediction the phase error is much smaller than expected if the effect of the two sidebands would not cancel.

carrier [dBm]	SB [dBm]	m_{el}	$\delta\varphi_{calc}$ [mrad _{pk}]	$\delta\varphi_{meas}$ [mrad _{pk}]	ratio
32.8	-6.0	0.0115	23.0	0.48	0.021
32.8	-2.5	0.0172	34.4	0.75	0.022
32.8	0.0	0.0229	45.8	1.00	0.022
32.8	2.0	0.0288	57.7	1.23	0.021
32.8	3.5	0.0343	68.6	1.53	0.026
32.8	5.0	0.0407	81.5	1.74	0.021
32.8	5.8	0.0447	89.3	1.94	0.022
32.8	7.8	0.0562	112.5	2.25	0.020
32.7	9.3	0.0676	135.2	2.88	0.021
32.7	10.9	0.0813	162.6	3.34	0.021

Table 7. Results of FM modulation. The column $\delta\varphi_{calc}$ shows the results that would be predicted if no cancellation of the sidebands would occur.

3.3.5 Origin of sidebands

It was known for a long time that the optical spectra of the heterodyne signals are disturbed by spurious sidebands at the heterodyne frequency. But with the theory and its verification it was possible to explain the coupling process quantitatively and it was possible to trace their origin back to the RF spectra of the AOM driving signals.

Figure 69 shows spectra measured at the output of the power amplifiers under various conditions.

The arrow at the boxes on the left side in Figure 69 indicate where each measurement was done. VCXOx means the pure oscillator of each AOM driver and PAx its dedicated power amplifier (see Section 2.3.3). The phase-locked loop (PLL) also described in Section 2.3.3 locks both VCXOs to each other with an offset of the heterodyne frequency. The spectrum of the phase noise performance, shown in Figure 18, has typical 100 and 200 Hz lines caused by the 50 Hz power supply which also occur in Figure 69 as sidebands near the 80 MHz carriers. For the first measurement in Figure 69, the PLL was turned off such that the VCXO frequency was not controlled and drifted to its limit.

These measurements show that the sidebands appear when the power amplifiers (PA) are switched on, indicating that they are caused by RF pickup (as opposed to crosscoupling via the PLL).

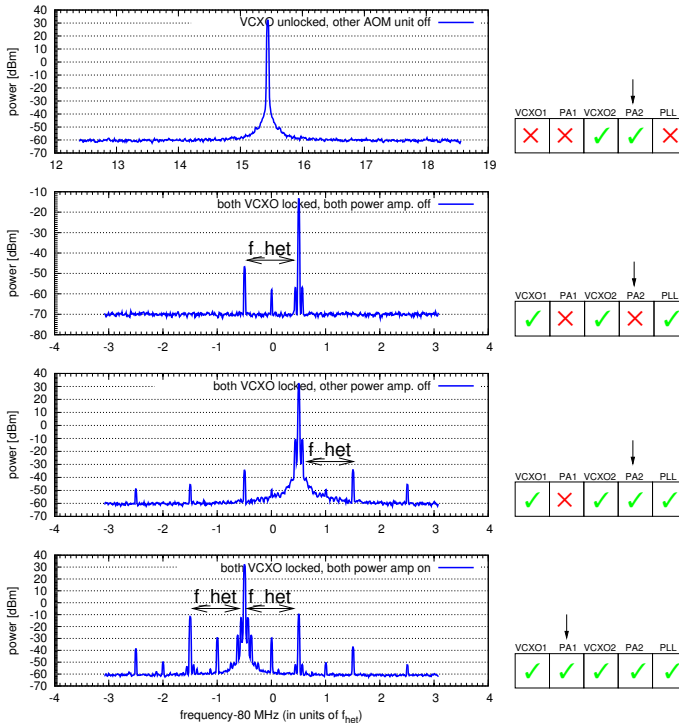


Figure 69. Spectra of AOM RF drive signal under various conditions. The arrow indicates where each measurement was done. Top: One VCXO together with its PA has a clean spectrum without sidebands. Second: Both VCXO's on and locked by the PLL, but both PA's off show some crosstalk of the other frequency, but no symmetrical sideband structure. Third: When the other PA is off, but both VCXOs are running, the symmetrical sideband structure already appears. Bottom: the symmetrical sideband structure gets stronger when the other VCXO is amplified in its PA.

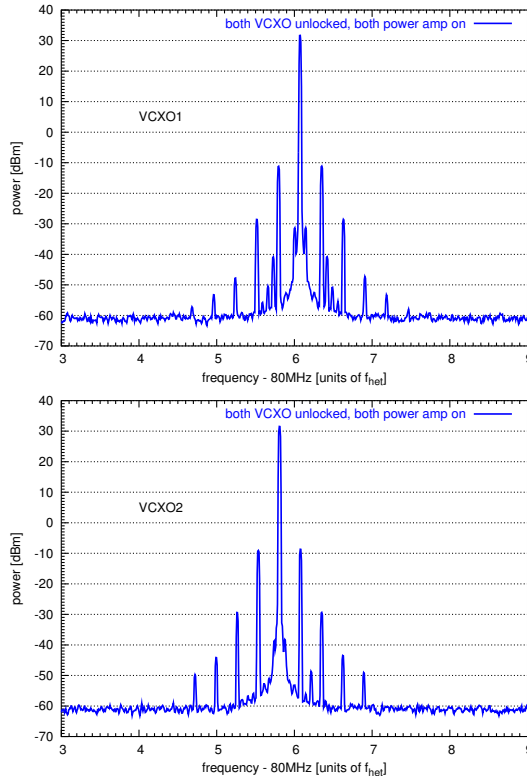


Figure 70. Spectra of AOM RF drive signal with PLL disconnected, showing that the PLL or its connections are not responsible for the sidebands.

This is confirmed by the measurements shown in Figure 70 which were taken with both VCXO's and PA's running, but the PLL disconnected, such that the frequencies drifted to their respective limits. Even with all PLL cables removed, the symmetrical sideband structure appears.

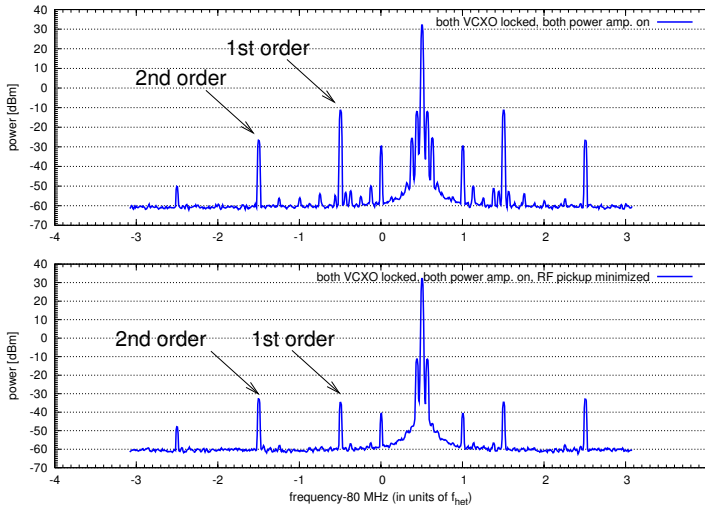


Figure 71. With the full configuration (everything on), the amount of the sidebands could be changed by physically moving the two power amplifiers, but without changing any connections.

Further measurements showed clearly that the sidebands are produced *in the power amplifier*¹. The sidebands also appear, even if the VCXOs and the PLL are completely disconnected and both ‘naked’ power amplifiers are driven from commercial RF generators instead. As soon as both amplifiers are running at frequencies close to each other, they start to interact and produce sidebands. Before that, it was suspected the VCXO’s to be responsible and such that they were shielded with a copper enclosure, without any noticeable effect.

This observation that the sidebands are caused by electro-magnetic pickup between the both amplifiers is confirmed by the measurements shown in Figure 71 which were taken with everything running. The amount of the sidebands could be changed by physically moving the two power amplifiers, but without changing any connections.

¹ The prototype electronics investigated here was built at AEI in 2001 and uses as power amplifier the Mitsubishi Module M67743L intended for up to 7 W RF output in broadcast applications

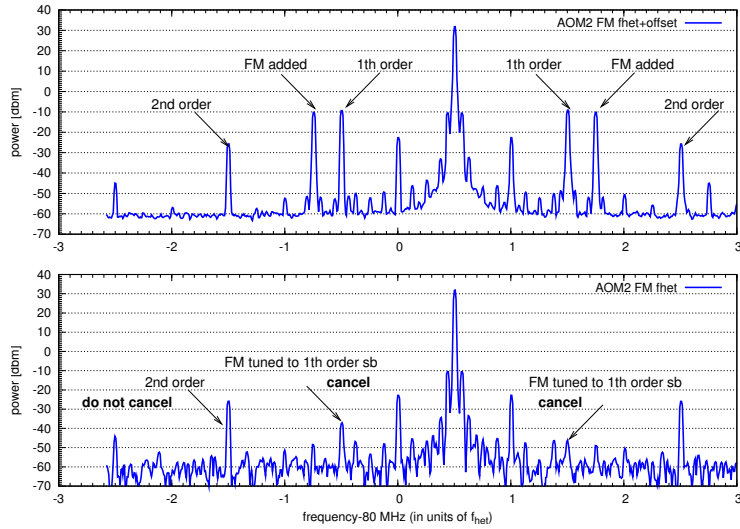


Figure 72. Spectra of AOM RF drive signal for AOM 2 with FM added. Top: the extra sidebands induced by the FM are at a shifted frequency (to adjust their amplitude). Bottom: They are shifted to the correct frequency and cancel the naturally occurring sidebands. Note that the second-order sidebands are unaffected.

Nature of the appearing first-order sidebands

COMPENSATION BY THE MEANS OF FM: The nature of the sidebands was investigated in another series of measurements. In Figure 72, a frequency modulation (FM) at f_{het} was added to VCXO2 while VCXO1 and both power amplifiers were also running. By adjusting the amplitude and phase of the frequency modulation, the first-order sidebands could almost completely be cancelled. This shows that the nature of the first-order sidebands is FM/PM instead of AM. This observation is confirmed by the fact that the effect of the first-order sidebands in the phase readout is much smaller than it should be if the sidebands were AM (see Section 3.2.2). The second-order sidebands are, however, unaffected. This indicates that they are not simply the J_2 sidebands associated with a FM/PM at f_{het} , but have another origin.

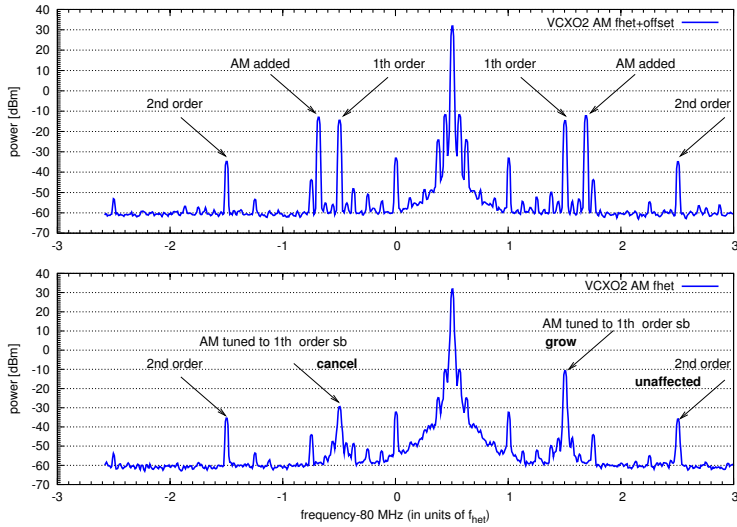


Figure 73. Spectra of AOM RF drive signal for AOM 2 with AM added. Top: the extra sidebands induced by the AM are at a shifted frequency (to adjust their amplitude). Bottom: They are shifted to the correct frequency, but cancel only one of the naturally occurring sidebands, while the other one grows. Note, that the second-order sidebands are unaffected.

COMPENSATION BY THE MEANS OF AM: In Figure 73, an amplitude modulation (AM) at f_{het} was added to VCXO2 while VCXO1 and both power amplifiers were also running. When the amplitude and phase of the amplitude modulation were adjusted such as to minimize the first-order sidebands in the spectrum, only one of the first-order sidebands disappeared, while the other grew. This confirms the PM-character of the first-order sidebands. Again, the second-order sidebands are unaffected.

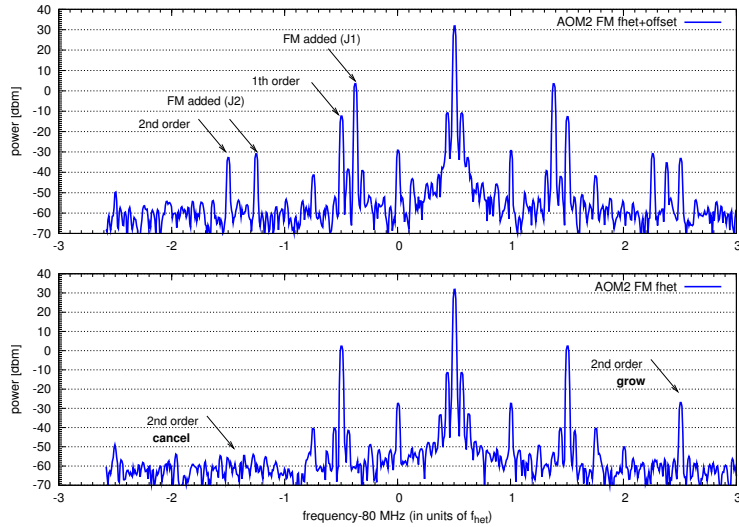


Figure 74. Spectra of AOM RF drive signal with FM with a modulation frequency of f_{het} added. Top: the extra sidebands induced by the FM are at a shifted frequency (to adjust their amplitude in an attempt to cancel the second-order sidebands by the J_2 components of FM at f_{het}). Bottom: They are shifted to the correct frequency, but cancel only one of the second-order sidebands, while the other one grows.

Nature of the appearing second-order sidebands

In Figure 74, a frequency modulation (FM) at f_{het} was added to VCXO2 while VCXO1 and both power amplifiers were also running. In contrast to the previous measurement, here the amplitude and phase of the frequency modulation were adjusted in order to minimize the *second-order* sidebands in the spectrum. This should be possible if the second order sidebands were the J_2 sidebands associated with the FM/PM at f_{het} .

The results show that

- more power than is really present in the first-order sidebands is needed to produce the observed level of second-order sidebands and more power than is really present in the first-order sidebands is needed to produce the observed level of second-order sidebands and
- even when the amplitude and phase of the FM/PM at f_{het} is adjusted such as to maximally suppress the second-order sidebands, the second-

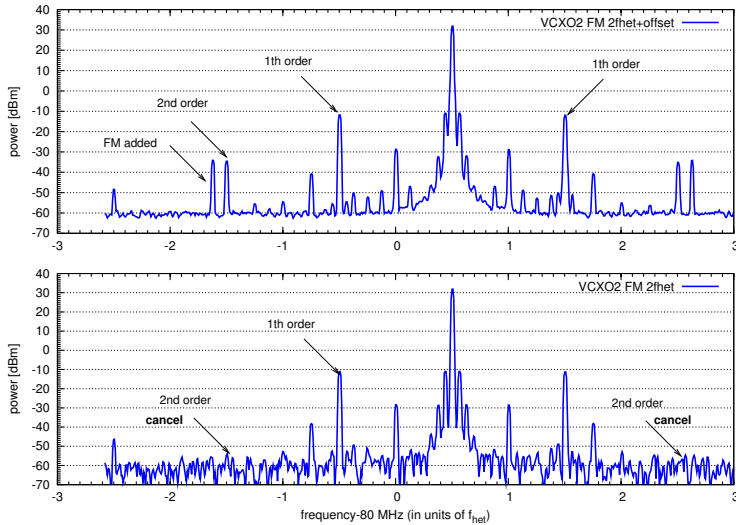


Figure 75. Spectra of AOM RF drive signal with added FM at $2f_{\text{het}}$. Top: the extra sidebands induced by the FM are at a shifted frequency (to adjust their amplitude in an attempt to cancel the second-order sidebands by the FM at $2f_{\text{het}}$). Bottom: They are shifted to the correct frequency. Thus both second-order sidebands can be removed.

order sidebands are affected asymmetrically (one grows while the other disappears).

This confirms the previous observation that they are not simply the J_2 sidebands associated with a FM/PM at f_{het} , but have another origin.

In Figure 75, a frequency modulation (FM) at $2f_{\text{het}}$ was added to VCXO2 while VCXO1 and both power amplifiers were also running. By adjusting amplitude and phase of the modulation, the second-order sidebands can be removed. This indicates that they have PM character with a modulation frequency of $2f_{\text{het}}$, although this PM is unrelated to the first-order sidebands.

Summary

It is interesting to note that in the very different experimental setup in Glasgow (ROBERTSON *et al.* (2005)), sidebands were also observed, including second-order sidebands for which simple cross-coupling of ‘the other’ frequency provides no explanation.

The observations concerning the origin of the RF sidebands can be summa-

rized as follows:

- The sidebands are created in the power amplifiers when these pick up RF at a frequency near (within a few kHz) of their operating frequency.
- Both first-order and second-order sidebands appear in pairs that have PM character (as opposed to AM).
- First- and second-order sidebands are not directly related; i.e. the second-order sidebands are not simply the J_2 terms associated with the first-order PM sidebands. Their amplitude is larger and they cannot be cancelled by either AM- or PM- first-order sidebands.
- Since first-order PM sidebands have no effect on the phase measurement (see Section 3.2.2), the second-order sidebands cause the largest error term.
- The appearance of the sidebands, in particular second-order sidebands, is no artifact of a singularly bad setup in Hannover, since they were also observed in a very different (and better shielded) setup in Glasgow.

3.4 CONCLUSION

Starting from the observation of residual phase noise at mrad respectively nanometer level and its association with optical pathlength difference fluctuations within the common interferometer paths, an OPD stabilization was implemented in order to mitigate this noise source. Since the coupling process turned out to behave nonlinearly, its understanding was nontrivial. However, based on a comprehensive analysis of the system, a theory, could be found and experimentally verified in a team work, which explains the nonlinearities as an effect of spurious sidebands on the AOM RF driving signal. Furthermore the origin of these sidebands was found to be crosstalk between the RF power amplifiers.

The conclusion for LTP are twofold: Stringent requirements on the AOM sideband performance and implementation of the OPD stabilization loop. The combination of these two requirements mitigates the nonlinearities in the phase readout - necessary in order to achieve the sensitivity requirement.

4

PHASE MEASUREMENT SYSTEM FOR LISA

*"Die Neugier steht immer an erster Stelle
eines Problems, das gelöst werden will."*

GALILEO GALILEI

(1564-1642) italienischer Physiker und Astronom

While Chapter 1 outlines the main scientific purpose and the overall concept of the LISA mission, a comprehensive mission design is described in the LISA final technical report and a mission study report (ESA-SCI, 2000) based on an industrial investigation by Astrium/EADS. The baseline concept of the mission described here is continually being reviewed since 2005 in an ongoing formulation phase by Astrium in Immenstaad.

This Chapter focuses on one aspect of the LISA core technologies to be developed – the phase measurement system (PMS) – that is responsible for the interferometric phase readout of a optical beat signal in the MHz range, which is the main science measurement of LISA¹.

Compared to the PMS of its precursor LISA Pathfinder, which was successfully implemented and is described in Section 2.3.6 and 2.3.7, the LISA PMS is more complex due to additional and tighter requirements. The first Section 4.1 of this Chapter provides an introduction to the main requirements of the LISA optical phase readout and compares the PMS of LISA pathfinder and LISA.

In order to fulfill the LISA requirements, a modified PMS design is necessary which is presented in Section 4.1. Worldwide a number of groups of the LISA community are working on the implementation. Implementations according to the baseline concept² are operated at JPL (SHADDOCK *et al.*, 2006) and at the University of Florida (THORPE, 2006).

The approach of a PMS implementation at the AEI in Hannover differs in one aspect from that of the other groups. In contrast to the other groups our design starts from the hardware side of the PMS implementation. Section 4.2

¹ Beside the main scientific readout the LISA PMS also needs to provide extra tasks which are mentioned in Chapter 5.

² proposed by JPL

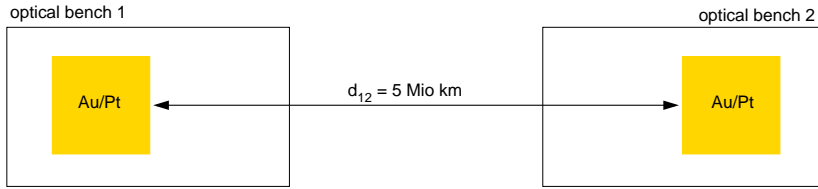


Figure 76. Direct measurement of variations of testmass distance.

focuses on the hardware development based on Field Programmable Gate Arrays (FPGAs) as main technology platform.

For the phasemeter prototype first measurement results are presented in Section 4.3.

The Chapter concludes with an outlook considering the further development steps.

4.1 THE LISA PHASE MEASUREMENT SYSTEM

LISA measures the path length variations between the free floating proof masses onboard the 3 LISA spacecraft by means of heterodyne interferometry¹. The precursor mission LISA Pathfinder is intended to test ultra stable heterodyne interferometry with picometer accuracy in space. The main difference is the interferometer arm length. While LISA measures the pathlength noise between test masses on different spacecraft separated by 5 million kilometers (Figure 76), for LISA Pathfinder the arm length is shrunk to approximately 30 centimeters between two test masses onboard one spacecraft. However, LISA Pathfinder will demonstrate the principle of heterodyne interferometry in space and will test many essential components needed for LISA. The current LISA baseline considers a split interferometric readout. This concept is illustrated in Figure 77. The arm length measurement is twice-shared into a local measurement of the test mass–spacecraft distance (comparable to LISA Pathfinder), and the long distance measurement between the spacecraft. Gravitational waves will change the measured distance between the test masses.

4.1.1 Requirements

The primary quantities to be measured by the LISA interferometers are the phases of the sinusoidal beat notes of the heterodyne interferometers coming from photodetectors located on the optical benches. Pathlength variations of

¹ The concepts of heterodyne interferometry are discussed in Section 2.1 for LISA pathfinder.

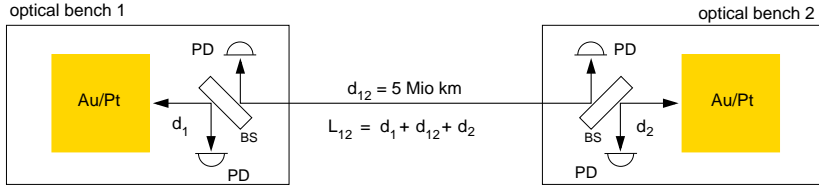


Figure 77. The current interferometry baseline is split into three independent measurements. The positions of the test masses will be measured with respect to the optical benches onboard the spacecraft. This measurement will be demonstrated by LISA Pathfinder. In an additional long distance measurement, fluctuations of the distance between the two optical benches will be measured.

one wavelength¹ ($\approx 1 \mu\text{m}$) translate into a phase variation of the heterodyne signal of one cycle or 2π rad.

LISA aims for a shot noise limited measurement performance within the measurement bandwidth of 0.1 mHz to 0.1 Hz. The shot noise limit for the pathlength measurement is of the order of $40 \text{ pm}/\sqrt{\text{Hz}}$. Below 5 mHz the measurement performance will be limited by acceleration noise.

The relative pathlength changes need to be measured² with a precision of $1 \text{ pm}/\sqrt{\text{Hz}}$ (allocated noise budget for the phase measurement system (PMS) out of the optical metrology budget of $12 \text{ pm}/\sqrt{\text{Hz}}$ for each single link), and thus the phase of the heterodyne signal needs to be measured with a sensitivity of $1 \mu\text{cycle}/\sqrt{\text{Hz}}$ or $2\pi \times 10^{-6} \text{ rad}/\sqrt{\text{Hz}}$. The relevant measurement band is the frequency regime from 0.1 mHz to 0.1 Hz.

Due to the relative spacecraft motion, depending on the orbital dynamics of each spacecraft, the heterodyne frequency gets affected by Doppler shifts of $\pm 10 \text{ MHz}$. This leads to variations of the heterodyne frequency from a few MHz up to 20 MHz. These variations are at frequencies of a few 1/year and are thus below the measurement bandwidth. This fact determines the choice of the heterodyne frequency, which has to be higher than the Doppler shift in order to avoid phase measurement at DC. Thus, the beat note needs to be digitized with at least $f_{\text{sampl}} = 40 \text{ MHz}$. In order to achieve a better SNR, which goes with $\sqrt{f_{\text{sampl}}}$, the sampling rate can be chosen to be 80 MHz. The dynamics of the signal level is approximately 8 bit, such that the intrinsic noise level of an ADC with 8 bit is sufficiently low enough. The induced phase noise due to the digitization - under the assumption that the phase noise is

¹ LISA also uses Nd:YAG lasers with a wavelength of 1064 nm (see Section 2.3.1).

² in each phasemeter

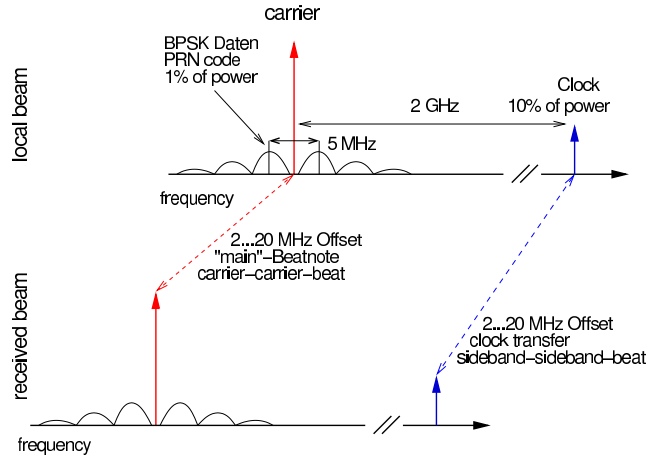


Figure 78. Proposed frequency scheme for LISA. Additionally to the main science carrier the first order FM sidebands contain the information of the USO noise of the independent spacecraft master oscillators. For the interspacecraft ranging a pseudo-random noise code sequence provides the length measurement.

white - is given by (see Section 2.2.3 and Appendix A.3):

$$\tilde{\Phi}_{\text{dig}} \approx \frac{2^{-B}}{\sqrt{6} \cdot f_{\text{Sampl}}}$$

The numerical value for $f_{\text{Sampl}} = 80 \text{ MHz}$ and $B = 8 \text{ bit}$ is $\tilde{\Phi}_{\text{dig}} \approx 1.78 \cdot 10^{-7} \text{ rad}/\sqrt{\text{Hz}}$ which is about a factor of 30 below the required shot noise limited measurement performance of $2\pi \cdot 10^{-6} \text{ rad}/\sqrt{\text{Hz}}$.

The beat note phase respectively frequency needs to be measured with respect to a system-wide reference oscillator (USO) on each spacecraft.

Besides the main science measurement, the phase fluctuations of each USO with respect to those on the other spacecraft need to be measured for the on ground data post-processing performed by Time Delay Interferometry (TDI) (SHADDOCK, 2003). This clock noise information will be exchanged between the spacecraft by additional frequency or phase modulation (F/PM) sidebands with a modulation frequency $f_{\text{mod}} \approx 2 \text{ GHz}$ (KLIPSTEIN *et al.*, 2006) and a modulation depth Δf such that 10% of the carrier light power is in both sidebands (see Figure 78 and Section 5.1.3). The power of the two sidebands is given by $m^2/2 \approx 0.1$ with $m = \Delta f/f_{\text{mod}}$, where m is the modulation index. The frequencies of these sidetones need to be chosen such that the sidetone-

sidetone beat of the local and the received beam is not at the same frequency as the carrier-carrier beat.

Another necessary information for the laser frequency noise subtraction performed by the TDI algorithm is the relative position of the spacecraft with respect to each other. Therefore, a GPS-like ranging measurement will be implemented by modulating a pseudo-random noise code with 1% of the carrier light power. This code sequence can also be used to transfer data between the spacecraft.

The LISA phase measurement system needs to provide the following features:

1. measure the relative phase variations between the detected heterodyne signals (carrier-carrier beat) and the local reference oscillator,
2. measure the clock noise between the individual spacecraft-wide master oscillators (sidetone-sidetone beat),
3. demodulate and decode the pseudo-random noise code sequence for inter-satellite ranging and data transfer (carrier-code spectrum beat).

Chapter 5 outlines the extra tasks 2 and 3 in more detail.

4.1.2 Comparison of the LISA and the LISA Pathfinder phase measurement system

Even since an appropriate phase measurement system was implemented for LISA Pathfinder, there are a number of additional features in the LISA PMS that need to be considered for the implementation. Table 8 gives an overview/-comparison of the main requirements of both systems. The required phase readout noise level of both systems are comparable, but the signal frequencies to be handled by the LISA PMS are a factor of 100 . . . 1000 higher than for LISA Pathfinder. Furthermore, the LISA PMS needs to be capable to measure the phases of more than one tone with frequencies close to each other (the phases of the sideband-sideband tones provide the clock noise).

A major design driver to be considered is the operation frequency range of LISA which is from 0.1 . . . 100 mHz. This frequency regime requires long term stability (on time scales of thousands of seconds) of all used components. For this reason, in particular thermal drifts of characteristics of the used electronic components need to be taken into account. From this point of view, the usage of digital circuits has advantages, since they are basically unaffected by thermal drifts once the analog signal is digitized. Thus the approach is to digitize the measurement signal as early as possible in the processing chain in order to perform the dedicated processing in digital electronics.

Requirement	LISA Pathfinder	LISA	units
measurement performance	$2\pi \cdot 10^{-6}$	$2\pi \cdot 10^{-6}$	rad/ $\sqrt{\text{Hz}}$
heterodyne frequency range	~ 0.001	2-20	MHz
max Doppler shift rate	~ 0	4	Hz/s
max Doppler shift	~ 0	± 10	MHz
signal Nyquist band	~ 0.002	40	MHz
signal dynamics	16	8	bit
phase dynamics	100	$\gg 100$	rad
phase update rate	100	3	Hz
measurement bandwidth	3-30	0.1-1000	mHz
additional side tones	no	yes	

Table 8. Comparison of the LISA and the LISA Pathfinder phase measurement system.

4.1.3 Phasemeter baseline concept

Different phase measurement techniques are currently under investigation. The zero crossing technique has been demonstrated for a single fixed frequency (POLLACK, 2006). This measurement is based on counting fast clock cycles between (e.g. positive) zero crossings of the heterodyne signal (see Section 2.3.6).

For the LISA precursor mission LISA Pathfinder, a different type of PMS has been successfully implemented (2.3.7). In contrast to the LISA beat signal, the LISA Pathfinder interferometer is operated at a constant heterodyne frequency in the kHz range. A digital two quadrature (I-Q) demodulator has been implemented as phase measurement system. This technique is called SBDFT (Single Bin Discrete Fourier Transform) and the principle of operation can be seen in Figure 79 (HEINZEL *et al.* (2005a), WAND *et al.* (2006)). In order to obtain a phase φ , the signal is first sampled by an ADC (represented as x_i) and then multiplied with both quadratures of the local oscillator of the same frequency and summed over the length N of a DFT:

$$\Re(F) = \sum_{i=0}^{N-1} x_i \cdot c_i \quad ; \quad \Im(F) = \sum_{i=0}^{N-1} x_i \cdot s_i, \quad (4.1)$$

where $c_i = \cos\left(\frac{2\pi i k}{N}\right)$ and $s_i = \sin\left(\frac{2\pi i k}{N}\right)$. This corresponds to picking the

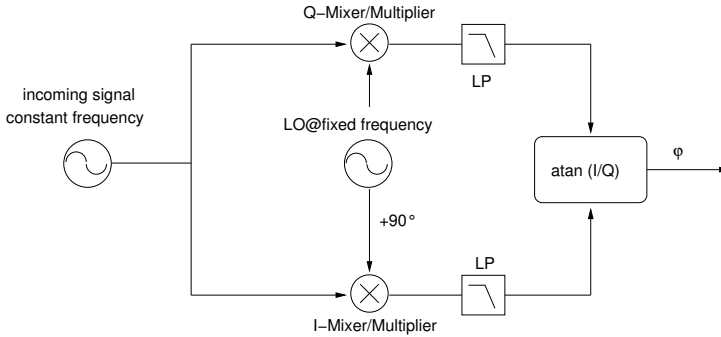


Figure 79. I-Q phase demodulation for a signal with constant frequency. A digital version was implemented in the PMS for LISA Pathfinder. Mathematically this demodulation is equivalent to a DFT (Discrete Fourier Transform) for one frequency (SBDFT).

single frequency bin ‘k’ out of a full discrete Fourier transform (DFT) result.

LISA PHASEMETER BASELINE Due to the frequency drift occurring to the LISA beat notes, a different phase measurement system will be necessary, where the frequency of the local oscillator can be locked to the frequency $f_{\text{het}}(t)$ of the heterodyne signal. The carrier-carrier beat (the main beatnote) can be written as:

$$f(t) = A \cdot \cos(\omega_{\text{het}}(t) t + \varphi_{\text{fine}}(t)), \quad (4.2)$$

where $\omega_{\text{het}}(t) = 2\pi f_{\text{het}}(t)$ with $f_{\text{het}}(t)$ as current heterodyne frequency. Considering the nominal heterodyne frequency¹ f_{hetnom} and Doppler-induced frequency shifts over one year with a Doppler drift rate of $0 \dots 4 \text{ Hz/s}$, $f_{\text{het}}(t)$ can be written as:

$$f_{\text{het}}(t) = \frac{f_{\text{hetnom}}}{2} + \int_0^t dt \frac{2 \text{ Hz}}{\text{s}} \sin\left(2\pi \frac{1}{\text{year}} t\right). \quad (4.3)$$

For $t=1$ year Equation (4.3) yields:

$$f_{\text{het}}(t) = \frac{f_{\text{hetnom}}}{2} - \frac{2 \text{ Hz}}{\text{s}} \frac{1}{2\pi \text{ year}} \cos\left(2\pi \frac{1}{\text{year}} t\right) \quad (4.4)$$

$$= 10 \text{ MHz} - 10 \text{ MHz} \cos\left(2\pi \frac{1}{\text{year}} t\right). \quad (4.5)$$

¹ determined by the offset locked lasers which have a frequency offset of about 20 MHz

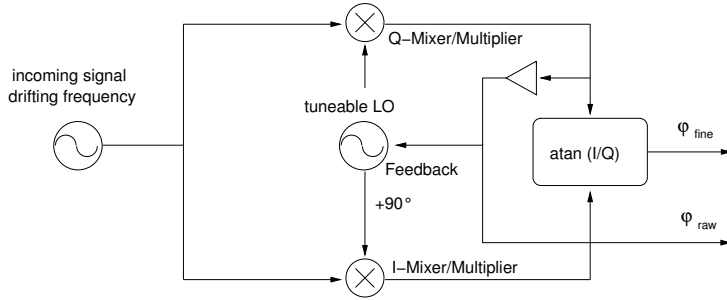


Figure 8o. I-Q phase demodulation for a signal with drifting frequency. The concept is very similar to the Pathfinder phasemeter with an additional PLL loop that tracks the drifting carrier frequency.

In order to track the heterodyne frequency $f_{\text{het}}(t)$, a phase-locked loop (PLL) is implemented in the LISA demodulation scheme. This leads to the [LISA PMS baseline](#) ([SHADDOCK *et al.* \(2006\)](#), [WARE *et al.* \(2006\)](#)). The frequency or phase measurement can be derived from the local oscillator feedback signal (φ_{raw} in Figure 8o). In order to measure phase noise outside the bandwidth of the PLL, or to measure residual noise within its bandwidth, the I-Q demodulation can be processed as implemented in the LISA Pathfinder PMS (φ_{fine} in Figure 8o).

The full phase argument of Equation (4.2) can be expressed as:

$$\Phi(t) = \underbrace{\omega_{\text{het}}(t)}_{\varphi_{\text{raw}}(t)} t + \varphi_{\text{fine}}(t). \quad (4.6)$$

A direct digital synthesis (DDS) system generates a signal with frequency $\omega_{\text{het}}(t)$, where $\omega_{\text{het}}(t)$ can be easily obtained/set from/by the phase increment register (PIR) of the DDS. Thus, $\varphi_{\text{raw}}(t)$ can be tracked over a wide dynamic range and delivers a raw phase estimation. The other information to be extracted from this model is $\varphi_{\text{fine}}(t)$. This can be obtained by calculating the argument of the ratio between the (low pass filtered) I- and the Q-path of the mixer such that:

$$\Phi(t) = \underbrace{\omega_{\text{het}}(t)}_{\varphi_{\text{raw}}(t)} \cdot t + \arg \frac{I(t)}{Q(t)}, \quad (4.7)$$

where I and Q can be derived directly from the low pass filtered mixer outputs. Assuming a digital system, the filters can be implemented e.g. as mov-

ing average (MA) filters such that $I(t)$ and $Q(t)$ are given by:

$$I(i) = \sum_{i=0}^{N-1} x_i \cdot c_i \quad ; \quad Q(i) = \sum_{i=0}^{N-1} x_i \cdot s_i, \quad (4.8)$$

where x_i is the digitized input signal, $c_i = \cos(\omega_{\text{het}}(t) \cdot t_i)$ represents the local oscillator phase and $s_i = \sin(\omega_{\text{het}}(t) \cdot t_i)$ is its quadrature and N the length of the moving average filter.

Due to the structure of the readout concept, the **PMS** can be divided into two major processing parts:

1. the integer arithmetic front end - responsible for the raw phase estimation by means of a **DDS** as part of a digital **PLL** and
2. a floating point arithmetic phase reconstruction back end - used to process the arctan operation and the calculation of the overall phase.

4.1.4 Modified approach

Since there exist a well established and tested **PMS** for **LISA Pathfinder**, which fulfills the necessary measurement performance of $2\pi \cdot 10^{-6} \text{rad}/\sqrt{\text{Hz}}$ with a margin of several orders of magnitude, this could be used as a basis for an extended version providing the additional requirement of varying frequencies in the MHz range. This proposal suggests a multi-(4)-channel *LISA PM tuning kit* (LPMTK) which is a device designed to mixing down the varying 20 MHz input frequency to a fixed frequency of 1 kHz that can be handled by the **LISA Pathfinder** phasemeter.

Figure 81 illustrates this concept. The four channels¹ of a **QPD** are mixed down to 1 kHz (fix) with a tuneable MHz slave oscillator (SLO) which can be implemented as **DDS** system. Since all four channels provide the same frequency (but probably different phases), only one channel needs to be used as **DDS** feedback (1-channel-feedback). Therefore, a digital **PLL** locks the output of one of the MHz mixers to the 1 kHz master oscillator (MLO) from the **LISA Pathfinder** phasemeter. The frequency scheme for this setup is illustrated in Figure 82.

The accuracy of the digital **PLL** does not need to be very high, since it is only needed for a raw phase estimation (φ_{raw} in Figure 81) with wide dynamic range. The raw phase will be corrected by the output of the micro radian accuracy **LISA Pathfinder**-like phasemeter (φ_{fine} in Figure 81). The overall phase can be obtained by the combination of both phases (similar to

¹ In reality **LISA** uses quadrant photodetectors for measurement of the beat note in order to obtain alignment information.

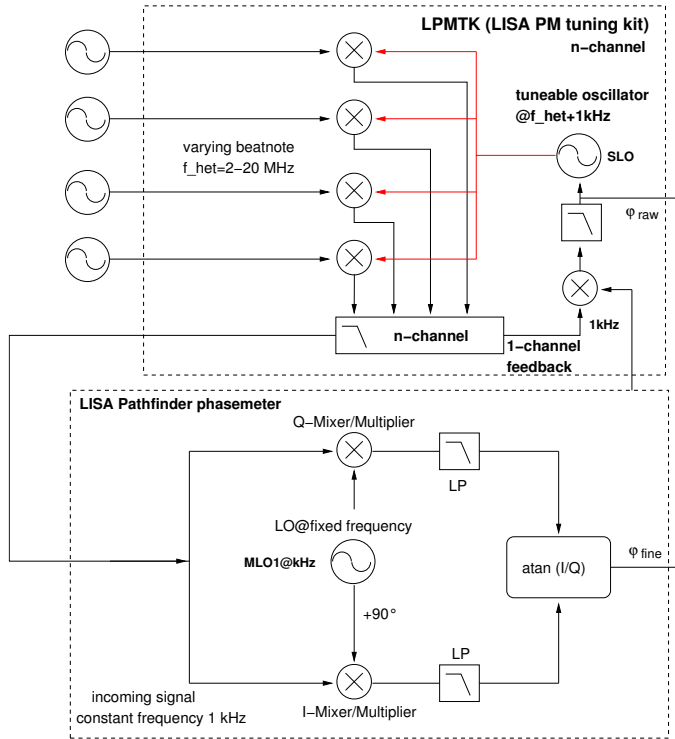


Figure 81. Modified phasemeter approach. This concept uses a LISA Pathfinder phasemeter with frequency tuning kit as add on.

the baseline concept). Thus the signal $f(t)$ to be analyzed can be written as:

$$f(t) = A \cdot \cos(\omega_{\text{het}}(t)t + \omega_{1\text{kHz}}t + \varphi_{\text{fine}}(t)), \quad (4.9)$$

with an arbitrary amplitude A . The full phase argument to be measured yields:

$$\Phi(t) = \underbrace{\omega_{\text{het}}(t)t}_{\varphi_{\text{raw}}(t)} + \underbrace{\omega_{1\text{kHz}}t}_{\text{known since } \omega_{1\text{kHz}}=\text{const.}} + \varphi_{\text{fine}}(t). \quad (4.10)$$

The DDS generates a signal with frequency $\omega_{\text{het}}(t)$ where $\omega_{\text{het}}(t)$ can be easily obtained from the PIR of the DDS. Thus $\varphi_{\text{raw}}(t)$ can be tracked over a wide dynamic range and delivers a raw phase estimation. The other bit of information to be extracted from this model is $\varphi_{\text{fine}}(t)$. This is provided by the LISA

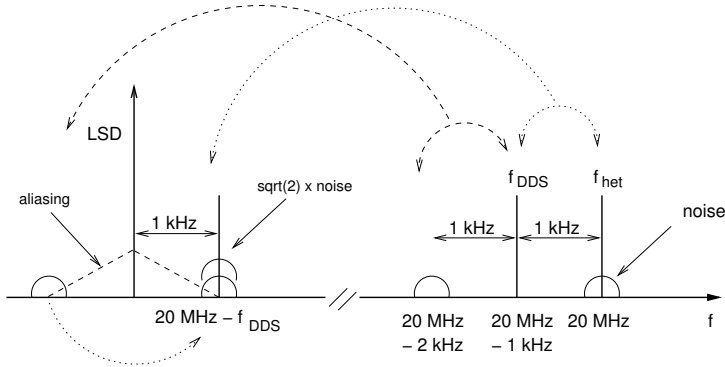


Figure 82. Noise aliasing in alternative concept. Due to aliasing effects the noise from $f_{\text{DDS}} \pm 1 \text{ kHz}$ contributes to the effective measurement noise.

Pathfinder-like phasemeter (PM) that analyzes the downmixed signal with the phase:

$$\Phi_{\text{down}}(t) = \omega_{1 \text{ kHz}} t + \varphi_{\text{fine}}(t). \quad (4.11)$$

This can be done with mrad accuracy and the full phase information can be derived as:

$$\varphi(t) = \varphi_{\text{raw}}(t) + \varphi_{\text{fine}}(t). \quad (4.12)$$

This concept provides two significant advantages compared to the baseline:

1. The development effort reduces dramatically since it uses the existing [LISA Pathfinder](#) phasemeter for the accuracy measurement. The only remaining item is the *LISA PM tuning kit* (LPMTK) – a simple digital [PLL](#) and [DDS](#).
2. Only one [DDS](#) is needed for each [QPD](#).

Besides these advantages from the implementation point of view, this concept yields a loss in [SNR](#) by a factor of $\sqrt{2}$ ([SHADDOCK and HEINZEL, 2006](#)). [Figure 82](#) illustrates how noise aliases in this modulation scheme. The main beatnote at $f_{\text{het}} = 20 \text{ MHz}$ is demodulated by the [DDS](#) output which is separated by a 1 kHz frequency offset and phase-locked to f_{het} . The resulting beat at 1 kHz is analyzed with the pathfinder phasemeter. Unfortunately in this scheme also noise contributions *from the other side of the demodulation frequency* f_{DDS} alias down to 1 kHz and disturbs the phase readout at this frequency.

Thus the concept is no appropriate alternative to the phasemeter baseline!

Component	type	specification	intended purpose
AD converter	AD9446	16 bit@ 125 MHz max.	front end, digitization of photodiode output
DA converter	AD9744	14 bit @ 210 MHz max.	DA conversion of feedback signals for Nd:YAG laser stabilization
EPP interface		output rate approximately 200 kB/s	transfer phase data intermediate integer results at approximately 100 Hz to floating point hardware, send RAM data to the PMS board for configuration
RAM	TI	1 Mword with 16 bit wordsize, 6 ns access time	store data e.g. sinetable or IIR/FIR filter coefficients
FPGA	ACTEL A3P250/1000	Flash pro- grammable, 250/1000 kGates	CPU

Table 9. List of components used on the new prototype PMS board.

4.2 IMPLEMENTATION

4.2.1 Hardware platform

The platform that was chosen for the hardware implementation of the phase-meter core is based on programmable logic. For this purpose [FPGAs](#) seem to be the most suitable choice since in particular ACTEL provides reprogrammable Flash versions which are optimal for development and in addition to that ACTEL also provides space qualifiable [FPGAs](#) which can be programmed with the same software tools.

Currently, a new hardware design has been implemented and is under testing. Its main components and features are listed in [Table 9](#) (circuits can be found in [Appendix C.1](#)) and [Figure 83](#) shows a photograph of the assembled board.

The AD conversion of the new PMS board will be realized by a 16 bit ADC, whereas 8 bit are effectively used (the extended resolutions can be used for diagnostics). The maximum sampling frequency is 125 MHz, but it is currently running at 80 MHz. These design restrictions were chosen, due to the

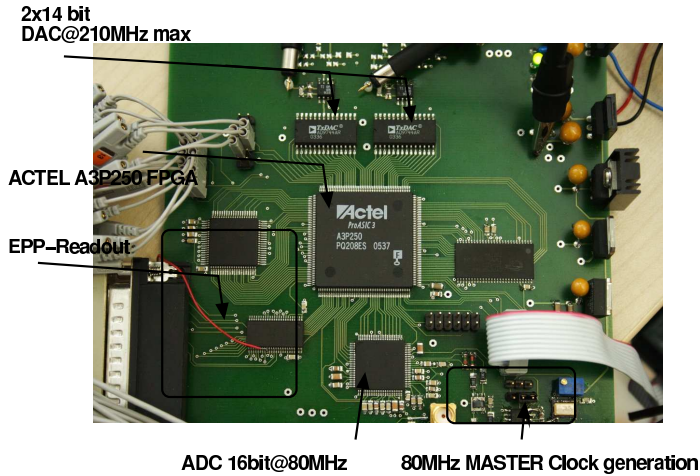


Figure 83. The photograph shows the implemented hardware of the LISA PMS prototype, which is under test now and is the first of several prototypes to be built during the prototyping process.

availability of space qualifiable components. Since the PMS needs to perform the frequency offset phase lock of the LISA lasers, two 14 bit DAC's are foreseen to control the piezo electric transducer (PZT) and crystal temperature frequency actuators of the laser. A dedicated RAM is provided to store sets of IIR/FIR¹ filter coefficients and/or sine look-up tables for the DDS. An enhanced parallel port (EPP) implementation, including a dedicated FIFO, is the interface in order to transfer data between the PMS board and a floating point digital signal processor (DSP) (e.g. a standard of the shelf PC).

4.2.2 PLL as phase measurement device

The (digitized) main beat signal is multiplied with the output of a DDS, in order to obtain the raw phase φ_{raw} . Therefore, a digital multiplier can be used as phase detector. The (low pass filtered) output can be used as feedback signal for the DDS. The control port of the DDS is the PIR. Thus, the phase of the DDS generated signal can be locked to the input signal. Assuming, that the locked DDS generated signal perfectly follows the phase of the input signal, φ_{raw} can be obtained either from the value m representing the phase increment of the DDS or directly from the value of its phase accumulator (PA).

¹ infinite impulse response/finite impulse response

While m represents a frequency (see Equation (4.19)), the value of the PA directly represents the phase of the synthesized signal.

4.2.3 DDS operation

As described above, independently from the chosen implementation of the phasemeter, in any case a digital PLL is needed in order to track the drifting beat signals of the interferometer outputs. In contrast to other types of digital PLLs which use partly analog components such as voltage controlled oscillator (VCO)s, the PLL here is implemented completely digital and is called also all digital phase-locked loop (ADPLL). Instead of a VCO, a numerically controlled oscillator (NCO) or DDS is used as tunable frequency generator. Besides the tracking functionality, the ADPLL is also needed to obtain the raw phase φ_{raw} .

The aim of a DDS is the generation of a periodic wave form $x(t)$ with a tunable frequency and/or phase. For various applications such as signal generators, the amplitude of the DDS output needs to be modulated as well¹.

Most computers use series or Chebychev polynomials to calculate the sine or cosine values for arbitrary. The estimation can be achieved with practically arbitrary precision.

Due to the complexity of the approximation algorithms these methods are inappropriate for an efficient hardware implementation running in real time.

Since for the DDS application high precision of the sine representation is not needed, and processing speed is an issue, a set of pre-computed values for one period of the sine wave can be stored in a look-up table (LUT). The precision of the sine wave is given by the resolution (or depth) M that represents the number of bits representing each sine value, and the length N counting the number of values stored in the LUT. In fact, only a quarter of a period is sufficient to generate the full sine wave as well as the cosine wave².

Such a LUT is the key for a real-time generation of periodic wave forms. Obviously the LUT can be filled with values of an arbitrary wave form. This method to synthesize a wave form from a LUT, is called DDS (direct digital synthesis).

PRINCIPLE OF OPERATION For the purpose described here, only a sinusoidal wave form will be considered. This can be described as

$$x(t) = \sin(\underbrace{2\pi f t}_{\varphi(t)} + \Phi) \quad (4.13)$$

The argument $\varphi(t)$ in this context is called the phase angle at the time t . Φ is an additional phase offset used to provide the required phase of the signal.

¹ For the use of the DDS in the context of a phase measurement system this is not needed here.

² Additional logic is necessary.

For a time discrete system, the parameter t is represented by the time steps t_i . Assuming a constant sampling interval Δt_s , it yields $t_i = i \cdot \Delta t_s$. In this notation, the phase angle is given as

$$\varphi_i = i \cdot \Delta\varphi = \sum_0^i \Delta\varphi \quad (4.14)$$

with $\varphi_i = \varphi(t_i)$ and $\Delta\varphi = 2\pi f t_i$. This means that the phase angle is being derived by accumulating the constant phase difference $\Delta\varphi$ - an operation that can be easily implemented in hardware.

The sine wave to be generated can be expressed now as

$$x_i = x(t_i) = \sin(\varphi(t_i) + \Phi). \quad (4.15)$$

The **LUT** of the length N contains the sine values for a full period of 2π

$$\sin(j) = \sin\left(2\pi \frac{j}{N}\right) \quad \text{with } j = 0, 1, 2, \dots, N-1 \quad (4.16)$$

The index j represents the phase angle $\varphi(t_i)$. For typical applications it is appropriate to choose the length N of the table as a power of two such that $N = 2^n$. If the sine table will be sampled at a sampling frequency f_S the phase increment is given by

$$\Delta\varphi = \frac{2\pi f}{f_S}, \quad (4.17)$$

where f is the frequency of the signal to be generated. Applying typical values for f and f_S , e.g. $f = 20$ MHz and $f_S = 80$ MHz this leads to a phase increment of $\Delta\varphi = \frac{\pi}{2}$, which is about the maximal useful value. On the other side, for a given phase increment $\Delta\varphi$, the output frequency of the **DDS** f is given by:

$$f = \frac{f_S \cdot \Delta\varphi}{2\pi}. \quad (4.18)$$

Assuming the sine look-up table contains a full period of sine wave represented by $N = 2^n$ samples, the output frequency of the **DDS** implementation yields:

$$f = \frac{f_S}{2^n} \cdot \frac{m}{\text{PIR}} \quad (4.19)$$

where m represents an integer number for the phase increment and **PIR** the length of the phase increment register. Applying the parameters $f_S = 80$ MHz and $n = 8$ such that $N = 2^n = 2^8 = 256$ and $m=1$ for a 8-bit **PIR** this leads to a base frequency of 1220.7 Hz that corresponds to the frequency resolution Δf of the **DDS**.

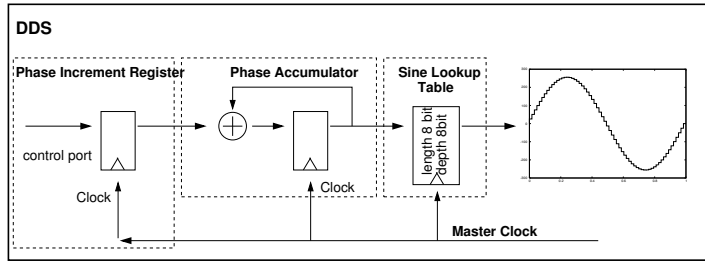


Figure 84. Simplified block scheme of a DDS.

This suggests that the phase quantization of a DDS is only determined by the ratio of generated signal and the operation/sampling frequency of the system, while the frequency resolution is determined by the length of the PIR of the DDS.

Figure 84 illustrates the components of a typical DDS implementation. The output frequency can be controlled via the phase increment register (PIR) and can be calculated according to Equation (4.19). The phase accumulator *integrates* the PIR with a time interval of $1/f_S = T_S$. A phase accumulation (PA) register is permanently updated with the new result. Assuming a PA register of the same length as the sine look-up table¹ (8 bit), the PA register corresponds to the index of the sinetable and consequently to the phase of the signal. If the PA register reaches its maximum value 2^8 , a full cycle of 2π of the sine wave is completed - the accumulator overflows and a new cycle starts.

4.2.4 VHDL Implementation of an ADPLL

In order to achieve higher frequency resolutions the phase increment register needs to provide more bits than the look-up table (see Equation (4.19)). Figure 85 illustrates an example for the prototype configuration. The phase increment register provides a length of 40-bit and is added up each clock cycle in the phase accumulator (PA). The PA provides a length of 72-bit. The upper 32 bit represent integer multiples of 2π . The next 8 bit of the PA are directly connected to the sine look-up table. The frequency resolution f_{res} is determined by the LSB of the phase increment register and the system clock

¹ In order to achieve a higher frequency resolution, practically the PA provides much more bits than the look-up table (see next section).

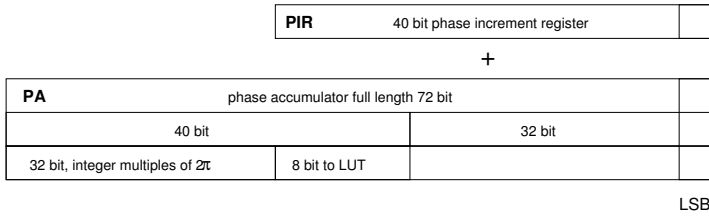


Figure 85. Length of phase increment register and phase accumulator. A 72-bit phase accumulator is each clock cycle increased by the value of the 40-bit phase increment register. The upper.

f_s and can be calculated as follows:

$$f_{\text{res}} = \frac{80 \text{ MHz}}{2^8} \frac{1}{2^{32}}. \quad (4.20)$$

Figure 86 shows a simplified schematic of the ADPLL. The heterodyne signal is digitized by an ADC and mixed in a 8x8 bit digital multiplier with the synthesized sine wave generated by a Direct Digital Synthesis (DDS) system. The DDS consists of a 72 bit phase accumulator with an effectively 40 bit phase increment register which is the core of the DDS. The output of the mixer is fed back via a conventional PI controller to the PIR of the DDS.

The 32 most significant bits (MSB's) of the phase accumulator are connected (via a modulo 256 operation) to a 256 element \sin^{-1} table with a precision of 8 bit. The whole design is synchronously driven with the same 80 MHz clock that drives the ADC frontend. The phase can be reconstructed from either the phase increment register (PIR) or the phase accumulator (PA) of the DDS.

4.2.5 Loop analysis

In order to understand the behavior and characteristics of the ADPLL and to determine the gain parameters of the proportional plus integral controller (component of a classical servo design) (PI) controller (that are the only free parameters), the open loop gain transfer function needs to be known. Therefore, an analysis of the loop is necessary.

LOOP CONFIGURATION The overall Open Loop Gain $G(\omega)$ of the system is given by the individual transfer functions of its components:

$$G(\omega) = G_{\text{DDS}}(\omega) \cdot G_{\text{PD}}(\omega) \cdot G_{\text{PI}}(\omega), \quad (4.21)$$

¹ For further processing, a 90 degree phase shifted DDS provides the second quadrature of the heterodyne signal.

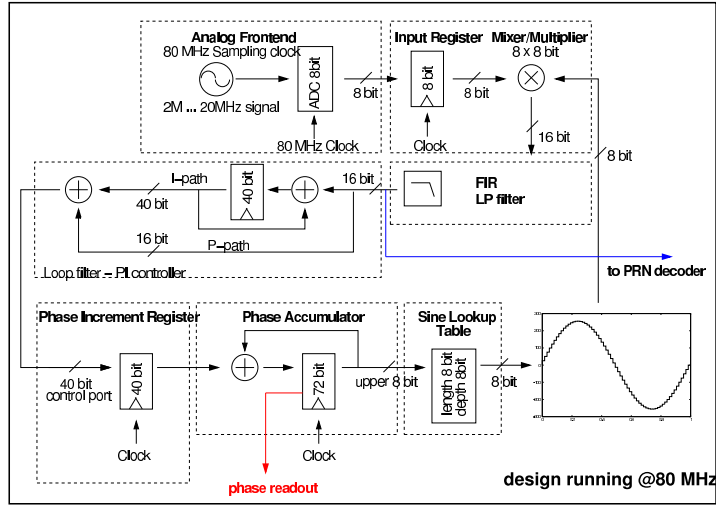


Figure 86. Overview of the phasemeter core design that mainly consists of an all digital phase lock loop (ADPLL) implemented on an Actel FPGA. The design was tested with a 80 MHz system clock.

where $G_{\text{DDS}}(\omega)$ is the transfer function of the DDS, $G_{\text{PD}}(\omega)$ the transfer function of the phase detector and $G_{\text{PI}}(\omega)$ the transfer function of the loop filter.

DDS TRANSFER FUNCTION Due to the intrinsic frequency to phase conversion in the phase accumulator, the transfer function of the DDS system has an integrator shape. The output of the DDS can be expressed as $\text{Hz}=\text{cycles/s}$ or $2\pi\text{rad/s}$. The unity gain frequency of the integrator is determined by the constant gain factor $K_{\text{DDS}}[\text{rad/s}]$. For a given value of the **PIR** this factor determines the resulting frequency of the DDS.

K_{DDS} depends on the system frequency f_s , the length of the PIR and the resolution of the sine look-up table (LUT). Thus, the transfer function of the DDS is given by:

$$G_{\text{DDS}}(\omega) = K_{\text{DDS}} \cdot \frac{1}{i\omega} = 2\pi \frac{80\text{ MHz}}{\text{PIR} \cdot 2^8} \cdot \frac{1}{i\omega}. \quad (4.22)$$

For a **PIR** length of 32 bit, the numerical value of K_{DDS} is

$$\frac{2\pi \cdot 7.276 \cdot 10^{-5} \text{ rad}}{i\omega} \frac{1}{\text{s}}. \quad (4.23)$$

TRANSFER FUNCTION OF PHASE DETECTOR An 8x8 bit multiplier acts as phase detector of the ADPLL¹. Thus for two sinusoidal signed 8 bit input signals, the DC component of the output varies from² -2^{14} to $+2^{14}$ (15 bit) depending on the phase difference of the signals. Assuming the phase detector is operated in its linear range, the transfer function is flat and can be expressed as:

$$G_{PD}(\omega) = 2^{14} \left[\frac{1}{\text{rad}} \right] \quad (4.24)$$

TRANSFER FUNCTION OF LOOP FILTER An appropriate low pass filter³ removes the higher frequency terms from the frequency mixing (sum frequency of both multiplier input signals). The filtered error signal is fed back to the phase increment register (PIR) of the DDS via a standard proportional-integral (PI) controller with a transfer function given by:

$$G_{PI}(\omega) = G_P + \frac{G_I}{i\omega}, \quad (4.25)$$

where G_P and G_I are constant gain factors for the proportional and the integral path of the controller respectively. The cut-off frequency of the controller is given by $f_c = \frac{G_I}{G_P}$.

OPEN LOOP GAIN Since the transfer functions of all loop components are known, the open loop gain can be calculated as follows:

$$G(\omega) = 2\pi \cdot [\text{rad}] \cdot \frac{80 \text{ MHz}}{\text{PIR} \cdot 2^8} \cdot \frac{1}{i\omega} \cdot 2^{14} \left[\frac{1}{\text{rad}} \right] \cdot \left[G_P + \frac{G_I}{i\omega} \right]. \quad (4.26)$$

With the parameter $s = i\omega$, Equation (4.26) yields:

$$G(s) = \frac{2\pi \cdot 80 \cdot 10^6 \cdot 2^6}{\text{PIR}} \cdot \frac{G_P s^2 + G_I}{s^2} \quad (4.27)$$

Figure 87 shows the open loop gain of the digital PLL for the following parameters:

1. PIR length: 32 bits

¹ The implemented multiplier processes signed 8 bit input signals.
² The multiplier output register is 16 bit, but the DC components of its output, used for the feedback, only varies from -2^{14} to $+2^{14}$ since $\sin(x)\sin(y) = 1/2(\sin(x-y) + \sin(x+y))$.
³ The current design relies on the intrinsic integrators of the DDS (frequency to phase conversion) and the PI controller in order to remove the sum frequency. This is sufficient for high heterodyne frequencies (tens of MHz). For smaller operation frequencies and additional lowpass filter will be necessary.

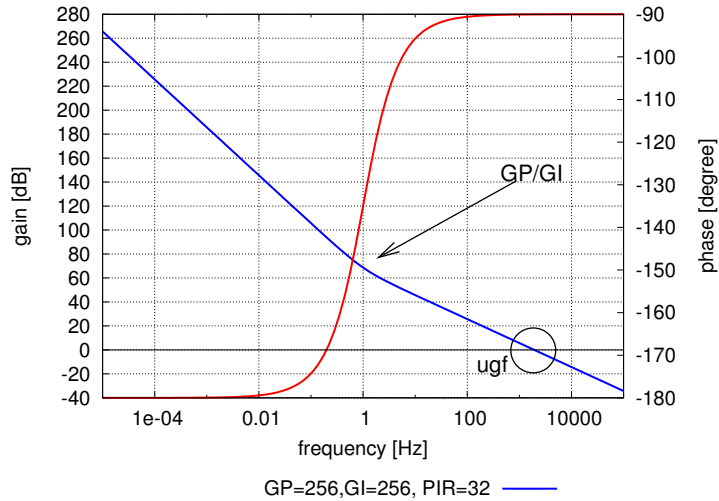


Figure 87. Open loop gain of the ADPLL. The dark curve of the Bode plot is the gain and the lighter curve is the phase representation of the transfer function. The unity gain frequency is in the order of a few kHz. The frequency of the transition from the $1/f$ in $1/f^2$ slope is determined by the ratio G_I/G_P .

$$2. G_P = G_I = 2^8$$

The unity gain frequency is in the order of a few kHz. Since the precision of the multiplier output is limited to effectively 15 bit, gain values >1 for $G_P = G_I$ decrease the precision of the frequency tuning by the factor of the gain.

Figure 88 illustrates the s-domain¹ model of the system. A disturbance x_S is suppressed by $1/(1 + G(s))$ such that x_O is given by $x_S \cdot 1/(1 + G(s))$. The open loop gain $G(s)$ is given by x_I/x_O .

¹ s is the Laplace variable. The Laplace transformation is often used in order to analyse time discrete systems and is very similar to the Fourier transform. For the special case $s = i\omega$ the Laplace transformation yields the Fourier transform.

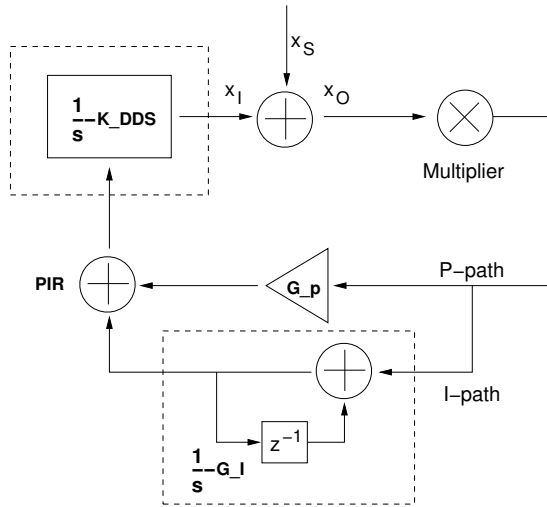


Figure 88. s-domain model of the ADPLL (see text).

4.2.6 Front end readout and phase reconstruction

The phasemeter re-samples the **PIR** at a frequency of $f_{\text{readout}} = 38 \text{ Hz}$ ($80 \text{ MHz}/2^{21}$) and transfers the data to the first in first out (**FIFO**) memory provided by the **PMS** prototype board. The readout of the **FIFO** memory is implemented via an EPP (enhanced parallel port) interface controlled by a C-program running on a standard PC with Linux as operating system. The program polls a status line of the parallel port that indicates the status of filling state of the **FIFO** memory. Since the EPP port provides 8 parallel data lines, the **PIR** is multiplexed in the phasemeter and reconstructed on the PC side. From this data, the phase of the input signal can be reconstructed.

Remark: Due to timing problems within the phasemeter implementation, the received data packets at the PC are affected by a varying offset such that a permutation of the **PIR** register must be rearranged.

The phase could also be obtained by a direct readout of the phase accumulator (see Figure 89). An open question is, which method provides the optimal readout noise performance. However, currently the **PA** is read out differentially ($\text{PA}(t + 1/f_{\text{readout}}) - \text{PA}(t)$). First tests showed, that this method delivers a better noise performance compared to the direct **PIR** readout at the same readout frequency.

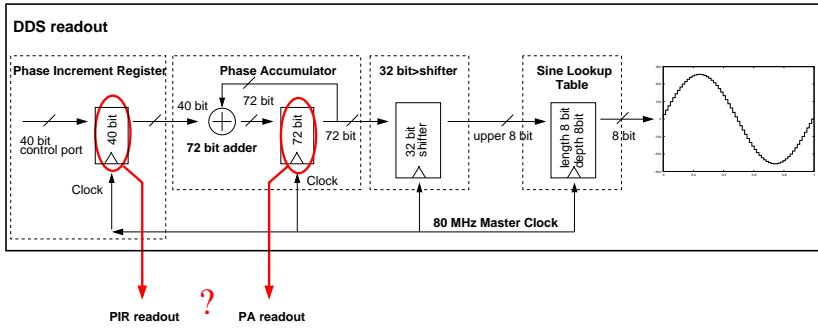


Figure 89. PIR vs. PA readout. The phase information can be either obtained directly from the PA or from the PIR

A POSSIBLE EXPLANATION The resolution of the **PIR** determines the minimal frequency step of the **DDS** $\Delta f = \text{LSB}_{\text{frequ}}$ (see Equation (4.20)). Thus, the frequency readout noise is given by:

$$\tilde{\delta f} = \frac{\text{LSB}_{\text{frequ}}}{\sqrt{6} \times f_{\text{sampl}}} = \frac{7.276^{-5} \text{ Hz}}{\sqrt{6} \times 80 \text{ MHz}} = 3.3 \times 10^{-9} \frac{\text{Hz}}{\sqrt{\text{Hz}}} \quad (4.28)$$

The phase noise of the readout is given by $\tilde{\delta f}/f_{\text{Fourier}}$. This shows that this readout method, inherently has a $1/f$ phase noise spectrum:

$$\tilde{\delta \varphi} = \frac{\tilde{\delta f}}{f_{\text{Fourier}}} \frac{\text{rad}}{\sqrt{\text{Hz}}}. \quad (4.29)$$

However, this point needs to be investigated in more detail and is topic of ongoing research.

4.2.7 Noise estimation

The **LISA PMS** readout scheme uses the **ADPLL** in order to track the carrier. The **PIR** used in the **DDS** of the **ADPLL** represents a frequency which is used to reconstruct the phase information. The length of the **PIR** determines the frequency resolution and thus the readout noise. Assuming a **PIR** length of 40 bit, the frequency resolution is given by Equation (4.19). Assuming the **ADPLL** is able to perfectly track the carrier, the comprehensive phase information is contained in the **PIR** readout. Since a perfectly working **ADPLL** is an idealized assumption, in addition to the **PIR** readout, the residual phase error also needs to be estimated. This is provided by the arctan-operation applied to the I- and Q mixer outputs (Figure 80).

For this phase readout scheme, two noise sources are need to be taken into account:

1. Quantization noise due to digitization of the input signal is the fundamental limitation of the readout process.
2. Quantization noise of the PIR readout. Due to the quantized frequency of the ADPLL and the limited readout frequency, the phase reconstructed from the PIR is affected by quantization noise.

ADC - DIGITIZATION NOISE The quantization noise due to digitization is given by (see Section 2.2.3):

$$\tilde{n}_{\text{dig}} = \frac{U_{\text{max}} 2^{-B}}{\sqrt{6} \cdot f_{\text{Sampl}}}. \quad (4.30)$$

U_{max} is the dynamic range, B is the effective resolution and f_{Sampl} the sampling rate of the ADC. Since the sampling rate is 80 MHz and the ADC resolution is 8 bit, this leads to a phase noise expressed as linear spectral density (LSD):

$$\tilde{\varphi}_{\text{dig}} \approx \frac{2^{-B}}{\sqrt{6} \cdot f_{\text{Sampl}}} = 1.78 \cdot 10^{-7} \frac{\text{rad}}{\sqrt{\text{Hz}}}. \quad (4.31)$$

PIR- READOUT NOISE The second limiting factor is the quantization of the readout method itself. Since the readout quantity is a frequency (PIR readout), its quantization noise, which is given by the frequency resolution of the DDS, converts into a phase noise $\tilde{\varphi}_{\text{DDS}}$ by integration. In the frequency domain this means a frequency f converts into phase by dividing by the Fourier frequency (not Fourier variable $\omega = 2\pi f_{\text{Fourier}}$). This becomes clear considering that $\varphi = \int dt \omega = \int dt 2\pi f$ - in the time domain. In the frequency domain a time integration converts into a division by the Fourier variable $\omega = 2\pi f_{\text{Fourier}}$ and thus:

$$\varphi = \frac{2\pi f}{\omega} = \frac{f}{f_{\text{Fourier}}}. \quad (4.32)$$

Assuming a frequency resolution Δf of the DDS which is given by the system clock = sampling rate= f_S and the length of the PIR (see Equation (4.19)). The quantization noise of Δf is given by:

$$\tilde{\delta f}_{\text{rms}} = \frac{1}{\sqrt{2}} \frac{\Delta f}{\sqrt{6} \cdot f_S}. \quad (4.33)$$

Since the readout frequency of the [PIR](#) is limited to a readout frequency f_R (38 Hz in case of the prototype board), the effective frequency readout noise $\tilde{\delta}f_{R,rms}$ leads to the same value (if an appropriate low pass filter is used):

$$\tilde{\delta}f_{R,rms} = \frac{1}{\sqrt{2}} \frac{\Delta f}{\sqrt{6 \cdot f_S}}. \quad (4.34)$$

Converting this frequency noise $\tilde{\delta}f_{R,rms}$ into readout phase noise $\tilde{\delta}\varphi_{R,rms}$ (in rad/ $\sqrt{\text{Hz}}$), it yields:

$$\tilde{\delta}\varphi_{R,rms} = \frac{\tilde{\delta}f_{R,rms}}{f} \quad (4.35)$$

The overall readout phase noise of the phasemeter is given by:

$$\tilde{\delta}\varphi = \sqrt{\tilde{\delta}\varphi_{R,rms}^2 + \varphi_{\text{dig}}^2} \quad (4.36)$$

An important result of this analysis is the fact that a [PIR](#) length of at least 40 bit is necessary (if only the [ADPLL](#) readout is used), in order to meet the [LISA](#) phasemeter noise budget of $2\pi \cdot 10^{-6}$ rad/ $\sqrt{\text{Hz}}$. This requirement can possibly be relaxed if the residual phase estimation by means of the I- and Q-mixer outputs is used.

4.3 RESULTS

All subcomponents of the phasemeter prototype were tested extensively:

- The [ADC](#) and digital to analog converter ([DAC](#)) interface was tested by applying an external signal to the [ADC](#) with following reconversion to an analog signal provided by the [DAC](#). The lower limit of the input signal of the [ADC](#) is determined by the transformer in the [ADC](#) input stage and is of the order of 1 kHz. Both- [ADC](#) and [DAC](#) - are able to work at clock frequencies up to around 80 MHz.
- The behavior of the [DDS](#) was tested by applying a defined value to the phase increment register while the output of the [DDS](#) was connected to a [DAC](#) of the prototype board. By monitoring the signal on an oscilloscope, the functionality of the [DDS](#) was verified. The system works as expected. The dynamic range of the system is $7.3 \cdot 10^{-5} \text{ Hz} \dots 20 \text{ MHz}$ tunable in steps of $7.3 \cdot 10^{-5} \text{ Hz}$. The minimal frequency respectively the tuning resolution is given by the length of the [PIR](#). The upper limit is given by the Nyquist bandwidth determined by the system clock of 80 MHz, i.e. 40 MHz but in reality only 20 MHz.
- The functionality of the [ADPLL](#) was verified. Therefore, an additional [DDS](#) was implemented on the [FPGA](#). This [DDS](#) was operated at a fixed frequency and was used as reference signal for the [ADPLL](#) that locks its own tunable [DDS](#) to the input signal. The outputs of both [DDS](#) were monitored with an oscilloscope. For this test, the lock behavior of the [ADPLL](#) was observed and the gain parameters for the controller were optimized.
- The test of the [FIFO](#) readout was combined with a test of the onboard random access memory ([RAM](#)). For this test, a bit sequence generated on the readout PC was written via the EPP interface to different addresses of the [RAM](#) on the board and was read back.

Since all subcomponents work as expected, several overall test of the phasemeter prototype including performance tests were performed.

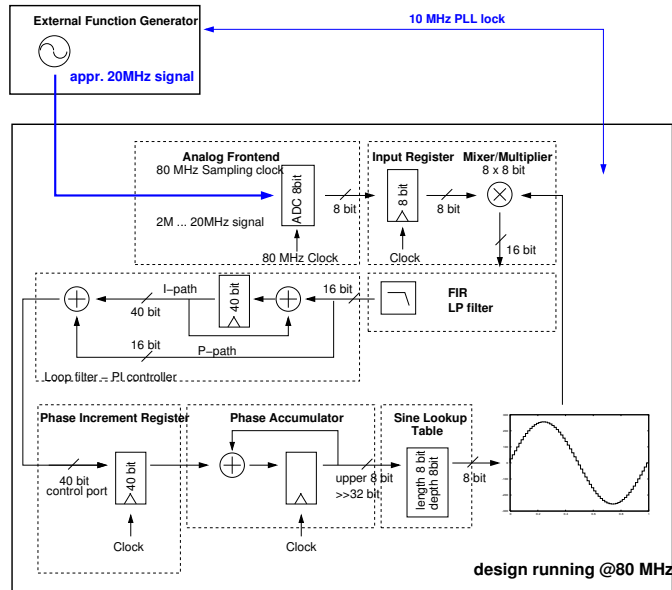


Figure 90. ADPLL test setup. An external function generator is phase locked by its internal PLL to the phasemeter clock. A 20 MHz signal from the generator is applied to the phasemeter.

4.3.1 Lock acquisition

Figure 90 illustrates the setup. An external signal generator was phase locked via its own internal 10 MHz PLL to the system clock of the phasemeter. The output of the generator was set to 19.999 MHz which was connected to the ADC of the phasemeter. The internal DDS frequency was initially detuned by a few hundred Hz. The acceptable detuning range of the DDS is determined by the *lock in range* of the ADPLL, which depends on the phase detector and the gain of the system. Figure 91 shows the lock in process of the PLL.

In any case, for a multiplier the *lock in range* is limited. For this reason, an additional phase detector was implemented in the design, in order to complement the multiplier. This additional phasemeter is a so called *phase-frequency detector*, consisting of two FlipFlops and a NAND gate. Due to the characteristics of this detector, its output can be used to lock the ADPLL independently from the detuning of the reference signal. On the other hand, a

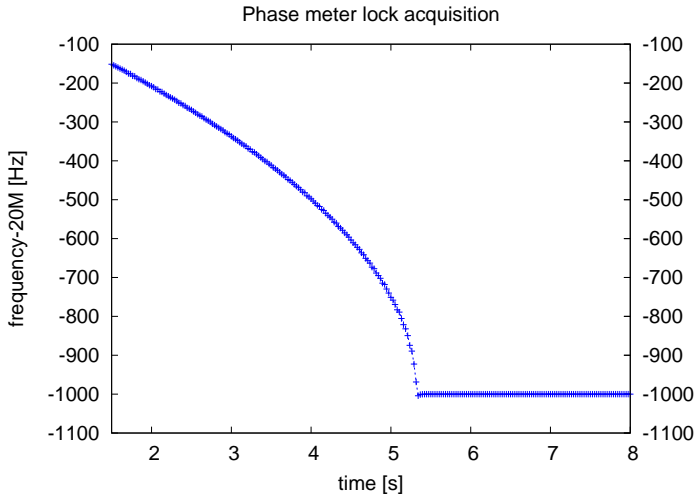


Figure 91. Measurement of lock acquisition of the ADPLL. A 20 MHz signal from the generator is applied to the phasemeter. The frequency offset between the internal DDS and the generator is a few hundred Hz (limited by the lock in range of the ADPLL).

phase-frequency detector provides a lower sensitivity to phase variations¹ such that it should be *switched off*, if the frequencies are locked and then a multiplier is used as phase detectors instead. However, both phasedetectors were tested and work properly.

4.3.2 Phasemeter calibration

In order to verify the frequency/phase reconstruction on the PC side, two calibration tests were performed. For a first test, a sequence of frequency steps was applied to the reference signal from the external function generator (see Figure 90), while the ADPLL was locked. Figure 92 shows the result of this test, where a 100 mHz step is followed by a 10 mHz step. A last 1 mHz step is disturbed by the intrinsic readout noise.

Since the phasemeter readout is a frequency (either directly from the PIR or as PA difference), the raw phase needs to be reconstructed. In order to verify the frequency to phase conversion on the readout side (in particular a factor

¹ The principle of operation of this phase detector the comparable with an zero crossing phasemeter, that counts clock cycles between e.g. positive zerocrossings of the signals.

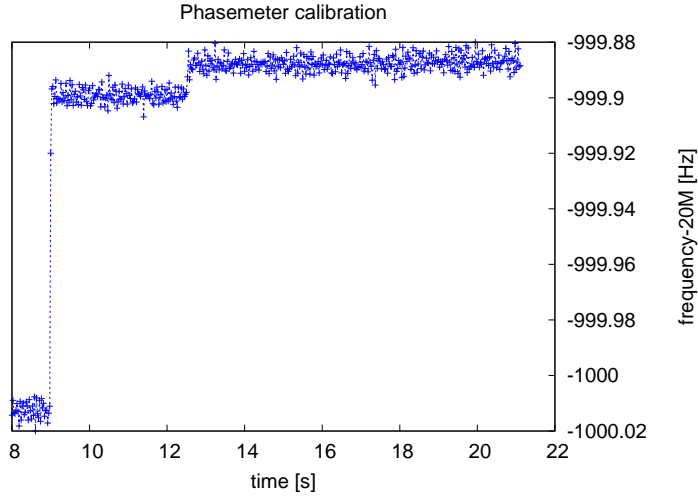


Figure 92. Frequency steps on phasemeter input. A sequence of frequency steps is applied to the phasemeter input frequency. The graph shows the readout result for a 100, 10 and 1 mHz step. The last 1 mHz step vanishes in the readout noise.

of 2π), a frequency modulation was applied to the 19.999 MHz reference oscillator. The modulation rate was $f_{\text{mod}} = 200$ mHz and the modulation depth $\Delta f = 12.5$ Hz. This corresponds to a phase modulation of :

$$\varphi_{\text{mod}} = \int dt \Delta f \cos(2\pi f_{\text{mod}} t) \quad (4.37)$$

$$= \frac{\Delta f}{2\pi f_{\text{mod}}} \sin(2\pi f_{\text{mod}} t) \text{ [cycles]} \quad (4.38)$$

$$= \frac{\Delta f}{f_{\text{mod}}} \sin(2\pi f_{\text{mod}} t) \text{ [rad]} \quad (4.39)$$

$$= 62.5 \sin(2\pi f_{\text{mod}} t) \text{ [rad]} \quad (4.40)$$

Figure 93 shows on the left vertical axis the measured frequency modulation and the corresponding phase modulation on the right vertical axis reconstructed from PIR.

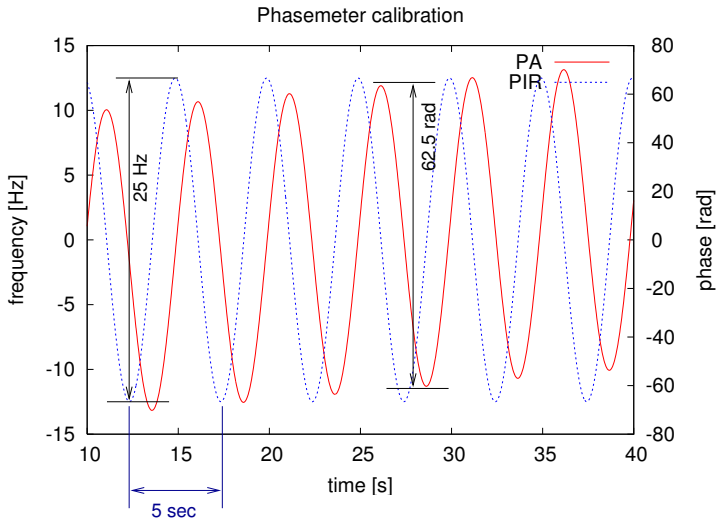


Figure 93. Verification of PM frequency to phase conversion. A phase modulation was applied to the phasemeter input signal. The phase modulation is recovered from the PIR readout.

4.3.3 Performance

A measurement of the (noise-) performance of the phasemeter is nontrivial, since a reference signal is needed the phase of which provides a proper¹ phase stability with respect to the phasemeter clock. For a first test, the configuration from above was used, where an external function generator is locked to the phasemeter clock. A 20 MHz signal from the generator was applied to the phasemeter via the ADC frontend of the PMS prototype. The result of the phase readout of the test can be seen in Figure 94.

The noise level is dominated by the quality of the internal 10 MHz PLL of the function generator. This could be shown by using different types of signal generators with different PLL behaviors. The measurement in Figure 94 shows a phase measurement with a generator providing the most stable² 10 MHz PLL. For the following prototype³ models, at least two phasemeter channels are planned to be implemented. A two channel PMS is capable of measuring the phases of two identical input signals, such that in the differ-

¹ in the order of the required phasemeter accuracy

² compared to other generators that were tested

³ The prototype described here was planned as testing platform for following models.

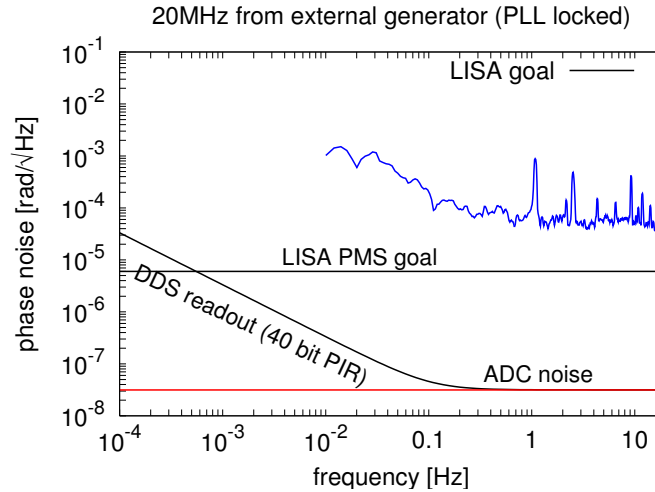


Figure 94. Measurement of the phase noise of an external 20 MHz signal. An external generated signal at 20 MHz is applied to the phasemeter. The phase noise was measured and is plotted as linear spectral density in this graph. The noise level is determined by the quality of the external lock provided by the PLL of the generator (see Figure 91).

ence of both, the pure phasemeter noise ¹ remains.

In order to test the performance of the implementation, a second independent DDS system synthesizes a signal of constant frequency at 20 MHz (instead of the external generator). This DDS was implemented on the same FPGA as the phasemeter itself. Both systems start with 5 kHz frequency offset with respect to each other². After the phasemeter locks in, at approximately 20 MHz input signal, the phase noise was measured. The aim of this test is to verify the expected performance of the ADPLL. The results can be seen in Figure 95. The readout noise behaves as expected (see caption of Figure 95).

¹ $1/\sqrt{2}$ times the measured noise for one channel if the noise in both channel can be assumed to be identically

² An offset is necessary in order to avoid an initial state where the PLL is already locked. With an initial frequency offset the servo in this *hardware simulation* acts actively.

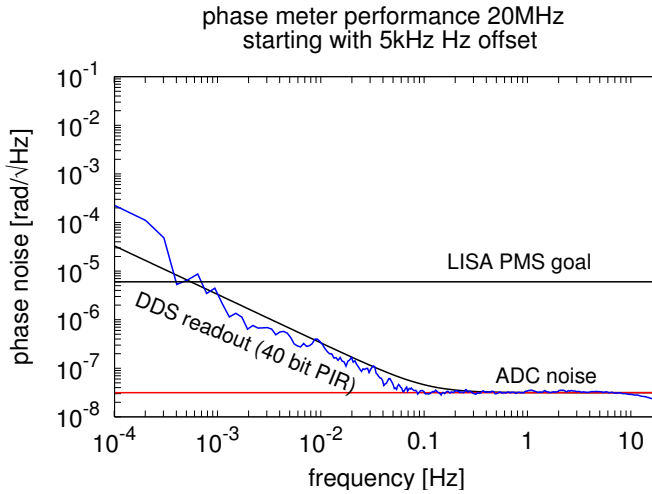


Figure 95. Performance of the PMS with an internally generated 20 MHz reference signal representing the heterodyne signal. The noise floor at high frequencies is dominated by the digitization noise induced by the 8-bit sine look-up table used by the DDS in order to generate the test signal. The increasing noise with $1/f$ characteristics is determined by the quantization of the readout.

4.4 CONCLUSION

A hardware prototype phasemeter board based on a commercial FPGA was developed, implemented and tested. After the hardware development, a very high speed hardware description language (VHDL) implementation of an all digital phase locked loop (ADPLL) was developed and tested on the phasemeter hardware. Thus, the core functionality of the phasemeter could be realized. The phase noise performance was measured and is in agreement with the expectations. For an ideal test, the setup meets the requirement of $2\pi \times 10^{-6}$ rad/ $\sqrt{\text{Hz}}$ allocated for the phase readout. A test with more realistic signals was performed and showed that the system was limited by the test setup. However, the development process is still at the beginning.

5

ADVANCED LINK CAPABILITIES

*“Wer will, dass ihm andere sagen, was sie wissen,
der muss ihnen sagen, was er selbst weiß.
Das beste Mittel, Informationen zu erhalten,
ist, Informationen zu geben.”*

NICCOLÓ MACHIAVELLI
(1469-1527) italienischer Schriftsteller,
Philosoph, Dichter und Staatsmann

This chapter gives an overview on a set of features needed for LISA which are closely related to each other and which are provided by the PMS of LISA.

Once the three LISA spacecraft have arrived at their nominal orbits, the laser links between the spacecraft will have to be established.

Before and during this initial acquisition and commissioning phase, the position and attitude of the individual spacecraft can only be estimated by the means of ground station ranging using the deep space network (DSN) via RF (X¹-, K²-band) communication and information from the star trackers of the spacecraft. Information from both methods will be used to perform a raw position and attitude alignment of the spacecraft.

Once the full acquisition of the constellation will have been achieved, meaning that all three bidirectional laser links have been established, the links can also provide additional functionality to the constellation in addition to their main scientific purpose - to measure the carrier phases between the optical benches.

Section 5.1 gives an overview of these *advanced link capabilities*. First the motivation for these additional tasks, which comes from the laser frequency noise requirement, is discussed (Section 5.1.1). Time delay interferometry (TDI) is explained as one of three methods for the frequency stabilization (Section 5.1.2). It requires two quantities to be measured:

¹ X-band: 7-12.5 GHz

² K_u-band: 12-18 GHz

The first important issue is the long term stability of the local ultra stable oscillator (USO) clocks onboard each spacecraft. In order to achieve the necessary interferometry performance the differential clock noise between the spacecraft needs to be measured.

The second quantity which needs to be measured is the absolute distance between each pair of spacecraft. In addition to coarse ranging with DSN, the laser link can be used to perform inter spacecraft ranging based on correlation of Pseudo Random sequences, similar to global positioning system (GPS).

A proposed modulation scheme designed to enable these two tasks is presented and discussed in Section 5.1.3.

In Section 5.2 an experimental demonstration of laser ranging is presented. Section 5.2.1 describes an implementation of the laser ranging technique in more detail. A modulator, developed during this work in order to provide this modulation, is discussed (Section 5.2.2) which was tested within an optical setup very similar to the planned LISA implementation (Section 5.2.3 and 5.2.4). The Chapter concludes with the presentation of the results of this ranging experiment (Section 5.2.5 and 5.2.6).

5.1 CLOCK SYNCHRONIZATION, RANGING AND DATA TRANSFER

5.1.1 Requirement for the laser's frequency stability

Laser frequency noise was identified as one major noise source of the LISA design which affects the main science phase measurement due to the armlength difference of the interferometer. Due to the orbital dynamics of the individual spacecraft their nominal distances of 5 million kilometers change during a year by about $\pm 1\%$. This means for the interferometry that an armlength difference of 50000 km need to be handled. Laser frequency fluctuations δf couple via an armlength difference ΔL into phase fluctuations:

$$\frac{\delta\varphi}{\delta f} = \frac{2\pi\Delta L}{c}. \quad (5.1)$$

In order to succeed in achieving the allocated phase noise budget, $\Delta\varphi = 6.9 \cdot 10^{-6}$ rad/ $\sqrt{\text{Hz}}$ (derived from the 40 pm/ $\sqrt{\text{Hz}}$ shot noise limitation plus margin), the required frequency stability is given by:

$$\begin{aligned} \delta f &= \frac{c}{2\pi\Delta L} \Delta\varphi = \frac{3 \cdot 10^8 \text{ m/s}}{2\pi \cdot 5 \cdot 10^7 \text{ m}} \cdot 6.9 \cdot 10^{-6} \text{ rad}/\sqrt{\text{Hz}} \\ &= 6.59 \cdot 10^{-6} \text{ Hz}/\sqrt{\text{Hz}} \end{aligned} \quad (5.2)$$

Taking the free running laser frequency noise which was estimated as $10 \text{ kHz}/f/\sqrt{\text{Hz}}$ into account, the noise suppression needs to be up to 10^{-13}

or 120 dB. Fulfilling this requirement is a challenging task. Currently, three individual steps are foreseen to remove the laser frequency noise:

1. Active pre-stabilization of the laser by the use of a tunable¹ Zerodur/ULE cavity or a molecular frequency standard such as iodine (TRÖBS *et al.* (2006), LEONHARDT and CAMP (2006)). Several experiments showed that a frequency stability of $30 \text{ Hz}/\sqrt{\text{Hz}}$ can be achieved with a Pound-Drever-Hall (PDH) control scheme using such a reference, although tuneability still needs to be shown.
2. Since the test mass-test mass distance is the most stable reference within the LISA constellation, this optical armlength can be used as an additional frequency standard. A technique called *arm locking* was developed and experimentally demonstrated. *Arm locking* compares the instantaneous oscillator phase noise of the local beatnote with its own copy that is delayed by one round-trip time ($\approx 33 \text{ s}$) and uses the difference to control the laser frequency. The main challenge of arm locking is the required unconventional design of a controller that achieves sufficient gain (120 dB in an optimal case) at 1 mHz while the first zero due to the delay of 33 s is at 30 mHz (GARCÍA MARIN *et al.* (2005), SHEARD (2003), SHEARD *et al.* (2005), THORPE and MÜLLER (2005)).
3. A technique called time delay interferometry (TDI) was developed which is a data post-processing approach to remove remaining frequency noise from the data transferred to ground (TINTO *et al.*, 2002).

5.1.2 Time delay interferometry

TDI is a technique that removes the remaining laser frequency noise on ground from the measured phases by calculating linear combinations of the 6 datastreams. TDI in its simplest form (configuration) can be understood in the Michelson mode of LISA, when spacecraft 1 (S/C1) is acting as a beam splitter. Its two local lasers (LO11 and LO12) will be brought to interfere while the beat signal is locked to a 20 MHz reference clock by controlling laser LO12. The phase φ_1 of this beatnote serves as reference for the other phase measurements². The beams of both lasers will be transmitted to the far spacecraft S/C2 and S/C3. Their corresponding lasers (LO21 and LO32) are configured as transponders such that they act as *frequency shifting mirrors*. This can be achieved by PLL, which lock the far lasers with an offset of 20 MHz to the received beam and send these beams back to S/C1. The "reflected" beams will

¹ In order to make a cavity tunable, one mirror of a linear cavity can be mounted on a PZT.

² Similar to the split interferometry concept of LISA Pathfinder, this phase contains all environmental noise onboard the spacecraft that will cancel in the phase differences.

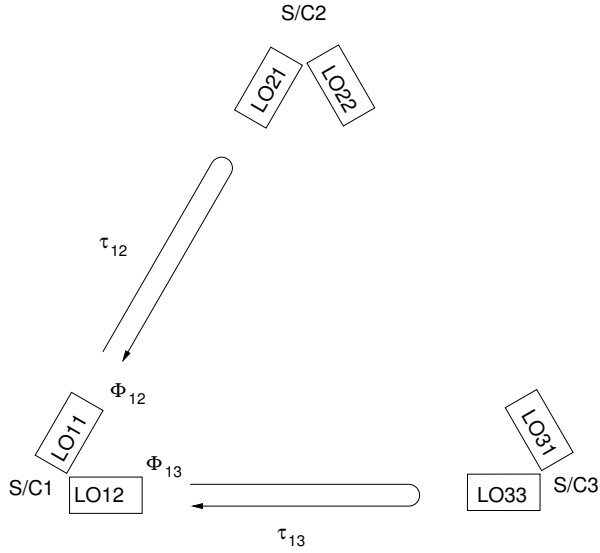


Figure 96. Illustration of TDI.

be brought to interfere with the local laser (LO11 and LO12)¹. These primary phases φ_{12} and φ_{13} of the beatnotes are measured and referred to the reference phase φ_1 . The round trip phases φ_{12} and φ_{13} contain the gravitational wave signals h as additional phase shifts $\pm\Phi_{\text{GW}}(t)$ (see Figure 96). Thus the main observables will be formed as follows:

$$\Phi_{12}(t) = \varphi_1(t) - \varphi_{12}(t) \quad (5.3)$$

$$\Phi_{13}(t) = \varphi_1(t) - \varphi_{13}(t). \quad (5.4)$$

Since the round trip phases $\varphi_{12}(t)$ and $\varphi_{13}(t)$ are copies of $\varphi_1(t)$ delayed by their round trip times, τ_{12} and τ_{13} , Equation (5.3) and (5.4) can be written as:

$$\Phi_{12}(t) = \varphi_1(t) - \varphi_1(t - \tau_{12}) + \Phi_{\text{GW}}(t) \quad (5.5)$$

$$\Phi_{13}(t) = \varphi_1(t) - \varphi_1(t - \tau_{13}) - \Phi_{\text{GW}}(t). \quad (5.6)$$

In the Fourier domain a delay τ transforms to $e^{-i\omega\tau}$ where ω is the Fourier

¹ This describes the baseline concept. In order to prevent stray light effect, in the backlink concept the received beams are interfered respectively with the laser of the other bench.

frequency:

$$\Phi_{12}(f) = \varphi_1(f) \cdot \left(1 - e^{-i\omega \tau_{12}}\right) + \Phi_{GW}(f) \quad (5.7)$$

$$\Phi_{13}(f) = \varphi_1(f) \cdot \left(1 - e^{-i\omega \tau_{13}}\right) - \Phi_{GW}(f). \quad (5.8)$$

Remark 1: The delays τ_{12} and τ_{13} are intentionally measured by the differences (5.3) and (5.4) but are only known modulo of 2π .

Remark 2: In order to simplify the following calculations which are intended to demonstrate the basic principle of TDI, the gravitational wave signal Φ_{GW} will be neglected. Detailed analysis (TINTO and ARMSTRONG (1999), TINTO et al. (2002), TINTO et al. (2003)) also reveals the transferfunction for Φ_{GW} .

Since unequal interferometer arms - represented by $\tau_{12} \neq \tau_{13}$ - induce the coupling of laser frequency noise into the phase readout of the interferometer, TDI simulates an equal arm interferometer. Therefore the measured round trip phase $\Phi_{12}(t)$ will be sent (numerically) along the second arm (S/C1-S/C3). This can be done by delaying $\Phi_{12}(t)$ with τ_{13} if the exact delay is known (SHEARD):

$$X1(t) = \Phi_{12}(t) \quad -\Phi_{12}(t - \tau_{13}) \quad (5.9)$$

$$= \underbrace{\varphi_1(t) - \varphi_1(t - \tau_{12})}_{\text{directly measured}} \quad - \underbrace{\varphi_1(t - \tau_{13}) - \varphi_1(t - \tau_{12} - \tau_{13})}_{\text{simulated}} \quad (5.10)$$

or in the Fourier representation:

$$X1(f) = \underbrace{\Phi_{12}(f)}_{\text{directly measured}} \cdot \underbrace{\left(1 - e^{-i\omega \tau_{13}}\right)}_{\text{simulated}} \quad (5.11)$$

$$= \underbrace{\varphi_1(f) \cdot \left(1 - e^{-i\omega \tau_{12}}\right)}_{\text{directly measured}} \cdot \underbrace{\left(1 - e^{-i\omega \tau_{13}}\right)}_{\text{simulated}} \quad (5.12)$$

τ_{13} represents the delay to be estimated. This means that the measured phase $\Phi_{12}(t)$ is sent along the other arm. The difference $X1$ of the measured phase $\Phi_{12}(t)$ and the delayed phase $\Phi_{12}(t - \tau_{13})$ can synthesize the length of the first interferometer arm as $\Delta L = L_1 - L_2$.

The same procedure is applied to $\Phi_{13}(t)$ which will be delayed by the round trip time τ_{12} to be estimated. Thus the length of the second arm is represented by $X2$:

$$X2(t) = \Phi_{13}(t) \quad -\Phi_{13}(t - \tau_{12}) \quad (5.13)$$

$$= \underbrace{\varphi_1(t) - \varphi_1(t - \tau_{13})}_{\text{directly measured}} \quad - \underbrace{\varphi_1(t - \tau_{12}) - \varphi_1(t - \tau_{12} - \tau_{13})}_{\text{simulated}} \quad (5.14)$$

The difference X_2 of the measured phase $\Phi_{13}(t)$ and the delayed phase $\Phi_{13}(t - \tau_{12})$ can be used to synthesize the length of the second interferometer arm as $\Delta L = L_1 - L_2$, too. The main **TDI** observable is obtained as follows:

$$X(t) = X_1(t) - X_2(t) \tag{5.15}$$

$$= [\Phi_{12}(t) - \Phi_{12}(t - \tau_{13})] - [\Phi_{13}(t) - \Phi_{13}(t - \tau_{12})]. \tag{5.16}$$

Thus **TDI** makes **LISA** work as an equal arm interferometer by using the knowledge of the absolute delays. Since the delays are not constant due to the varying armlength, in reality **TDI** is much more complex (**SHADDOCK (2003)**). In this context the main requirement coming from **TDI** is the precise knowledge of the delays τ .

RANGING The laser frequency noise cancellation due to **TDI** depends on the initial laser frequency noise and on the knowledge about τ . For the **PDH** pre-stabilized laser an estimation of τ corresponding to an absolute armlength measurement of 16 m (10^{-9} absolute armlength knowledge) is sufficient for the **TDI** post-processing (**TINTO et al. (2003)**)¹. An additional active laser stabilization due to *arm locking* implies a relaxed requirement for the armlength knowledge. However, τ is needed to be measured with a precision in the order of 50 ns.

CLOCK TRANSFER Since each spacecraft provides its own **USO** as local time base (the timing data are measured in terms of **USO** clock cycles) which are affected by offsets, short term phase noise and long term drift against each other, the time series of the individual primary phase measurements need to be synchronized. Therefore time stamps will be added to the data streams with the same accuracy as the delay measurement above (50 ns). By measuring the **USO** noise these time stamps can be synchronized, either actively in real-time by feedback to the **USOs**, or virtually in post-processing on ground.

Thus **TDI** generates two additional requirements to the constellation:

1. Transfer of the local **USO** phase noise to the other spacecraft for comparison.
2. Measurement of the light travel time between the spacecraft.

5.1.3 Modulation scheme

In order to achieve the additional **TDI** driven requirements, one approach is to use the existing coherent inter-spacecraft laser links. The information about

¹ For **LISA** the **DSN** can provide an accuracy of approximately 30 km for the spacecraft positions.

the clock noise and ranging need to be modulated onto the carrier¹. Figure 97 shows the proposed modulation scheme. The phase of the USO can be transferred to a remote spacecraft by modulating its phase (up-scaled to approximately 2 GHz) directly onto the carrier such that upper and lower frequency sidebands appear in the spectrum separated by the modulation frequency. Figure 97 only shows the first order sidebands. This signal is transmitted to the remote spacecraft. The local carrier is phase locked with a 20 MHz offset to the incoming carrier and has its local USO phase noise modulated in its sidebands. The carrier-carrier beatnote contains the main scientific information while the phases of sideband-sideband beats provide the differential USO phase noise. In principle the ranging could be applied in the same way. But this would cause additional sidebands and a large set of spurious beat notes. Thus the ranging is planned to be implemented as spread spectrum modulation that does not harm the phase measurement with spurious beat notes. Since additional modulations on the light decrease the remaining light power of the science carrier, the fractions that can be used for clock noise transfer and ranging are limited. The current baseline allocates 10% of the carrier power² for the clock transfer and 1% for the ranging.

Clock noise transfer

The limited light power for the clock sidebands implies a much lower SNR (due to shot noise limitation of the measurement). In order to achieve the required phase accuracy for the clock noise transfer, the initial frequency of the USO, which is in the order of 10 MHz, and consequently its phase noise need to be scaled. For this reason the clocks are multiplied to higher frequencies (1-2 GHz) increasing the phase noise of the original frequency (HELLINGS (2001), KLIPSTEIN *et al.* (2006)). At the receiver, the PDs are a limiting factor since current PDs are not able to reach high bandwidths whilst maintaining the required noise performance. By demodulating the sideband with the sideband of a 20 MHz frequency shifted copy of the spectrum the sideband-sideband beat is shifted to a frequency that can be measured by photodiodes with sufficient low noise. Since the scaled oscillator phase noise remains, the frequency multiplication increases the signal to shot noise ratio for the phase measurement of the sidebands.

Nevertheless, this concept contains significant technical challenges, and the demonstration of the feasibility of the clock noise transfer scheme is topic of current research at the AEI:

- ¹ To establish a RF link between the spacecraft requires additional power and causes additional heat dissipation.
- ² The 10 % of the carrier power are distributed mainly into both first-order sideband.

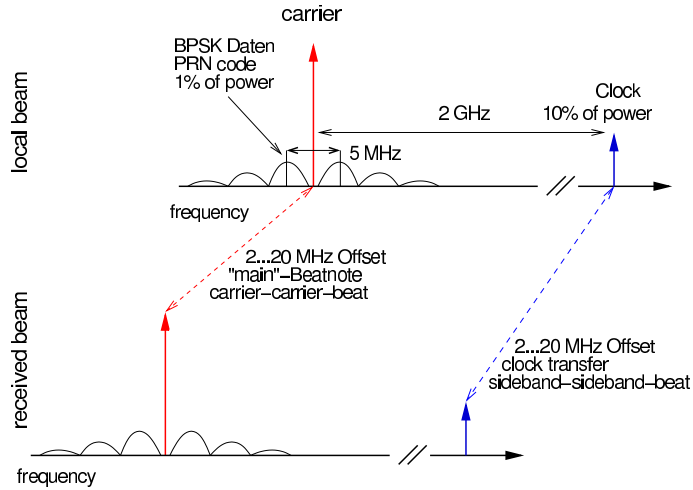


Figure 97. Proposed frequency scheme for LISA. Besides the main science carrier the first-order FM sidebands contain the information of the USO noise of the independent spacecraft master oscillators. For the inter-spacecraft ranging a pseudo-random noise code sequence provides the length measurement.

1. Frequency scaling to GHz with high phase reliability,
2. GHz modulation electronics such as frequency multipliers and GHz EOMs,
3. Phase stability of sidebands after additional amplification (by fiber amplifier),
4. Design of low noise photodiode preamplifiers.

Within this work the efficiency of a fiber-coupled EOM was tested for different operating frequencies.

Ranging, slow clock synchronization and data transfer

As already mentioned above, ranging could be also implemented by the use of additional sinusoidal side tones. Due to the fact that the local oscillator at the receiver already contains the outgoing modulation of that spacecraft, this would create a multitude of drifting beat notes, which would be very difficult to separate. A better way is to use spread-spectrum modulation, as used in many modern wireless communication systems as well as in GPS. A spread

spectrum can be generated by a 2-state¹ (binary phase shift keying (BPSK)) phase modulation of the carrier where the phase states follow a well-defined pseudo random noise (PRN) code sequence. In addition, the carrier amplitude can also be used to encode information. These methods are known as quadrature amplitude modulation (QAM). These modulation techniques offer a higher data transfer rate per bandwidth. In order maintain the amplitude of the carrier unaltered, and since the necessary bandwidth is available these are not considered.

One major difference between the BPSK scheme planned to be applied for LISA and the standard BPSK known from telecommunication applications is the modulation index. In order to provide the best SNR, the standard BPSK applies a phase shift of $\pm\pi/2$ to the carrier. An implemented example of this technique is shown in Section 5.2.2. A phase shift of $\pm\pi/2$ suppresses the carrier completely, and an additional control loop (Costas-Loop) is necessary to recover the carrier phase that in LISA provides the main measurement. Since the LISA PMS is very sensitive to phase fluctuations, a smaller ($m=0.1$, see Section 5.2.1) phase modulation is sufficient and can be detected.

RANGING The basic idea of the spread spectrum ranging is to transmit a PRN (pseudo random noise) sequence (see Section 5.2.2) from one spacecraft to the other, where the reconstructed sequence of the code will be correlated with a local replica (i.e. with the same code sequence). Since PRN sufficiently fulfills the requirement to look like uncorrelated white noise, the (auto-) correlation function is approximately a delta peak - occurring at zero delay time between the code and its replica. From the measurement of the actual delay, the distance between the spacecraft can be derived.

The effect of the PRN modulation applied as phase modulation to the carrier is to symmetrically spread the spectrum into a wide band around the carrier (see Section 5.2.2). The remaining power in the carrier depends on the modulation index. By choosing an appropriate modulation index and modulation frequency, it is possible to spread the power of the modulation such that the spread spectrum is comparable with white noise with a power per frequency which is far below the detection limit - meaning the shot noise level for the optical link. Only by correlation of this spectrum with a replica of itself the code sequence can be reconstructed.

In order to estimate the delay time of the PRN code accumulated along the 5 million kilometers, a delay-locked loop continually adjusts the delay of the local demodulation code such that the maximum of the correlation peak is tracked. For this purpose, two more replicas of the code are generated in the receiver, with positive and negative shifts of typically $1/2$ bit length. The

¹ more than two phase states can be defined (n-phase shift keying (PSK)). In telecom application a 4-state phase modulation (quadrature phase shift keying (QPSK)) is very common.

difference of their correlations with the incoming signal provides an error signal for a closed loop control system.

5.2 FIRST EXPERIMENTAL STEPS TOWARDS ADVANCED LINK CAPABILITIES

5.2.1 Spectrum of a PSK modulated signal

In order to quantify the modulation depth needed to spread 1 % of the carrier power into the code spectrum, the power spectrum of the modulated carrier is required.

SPECTRUM OF THE PRN CODE In order to describe its spectrum a bipolar PRN code sequence is assumed here. The code sequence $s_{\text{Code}}[n]$ can be expressed as a series of θ -functions (box-functions) and can be written as:

$$s_{\text{Code}}(t) = \sum_{-\infty}^{\infty} s_{\text{Code}}[n] p(t - nT) \quad \text{with} \quad s_{\text{Code}}[n] = \pm 1. \quad (5.17)$$

In this notation the code sequence is combined as a sum of individual pulses

$$p(t) = \begin{cases} m & 0 \leq t \leq T \\ 0 & \text{else} \end{cases} \quad (5.18)$$

with a duration T which is the inverse of the clock frequency f_{clock} of the code and an amplitude m . The Fourier transformed box function is a sinc-function such that the power spectrum of a single pulse $(0, m, 0)$ can be calculated as:

$$\begin{aligned} P(f) &= \int_{-\infty}^{\infty} dt e^{-i\omega t} p(t - nT) \\ &= e^{-inT} \cdot \int_{-\infty}^{\infty} dt e^{-i\omega t} p(t) \\ &= e^{-inT} \cdot m T \frac{\sin(\pi f T)}{\pi f T} \end{aligned} \quad (5.19)$$

with $\omega = 2\pi f$ and the modulation index m . The power spectral density

$$|S(f)|^2 = \frac{|P(f)|^2}{T} \quad (5.20)$$

for the full sequence is (COUCH II (1997))

$$|S(f)|^2 = m^2 T \left(\frac{\sin(\pi T f)}{\pi T f} \right)^2 \quad (5.21)$$

or written with the code clock f_{clock} :

$$|S(f)|^2 = \frac{m^2}{f_{\text{clock}}} \left(\frac{\sin(\pi \frac{f}{f_{\text{clock}}})}{\pi \frac{f}{f_{\text{clock}}}} \right)^2 \quad (5.22)$$

SPECTRUM OF THE SIGNALS WITH PRN-MODULATED PHASE This paragraph discusses the power spectrum of a signal with PRN-modulated phase. For the standard BPSK the phase of the carrier is shifted by $\pm\pi/2$. This BPSK signal can be written as a sinusoidal signal with the constant amplitude A with a phase modulation $\varphi(t)$:

$$f_{\text{mod}}(t) = A \sin(2\pi f_0 t + \varphi(t)) \quad (5.23)$$

with

$$\varphi(t) = \sum_{-\infty}^{\infty} s_{\text{Code}}[n] p(t - nT) = m s_{\text{Code}}(t) \quad (5.24)$$

$p(t)$ is here again a rectangular pulse with an amplitude $m = \pi/2$, of the duration T and $s_{\text{Code}}[n]$ is the code sequence. Due to the fact that a phase shift of effectively π inverts the sinusoidal signal the phase modulation can be expressed as an amplitude modulation:

$$f_{\text{mod}}(t) = s_{\text{Code}}(t) \cos(2\pi f_0 t). \quad (5.25)$$

with

$$s_{\text{Code}}(t) = \sum_{-\infty}^{\infty} s_{\text{Code}}[n] p(t - nT). \quad (5.26)$$

In this form $f_{\text{mod}}(t)$ is a product of two functions. The spectrum of $s_{\text{Code}}(t)$ is known from the last paragraph. Since the Fourier transform of a function $w(t) \cos(2\pi f_0 t)$ is $W(f)$ shifted by¹ f_0 (Table 10 in Section A.2) the spectrum of $f_{\text{mod}}(t)$ can be found as

$$|S(f_{\text{mod}})|^2 = |S(f + f_0)|^2 \quad (5.27)$$

¹ only the right hand spectrum for $f > 0$ is taken into account

whereas $S(f)$ is the spectrum of the PRN noise sequence:

$$|S(f)|^2 = \frac{m^2}{f_{\text{clock}}} \left(\frac{\sin(\pi \frac{f}{f_{\text{clock}}})}{\pi \frac{f}{f_{\text{clock}}}} \right)^2. \quad (5.28)$$

Equation (5.28) shows that no power remains at the carrier frequency f_0 . In contrast to this standard BPSK spectra, for the LISA ranging only a fraction of the carrier is used to be spread around the carrier. This means that the modulation index m needs to be much smaller than π . Therefore the modulated carrier f_{mod} can be expressed as:

$$f_{\text{mod}}(t) = \sin(2\pi f_0 t + \varphi(t)) \quad (5.29)$$

$$= \sin(2\pi f_0 t) \cos(\varphi(t)) + \cos(2\pi f_0 t) \sin(\varphi(t)). \quad (5.30)$$

$\varphi(t)$ is a binary phase modulation with a modulation index m :

$$\varphi(t) = m s_{\text{Code}}(t), \quad (5.31)$$

where $s_{\text{Code}}(t)$ is chosen such that it takes only the values ± 1 . Since $\cos(-x) = \cos(x)$, Equation (5.30) can be rewritten in terms of $\sin(\omega_0 t) = \sin(2\pi f_0 t)$ and $\sin(\omega_0 t) = \cos(2\pi f_0 t)$ as follows:

$$f_{\text{mod}}(t) = \cos(m) \sin(\omega_0 t) + \sin(m s_{\text{Code}}(t)) \cos(\omega_0 t) \quad (5.32)$$

The first term in Equation (5.32) represents the unmodulated carrier with the effective amplitude of $\cos(m)/\sqrt{2}$. The remaining carrier power P_C is

$$P_C = \frac{\cos^2(m)}{2}. \quad (5.33)$$

The second term in Equation (5.32) represents the power in the data modulation of

$$P_m = \frac{\sin^2(m)}{2}. \quad (5.34)$$

The total power is

$$P = P_C + P_m = \frac{\cos^2(m)}{2} + \frac{\sin^2(m)}{2} = \frac{1}{2}. \quad (5.35)$$

The remaining carrier power P_C and the power of the modulation P_m can be expressed now in terms of total power P :

$$P_C = P \cdot \cos^2(m) \quad (5.36)$$

$$P_m = P \cdot \sin^2(m). \quad (5.37)$$

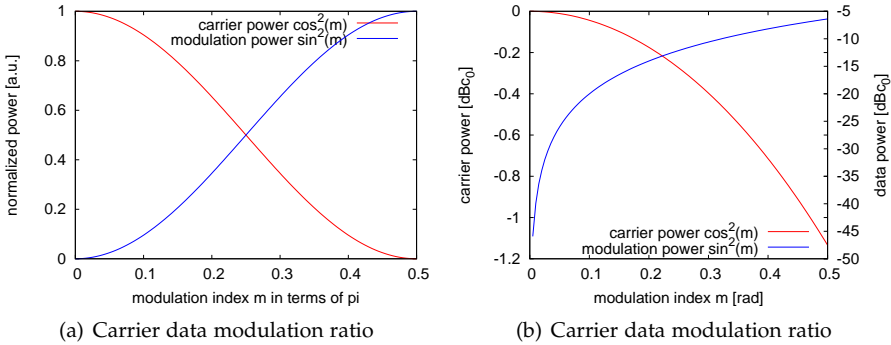


Figure 98. Carrier- and data power vs. modulation index.

Figure 98(a) shows the remaining carrier power and the power in the data modulation. The modulation index m is plotted in terms of π on the x axis. This graph shows, that for a modulation index of $\pi/2$, no power remains in the carrier.

Figure 98(b) shows the remaining carrier power (left y axis) and the power in the data modulation (right y axis). The modulation index m extends from 0 to 0.5 rad on the x axis. This graph shows, that for $m=0.1$ the data spectrum contains -20 dBc that corresponds to 1% of the total power.

5.2.2 Pseudo Random noise code generation

For a number of applications a noise source is needed. A typical application where a noise generator is needed is the analysis of the behavior of electronic systems (e.g. the estimation of their transfer function) by the use of network analyzers. Depending on the individual task, different requirements have to be fulfilled by the source. Often a near white Gaussian noise¹ is of interest but also other shapes of noise spectra are useful. In addition to requirements on the shape of the spectrum other properties such as precisely controlled noise power levels are needed. Ideal white Gaussian noise as such is a statistical process which can not be described or generated by a deterministic system e.g. an algorithm. Another statistical process to be addressed here are sequences of random numbers or - in the binary system - sequences of random bits.

Modern digital electronics offers an amazing simple approach to generate

¹ or at least band limited white noise

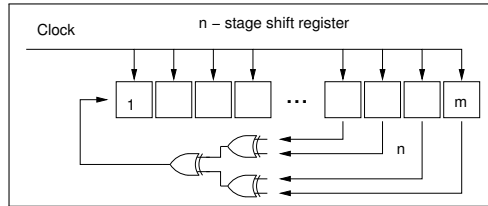


Figure 99. Typical implementation of the LFSR. A series of m registers is driven by a common clock. The input bit is generated by a cascade of XOR gates whose inputs are coming from n feedback paths. The output of the LFSR is a pseudo random bit sequence.

sequences of bits which are, due to the length of the sequence and its local indeterminacy, for all practical purposes random (HOROWITZ and HILL, 1996). These sequences are called pseudo random bit sequences or pseudo random noise and can be lowpass filtered to produce white band limited analog noise.

The standard approach to generate a PRN code is by the use of a LFSR characterized by the numbers m and n and the tap indices. Figure 99 illustrates the circuit of a LFSR. The m individual bits of the registers are implemented as Flip-Flops and will be preloaded before the generator starts. The pre-loading is necessary to ensure that the initial state of the register is not zero for all stages¹. During each clock cycle the bit state of each FlipFlop will be transferred to the next one. One or more feedback paths combined via XOR gates are connected to the input of the first FlipFlop. Such a system which consists of m stages can produce a sequence with a length of $2^m - 1$ bits at maximum if the taps are properly chosen (HOROWITZ and HILL, 1996). This maximum sequence length can only be reached for more than two feedback paths.

IMPLEMENTED EXAMPLE In order to allow a more universal usage, the LISA phasemeter prototype board was designed to provide additional features such as two DA converters which are not essential for the core phasemeter application. These DACs offer the possibility to use the board as a PRN code modulator. A VHDL program was written to make the FPGA work as a LFSR to generate a PRN code sequence. This code sequence is a typical non return to zero (NRZ) (see below) code. In order to test the VHDL implementation of the LFSR a simple low frequency example of a PRN code generator was configured and tested.

- 78 kHz carrier frequency

¹ If all FlipFlops would be zero, the whole system will stay in this state for all time.

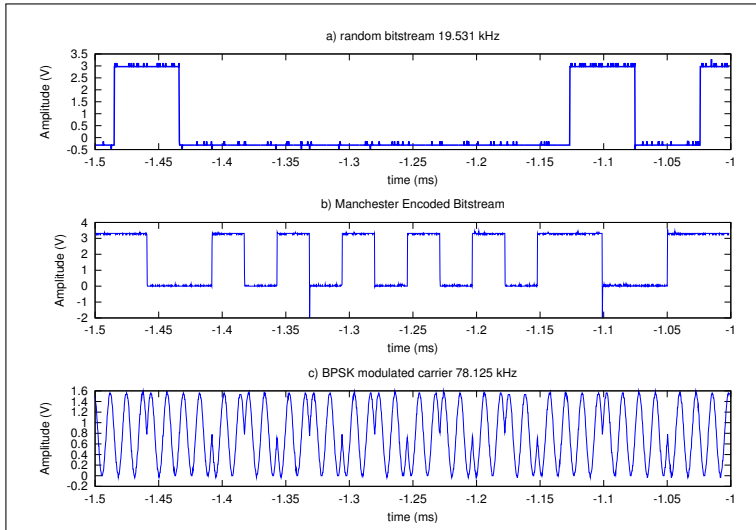


Figure 100. First test results of a VHDL implementation of PRN code generator. The upper graph (a) shows a short section of the raw output of the LFSR. This code type is a typical non return to zero code sequence. The middle graph (b) is the same code sequence as (a) but folded with the code clock. This yields to a code sequence changing its level once per each bit (Manchester code). The lower graph (c) is the Manchester code applied as a phase modulation to a sinusoidal carrier of 78 kHz with a modulation depth of 90 degree.

- Pseudo Random Noise Code - 19.5 kHz XOR Code Clock = Manchester encoded Bitstream
- PRN applied to carrier as BPSK modulation
- in contrast to LISA - full carrier suppression due to $\pm 180^\circ$ phase shift

A short segment of the results is shown in Figure 100. The upper graph labeled as (a) is the pseudo random bit sequence as direct output of the last register of the LFSR. Due to the fact that the signal power stays at the same level until the next bit change occurs this code type is called non return to zero (NRZ). Each bit is coded as *level high* or *level low*. A sequence of several 0 or several 1 states can cause problems on the decoding side as there is no code clock within the signals. This can result in a loss of lock in the decoder. For this reason the code clock can be transferred simultaneously to the bits itself. Therefore an additional XOR gate is used that combines the bit sequence from

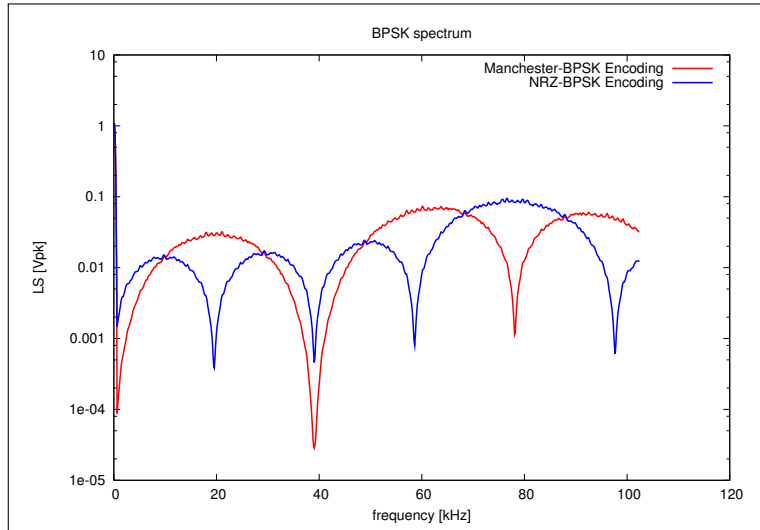


Figure 101. (blue) Spectrum of a PRN - Manchester Code (includes clock), (red) Spectrum of non-return-to zero (NRZ) PRN Codes.

the **LFSR** with the code clock. Each bit is now coded not as a simple level but as level transition (Manchester encoding): In this example a '1' is coded as high/low change and a '0' as low/high transition such that a level transition occurs at each bit and not only at a bit change (Figure 100 (b)).

In contrast to **LISA** where only 1% of the carrier power needs to be spread into the code spectrum, for demonstration and diagnostic purposes, in this example the modulation was applied in accordance to standard telecommunication applications as **BPSK** scheme - meaning the two bit states were applied as phase shift of $\pm 90^\circ$ with respect to the carrier phase. The time series of this signal is shown in Figure 100 as curve (c).

The spectrum of the time series of the **BPSK** signal shown as lower graph (c) in Figure 100 is plotted in Figure 101 as lighter curve with zeros at a distance of $2 \times n \times 19.5$ kHz from the carrier at 78 kHz which is fully suppressed.

5.2.3 The optical phase modulator

A challenging task is the implementation of the **EOM** into the laser preparation chain on each optical bench: from the design point of view there are two possible types of **EOMs**. The first one are the bulk **EOMs** which are widely used in laboratory environments. The bulk type **EOM** can be operated in a broadband

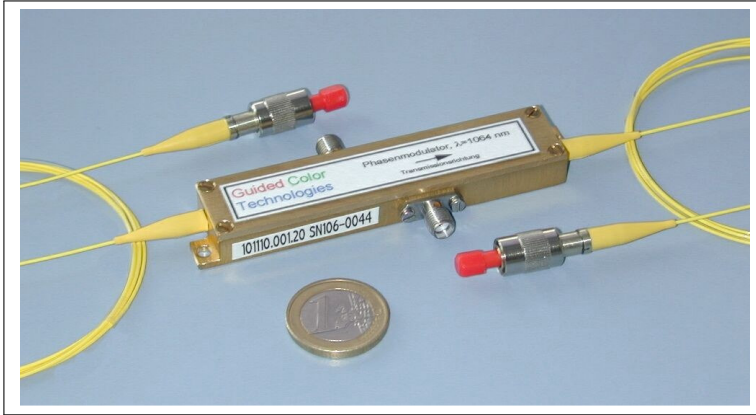


Figure 102. Picture of the fiber coupled EOM.

or in a resonant mode. For the broadband mode, the two macroscopic electrodes, mounted on two opposite sides of the approximately three centimeter long crystal, will be driven by a high voltage amplifier in order to achieve the electric field amplitudes between the electrodes on the approximately 0.5 cm thick crystal. In the resonant mode, an additional coil is placed in series with the capacitance of the crystal such that a resonant circuit is formed. Depending on the bandwidth of the resonance, a low voltage can be used to drive the device.

Due to the low operation voltages and its compact design the second type of EOM seems to be more promising (see Figure 102). In addition to that, microscopic high frequency (HF) electrodes acting as waveguides are designed to guarantee an identical propagation velocity of the electric modulation field and the electro-magnetic wave inside the crystal. The HF matched electrodes provide an operation range from a few MHz up to tens of GHz. Figure 103 shows the measured modulation depth as function of the modulation power for different modulation frequencies.

The compact setup, the low driving power and the wide frequency range make this EOM type an ideal candidate for LISA. However, there is one important disadvantage: due to insertion losses of approximately 3 dB, mainly caused by coupling losses between the crystal and the fiber, the device wastes half of the optical power and can be operated with just 50 mW optical power maximum¹.

¹ The power absorbed within the EOM could damage the crystal.

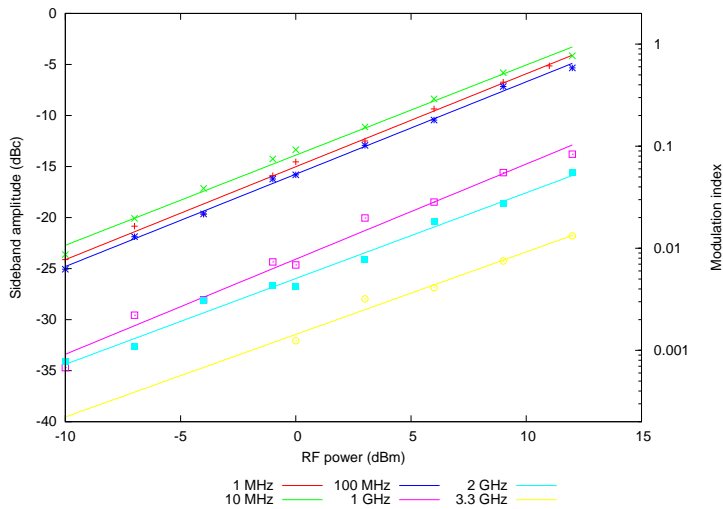


Figure 103. Modulation index measurement of the fiber coupled EOM for 1 MHz to 3.3 GHz

EOM CHARACTERISTICS

- fiber coupled EOM
- specified for 50 mW optical power
- operation range from 100 kHz up to 10 GHz
- low modulation power: <5 V for $\lambda/2$

5.2.4 Ranging setup

For demonstrating purposes a simple test setup was built very similar to the real LISA ranging and data transfer configuration. Figure 104 illustrates the setup. A standard INNOLIGHT Nd:YAG laser (laser 1 in Figure 104) represents a far spacecraft (spacecraft 1) in the LISA configuration and was fiber coupled. The optical fiber was fed through a waveguiding EOM. Afterwards the beam was injected onto an ultra stable Zerodur optical bench acting as a substitute for the LISA arm and the local optical bench on spacecraft 2. A second laser (laser 2 in Figure 104), also fiber coupled, was brought to interference with the first laser at a beam combiner (optical mixer).

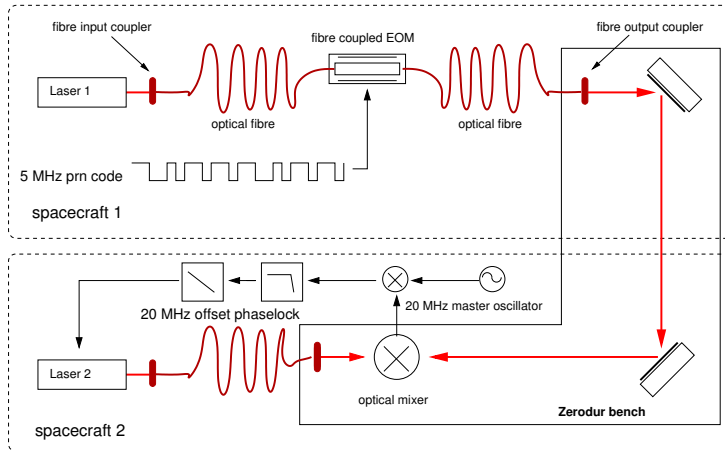


Figure 104. Ranging setup. Laser 2 is frequency offset phase locked to laser 1. Phase fluctuations of the lasers w.r.t. each other which occur outside the control bandwidth will be detected at the lowpass filter output. A PRN code sequence is applied by the EOM as a phase modulation to laser 1. The phase modulation is detected at the low pass filter output.

The beat note of both lasers was phase locked to a 20 MHz reference clock such that the frequency of laser 2 was phase locked with an offset of 20 MHz to laser 1. In order to achieve this the beat note and the 20 MHz reference oscillator signal were mixed. The sum frequency was removed by a lowpass filter with a cutoff frequency of 5 MHz. The remaining signal was the error signal that was fed back to the frequency control inputs of laser¹ 2. The overall loop bandwidth is of the order of a few tens kHz.

A PRN code sequence was applied by the EOM to the first laser. The modulation index was chosen such that approximately 0.01 % of the carrier power was spread into the code spectrum. Therefore the PRN modulator, based on a $m=16$ bit LFSR with feedbacks from taps $n=4,13,15$ was driven by a $f_{\text{clock}} = 5$ MHz clock. In this configuration the LFSR generated a maximum code length K given by:

$$K = 2^{16} - 1 = 65535. \quad (5.38)$$

¹ In fact the INNOLIGHT lasers provide two frequency control ports - a fast piezo electric transducer with a bandwidth of approximately hundred kHz and a slow wide range frequency steering input realized by a Peltier element mounted onto the laser crystal. The bandwidth of the second actuator was of the order of 1 Hz. Both actuators were used to stabilize the laser. For practical reasons instead of laser 2 the other laser 1 was phase locked. However, since the propagation delay is negligible in this case, this does not affect the basic idea of this experiment.

The duration t_{code} of the code sequence was:

$$t_{\text{code}} = \frac{K}{f_{\text{clock}}} = \frac{2^{16} - 1}{5 \text{ MHz}} = 0.013 \text{ s.} \quad (5.39)$$

This resulted in a total code length of approximately 3.9×10^6 meters - roughly 1/1000 of a [LISA](#) armlength, but easily long enough to resolve ambiguities by use of coarse [DSN](#) ranging. The parameters used are summarized in the following list:

PARAMETERS

- 16 bit shift register
- taps 4, 13, 15 (maximum length sequence) $2^{16} = 65535$ bit length
- 5 MHz clock
- code length 0.013 s resp. 3.9 million meters, appr. 1/1000 [LISA](#) armlength

The envelope E of this kind of spectrum (power spectrum) has a sinc function shape and is mainly dominated by the clock frequency f_{clock} :

$$E = \frac{\sin(\pi \frac{f}{f_{\text{clock}}})}{\frac{\pi f}{f_{\text{clock}}}}. \quad (5.40)$$

The variable f in Equation (5.40) is the Fourier frequency. The time series of this [PRN](#) code was folded with the code clock by the use of an additional XOR gate such that the resulting code is a Manchester code. The spectrum of this code is shown in Figure 105. The code signal prepared in such a manner was applied to the [EOM](#) and the resulting spread spectrum was transferred through the optical bench (Figure 104) and demodulated by the use of the second laser (laser 2 in Figure 104). The dark curve in Figure 106 shows the pure carrier-carrier beat at the beam combiner measured with a fast [PD](#) where laser 1 was unmodulated and interfered with laser 2. The lighter curve in Figure 106 is the spectrum of the beat signal of the modulated laser 1 and the demodulating laser 2. The error signal of the feedback loop performing the offset lock delivers the reconstructed code sequence. The error signal and the code sequence were sampled by the use of an 100 MHz oscilloscope (Figure 107 below).

5.2.5 Demodulation results

Figure 107 shows as dark curve a sequence of the code signal applied to the [EOM](#) and the demodulated data measured at the error point of the loop as

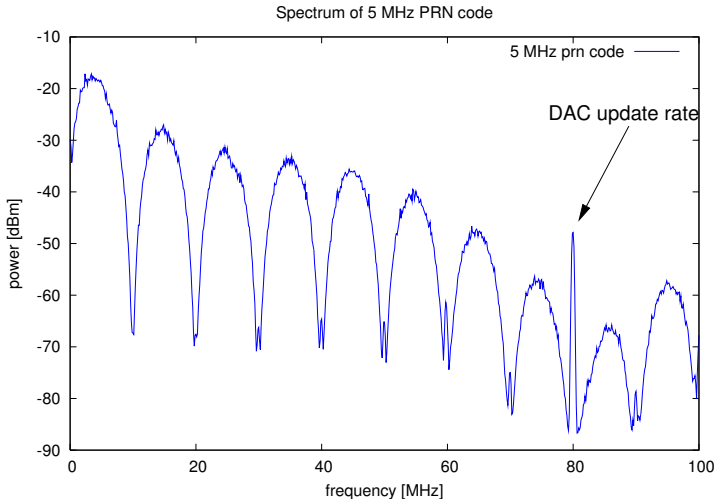


Figure 105. Spectrum of generated PRN code.

lighter curve. Since the low-pass filter of the offset lock between the lasers has a cutoff frequency of 5 MHz the frequency of the code was reduced to 1.25 MHz. The time series of the voltage applied to the EOM shown in Figure 107 has an amplitude of 0.05 V. Taking the half wave voltage of 5 V for the EOM into account this leads to applied phase modulation of 0.01574 rad which corresponds to a 0.02% of the unmodulated carrier power in the spread spectrum¹. Figure 106 shows the Carrier-carrier beat at 20 MHz - dark curve for the unmodulated laser - and lighter curve with applied PRN code sequence. The carrier-spread-spectrum ratio is -40 dBc. From this the modulation index can be estimated as

$$m = 10^{\frac{-40 \text{ dBc}}{20}} = 0.01. \quad (5.41)$$

¹ A factor of 10 in modulation index means a factor 100 in spread spectrum power. In the experiment the modulation index was limited by the output power provided by the transimpedance amplifier at the output of the FPGA board. For 1% carrier power in the data spectrum a modulation index of $0.01574 \cdot \sqrt{50} \text{ rad} = 0.1 \text{ rad}$ is needed corresponding to a +/- 0.35 V driving voltage for the EOM

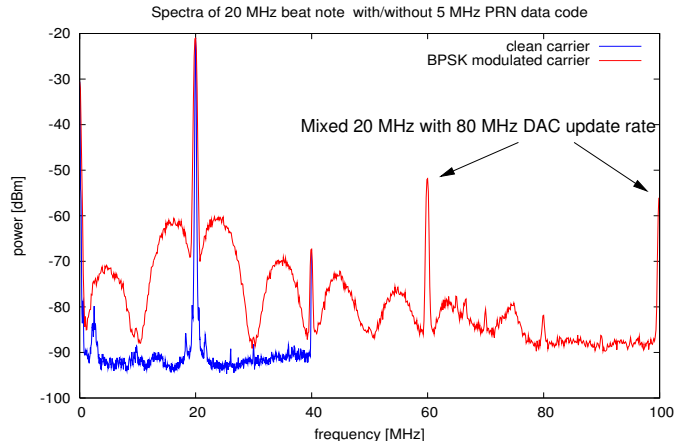


Figure 106. Spectrum of PRN modulated beat signal. Carrier-carrier beat at 20 MHz - dark curve unmodulated laser - lighter curve with applied PRN code sequence.

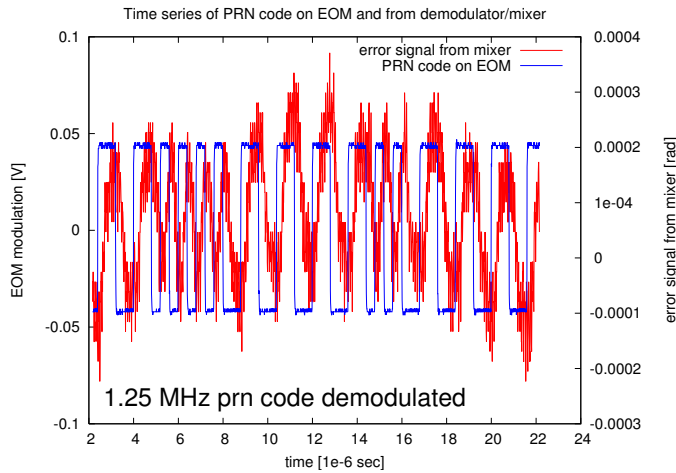


Figure 107. Demodulated PRN sequence. The graph shows as dark curve a sequence of the code signal applied to the EOM and the demodulated data, measured at the error point of the loop, as lighter curve.

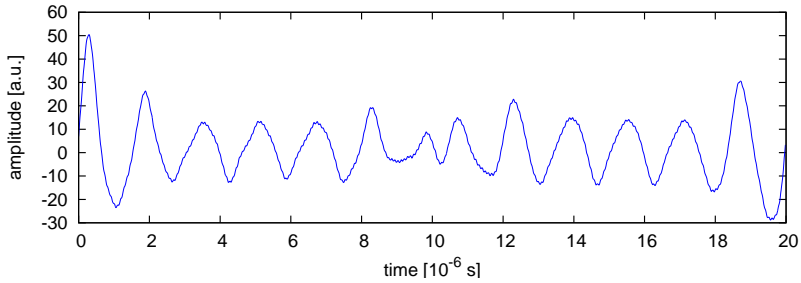


Figure 108. Correlation of the initial PRN code and the demodulated replica. The maximum peak is at approximately 30 ns.

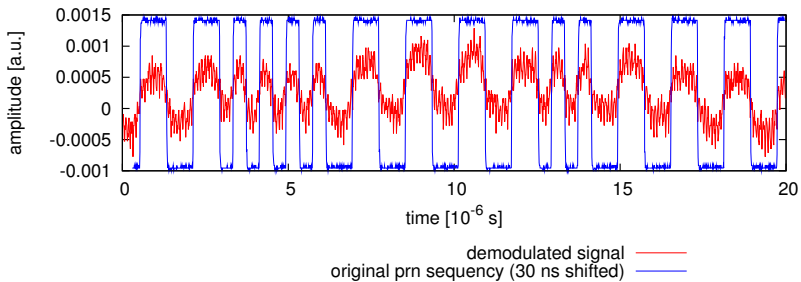


Figure 109. PRN code and demodulated replica (30 ns time shifted).

5.2.6 Correlation results

A correlator circuit can be used in order to perform a full ranging measurement. Such a correlator circuit multiplies the demodulated PRN sequence that was received from the far spacecraft with a local generated replica of the code. The correlation delivers the time delay between both code sequences and thus the distance between the two spacecraft. Due to the unavailability of a hardware correlator circuit, the delay estimation was performed in software. Therefore, the (Fourier domain) correlation of both time series was calculated using the FFTW algorithm (FRIGO (1999), FRIGO and JOHNSON (1997)).

The inverse Fourier transform delivers the time domain correlation of both signals. Figure 108 shows the result. The periodicity of time series is given by the clock frequency of the code (1.25 MHz).

From this time series in Figure 108, a delay of 30 ns was estimated (see Figure 109). Additionally to the light travel time it includes several electron-

ical delays and phase offset due to the transfer function of the setup (mixer, loop-filter).

5.3 CONCLUSION

The principle of the spread spectrum modulation was successfully demonstrated. A PRN code modulator was implemented on a FPGA. According to the proposed LISA modulation scheme this code was applied by an EOM to a laser and transmitted via a dummy arm to an optical bench. The spectrum was demodulated with an analog PLL that carries the frequency of the demodulation laser fixed at an offset of 20 MHz. The demodulated PRN code provides a good SNR such that its correlation with the original code sequence is obvious. For demonstration purposes, a software correlator was implemented. Thus a delay of 30 ns was estimated. However, as a next step a hardware correlator circuit needs to be built, according to the planned LISA implementation, that estimates the delay between the demodulated signal and a second copy of the same code.

SUMMARY AND OUTLOOK

*"Die Wissenschaft fängt eigentlich erst da an
interessant zu werden, wo sie aufhört."*

JUSTUS VON LIEBIG (1803-1873) deutscher Chemiker

This Chapter provides a summary of the achieved progress and the results concerning the development of the interferometry for LISA and its precursor mission LISA pathfinder. The main objective of LISA Pathfinder is the verification of the drag-free motion of two free floating proof masses. In this context the LISA Pathfinder interferometry is the measurement device in order to perform this verification.

6.1 LISA PATHFINDER INTERFEROMETRY

During this work, the interferometric concept of LISA Pathfinder based on non-polarizing heterodyne Mach-Zehnder interferometers was implemented and tested on laboratory level. Thus the comprehensive design, including all necessary supplementing subsystems such as electronics and readout software could be verified. In parallel, industrial prototype development of the hardware began, accompanied by laboratory prototyping hardware and support of the AEI LISA Pathfinder team.

Important key subsystems of the LISA Pathfinder interferometry are the phase measurement system (PMS) and the modulation electronics which were developed within this works. Both systems were tested successfully together with an *engineering model* of the optical bench containing the main interferometry¹. During a measurement campaign, performed by the AEI LISA Pathfinder team, the required longitudinal measurement sensitivity of $10 \text{ pm}/\sqrt{\text{Hz}}$ was achieved. In addition to that, a sensitivity of $10 \text{ nrad}/\sqrt{\text{Hz}}$ to proof mass angular misalignments could be demonstrated.

In order to achieve this requirement, slightly design modifications of the initial interferometry baseline were necessary. This is due to unexpected

¹ the ultrastable parts of the interferometers

noise source discovered during laboratory prototyping. In polarizing heterodyne interferometers, nonlinearities in the phase readout are known as a disturbing phenomena (Wu and Su (1996), Wu and LAWALL (1999)). Due to this fact, the LISA Pathfinder design was based on nonpolarizing interferometers. However, the measurement sensitivity was limited on picometer level by such nonlinearities. As origin of this effect, spurious sidebands of the modulation frequencies could be identified and mitigated. The coupling process became fully understood during the investigation performed by the AEI LISA Pathfinder team.

6.2 LISA INTERFEROMETRY

According to the experiences of the LISA Pathfinder development, the phase measurement system is a key development issue for LISA. Even with the know-how from the LISA Pathfinder phasemeter development, there are a number of challenges concerning to the LISA phasemeter. The main difference is the operation frequency of the phasemeter, which is constant in the kHz range for LPF while LISA is being operated at heterodyne frequencies varying in the range from 2-20 MHz. Due to the non-constant heterodyne frequency, the LISA phasemeter needs to provide a frequency tracking functionality. Within the second part of this work, the requirements of a LISA phase measurement system were analyzed.

In contrast to other groups working on the LISA phasemeter, the development at the AEI is focused on the hardware implementation of an appropriate phasemeter. For this reason, a prototype board was developed, based on a field programmable gate array (FPGA). Besides this *central processing unit*, a dedicated ADC acquires the input signal whose phase needs to be measured.

The core functionality of the phasemeter is provided by an all digital phase locked loop (ADPLL) which was implemented on the FPGA using VHDL. The functionality of the ADPLL could be demonstrated and tested in an ideal test environment. The requirement for the phase noise of the readout has been achieved under these conditions. Nevertheless, the phasemeter is object of ongoing development and research activities, since the current design has not been fully tested on an interferometer. An important modification to the prototype hardware, is the extension to several phasemeter channels.

A further objective of this work, closely related to the phasemeter, is a ranging measurement which needs to be implemented for LISA. Based on the phasemeter prototype board, a pseudo-random noise code (PRN) generator was developed. In a table-top experiment, the generator was used (supplemented by an EOM) to modulate a laser beam. A second laser was frequency-offset-phase-locked to the modulated laser and thus the PRN code could be recovered. By correlating (in software, offline) the demodulated (and

delayed) PRN sequence with a replica, the time delay of 30 ns could be measured. Thus the next implementation step is a hardware correlator circuit, in order to provide a real-time ranging measurement.

Once the performance of the phasemeter has been demonstrated in a real optical setup, and the hardware correlator has been implemented, both systems can be combined to a complete [LISA](#) phasemeter prototype.

A

APPENDIX A - DIGITAL SIGNAL PROCESSING

A.1 DIGITAL SIGNAL PROCESSING - NYQUIST THEOREM

Digital signal processing is based on the measurement of a time continuous signal $x(t)$ at equidistant time stamps (sampling). Each measurement n is taken at the time (stamp) t_n . T_S is the sampling interval such that $T_S = t_n - t_{n-1}$. Thus the time stamps are given by:

$$t_n = nT_S. \quad (\text{A.1})$$

The time discrete measurements values $x(nT_S)$ represent a time continuous analog input signal. In order to ensure that this representation is definite the sampling theorem needs to be fulfilled. This means that the bandwidth of the signal to be digitized needs to be limited by the half sampling rate. This from the sampling or Nyquist theorem can be expressed as:

$$T_S \leq \frac{\pi}{\omega_{\max}} = \frac{1}{2f_{\max}} \quad (\text{A.2})$$

$\omega_{\max} = 2\pi f_{\max}$ is the bandwidth of the analog signal and represents the maximum acceptable Fourier frequency component. This bandwidth is called Nyquist bandwidth. For the sampling frequency Ω_S it is necessary that:

$$\Omega_S \geq 2\omega_{\max}. \quad (\text{A.3})$$

ω_{\max} is called *Nyquist*- frequency. If the Nyquist theorem is fulfilled, $x(t)$ can be reconstructed from a discrete time series $x(nT_S)$ (COUCH II, 1997):

$$x(t) = \sum_{n=-\infty}^{\infty} x(nT_S) \frac{\sin(\pi(t - nT_S)/T_S)}{\pi(t - nT_S)/T_S}. \quad (\text{A.4})$$

A.2 SOME ASPECTS OF THE FOURIER TRANSFORM AND APPLICATIONS

The Fourier transform is part of the most powerful utilities of physics and is applied in an amount of fields such as numerical integration and differentiation and in particular for the calculation of spectra or correlations. Its

importance for digital signal processing is based on the application in filtering operations respectively folding operations.

Fourier transformation (FT)

Mostly, physical quantities are continuously and are described in the time domain. We assume such a quantity as:

$$w = w(t). \tag{A.5}$$

The Fourier transform translates the quantity $w(t)$ into a function containing the same information which is defined in the Fourier domain.

$$W(f) = \int_{-\infty}^{\infty} dt e^{-2\pi i f t} w(t). \tag{A.6}$$

$W(f) = H(f)$ the Fourier transformed of $w(t)$. Table 10 summarizes often used Fourier transform theorems:

Operation	Function	Fourier Transform
Linearity	$a_1 w_1(t) + a_2 w_2(t)$	$a_1 W_1(f) + a_2 W_2(f)$
Time delay	$w(t - T_d)$	$W(f) e^{-i\omega T_d}$
Scale change	$w(at)$	$\frac{1}{ a } W\left(\frac{f}{a}\right)$
Conjugation	$w^*(t)$	$W^*(-f)$
Duality	$W(t)$	$w(-f)$
Real signal frequency translation	$w(t) \cos(\omega_c t + \theta)$	$\frac{1}{2} [e^{i\theta} W(f - f_c) + e^{-i\theta} W(f + f_c)]$
Complex signal frequency translation	$w(t) e^{-i\omega_c t}$	$W(f - f_c)$
Bandpass signal	$\Re(g(t)) e^{-i\omega_c t}$	$\frac{1}{2} [G(f - f_c) + G^*(-f - f_c)]$
Differentiation	$\frac{d^n w(t)}{dt^n}$	$(i 2 \pi f)^n W(f)$
Integration	$\int_{-\infty}^t w(\lambda) d\lambda$	$(i 2 \pi f)^{-1} W(f) + \frac{1}{2} W(0) \delta(f)$
Convolution	$w_1(t) * w_2(t)$	$W_1(f) W_2(f)$
Multiplication	$w_1(t) w_2(t)$	$W_1(f) * W_2(f)$
Multiplication by t^n	$t^n w(t)$	$(-i 2 \pi) \frac{d^n W(f)}{df^n}$

Table 10. Fourier transform theorems [COUCH II \(1997\)](#)

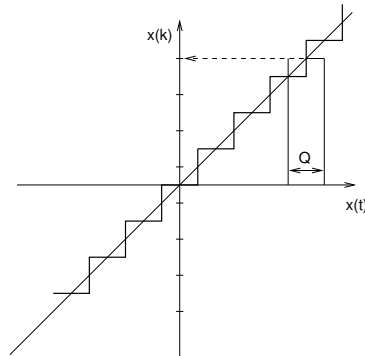


Figure 110. Illustration of the digitization process

A.3 DIGITIZATION NOISE

Quantization noise is e.g. occurs if an analog (continuous) quantity $x(t)$ is quantized by an ADC with a resolution of B bits at a sampling rate of f_s . The digital representation x_k of the quantity $x(t)$ is quantized as integer values from $0 - 2^B$. Each quantization step represents a fraction of $\frac{1}{2^B}$ of the full analog input range U of the ADC. This defines the quantization step of the a digitized signal:

$$Q = U_{\text{LSB}} = \frac{U}{2^B} \quad (\text{A.7})$$

Thus each digital value x_k represents an interval Q of the analog signal (see Figure 110). The error $e(t)$ occurring to the digital representation of the input signal $X(t)$ is given by:

$$e(t) = X(t) - x_k \quad (\text{A.8})$$

and varies from $-Q/2 \dots + Q/2$ while the probability p of each value in this range is the same: $1/Q$.

The power P of this quantization noise is given by the square of its variance

σ of the error and is defined as:

$$P = \sigma^2 = \int_{-Q/2}^{Q/2} de p e(t)^2 \quad (\text{A.9})$$

$$= \frac{1}{Q} \int_{-Q/2}^{Q/2} de e(t)^2 = \frac{1}{Q} \left[\frac{1}{3} e(t)^3 \right]_{-Q/2}^{Q/2} = \frac{Q}{12} \quad (\text{A.10})$$

This noise power is distributed over a frequency range from $-f_s/2 \dots + f_s/2$:

$$P = \int_{-f_s/2}^{f_s/2} df |S_v(f)|^2 = \frac{Q}{12}. \quad (\text{A.11})$$

where $S_v(f)$ is the (linear) spectral density and its square the power spectral density. This leads to the expression:

$$|S_v(f)|^2 = \frac{Q^2}{6f_s} \quad (\text{A.12})$$

and consequently for the linear spectral density of the quantization noise:

$$S_v(f) = \frac{Q}{\sqrt{6f_s}} \quad (\text{A.13})$$

B

APPENDIX B - SUPPLEMENTAL MEASUREMENTS

B.1 TRANSFER FUNCTION OF THE AM INPUT OF THE AOM DRIVER

Figure 111 shows the measured transfer function from the AOM driver AM input to the light power at the fiber end. By means of this actuator the laser power stabilization was implemented which was used for all LISA pathfinder performance tests.

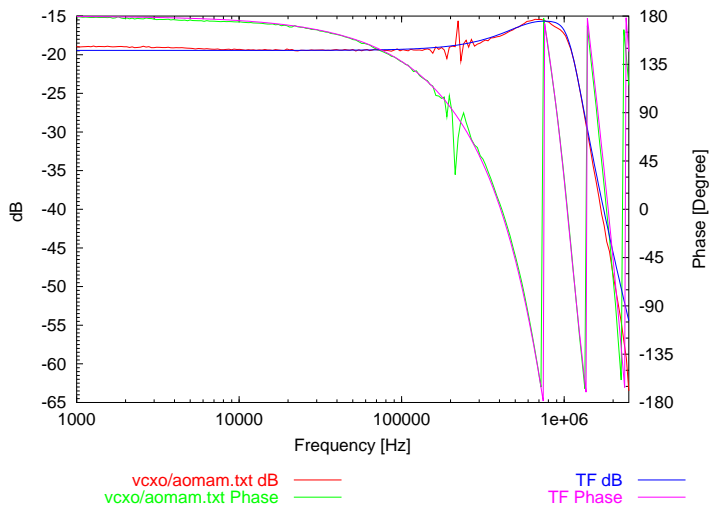


Figure 111. Transfer function of the AOM driver AM input.

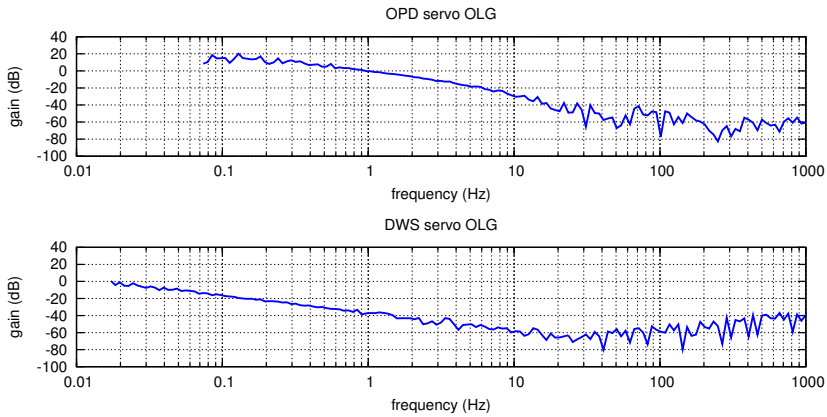


Figure 112. Open loop gain of digital OPD stabilization and DWS servo.

B.2 OPEN LOOP GAIN OF DIGITAL OPD STABILIZATION AND DWS SERVO

In addition to the analog implementation of the OPD servo according to the planned implementation scheme onboard LISA Pathfinder, a digital version of the servo was tested.

The upper graph in Figure B.2 shows the measured open loop gain of the OPD control loop using the digital implementation of the servo. The bandwidth is approximately 1 Hz. For the noisy laboratory environment this servo implementation was insufficient¹ but, however, a functional demonstration of the real servo implementation using the output of the phasemeter.

The lower graph in Figure B.2 shows the measured open loop gain of an implementation of the DWS servo used in an automatic alignment procedure of the interferometer. By means of this servo the interferometer could be aligned automatically using PZT mounted mirrors instead of the real test masses. The bandwidth was limited in order to monitor the alignment procedure online at the graphical user interface of the phasemeter.

¹ The OPD servo suppresses differential fiber pathlengths variations.

C

APPENDIX C - CIRCUITS

C.1 PHASEMETER CIRCUITS

The phasemeter prototype board was designed using the software *EAGLE*. As core an *ACTEL* FPGA A3P250 respectively an A3P1000 was used as central processing unit. Both are pin compatible. The package of the chip provides totally 208 pins for power supply and digital I/Os.

The signal acquisition is performed by an 16bit ADC (AD9446) by *Analog Devices*. The maximum sampling rate is specified with 125 MHz. The digitized signal is provided in parallel and can be interface either in LVDS or in CMOS mode. In this implementation the CMOS output was used.

Furthermore the design provides an **FIFO** memory for the data transmission to the PC that can be connected via an enhanced parallel port (EPP) interface.

An onboard clock circuit with an 20 MHz **VCO** is foreseen. Its output is scaled by a programmable digital PLL chip (ICS501) to 80 MHz. Due to unexpected high jitter of its output an external 80 MHz clock from a signal generator was used as master clock for the design.

In order to store data on the board, a **RAM** chip is implemented in the design. This additional memory is intended to store sine lookup table data or FIR/IIR coefficients. Therefor 1M word (16 bit) memory is available.

As output ports two DACs (AD9744) can be used. They provide an update rate of 210 MHz maximum and a resolution of 14 bit. Theirs output current is converted using transimpedance amplifiers into a voltage and lowpass filtered.

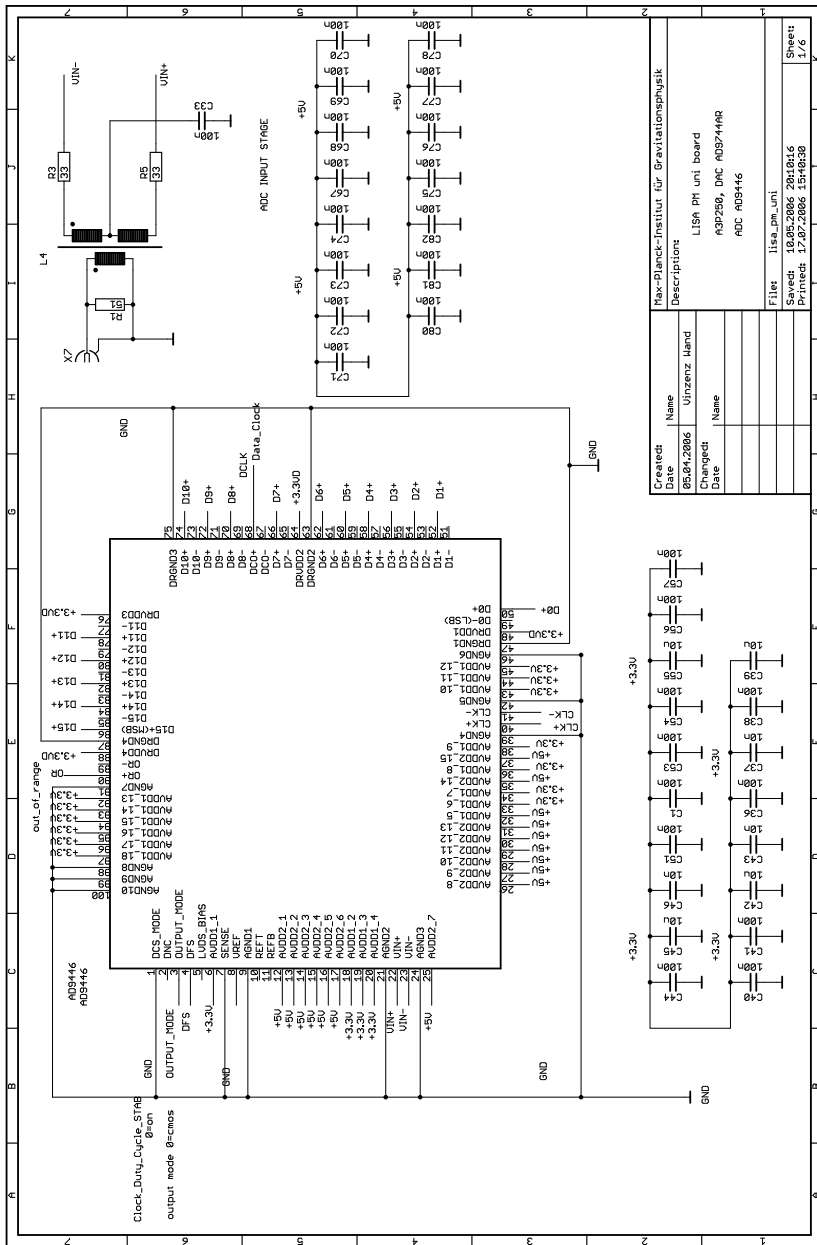
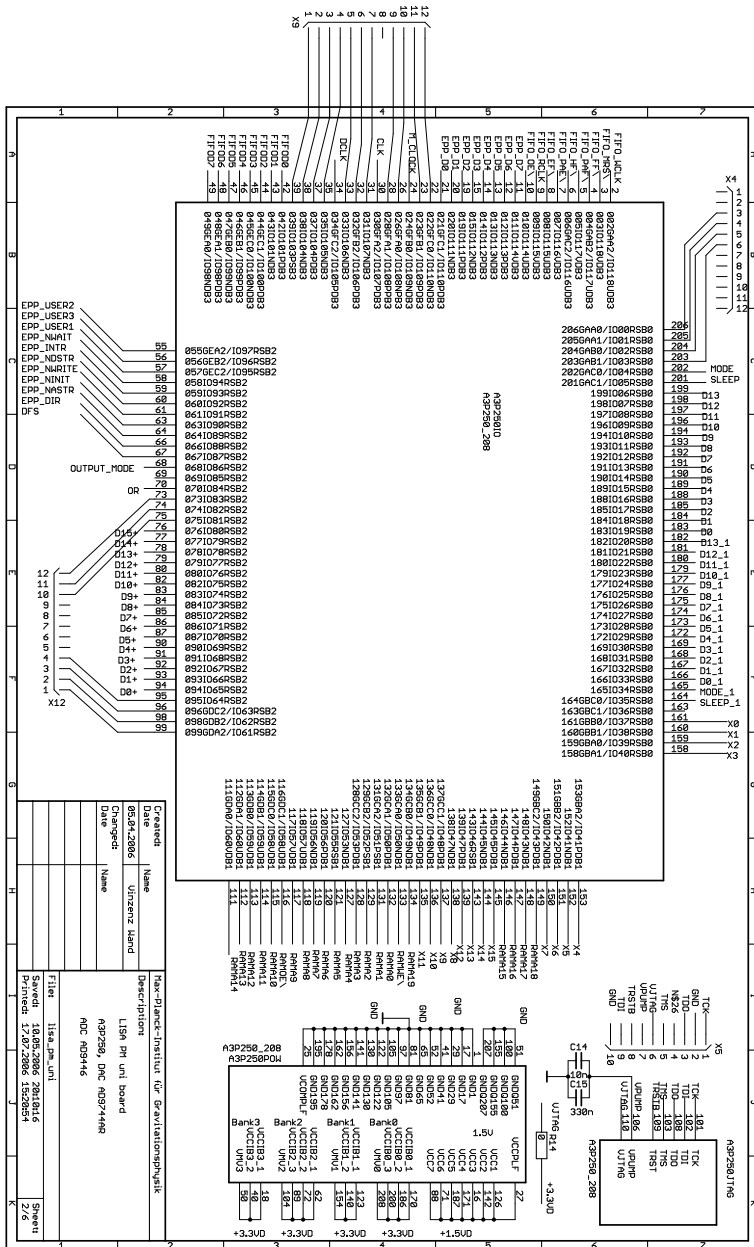


Figure 113. Schematic of the phasemeter prototype board - ADC converter.

C.1 PHASEMETER CIRCUITS



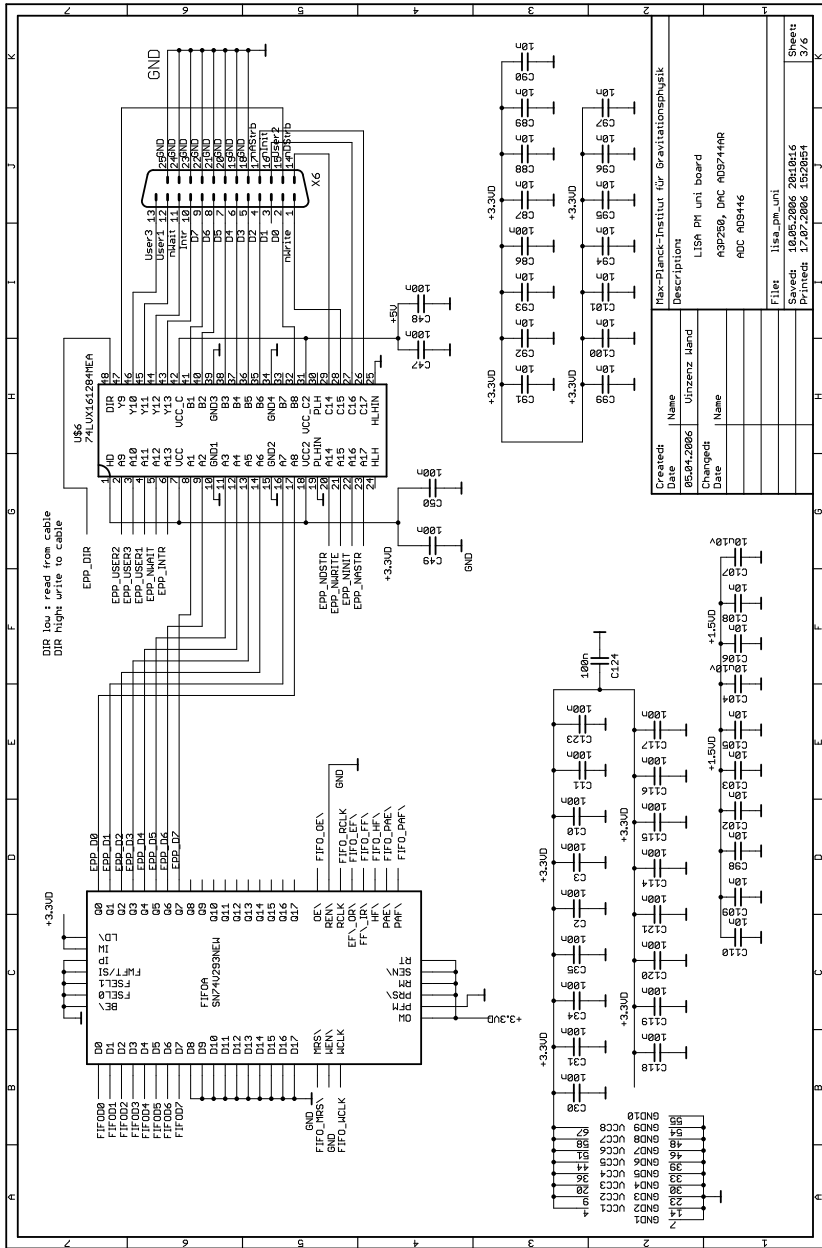


Figure 115. Schematic of the phasemeter prototype board - parallel port interface with FIFO.

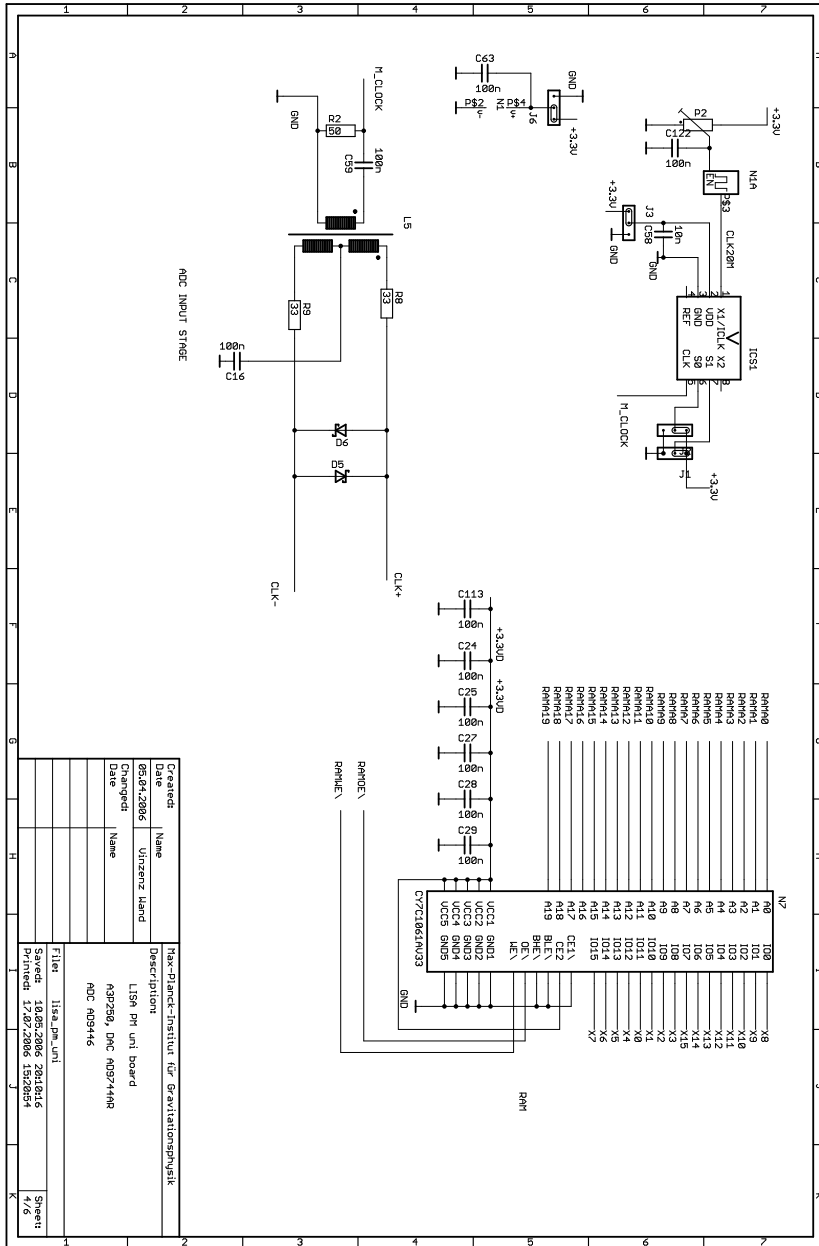


Figure 116. Schematic of the phasemeter prototype board - clock generation and RAM.

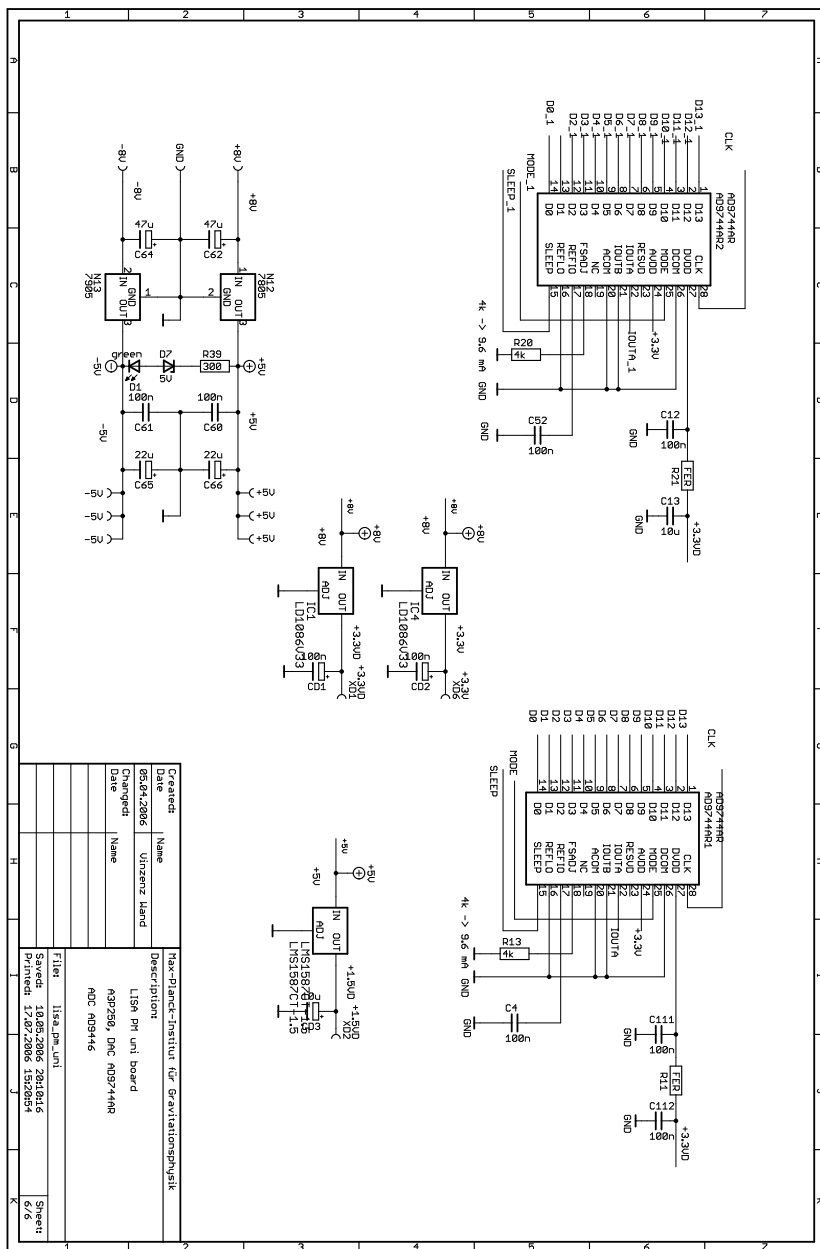


Figure 118. Schematic of the phasemeter prototype board - DACs

C.2 SAMPLE AND HOLD CIRCUITS

The first LISA Pathfinder phasemeter prototypes PM1 and PM2, used during the TNO measurement campaign, are based on off-the-shelf PC data acquisition cards (MicroStar Laboratories). These cards provide multiplexed [ADC](#) converters. In order to guarantee simultaneous sampling a 16 channel Sample-and-Hold circuit (based on AD781) was built.

D

APPENDIX D - LISTINGS

D.1 VHDL CODE OF THE DDS (ABSTRACT)

```
2  -- nco.vhd
4  LIBRARY IEEE;
   use IEEE.std_logic_1164.all;
6  use IEEE.std_logic_arith.all;
   use IEEE.std_logic_signed.all;
8  --library APA;
10
11 ENTITY nco IS
12   GENERIC ( k : INTEGER := 56;
            test:STD_LOGIC_vector (3 downto 0):="0010");
14
15   PORT(reset : IN  STD_LOGIC;
16        Clock : IN  STD_LOGIC;
17        phase_word: IN STD_LOGIC_vector (k-1 downto 0);
18        phase_off: IN STD_LOGIC_vector (1 downto 0);
19        nco_out: OUT STD_LOGIC_vector (7 downto 0);
20        phase_acum32:out STD_LOGIC_vector (71 downto 0)
21        );
22 END nco;
24
25 ARCHITECTURE Structure OF nco IS
26
27   COMPONENT sintab8bit
28     port(index : in std_logic_vector(39 downto 0);
29          off  : in std_logic_vector(1 downto 0);
30          sinval : out std_logic_vector(7 downto 0);
31          clock:in std_logic
```

```
32     );
33     end COMPONENT;
34
35
36 COMPONENT accum
37     GENERIC ( k :INTEGER := 56 );
38     PORT ( Resetn, Clock : IN STD_LOGIC ;
39           X : IN STD_LOGIC_VECTOR(k-1 DOWNT0 0) ;
40           Result : out STD_LOGIC_VECTOR(71 DOWNT0 0) ) ;
41     END COMPONENT ;
42
43
44 COMPONENT regne -- n-bit register with enable
45     GENERIC ( n : INTEGER := 56 ) ;
46     PORT ( D : IN STD_LOGIC_VECTOR(n-1 DOWNT0 0) ;
47           Resetn : IN STD_LOGIC ;
48           E, Clock : IN STD_LOGIC ;
49           Q : OUT STD_LOGIC_VECTOR(n-1 DOWNT0 0) ) ;
50     END COMPONENT ;
51     --component accum1_behave
52     --port(DataA : in std_logic_vector(17 downto 0);
53           --      Enable : in std_logic;
54           --      Aclr : in std_logic;
55           --      Clock : in std_logic;
56           --      Sum : out std_logic_vector(17 downto 0));
57     --end component;
58
59
60 signal phase_acum: STD_LOGIC_VECTOR(39 DOWNT0 0);
61 signal phase_word_int: STD_LOGIC_VECTOR(55 DOWNT0 0);
62 signal nco_out1: STD_LOGIC_VECTOR(7 DOWNT0 0);
63 signal dummy: STD_LOGIC_VECTOR(71 DOWNT0 0);
64 --signal phase_incr_reg:STD_LOGIC_VECTOR(k-1 DOWNT0 0);
65 --signal nco1: STD_LOGIC_VECTOR(7 DOWNT0 0) ;
66 --signal dummy: STD_LOGIC_VECTOR(7 DOWNT0 0) ;
67
68 BEGIN
69     accum1:accum
70     GENERIC MAP ( k =>56 )
71     PORT MAP(
72     Resetn =>reset,
73     Clock => Clock,
74     X=>phase_word_int,
75     Result => dummy);
76
```

```
78 --accum2:accum1_behave
--PORT MAP(
80 --DataA=>phase_word,
--Enable=>'1',
82 --Aclr =>reset,
--Clock => Clock,
84 --Sum => phase_acum18);

86

88 sintaba: sintab8bit
  PORT MAP(
90     index =>phase_acum ,
    off => phase_off,
92     sinval => nco_out1,
    clock=>clock);
94
--procl: process( Clock,reset)
--begin
--if (reset = '0') then
96     --phase_acum    <= (others => '0');
98     --elsif (rising_edge(Clock)) then
100
102
--end if;
104 --end process;

106 reg: regne
  GENERIC MAP ( n =>8 )
  PORT MAP (D=>nco_out1,
108     Resetn=>reset,
110     E=>'1',
    Clock=>Clock,
112     Q=>nco_out) ;

114
reg1: regne
116  GENERIC MAP ( n =>72 )
  PORT MAP (D=>dummy,
118     Resetn=>reset,
120     E=>'1',
    Clock=>Clock,
    Q=>phase_acum32) ;
122
reg2: regne
```

```

124 GENERIC MAP ( n =>56 )
PORT MAP (D=>phase_word,
126     Resetn=>reset,
        E=>'1',
128     Clock=>Clock,
        Q=>phase_word_int) ;
130
132 --phase_acum32<=dummy;
134 process(clock)
    begin
136     if (rising_edge(Clock)) then
138     phase_acum(39 downto 0)<=dummy(71 downto 32);
        end if;
140     end process;
        --phase_acum(6)<=dummy(46);
142     --phase_acum(5)<=dummy(45);
        --phase_acum(4)<=dummy(44);
144     --phase_acum(3)<=dummy(43);
        --phase_acum(2)<=dummy(42);
146     --phase_acum(1)<=dummy(41);
        --phase_acum(0)<=dummy(40);
148 --phase_acum<=dummy%256;
150 END Structure;

```

D.2 C IMPLEMENTATION OF A PHASETRACKING ALGORITHM

```

void phasetrack (double old, double *new) {
2   double n = *new, d;
   for ( ; ; ) {
4     n = *new + phaseoff;
       d = n - old;
6     if (d <= -360){
           phaseoff += 360;
8         continue;
           }
10    if (d > -360)
        break;
12    }
   for ( ; ; ){
14     n = *new + phaseoff;

```

```

16   d = n - old;
17   if (d >= 360)
18   {
19       phaseoff -= 360;
20       continue;
21   }
22   if (d < 360) break;
23   }
24   assert (d > -360 && d < 360);
25   if (d < (-180 - PHASETRACKEPS))
26   phaseoff += 360;
27   else if (d > (180 - PHASETRACKEPS))
28   phaseoff -= 360;
29   *new += phaseoff;
30   }

```

D.3 C EMBEDDED CONFIGURATION OF THE DAP5216A

```

1  /*****
2  /* DAP - INIT
3  /*****
4  int
5  Dap_Init (int n_c, int s_f, int d_l)
6  {
7     int i;
8     char Command[255];
9
10    d_l = 1;
11
12    /* Open handles to DAP text and binary communication pipes */
13    if ((fdSysOut = open ("/dev/Dapo/$SysOut", O_RDONLY)) <= 0)
14    {
15        printf ("Error opening accel0, errno=%d\n", errno);
16        return 1;
17    }
18    if ((fdDapTxt = open ("/dev/Dapo/$SysIn", O_WRONLY)) <= 0)
19    {
20        printf ("Error opening accel0, errno=%d\n", errno);
21        return 1;
22    }
23    if ((fdDapBin = open ("/dev/Dapo/$BinOut", O_RDONLY)) <= 0)
24    {
25        printf ("Error opening accel1, errno=%d\n", errno);
26        return 1;

```

```
27     }

29     /* Stop DAP processing and flush old data still in com pipes */
DAPSendString (fdDapTxt, "\rRESET\r");
31     DAPFlush (fdDapTxt);
DAPFlush (fdDapBin);
33     DAPFlush (fdSysOut);

35     /* Enables sending buffer overflow information into SysOut-Pipe */
DAPSendString (fdDapTxt, "OPTIONS OVERFLOWQ = ON\r");
37

39     /* Configure the DAP for sampling 1-12 channel */

41     sprintf (Command, "IDEFINE A %d\r", n_c);
DAPSendString (fdDapTxt, Command);
43

45     sprintf (Command, "CLOCK EXTERNAL \r");
DAPSendString (fdDapTxt, Command);

47     sprintf (Command, "CLOCKING ON \r");
DAPSendString (fdDapTxt, Command);
49

51     for (i = 0; i < n_c; i++)
    {
53         sprintf (Command, "SET IPIPE%d S%d\r", i, i);
DAPSendString (fdDapTxt, Command);
    }

55     DAPSendString (fdDapTxt, " TIME 3\r");
57     DAPSendString (fdDapTxt, " END\r");
DAPSendString (fdDapTxt, "PDEFINE B\r");
59     DAPSendString (fdDapTxt, " BPRINT\r");
DAPSendString (fdDapTxt, " END\r");
61

63     /* Configures output trigger */
/* DAPSendString (fdDapTxt, "ODEFINE C 1\r");
DAPSendString (fdDapTxt, "CLOCK EXTERNAL\r");
65     DAPSendString (fdDapTxt, "END\r");
*/

67     DAPSendString (fdDapTxt, "START\r");

69     /*Asks DAP about CPU-Use information */
71     DAPSendString (fdDapTxt, "TASKSTAT CLEAR\r");
DAPSendString (fdDapTxt, "TASKSTAT STATUS\r");
```



```
73 |  
74 |     printf ("Reading Data\n");  
75 |     return 0;  
76 |  
77 | }
```

INDEX

- acceleration noise, 3
- ADPLL, 134
- anti aliasing filter, 43
- AOM, 11, 26
- AOM, driving electronic, 27
- arm locking, 153

- beam combiner, 12
- binary phase shift keying, 163
- BPSK, 158, 161, 165

- carrier-sideband-ratio, 93
- clock noise transfer, 157
- clock synchronization, 152
- conservation of energy, 12
- control loop, 12
- correlator, 173

- DAP, 45
- DAQ, 44
- DC signals, 66
- DDS, 126, 132
- DFT, 41
- digitization noise, 21, 141
- DWS, 50, 66

- electro optical modulator, 166
- engineering model, 30
- engineering model, optical bench, 30
- EOM, 166
- ESA, 2

- FFTW, 43
- fiber injector, 35
- field programmable gate array, 164
- FIFO, 131

- FIR, 131
- FPGA, 164
- frequency interferometer, 33
- frequency modulation, 18
- frequency offset phase lock, 170
- frequency stabilization, 153
- frequency standard, molecular, 153
- frequency synthesizers, 27
- full stroke test, 57
- functional test, 56

- gravitational waves, 1
- ground bases detectors, 2
- ground testing, 53

- heterodyne, 11
- heterodyne interferometry, 10, 12
- Heterodyne signal, 15
- hydroxy catalysis bonding, 35

- I-Q demodulation, 126
- IIR, 131
- InGaAs, 36
- interferometer, 34
- iodine, 153

- Lagrange point, 6
- laser frequency noise, free running, 25
- laser power noise, 19
- laser ranging, 168
- LFSR, 164
- linear feedback shift register, 164
- LISA, 1
- lock acquisition, LISA PMS, 144
- longitudinal phase, 16
- longitudinal readout, 49

- look-up table, 131
- LTP, 9
- Mach-Zehnder interferometer, 10
- Manchester Code, 166
- master clock, 12
- mixer, 38
- modulation bench, 16, 26
- modulation scheme, 156
- modulation, amplitude, phase, 90
- MZI, 9
- NASA, 2
- NCO, 132
- Nd:YAG, 25
- Nd:YAG laser, 10
- noise cancellation, 17
- noise sources, 18
- noise, periodic, 78
- non-linearities, 75
- NPRO, 25
- offset phase lock, 170
- OMS, 9, 11
- OPD, 99
- optical bench, 30
- optical fiber, 79
- optical pathlength stabilization, 79
- OptoCAD, 31
- pathlength fluctuations, 76
- pathlength fluctuations, 16
- performance test, 70
- phase accumulator, 131
- phase increment register, 131
- phase jump, 15
- phase measurement concept, LISA Pathfinder, 42
- phase measurement system, 38
- phase measurement system, LISA, 120
- phase measurement, DFT, 41
- phase noise, residual, 76
- phase reconstruction, 139
- phase tracking, 57
- piezo-electric transducer, 26
- PLL, 126, 131, 153, 170
- PMS, comparison, 123
- PMS, LISA baseline, 124
- PMS, LISA modified approach, 127
- PRN, 160, 161, 163, 164
- pseudo random noise, 163, 164
- PSK, 158, 160
- PZT, 10, 26, 58
- QPSK, 158
- RAL, 35
- ranging, 156, 158, 168
- ranging and data transfer, 152
- reference interferometer, 32
- reflection coefficient, 12
- relative intensity noise, 20
- requirements, 24
- requirements, LISA Pathfinder, 23
- requirements, PMS LISA, 120
- responsivity, 36
- RIN, 20
- sample and hold, 45
- SBDFT, 45
- shift register, 164
- shot noise, 3
- sidebands, 81
- sidebands, first-order, 88
- sidebands, nature, 114
- sidebands, origin, 110
- sidebands, second-order, 91
- silicate bonding, 35
- single bin discrete Fourier transform, 45
- small vector (-noise), 84
- split interferometry, 16
- spread spectrum, 162
- stabilization, OPD, 80

TCVCXO, 27, 29
TDL, 153
telescope, aperture, 3
test mass, free floating, 2
tilt test, 63
time delay interferometry, 153
time stamps, 156
transmission coefficient, 12

ultra stable, 17, 77
USO, 152, 156

VCO, 132
VHDL, 134, 164

X1 interferometer, 33
X12 interferometer, 32

zero crossing, 41
Zerodur, 35

BIBLIOGRAPHY

S. ANZA, M. ARMANO, E. BALAGUER, M. BENEDETTI, C. BOATELLA, P. BOSETTI, D. BORTOLUZZI, N. BRANDT, C. BRAXMAIER, M. CALDWELL, L. CARBONE, A. CAVALLERI, A. CICOLELLA, I. CRISTOFOLINI, M. CRUISE, M. D. LIO, K. DANZMANN, D. DESIDERIO, R. DOLESI, N. DUNBAR, W. FICHTER, C. GARCIA, E. GARCIA-BERRO, A. F. GARCIA MARIN, R. GERNDT, A. GIANOLIO, D. GIARDINI, R. GRUENAGEL, A. HAMMESFAHR, G. HEINZEL, J. HOUGH, D. HOYLAND, M. HUELLER, O. JENNRICH, U. JOHANN, S. KEMBLE, C. KILLOW, D. KOLBE, M. LANDGRAF, A. LOBO, V. LORIZZO, D. MANCE, K. MIDDLETON, F. NAPPO, M. NOFRARIAS, G. RACCA, J. RAMOS, D. ROBERTSON, M. SALLUSTI, M. SANDFORD, J. SANJUAN, P. SARRA, A. SELIG, D. SHAUL, D. SMART, M. SMIT, L. STAGNARO, T. SUMNER, C. TIRABASSI, S. TOBIN, S. VITALE, V. WAND, H. WARD, W. J. WEBER and P. ZWEIFEL.

The LTP experiment on the LISA pathfinder mission.

Class. Quantum Grav., volume 22: (2005) pages 125–138.

(Cited on page 6.)

C. BRAXMAIER, G. HEINZEL, K. F. MIDDLETON, M. E. CALDWELL, W. KONRAD, H. STOCKBURGER, S. LUCARELLI, M. B. TE PLATE, V. WAND, A. C. GARCIA, F. DRAAISMA, J. PIJNENBURG, D. I. ROBERTSON, C. KILLOW, H. WARD, K. DANZMANN and U. A. JOHANN.

LISA pathfinder optical interferometry.

In J. HOUGH and G. H. SANDERS, editors, *Gravitational Wave and Particle Astrophysics Detectors.*, volume 5500 (2004) pages 164–173.

doi:10.1117/12.555266.

(Cited on page 10.)

P. BURDACK, M. TRÖBS, M. HUNNEKUHLE, C. FALLNICH and I. FREITAG.

Modulation-free sub-Doppler laser frequency stabilization to molecular iodine with a common-path, two-color interferometer.

OE, volume 12: (2004) pages 644–650.

(Cited on page 25.)

L. W. COUCH II.

Digital and analog communication systems.

Prentice Hall (1997).

(Cited on pages xv, 161, 179, and 181.)

ESA-SCI.

- LISA Laser Interferometer Space Antenna* (2000).
(Cited on page 119.)
- M. FRIGO.
A Fast Fourier Transform Compiler.
(Cited on pages 43, 45, and 173.)
- M. FRIGO and S. G. JOHNSON.
Eftw software package.
available from <http://www.fftw.org> ().
(Cited on pages 43 and 45.)
- M. FRIGO and S. G. JOHNSON.
The Fastest Fourier Transform in the West.
Technical Report MIT-LCS-TR-728, MIT (1997).
(Cited on pages 43, 45, and 173.)
- A. F. GARCÍA MARIN, G. HEINZEL, R. SCHILLING, A. RÜDIGER, V. WAND,
F. STEIER, F. G. CERVANTES, A. WEIDNER, O. JENNRICH, F. J. M. MECA and
K. DANZMANN.
Phase locking to a LISA arm: first results on a hardware model.
Class. Quantum Grav., volume 22: (2005) pages 235–242.
(Cited on page 153.)
- G. HEINZEL.
Advanced optical techniques for laser-interferometric gravitational-wave detectors.
Ph.D. thesis, Universität Hannover (1999).
MPQ-Report 243.
(Cited on pages 12, 90, and 91.)
- G. HEINZEL, C. BRAXMAIER, M. CALDWELL, K. DANZMANN, F. DRAAISMA,
A. GARCÍA, J. HOUGH, O. JENNRICH, U. JOHANN, C. KILLOW, K. MIDDLETON,
M. TE PLATE, D. ROBERTSON, A. RÜDIGER, R. SCHILLING, F. STEIER, V. WAND
and H. WARD.
*Successful testing of the LISA technology package (LTP) interferometer engineering
model*.
Class. Quantum Grav., volume 22: (2005a) pages 149–154.
(Cited on pages 10 and 124.)
- G. HEINZEL and S. HERDEN.
Optical Bench for SMART2, wp2300:Polarization Optics Pre-Experiments.
Technical report, AEI Hannover (2002).
(Cited on page 31.)

- G. HEINZEL, A. RÜDIGER and R. SCHILLING.
Spectrum and spectral density estimation by the Discrete Fourier transform (DFT), including a comprehensive list of window functions and some new at-top windows.
Technical report, Max-Planck-Institut für Gravitationsphysik (Albert-Einstein-Institut) (2002a).
(Cited on page [102](#).)
- G. HEINZEL, V. WAND and A. GARCÍA.
Lisa Pathfinder Optical Bench Engineering model: functional and performance tests-Test Report.
Technical report, AEI Hannover (2004a).
(Cited on page [53](#).)
- G. HEINZEL, V. WAND, A. GARCÍA, F. GUZMÁN, F. STEIER, C. KILLOW, D. ROBERTSON, H. WARD and C. BRAXMAIER.
S2-AEI-TN-3028: Investigation of noise sources in the LTP interferometer.
Technical report, AEI Hannover (2005b).
(Cited on pages [76](#) and [85](#).)
- G. HEINZEL, V. WAND, A. GARCÍA, O. JENNRICH, C. BRAXMAIER, D. ROBERTSON, K. MIDDLETON, D. HOYLAND, A. RÜDIGER, R. SCHILLING, U. JOHANN and K. DANZMANN.
The LTP interferometer and phasemeter.
Class. Quantum Grav., volume 21: (2004b) pages 581–587.
(Cited on pages [42](#), [45](#), and [63](#).)
- G. HEINZEL, V. WAND and A. F. GARCÍA.
Optical Bench for SMART₂, wp3100: Preinvestigation of Differential Wavefront Sensing.
Technical report, AEI Hannover (2002b).
(Cited on page [51](#).)
- G. HEINZEL, V. WAND and A. F. GARCÍA.
Optical Bench for SMART₂, wp3200:Preinvestigation of Phasemeter.
Technical report, AEI Hannover (2002c).
(Cited on page [19](#).)
- R. W. HELLINGS.
Elimination of clock jitter noise in spaceborne laser interferometers.
PHYSICAL REVIEW D, volume 64, no. 022002.
(Cited on page [157](#).)
- HOROWITZ and HILL.
Die Hohe Schule der Elektronik.
Elektor-Verlag GmbH, Elektor-Verlag GmbH, Aachen (1996).

(Cited on page 164.)

W. KLIPSTEIN, P. G. HALVERSON, R. PETERS, R. CRUZ and D. SHADDOCK.

Clock noise removal in LISA.

AIP Conference Proceedings, LASER INTERFEROMETER SPACE ANTENNA: 6th International LISA Symposium, volume Volume 873: (2006) pages 312–318.

(Cited on pages 122 and 157.)

M. LANDGRAF, M. HECHLER and S. KEMBLE.

Mission design for LISA Pathfinder.

Class. Quantum Grav., volume 22: (2005) pages 487–492.

(Cited on page 6.)

V. LEONHARDT and J. B. CAMP.

Space interferometry application of laser frequency stabilization with molecular iodine.

Appl. Opt., volume 45: (2006) pages 4142–4146.

(Cited on page 153.)

E. MORRISON, B. MEERS, D. ROBERTSON and H. WARD.

Experimental demonstration of an automatic alignment system for optical interferometers.

Appl. Opt.

(Cited on page 50.)

MSTARLABS.

Dap 5216a website.

<http://www.mstarlabs.com/hardware/5216/5216spec.html> ().

(Cited on page 44.)

S. E. POLLACK.

Demonstration of the zero-crossing phasemeter with a LISA test-bed interferometer.

Class. Quantum Grav., pages 4189–4200.

(Cited on page 124.)

D. ROBERTSON, C. KILLOW, H. WARD, J. HOUGH, G. HEINZEL, A. GARCÍA, V. WAND, U. JOHANN and C. BRAXMAIER.

LTP interferometer noise sources and performance.

Class. Quantum Grav., volume 22: (2005) pages S155–S163.

(Cited on pages 42 and 117.)

D. SHADDOCK and G. HEINZEL.

personal communication (2006).

(Cited on page 129.)

- D. SHADDOCK, B. WARE, P. HALVERSON, R. SPERO and B. KLIPSTEIN.
Overview of the LISA phasemeter.
AIP Conference Proceedings, LASER INTERFEROMETER SPACE ANTENNA: 6th International LISA Symposium, volume Volume 873: (2006) pages 654–660.
(Cited on pages [119](#) and [126](#).)
- D. A. SHADDOCK.
Data combinations accounting for LISA spacecraft motion.
Phys. Rev. D, volume 68, no. 061303.
(Cited on pages [122](#) and [156](#).)
- B. S. SHEARD.
Discussion of frequency noise requirements for LISA.
internal note ().
(Cited on page [155](#).)
- B. S. SHEARD.
Laser frequency stabilization by locking to a LISA arm.
Physics Letters A, volume 320: (2003) pages 9–21.
(Cited on page [153](#).)
- B. S. SHEARD, M. B. GRAY, D. A. SHADDOCK and D. E. MCCLELLAND.
Laser frequency noise suppression by arm-locking in LISA: progress towards a bench-top demonstration.
Class. Quantum Grav., volume 22(10): (2005) pages 221–226.
(Cited on page [153](#).)
- J. I. THORPE.
Laboratory studies of arm-locking using the laser interferometer space antenna simulator at the University of Florida.
Ph.D. thesis (2006).
(Cited on page [119](#).)
- J. I. THORPE and G. MÜLLER.
Experimental verification of armlocking for LISA using electronic phase delay.
Phys. Lett. A, volume 342: (2005) pages 199–204.
(Cited on page [153](#).)
- M. TINTO and J. W. ARMSTRONG.
Cancellation of laser noise in an unequal-arm interferometer detector of gravitational radiation.
PHYSICAL REVIEW D, volume 59.
(Cited on page [155](#).)

- M. TINTO, F. B. ESTABROOK and J. ARMSTRONG.
Time-delay interferometry for LISA.
Phys. Rev. D, volume 65, no. 082003.
(Cited on pages 153 and 155.)
- M. TINTO, D. A. SHADDOCK, J. SYLVESTRE and J. W. ARMSTRONG.
Implementation of time-delay interferometry for LISA.
PHYSICAL REVIEW D, volume 67.
(Cited on pages 155 and 156.)
- M. TRÖBS.
Laser development and stabilization for the spaceborne interferometric gravitational wave detector LISA.
Ph.D. thesis, University Hannover (2005).
(Cited on page 25.)
- M. TRÖBS and G. HEINZEL.
Improved spectrum estimation from digitized time series on a logarithmic frequency axis.
Measurement, volume 39: (2006) pages 120–129.
(Cited on page xviii.)
- M. TRÖBS, P. WESSELS, C. FALLNICH, M. BODE, I. FREITAG, S. SKORUPKA, G. HEINZEL and K. DANZMANN.
Laser development for LISA.
Class. Quantum Grav., volume 23, no. 8: (2006) pages 151–158.
(Cited on page 153.)
- S. VITALE.
LISA and its in-flight test precursor SMART-2.
Nucl. Phys. B, Proc. Suppl., volume 110: (2002) pages 209–216.
(Cited on page 7.)
- V. WAND.
Heterodyn Interferometrie uns Phasenauslesung für die wissenschaftliche Weltraummission SMART2 (2003).
(Cited on page 42.)
- V. WAND, J. BOGENSTAHL, C. BRAXMAIER, K. DANZMANN, A. GARCÍA, F. GUZMÁN, G. HEINZEL, J. HOUGH, O. JENNRICH, C. KILLOW, D. ROBERTSON, Z. SODNIK, F. STEIER and H. WARD.
Noise sources in the LTP heterodyne interferometer.
Class. Quantum Grav., volume 23, no. 8: (2006) pages 159–167.
(Cited on page 124.)

- B. WARE, W. FOLKNER, D. SHADDOCK, R. SPERO, P. HALVERSON, I. HARRIS and T. ROGSTAD.
Phase measurement system for inter-spacecraft laser metrology.
Proceedings of the sixth annual NASA Earth Science Technology Conference.
(Cited on page [126](#).)
- L. WERNER, R. FRIEDRICH, U. JOHANNSEN and A. STEIGER.
Precise scale of spectral responsivity for InGaAs detectors based on a cryogenic radiometer and several laser sources.
Metrologia, volume 337, no. Issue 5: (2000) pages 523–526.
(Cited on page [36](#).)
- C. M. WU and J. LAWALL.
Heterodyne interferometer with subatomic periodic nonlinearity.
Applied Optics, volume 38, no. 19.
(Cited on page [176](#).)
- C. M. WU and C. S. SU.
Nonlinearity in measurements of length by optical interferometry.
Meas. Sci. Technol., volume 7: (1996) pages 62–68.
(Cited on page [176](#).)
- A. YARIV.
Quantum electronics.
J. Wiley & Sons, 3rd edition (1989).
(Cited on page [26](#).)

DANKSAGUNG

"Keine Schuld ist dringender, als die, Dank zu sagen."

MARCUS TULLIUS CICERO
(106-43), röm. Redner u. Schriftsteller

LISA ist ein faszinierendes Projekt, welches dutzende von Herausforderungen bietet und unzählige Möglichkeiten eröffnet verschiedenste Aspekte der Physik zu studieren. Diese Vielseitigkeit der Arbeit war für mich eine großartige Erfahrung.

Auf der Titelseite dieser Arbeit erscheint zwar nur ein Name, dennoch ist diese Arbeit das Ergebnis des Zusammenwirkens vieler Menschen, denen ich an dieser Stelle meinen Dank ausdrücken möchte:

Prof. Dr. Karsten Danzmann möchte ich an erster Stelle dafür danken, die Chance gehabt zu haben, am Projekt LISA mitwirken zu können, sowie für seine Betreuung und das Interesse an meiner Arbeit. In zahlreichen Projektmeetings haben seine Ideen maßgeblich zur erfolgreichen Durchführung dieser Arbeit beigetragen. Nicht zuletzt hat er mich durch seine Persönlichkeit stets motiviert und inspiriert.

Prof. Dr. Wolfgang Ertmer danke ich für die Übernahme des Korreferates dieser Arbeit.

Die Zusammenarbeit mit Dr. Gerhard Heinzel hat mein wissenschaftliches Denken und Arbeiten nachhaltig geprägt. Mein besonderer Dank gilt ihm für seine umfassende Unterstützung. Die zahlreichen Diskussionen und die gemeinsame Projektarbeit machten die vorliegende Arbeit erst möglich.

Die Zusammenarbeit mit der LISA/LISA-Pathfinder Gruppe des AEI Hannover und deren Beiträge zur erfolgreichen Implementierung der LISA Pathfinder Interferometrie waren sehr hilfreich. Ich danke Antonio F. García Marín, Frank Steier und Felipe Guzmán Cervantes für ihren tatkräftigen Einsatz insbesondere bei der Aufklärung des *kleinen Vektors*.

Gerne erinnere ich mich an die Besuche von Dr. Oliver Jennrich. Die Zeiten seines Verweilens am AEI haben stets *progress* beschehrt.

Nicht zu vergessen ist der Einsatz unseres Projektmanagers Dr. Jens Reiche, der für einen (für mich) reibungslosen Projektablauf sorgte.

Vielen Dank an die elektronische Werkstatt, besonders an Heiko zur Mühlen, der auch nicht davor zurückschreckte, Lötarbeiten an *meinem* 208-Pin Chip vorzunehmen. Andreas Weidner danke ich herzlich für die Unterstützung in Eagle Fragen und bei der Umsetzung des Board Layouts des Phasemeter Prototyps.

Philipp Schauzu, Hans-Joachim Melching, Jan Diedrich und Stefan Bertram aus der feinmechanischen Werkstatt danke ich für die präzise und prompte - wenn notwendig - auch unkonventionelle Lösung technischer Probleme.

Vielen herzlichen Dank an die Korrektoren. Felipe Guzman Cervantes, Dr. Gerhard Heinzl, Dr. Benjamin Sheard, Frank Steier, Dr. Michael Tröbs und Konstanze Wand haben in z.T. nächtlichem Einsatz und durch zahlreiche Hinweise diese Arbeit verbessert und bereichert. Selbstverständlich bin ich, für verbleibendes *Ungemach*, verantwortlich.

Herzlichen Dank auch an die L^AT_EX-Gemeinde für eine grossartige Software und insbesondere an André Miede für die Diskussionen über sein *Classicthesis*-Template, welches typographische Grundlage dieser Arbeit ist.

Meiner Familie danke ich für die Liebe und das mir entgegengebrachte Verständnis.

Ganz wichtig war auch die emotionale Unterstützung meiner Freunde. Gerne denke ich an die in Zeiten des Stillstands befreienden Bowling Nächte mit Sascha, Matze und Waldi zurück.

Nicht genug danken kann ich meiner lieben Frau Konstanze. Ihr widme ich diese Arbeit.

CURRICULUM VITAE

VINZENZ WAND

Kleine Pfahlstrasse 15
30161 Hannover
Germany

Date of birth: 13th of November, 1976
Place of birth: Hagenow/Mecklenburg, Germany
Marital status: married, no children

since 04/2007	Postdoctoral research fellow, Department of Physics University of Florida, USA
04/2003–05/2007	Ph.D. studies at the Max Planck Institute and Gottfried Wilhelm Leibniz Universität, Hannover
2002–05/2007	Scientific Assistant
11/2001–03/2003	Diploma thesis in Physics at the University of Hannover
10/1997–11/2001	Diploma studies in Physics at the University of Hannover
11/1998 – 01/2000	Managing partner of IT networks company
10/1994–10/1997	Undergraduate studies in physics at the University of Hannover
07/1994	High school degree (Abitur), Gymnasium Hagenow
09/1993–10/1999	Adult education: teaching in an adult education center in Hagenow as IT lecturer
09/1990 - 07/1994	Gymnasium Hagenow
09/1982 - 08/1990	Polytechnische Oberschule Hagenow

PUBLICATIONS

PUBLISHED IN JOURNALS

1. *LISA Phasemeter development*
VINZENZ WAND, FELIPE GUZMÁN, GERHARD HEINZEL AND KARSTEN DANZMANN, 2006, AIP Conference Proceedings Volume 873 LASER INTERFEROMETER SPACE ANTENNA: 6th International LISA Symposium
2. *Interferometric characterization of the optical window for LISA Pathfinder and LISA*
ANTONIO F. GARCÍA MARÍN, JOHANNA BOGENSTAHL, FELIPE GUZMÁN CERVANTES, FRANK STEIER, JENS REICHE, SASCHA SKORUPKA, VINZENZ WAND, MIQUEL NOFRARIAS, JOSEP SANJUAN, OLIVER JENNRICH, GERHARD HEINZEL AND KARSTEN DANZMANN, 2006, AIP Conference Proceedings Volume 873 LASER INTERFEROMETER SPACE ANTENNA: 6th International LISA Symposium
3. *Noise sources in the LTP heterodyne interferometer*
V. WAND, J. BOGENSTAHL, C. BRAXMAIER, K. DANZMANN, A. GARCÍA, F. GUZMÁN, G. HEINZEL, J. HOUGH, O. JENNRICH, C. KILLOW, D. ROBERTSON, Z. SODNIK, F. STEIER AND H. WARD, 2006 Class. Quantum Grav. 23, pp. 159–167 doi:10.1088/0264-9381/23/8/S21
4. *On-orbit alignment and diagnostics for the LISA Technology Package*
A. F. GARCÍA MARÍN, V. WAND, F. STEIER, F. GUZMÁN CERVANTES, J. BOGENSTAHL, O. JENNRICH, G. HEINZEL AND K. DANZMANN, 2006 Class. Quantum Grav. 23, pp. 133–140 doi:10.1088/0264-9381/23/8/S18
5. *Interferometry for the LISA technology package LTP: an update*
G. HEINZEL, J. BOGENSTAHL, C. BRAXMAIER, K. DANZMANN, A. GARCÍA, F. GUZMÁN, J. HOUGH, D. HOYLAND, O. JENNRICH, C. KILLOW, D. ROBERTSON, Z. SODNIK, F. STEIER, H. WARD AND V. WAND, 2006 J. Phys.: Conf. Ser. 32, pp. 132–136 doi:10.1088/1742-6596/32/1/021

6. *The LTP experiment on the LISA Pathfinder mission*

S. ANZA, M. ARMANO, E. BALAGUER, M. BENEDETTI, C. BOATELLA, P. BOSETTI, D. BORTOLUZZI, N. BRANDT, C. BRAXMAIER, M. CALDWELL, L. CARBONE, A. CAVALLERI, A. CICCOLELLA, I. CRISTOFOLINI, M. CRUISE, M. DA LIO, K. DANZMANN, D. DESIDERIO, R. DOLESI, N. DUNBAR, W. FICHTER, C. GARCIA, E. GARCIA-BERRO, A. F. GARCIA MARIN, R. GERNDT, A. GIANOLIO, D. GIARDINI, R. GRUENAGEL, A. HAMMESFAHR, G. HEINZEL, J. HOUGH, D. HOYLAND, M. HUELLER, O. JENNRICH, U. JOHANN, S. KEMBLE, C. KILLOW, D. KOLBE, M. LANDGRAF, A. LOBO, V. LORIZZO, D. MANCE, K. MIDDLETON, F. NAPPO, M. NOFRARIAS, G. RACCA, J. RAMOS, D. ROBERTSON, M. SALLUSTI, M. SANDFORD, J. SANJUAN, P. SARRA, A. SELIG, D. SHAUL, D. SMART, M. SMIT, L. STAGNARO, T. SUMNER, C. TIRABASSI, S. TOBIN, S. VITALE, V. WAND, H. WARD, W. J. WEBER AND P. ZWEIFEL, 2005 *Class. Quantum Grav.* 22, pp. 125–138 doi:10.1088/0264-9381/22/10/001

7. *Successful testing of the LISA Technology Package (LTP) interferometer engineering model*

G. HEINZEL, C. BRAXMAIER, M. CALDWELL, K. DANZMANN, F. DRAAISMA, A. GARCÍA, J. HOUGH, O. JENNRICH, U. JOHANN, C. KILLOW, K. MIDDLETON, M. TE PLATE, D. ROBERTSON, A. RÜDIGER, R. SCHILLING, F. STEIER, V. WAND AND H. WARD, 2005 *Class. Quantum Grav.* 22, pp. 149–154 doi:10.1088/0264-9381/22/10/003

8. *LTP interferometer noise sources and performance*

DAVID ROBERTSON, CHRISTIAN KILLOW, HARRY WARD, JIM HOUGH, GERHARD HEINZEL, ANTONIO GARCÍA, VINZENZ WAND, ULRICH JOHANN AND CLAUS BRAXMAIER, 2005 *Class. Quantum Grav.* 22, pp. 155–163 doi:10.1088/0264-9381/22/10/004

9. *Phase locking to a LISA arm: first results on a hardware model*

ANTONIO F GARCÍA MARÍN, GERHARD HEINZEL, ROLAND SCHILLING, ALBRECHT RÜDIGER, VINZENZ WAND, FRANK STEIER, FELIPE GUZMÁN CERVANTES, ANDREAS WEIDNER, OLIVER JENNRICH, FRANCISCO J MECA MECA AND KARSTEN DANZMANN, 2005 *Class. Quantum Grav.* 22, pp. 235–242 doi:10.1088/0264-9381/22/10/015

10. *LISA pathfinder optical interferometry*
C. BRAXMAIER, G. HEINZEL, K.F. MIDDLETON, M.E. CALDWELL, W. KONRAD, H. STOCKBURGER, S. LUCARELLI, M.B. TE PLATE, V. WAND, A. GARCÍA, F. DRAAISMA, J. PIJNENBURG, D.I. ROBERTSON, C. KILLOW, H. WARD, K. DANZMANN, U.A. JOHANN, 2004, Gravitational Wave and Particle Astrophysics Detectors. Edited by Hough, James; Sanders, Gary H. Proceedings of the SPIE, Volume 5500, pp. 164–173
11. *The LTP interferometer and phasemeter*
G. HEINZEL, V. WAND, A. GARCÍA, O. JENNRICH, C. BRAXMAIER, D. ROBERTSON, K. MIDDLETON, D. HOYLAND, A. RÜDIGER, R. SCHILLING, U. JOHANN AND K. DANZMANN, 2004 Class. Quantum Grav. 21, pp. 581–587 doi:10.1088/0264-9381/21/5/029
12. *Interferometry for the LISA technology package (LTP) aboard SMART-2*
G. HEINZEL, C. BRAXMAIER, R. SCHILLING, A. RUDIGER, D. ROBERTSON, M. TE PLATE, V. WAND, K. ARAI, U. JOHANN AND K. DANZMANN, 2003 Class. Quantum Grav. 20, pp. 153–161 doi:10.1088/0264-9381/20/10/318
13. *Phasenauslesung für die wissenschaftliche Weltraummission SMART-2*
V. WAND, Diploma Thesis, University Hannover, 2003

TECHNICAL NOTES (SELECTION)

1. *Optical Bench for SMART₂, WP₃₁₀₀: Preinvestigation of Differential Wavefront Sensing*
G. HEINZEL, V. WAND AND A. F. GARCIA, 2002, AEI Hannover
2. *Optical Bench for SMART₂, WP₃₂₀₀: Preinvestigation of Phasemeter*
G. HEINZEL, V. WAND AND A. F. GARCÍA, 2002, AEI Hannover
3. *S₂-AEI-TN-3017: Lisa Pathfinder Optical Bench Engineering model: functional and performance tests-Test Report*
GERHARD HEINZEL, VINZENZ WAND AND ANTONIO GARCÍA, 2004, AEI Hannover
4. *S₂-AEI-TN-3028: Investigation of noise sources in the LTP interferometer*
G. HEINZEL, V. WAND, A. GARCÍA, F. GUZMÁN, F. STEIER, C. KILLOW, D. ROBERTSON, H. WARD, C. BRAXMAIER, 2005, AEI Hannover, University of Glasgow, EADS Immenstaad